VOL. 107 NO. GT10. OCT. 1981

JOURNAL OF THE GEOTECHNICAL ENGINEERING DIVISION

PROCEEDINGS OF
THE AMERICAN SOCIETY
OF CIVIL ENGINEERS

VOL.107 NO.GT10. OCT. 1981

JOURNAL OF THE GEOTECHNICAL ENGINEERING DIVISION

PROCEEDINGS OF
THE AMERICAN SOCIETY
OF CIVIL ENGINEERS

Copyright© 1981 by
American Society
of Civil Engineers
All Rights Reserved
ISSN 0093-6405

William F. Marcuson III, Editor
U.S. Army Engineers

AMERICAN SOCIETY OF CIVIL ENGINEERS

BOARD OF DIRECTION

President
Irvan F. Mendenhall

Past President
Joseph S. Ward

President Elect
James R. Sims

Vice Presidents
Robert D. Bay
Francis J. Connell
Lyman R. Gillis
Albert A. Grant

Directors
Martin G. Abegg
Floyd A. Bishop
L. Gary Byrd
Larry J. Feeser
John A. Focht, Jr.
Sergio Gonzalez-Karg
James E. Humphrey, Jr.
Richard W. Karn
Leon D. Luck
Arthur R. McDaniel
Paul R. Munger
William R. Neuman
Leonard S. Oberman
John D. Parkhurst
Celestino R. Pennoni
Robert B. Rhode
S. Russell Stearns
William H. Taylor
Stafford E. Thornton
Robert E. Whiteside
Richard S. Woodruff

EXECUTIVE OFFICERS

Eugene Zwoyer, *Executive Director*
Julie E. Gibouleau, *Assistant to the Executive Director*
Louis L. Meier, *Washington Counsel/Assistant Secretary*
William H. Wisely, *Executive Director Emeritus*
Michael N. Salgo, *Treasurer*
Elmer B. Isaak, *Assistant Treasurer*

STAFF DIRECTORS

Donald A. Buzzell, *Managing Director for Education and Professional Affairs*
Robert A. Crist, Jr., *Managing Director for Publications and Technical Affairs*
Alexandra Bellow, *Director, Human Resources*
David Dresia, *Director, Publications Production and Marketing*
Barker D. Herr, *Director, Membership*
Richard A. Jeffers, *Controller*
Carl E. Nelson, *Director, Field Services*
Don P. Reynolds, *Director, Policy, Planning and Public Affairs*
Bruce Rickerson, *Director, Legislative Services*
Albert W. Turchick, *Director, Technical Services*
George K. Wadlin, *Director, Education Services*
R. Lawrence Whipple, *Director, Engineering Management Services*

COMMITTEE ON PUBLICATIONS

Stafford E. Thornton, *Chairman*
Martin G. Abegg
John A. Focht, Jr.
Richard W. Karn
Paul R. Munger
William R. Neuman

GEOTECHNICAL ENGINEERING DIVISION

Executive Committee
Robert Schuster, *Chairman*
Ernest T. Selig, *Vice Chairman*
William F. Swiger
Harvey E. Wahls
Robert T. Darragh, Jr., *Secretary*
Roy E. Olson, *Management Group E Contact Member*

Publications Committee
William F. Marcuson III, ***Chairman and Editor***
O. B. Andersland
John E. Anderson
Warren J. Baker
Don C. Banks
James M. Bell
Chandra S. Brahama
John T. Christian
G. W. Clough
Tuncer B. Edil
Herbert H. Einstein
Arley G. Franklin
D. H. Gray
Bobby Hardin
Cornelius J. Higgins
William H. Highter
Robert D. Holtz
Izzat M. Idriss
L. H. Irwin
Jey K. Jeyapalan
Reuben H. Karol
H. Y. Ko
William D. Kovacs
Leland M. Kraft
Raymond J. Krizek
C. C. Ladd
Poul V. Lade
Leonard J. Langfelder
Felipe A. Len-Rios
Gholamreza Mesri
Donald J. Murphy
S. V. Nathan
Thom L. Neff
Edward A. Nowatzki
Michael W. O'Neill
Jean H. Prevost
Adel Saada
Surendra K. Saxena
Robert L. Schiffman
Woodland G. Schockley
Marshall L. Silver
G. R. Thiers
D. D. Treadwell
Charles R. Ullrich
J. Lawrence Von Thun
R. N. Yong
E. T. Selig, *Exec. Comm. Contact Member*

PUBLICATION SERVICES DEPARTMENT

David Dresia, *Director, Publications Production and Marketing*

Technical and Professional Publications

Richard R. Torrens, *Manager*
Chuck Wahrhaftig, *Chief Copy Editor*
Corinne Bernstein, *Copy Editor*
Linda Ellington, *Copy Editor*
Walter Friedman, *Copy Editor*
Shiela Menaker, *Production Co-ordinator*
Richard C. Scheblein, *Draftsman*

Information Services

Melanie G. Edwards, *Editor*

PERMISSION TO PHOTOCOPY JOURNAL PAPERS

Permission to photocopy for personal or internal reference beyond the limits in Sections 107 and 108 of the U.S. Copyright Law is granted by the American Society of Civil Engineers for libraries and other users registered with the Copyright Clearance Center, 21 Congress Street, Salem, Mass. 01970, provided the appropriate fee is paid to the CCC for all articles bearing the CCC code. Requests for special permission or bulk copying should be addressed to the Manager of Technical and Professional Publications, American Society of Civil Engineers.

CONTENTS

Geotechnical Applications of Borehole Geophysics
by James W. Crosby III, Byron Konstantinidis, and Paul Davis 1255

Field and Laboratory Determination of Soil Moduli
by William F. Marcuson III and Joseph R. Curro 1269

Sand Waves in Lower Cook Inlet, Alaska
by Arshud Mahmood, Clarence J. Ehlers, and Blase A. Cilweck 1293

Seismic Techniques in the Laboratory
by Richard D. Woods and Robert Henke . . . . . -1309

Drilled-Shaft Integrity by Wave Propagation Method
by Thomas M. Hearne, Jr., Kenneth H. Stokoe II, and Lyndon C. Reese 1327

Estimation of SPT-N and Relative Density
by Michael N. Fardis and Daniele Veneziano 1345

Statistical Analysis of Sand Liquefaction
by Michael N. Fardis and Daniele Veneziano 1361

The Journal of the Geotechnical Engineering Division (ISSN 0093-6405) is published monthly by the American Society of Civil Engineers. Publications office is at 345 East 47th Street, New York, N.Y. 10017. Address all ASCE correspondence to the Editorial and General Offices at 345 East 47th Street, New York, N.Y. 10017. Allow six weeks for change of address to become effective. Subscription price to members is $16.00. Nonmember subscriptions available; prices obtainable on request. Second-class postage paid at New York, N.Y. and at additional mailing offices. GT.

POSTMASTER: Send address changes to American Society of Civil Engineers, 345 East 47th Street, New York, NY 10017.

The Society is not responsible for any statement made or opinion expressed in its publications.

Time-Dependent Behavior of Solution Caverns in Salt
by Jamshid Ghaboussi, Randall E. Ranken, and Alfred J. Hendron . . . 1379

Road on Peat: Observations and Design
by Edward T. Hanrahan and Martin G. Rogers 1403

TECHNICAL NOTES

Proc. Paper 16530

Instrumentation Corrections to Wave Velocity Data
by John R. Hall, Jr., John T. Christian, Eduardo Kausel, and James L. Wolfgang 1419

Total Lateral Surcharge Pressure Due to Strip Load
by Ramon Jarquio 1424

Embedded Foundations under Vertical Vibration
by A. Sridharan, M. V. Nagendra, and C. Chinnaswamy 1429

DISCUSSION

Proc. Paper 16525

Particle Contacts in Discrete Materials,* by Dimitri Athanasiou-Grivas and Milton E. Harr (May, 1980).
by Roland Gourves 1437
by Robert D. Holtz 1437
closure 1440

Response of Buried Structures to Traveling Waves, by Richard N. Hwang and John Lysmer (Feb., 1981).
errata 1441

*Discussion period closed for this paper. Any other discussion received during this discussion period will be published in subsequent Journals.

16585 GEOTECHNICAL APPLICATIONS OF BOREHOLE GEOPHYSICS

KEY WORDS: **Borehole geophysics;** Borehole logging; **Boreholes;** Consultants; Density; Geophysical exploration; **Geophysical logging; Instrumentation; Miniaturization;** Moisture content; Porosity

ABSTRACT: Miniaturization of instrumentation has opened up the use of borehole geophysical techniques to geotechnical consultants, but most are not yet acquainted with the capabilities of the procedures. Borehole geophysics has been used widely in studies of nuclear power plant sites, waste disposal problems, and local and regional geohydrological relationships. Most investigations have been oriented toward stratigraphic correlation and assessment of lithologies. However, there is a wealth of semi-quantitative or quantitative data available which is often overlooked. Because of the environments in which the geotechnical specialist works, exploratory borings are most frequently cased, and the radiation group of geophysical devices must be used. In properly engineering borings and with appropriate calibration, these devices can evaluate moisture content, density, and porosity.

REFERENCE: Crosby, James W., III (Prof. and Head of Geological Engrg. Section, Dept. of Civ. & Environmental Engrg., Washington State Univ., Pullman, Wash. 99164), Konstantinidis, Byron, and Davis, Paul, "Geotechnical Applications of Borehole Geophysics," *Journal of the Geotechnical Engineering Division,* ASCE, Vol. 107, No. GT10, **Proc. Paper 16585**, October, 1981, pp. 1255-1267

16591 DETERMINATION OF SOIL MODULI

KEY WORDS: Damping; **Dynamic properties;** Field tests; **Foundation stability analysis;** Laboratory tests; **Shear modulus; Soil stresses;** Strain; Wave velocity; **Youngs modulus**

ABSTRACT: A field geophysical investigation was performed to determine the shear and Young's moduli as a function of depth for a site in southern Ohio. This investigation included crosshole, downhole, surface refraction, and surface vibratory techniques. A supplementary set of laboratory resonant column tests was performed with the Drnevich resonant column device. Laboratory undisturbed specimens were excited in both the longitudinal and torsional modes to obtain both shear and Young's moduli as a function of strain. Both laboratory and field data are presented and compared.

REFERENCE: Marcuson, William F., III (Research Civ. Engr., Geotechnical Laboratory, U.S. Army Engr. Waterways Experiment Station, Vicksburg, Miss), and Curro, Joseph R., Jr., "Field and Laboratory Determination of Soil Moduli," *Journal of the Geotechnical Engineering Division,* ASCE, Vol. 107, No. GT10, **Proc. Paper 16591**, October, 1981, pp. 1269-1291

16583 SAND WAVES IN LOWER COOK INLET, ALASKA

KEY WORDS: Acoustic measurement; **Acoustic surveillance;** Alaska; Flow patterns; **Geological surveys;** Geophysical exploration; **Geophysical surveys; Marine engineering; Ocean bottom;** Offshore structures; **Sand waves**

ABSTRACT: Acoustic (geophysical) methods were applied to investigate the sea-floor geological conditions, particularly sand waves, which might place constraints on construction in an area of potential offshore development in lower Cook Inlet, Alaska. Multisystem, high resolution, marine acoustic survey data were collected using a sparker, tuned transducer, acoustipulse, fathometer, and side-scan sonar. Based on 65 sea-floor samples obtained in the northern portion of the study area, the sea-floor soils consisted of over 90 percent sand by volume. This portion of lower Cook Inlet contained the most numerous sand waves and contained sand waves of 5 ft (1.5 m) or greater height over an 80 percent length of the survey lines. The possibility of sand wave movement is examined by reviewing the two phase (water-sand) flow regime and by repeat geophysical profiling. The present flow regime appears to be conducive to the formation of ripples and dunes, but tidal flow durations may be insufficient for the formation of large bedforms.

REFERENCE: Mahmood, Arshud A. (Engr. Mgr., McClelland Engineers, Inc., Houston, Texas), Ehlers, Clarence J., and Cilweck, Blase A., "Sand Waves in Lower Cook Inlet, Alaska," *Journal of the Geotechnical Engineering Division,* ASCE, Vol. 107, No. GT10, **Proc. Paper 16583**, October, 1981, pp. 1293-1307

16599 SEISMIC TECHNIQUES IN THE LABORATORY

KEY WORDS: Bulk modulus; Compression waves; Geophysics; **Laboratory tests; Rayleigh waves;** Seismic studies; **Seismic tests; Shear modulus;** Shear waves; **Soil dynamics; Velocity**

ABSTRACT: Applications of scaled-down seismic cross-hole and steady-state Rayleigh wave tests to characterize dynamic soil properties in laboratory facilities are described. The nondestructive nature of seismic tests make them highly advantageous in laboratory settings. The major changes in test procedures and equipment to scale-down from field seismic tests are associated with: (1) Size and energy content of seismic source; (2) receiver size and sensitivity; (3) wave speed timing; (4) electronic triggering requirements; and (5) precision of distance or spacing measurements, or both. The seismic cross-hole test proved to be most effective in determining the spacial and temporal variation of elastic soil properties and proved to be a very sensitive indicator of small changes in confining pressure. In addition, a sand bin testing facility which is fitted with air bags to provide surface confining pressure and new torsional cross-hole hammer are described.

REFERENCE: Woods, Richard D. (Prof. of Civ. Engrg., Univ. of Michigan, Ann Arbor, Mich.), and Henke, Robert, "Seismic Techniques in the Laboratory," *Journal of the Geotechnical Engineering Division,* ASCE, Vol. 107, No. GT10, **Proc. Paper 16599**, October, 1981, pp. 1309-1325

16582 DRILLED SHAFT INTEGRITY

KEY WORDS: **Compression waves;** Concrete; Deep foundations; Field tests; **Nondestructive tests;** Piers; **Shafts;** Soil mechanics; **Structural analysis; Wave propagation**

ABSTRACT: Compression wave propagation methods provide an economical and rapid nondestructive means of assessing the structural integrity of drilled shafts shortly after construction. Several source-receiver configurations can be employed. The most successful configuration used involved a mechanical hammer with which a vertical impulse was applied at the top of the shaft and vertical velocity transducers which were cast in place in the shaft at preselected depths. Successful application of this configuration required identification of reflected compression wave arrivals with transducers allowing travel times of reflected waves to be used with propagation velocity to determine elevations of reflection points. Examples of the results for tests with sound shafts and for shafts with known defects of different sizes are presented.

REFERENCE: Hearne, Thomas M., Jr. (Research Asst., Dept. of Civ. Engrg., Univ. of Texas, Austin, Tex. 78712), Stokoe, Kenneth H., II, and Reese, Lyndon C., "Drilled-Shaft Integrity by Wave Propagation Method," *Journal of the Geotechnical Engineering Division,* ASCE, Vol. 107, No. GT10, **Proc. Paper 16582**, October, 1981, pp. 1327-1344

16590 ESTIMATION OF SPT-N AND RELATIVE DENSITY

KEY WORDS: Field tests; Laboratory tests; Probability theory; **Relative density;** Relative density determination; **Sands; Soil density;** Soil engineering; **Standard penetration tests;** Statistical analysis

ABSTRACT: A consistent set of models is developed for inference of the relative density (D_r) from the blowcount number of the SPT (N) under both laboratory and field conditions. The model in the laboratory (reference model) is based on a large data set, which consists of essentially all available laboratory information on joint measurements of N, D_r and vertical effective stress. It takes explicitly into account errors in the laboratory determination of D_r and is of a form which makes its use particularly simple. The reference model is not directly applicable in situ. However, the model can be applied in the field after a simple, but sometimes depth dependent, modification which requires a few measurements of N and D_r at the site.

REFERENCE: Fardis, Michael A. (Asst. Prof. of Civ. Engrg., Massachusetts Inst. of Technology, Cambridge, Mass.), and Veneziano, Daniele, "Estimation of SPT-N and Relative Density," *Journal of the Geotechnical Engineering Division,* ASCE, Vol. 107, No. GT10, **Proc. Paper 16590**, October, 1981, pp. 1345-1359

16604 STATISTICAL ANALYSIS OF SAND LIQUEFACTION

KEY WORDS: Laboratory tests; **Liquefaction;** Relative density; **Sands; Sandy soils;** Shear stress; **Shear tests;** Statistical analysis

ABSTRACT: A consistent set of stochastic models is developed for the liquefaction resistance of a homogeneous mass of sand, such as a laboratory sample or small element of in situ material. A probabilistic model for liquefaction in the laboratory for undrained simple shear tests is developed first. This model gives the probability distribution of the number of cycles to liquefaction as a function of uniform shear stress amplitude, mean initial effective stress, and relative density. Corrections are quantified and incorporated into the model. Parameters are estimated from a large number of simple shear test results obtained by eight different groups of researchers using several sands and testing techniques. The laboratory liquefaction model is converted into one applicable in the field. Finally, the model is generalized to load cycles with nonuniform shear stress amplitude.

REFERENCE: Fardis, Michael N. (Asst. Prof., Dept. of Civ. Engrg., Mass. Inst. of Technology, Cambridge, Mass.), and Veneziano, Daniele, "Statistical Analysis of Sand Liquefaction," *Journal of the Geotechnical Engineering Division,* ASCE, Vol. 107, No. GT10, **Proc. Paper 16604**, October, 1981, pp. 1361-1377

16597 SOLUTION CAVERNS IN ROCK SALT

KEY WORDS: **Caves; Creep;** Deformation; **Finite elements; Internal pressure; Rock salt; Salt domes; Stress;** Time factors

ABSTRACT: Creep finite-element analyses of several solution caverns in rock salt were performed to study the long-term behavior of such caverns. The effect of cavern shape (height-to-diameter ratio) and the internal pressure on the time-dependent behavior of caverns were the main objectives. The pattern of creep-induced stress changes around the caverns were studied, and the main aspects were demonstrated through the results of the analyses. The cavern volume closures can be expressed by a simple equation as a function of time, and the accuracy of this expression was verified by the results of the analyses. The other aspects of the time-dependent behavior of the caverns studied were: (1) the influence of a drop in internal pressure; (2) the influence of creep deformations on the results and interpretation of pressure tests for cavity tightness; and (3) the influence of gradual cavity growth due to the leaching process as compared to the analysis of cavity assumed at full size initially.

REFERENCE: Ghaboussi, Jameshid (Assoc. Prof., Dept. of Civ. Engrg., Univ of Illinois at Urbana-Champaign, Urbana, Ill.), Hendron, Afred J., Jr., and Ranken, Randall E., "Time-Dependant Behavior of Solution Caverns in Salt," *Journal of the Geotechnical Engineering Division,* ASCE, Vol. 107, No. GT10, **Proc. Paper 16597**, October, 1981, pp. 1379-1401

16588 ROAD ON PEAT: OBSERVATIONS AND DESIGN

KEY WORDS: Consolidation; Deformation; Models; Peat; **Peat bog; Rheology; Road construction; Road design;** Stress; **Time factors**

ABSTRACT: In 1953, a road was reconstructed on a uniform peat bog. Certain lengths were overstressed by an excessive thickness of road material, and in places it was necessary to replace the gravel filling with a light-weight substitute. Road levels and settlements have since been recorded over a period of 26 years. Following an investigation in 1963, a simple method of design was formulated which requires settlement to be separately estimated under three headings: elastic (immediate), consolidation, and creep. These are then added together to give total settlements. Satisfactory agreement was found between observed settlements and those values estimated by the simple method. This agreement is again confirmed after 16 years. During the last twelve years, a general constitutive model has been developed for predicting settlements under three-dimensional stress.

REFERENCE: Hanrahan, Edward T. (Assoc. Prof. of Civ. Engrg., University College, Dublin, Ireland), and Rogers, Martin G., "Road on Peat: Observations and Design," *Journal of the Geotechnical Engineering Division,* ASCE, Vol. 107, No. GT10, **Proc. Paper 16588**, October, 1981, pp. 1403-1415

U.S. Customary-SI Conversion Factors

In accordance with the October, 1970 action of the ASCE Board of Direction, which stated that all publications of the Society should list all measurements in both U.S. Customary and SI (International System) units, the following list contains conversion factors to enable readers to compute the SI unit values of measurements. A complete guide to the SI system and its use has been published by the American Society for Testing and Materials. Copies of this publication (ASTM E-380) can be purchased from ASCE at a price of $3.00 each; orders must be prepaid.

All authors of *Journal* papers are being asked to prepare their papers in this dual-unit format. To provide preliminary assistance to authors, the following list of conversion factors and guides are recommended by the ASCE Committee on Metrication.

To convert	To	Multiply by
inches (in.)	millimeters (mm)	25.4
feet (ft)	meters (m)	0.305
yards (yd)	meters (m)	0.914
miles (miles)	kilometers (km)	1.61
square inches (sq in.)	square millimeters (mm^2)	645
square feet (sq ft)	square meters (m^2)	0.093
square yards (sq yd)	square meters (m^2)	0.836
square miles (sq miles)	square kilometers (km^2)	2.59
acres (acre)	hectares (ha)	0.405
cubic inches (cu in.)	cubic millimeters (mm^3)	16,400
cubic feet (cu ft)	cubic meters (m^3)	0.028
cubic yards (cu yd)	cubic meters (m^3)	0.765
pounds (lb) mass	kilograms (kg)	0.453
tons (ton) mass	kilograms (kg)	907
pound force (lbf)	newtons (N)	4.45
kilogram force (kgf)	newtons (N)	9.81
pounds per square foot (psf)	pascals (Pa)	47.9
pounds per square inch (psi)	kilopascals (kPa)	6.89
U.S. gallons (gal)	liters (L)	3.79
acre-feet (acre-ft)	cubic meters (m^3)	1,233

GEOTECHNICAL APPLICATIONS OF BOREHOLE GEOPHYSICS[a]

By James W. Crosby III,[1] M. ASCE, Byron Konstantinidis,[2] A. M. ASCE, and Paul Davis[3]

INTRODUCTION

Borehole geophysics has been widely used in petroleum exploration and development for nearly half a century. In these applications it has proved to be a tool of great value, but one that is excessively expensive by geotechnical engineering standards. During the last two decades, however, the general availability of inexpensive, miniaturized electronic components has placed these same capabilities at the disposal of the geotechnical consultant. However, the potential for application of borehole geophysics in geotechnical engineering is far from being fully realized. This is primarily because geotechnical engineers, in general, are not familiar with the capabilities of geophysical borehole logging techniques. The purpose of this paper is to demonstrate the capabilities and limitations of geophysical logging as a tool for obtaining both qualitative and quantitative subsurface information.

Geophysical borehole logging has been used extensively by the writers for stratigraphic characterization and correlation. However, quantitative and semi-quantitative information about physical properties such as in-situ moisture content, density, porosity, and degree of saturation can also be derived from the geophysical logs. With proper site specific calibrations, data derived from geophysical logs can be used with a limited amount of laboratory test data to provide a detailed picture of subsurface conditions.

The methodology described in this paper draws upon a well-established body of theoretical knowledge and a variety of studies conducted by the writers over an eight-year period. Most of the field applications have been related to siting studies for nuclear power plants, but others include missile site studies,

[a]Presented at the October 22–26, 1979, ASCE Annual Convention and Exposition, held at Atlanta, Ga.

[1]Prof. and Head of Geological Engrg. Section, Dept. of Civ. and Environmental Engrg., Washington State Univ., Pullman, Wash.

[2]Sr. Engr., Fugro, Inc., Long Beach, Calif.

[3]Chf. Geologist, Medall, Aragon, Worswick & Associates, Inc., Santa Ana, Calif.

Note.—Discussion open until March 1, 1982. To extend the closing date one month, a written request must be filed with the Manager of Technical and Professional Publications, ASCE. Manuscript was submitted for review for possible publication on February 17, 1981. This paper is part of the Journal of the Geotechnical Engineering Division, Proceedings of the American Society of Civil Engineers ©ASCE, Vol. 107, No. GT10, October, 1981. ISSN 0093-6405/81/0010-1255/$01.00.

waste disposal studies, and geohydrological studies. The concepts presented in this paper are illustrated by examples selected from such studies.

Logging Functions

Geophysical logging tools (sondes) have been developed at various times to accomplish various types of downhole measurements. Many are limited application devices, and only a few are routinely used in geotechnical engineering studies. Among the most frequently used tools are those which comprise the radiation and electric groups (Fig. 1). The radiation sondes can be used in cased or uncased holes which are air or fluid-filled. Electric logging tools are generally run in fluid-filled, uncased holes.

Radiation Logs.—The radiation logs are of great interest in geotechnical practice, both from the standpoint of desired information and required flexibility. For their operation, the radiation logs depend upon elementary particles—gamma

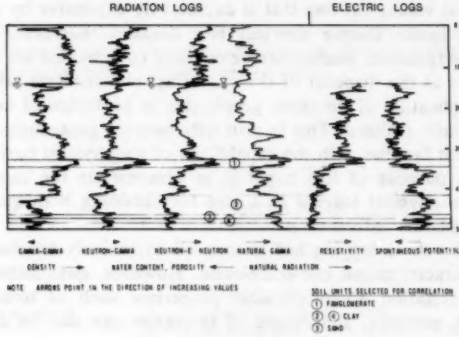

FIG. 1.—Full Suite Geophysical Logs (Sundesert Boring B-DH-35)

photons or neutrons which have the ability to penetrate matter. The gamma photons can be generated naturally by radioactive elements in the tested formations or by fabricated gamma-emitting sources. The neutrons are generated exclusively by introduced sources.

In counting radiation pulses, some form of ratemeter is utilized. Each ratemeter has a characteristic dead time or a time increment between near-coincident pulses less than which the meter cannot discriminate between them. The dead time relationship can be expressed

$$t_d = \frac{R - R_o}{RR_o} \quad \ldots\ldots\ldots\

also incorporate a time constant—a time period, in seconds, over which radiation pulses are averaged). Pulse averaging is accomplished by an integrator, composed of a capacitor in series, with a resistance. With such an integrator it is obvious that the longer the time constant, the closer will be the registered count rate to the average count rate. Similarly, a short time constant will not give a good sample of the average pulse rate because of the statistical variation of the radiation within the averaging period. If a ratemeter is subjected to an instantaneous change from one average count rate to another, the RC circuit will not permit it to react immediately. Instead, the change from the first to the second rate will occur exponentially with time. In borehole logging the time constant associated with a moving sonde has the effect of slurring lithologic contacts in the direction of logging.

To compensate for this slurring effect, the digital recording systems utilized in the described studies incorporate a 0.5-sec time constant. This short time constant reduces the effects of contact slurring but introduces statistical errors which are most pronounced at low count rates. To compensate for statistical errors, the digital data are subjected to a mathematical filter during computer processing. This procedure reduces the slurring effect, and all indications are that the integrity of the data is maintained.

The radiation group of logs consists of natural gamma (Nat-γ), gamma-gamma (γ-γ), neutron-gamma (n-γ), and neutron-epithermal neutron (n-n) logs. Of these, the natural gamma log is a passive radiation log, while the others are induced radiation logs.

The natural gamma (Nat-γ) log records the gamma photon emission of materials being investigated. The device used for this purpose responds to the potassium 40 (K-40) found in most soils and rock, but can also be influenced by small amounts of uranium and thorium. Clays typically have a high K-40 content. Therefore, in most environments, the log shows a positive response to clay content in the formation. By contrast, the natural gamma log shows a low count rate in clean quartz sands. Because of such an intimate relationship with soil and rock chemistry, the log is used extensively in stratigraphic correlations.

The gamma-gamma (γ-γ) log records the backscattered gamma radiation induced by a cobalt-60 source and detected by a thallium-activated sodium iodide crystal. In the process, gamma photons are degraded in proportion to the number of electrons in the interrogated field. Since electron density is proportional to bulk density when properly calibrated for borehole effects, the log can be used to derive bulk density. The principle of operation is very similar to that of nuclear density devices used for earthwork inspection. Cobalt-60 has a relatively short half-life (5.27 yr). Therefore, the decay characteristics must be accounted for in quantitative work.

The neutron-gamma (n-γ) log also records gamma radiation, like the gamma-gamma log, but the source mechanism involved is different. As neutrons emitted by a Pu-Be or Am-Be source are slowed down to thermal energy levels, they are captured by the nuclei of atoms in the material being penetrated. At collision, gamma photons are released by the capturing atom. These photons have energies characteristic of the element. Water molecules are the most effective neutron moderators in a natural system. Thus, gamma photon production becomes a function of water content. However, the log is not always a reliable moisture indicator because it is also affected by formation chemistry. On occasion, the

neutron-gamma log is diagnostic of stratigraphy because of chemical anomalies associated with some formations.

The neutron-epithermal neutron (*n-n*) log is the most reliable moisture indicator of all radiation logs. The source is the same as that of the neutron-gamma log, but the detection mechanism is different. Fast neutrons, reduced to epithermal energy levels by interaction with materials surrounding the logging device, are detected by a europium-activated lithium iodide crystal, enriched in lithium (3). Again, since hydrogen atoms are the most effective neutron moderators, the log is indicative of the water content of the tested materials. In addition, below the water table the log becomes an indicator of porosity. This log is not affected by formation chemistry and is used most often for determination of moisture content and porosity. The sources used in neutron devices have long half-lives, thus frequent calibration for source decay is not essential.

Electric Logs.—In uncased, fluid-filled holes, valuable data can be provided by electric logs which measure spontaneous potential and single point resistance. The spontaneous potential log provides a continuous record of natural potentials developed between the downhole sonde and an electrode at the ground surface. The single point resistance log records the apparent formation resistance between a close-coupled lead plummet and the shell of the measuring sonde. Both logs are basically indicators of lithology but are also affected by water content. They are best used in engineering studies where water tables are shallow, such as in the eastern United States.

Although the electric logging devices can be run in fluid-filled holes above the water table, logs so developed are difficult to interpret and do not necessarily present the same response to lithology as they do below the water table. Working generally with deep water tables, the writers found the electric logs to be of limited use in geotechnical investigations, and they are not discussed further in this paper.

Logging Equipment and Procedures.—The geophysical systems used in the studies described herein were custom-built in university facilities for the express purpose of gathering engineering and geohydrological data. The tools (sondes) are less than 7 ft (2.1 m) in length and range from 1.0–2.25 in. (25 mm–57 mm) in diameter. The larger diameters are associated with the most sensitive radiation devices. Tools are fabricated from stainless steel and can be used in any environment where temperatures are below 90° C. Although the geophysical systems used for the studies described herein were mounted in a two ton truck, operations have been successfully conducted from the back of a pickup truck or jeep using a portable winching system and generator.

Downhole intelligence from the sondes is transmitted to the electric modules at the ground surface where the signals are bifurcated; one portion of the signal generates a hard copy output for immediate review, while the other portion generates a digital record for computer processing. Digital sampling of the downhole data is normally accomplished at 1 ft (0.3 m) intervals, but sampling intervals could be decreased to 0.5 or 0.25 ft (0.15 or 0.075 m) intervals if the additional data warranted the extra processing and storage. In most cases, such refinement is not warranted.

Geotechnical Applications

Geophysical Response to Stratigraphy.—The primary geotechnical application

of borehole geophysics has been in stratigraphic characterization and correlation. Since geotechnical intelligence represents a response to chemical and physical parameters, subtle lithologic changes within a stratigraphic section can often be delineated by geophysical techniques. Such information is invaluable for a clear definition of stratigraphic subunits, and investigation of a number of boreholes will permit subunit correlation over a wide area. This correlation "blanket" has been used to convincingly demonstrate the absence of significant faulting in near-surface strata. Such information can also be used in constructing consolidation or seepage models of stratified deposits.

For stratigraphic correlations, the logs provide detailed information about top and bottom contacts, thicknesses, and lateral continuity of diagnostic lithologic units. Such diagnostic units must have one or more geophysical responses which are unique and lend the unit a distinctive "signature." Individual stratigraphic units or sequences which are less diagnostic can often be correlated on the basis of gross similarity of response, but such determinations are less certain and should be supported by other geologic evidence.

In establishing stratigraphic correlations, some knowledge of the depositional environment is essential for proper interpretation of logs. The stratigraphic characteristics will be different for stream, lake, or wind deposits. In the writers' experience, good stratigraphic correlations were most often obtained in layered fluvial or lacustrine deposits.

An example of excellent stratigraphic correlations is the site of the Palo Verde Nuclear Generating Station (PVNGS), located approximately 60 mile (100 km)

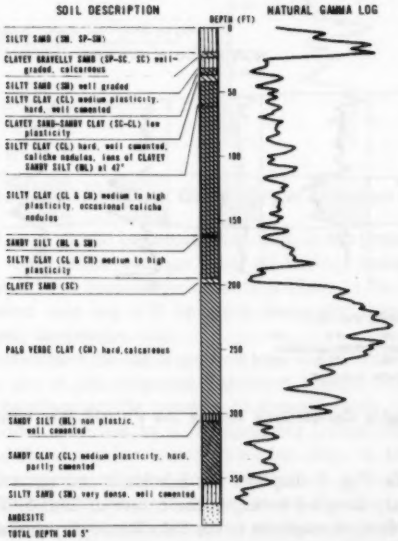
SOIL DESCRIPTION
NATURAL GAMMA LOG
DEPTH (FT)
0
50
100
150
200
250
300
350
SILTY SAND (SM, SP-SM)
CLAYEY GRAVELLY SAND (SP-SC, SC) well-graded, calcareous
SILTY SAND (SM) well graded
SILTY CLAY (CL) medium plasticity, hard, well cemented
CLAYEY SAND-SANDY CLAY (SC-CL) low plasticity
SILTY CLAY (CL) hard, well cemented, caliche nodules, lens of CLAYEY SANDY SILT (ML) at 42'
SILTY CLAY (CL & CH) medium to high plasticity, occasional caliche nodules
SANDY SILT (ML & SM)
SILTY CLAY (CL & CH) medium to high plasticity
CLAYEY SAND (SC)
PALO VERDE CLAY (CH) hard, calcareous
SANDY SILT (ML) non plastic, well cemented
SANDY CLAY (CL) medium plasticity, hard, partly cemented
SILTY SAND (SM) very dense, well cemented
ANDESITE
TOTAL DEPTH 366 5'

FIG. 2.—Soil Description and Natural Gamma Log (PVNGS Boring U5-B43)

west of Phoenix, Arizona. The site is underlain by 300–400 ft (90–120 m) of alluvial and lacustrine sediments, consisting of alternating layers of clays, silts, and sands. Stratification at the site approximately parallels the existing ground surface that has a southerly gradient of about one percent.

The most diagnostic and continuous soil unit beneath the site is the Palo Verde clay, a deposit of hard plastic-like clay interbedded with minor layers

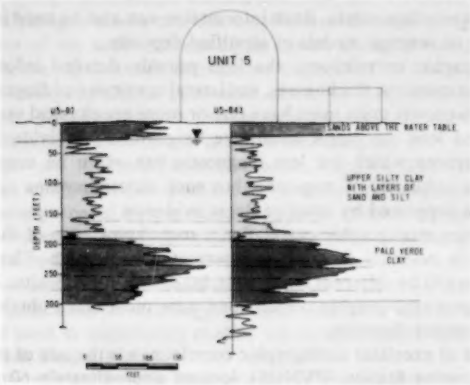

FIG. 3.—Stratigraphic Correlations Between Two Borings at PVNGS Using Natural Gamma Logs

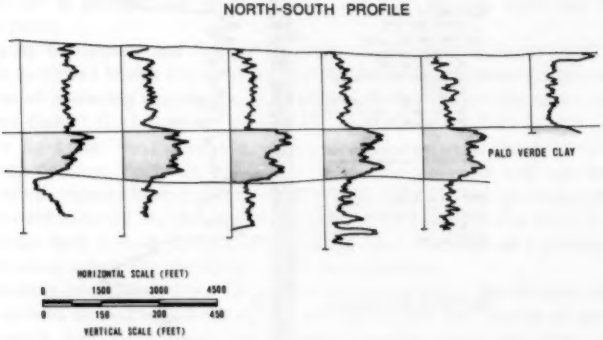

FIG. 4.—Stratigraphic Correlations Across the PVNGS Site Using Natural Gamma Logs

of silts and sands. Fig. 2 displays the lithologic and natural gamma log of a nearly continuously sampled boring at the center of Unit 5. The natural gamma log shows a very distinct response to the Palo Verde clay and a positive response to all clay layers in general.

The Palo Verde clay is traceable as a continuous deposit not only within

the power block areas (Fig. 3), but also over the entire site, and along profiles extending several miles (Fig. 4). In the power block area, subunits within and above the Palo Verde clay are also traceable across borings spaced about 300 ft (90 m) apart (Fig. 3). Some of these subunits are not easily traceable across the entire site (Fig. 4). In both profiles, the natural gamma log has been used for correlations. Similar results were obtained with other geophysical logs.

At this site, the use of geophysical logs was essential in distinguishing the various clay layers across borings spaced 1/2 mile (0.8 km) apart. In the power block areas, however, where boring spacing was much closer, adequate stratigraphic correlations could have been established on the basis of lithology and soils data.

Although individual logs have been discussed as valuable instruments for correlation, it must be stressed that the use of a single log can be grossly misleading and can often lead to erroneous findings. All logs comprising the

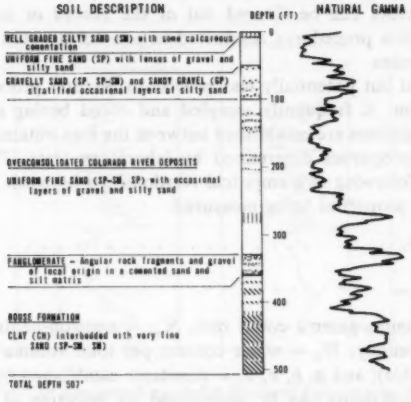
SOIL DESCRIPTION
DEPTH (FT)
NATURAL GAMMA LOG
WELL GRADED SILTY SAND (SM) with some calcareous cementation
UNIFORM FINE SAND (SP) with lenses of gravel and silty sand
GRAVELLY SAND (SP, SP-SM) and SANDY GRAVEL (SP) stratified occasional layers of silty sand
OVERCONSOLIDATED COLORADO RIVER DEPOSITS
UNIFORM FINE SAND (SP-SM, SP) with occasional layers of gravel and silty sand
FANGLOMERATE - Angular rock fragments and gravel of local origin in a cemented sand and silt matrix
BOUSE FORMATION
CLAY (CH) interbedded with very fine SAND (SP-SM, SM)
TOTAL DEPTH 503'
0
100
200
300
400
500

FIG. 5.—Soil Description and Natural Gamma Log of Sundesert Boring B-DH-35

suite from a given boring should be considered jointly in the process of composite log interpretation. Only when all logs from all borings being correlated are mutually supportive of the same correlation is it likely to be the correct one. Quite often, however, one log will be more diagnostic than the others and will become the basic correlation tool.

An example of a site where the use of multiple logs was essential for stratigraphic correlations is the site of the proposed Sundesert Nuclear Plant near Blythe, California. The subsurface profile consists of approximately 330 ft (100 m) of Colorado River sands, underlain by a fanglomerate (cemented rock fragments of local origin) and the lacustrine Bouse formation (Fig. 5). Of interest at this site is the positive response of the natural gamma log to both clays and local rock or gravels. Natural gamma activity alone did not, therefore, serve to identify these stratigraphic units. It became necessary at this site to define geophysical units in terms of porosity plus natural gamma activity (Fig. 1), or the vertical distribution of natural gamma activity, or both, within a single unit. Fortunately,

the stratigraphic sequence above the Bouse formation (Fig. 5) displayed a considerable amount of continuity which facilitated the correlations.

Geophysical Response to Physical Properties.—The induced radiation logs can also be used in quantitative or semi-quantitative fashion to determine the physical properties of the materials found in the borehole (1). To obtain quantitative data from the induced radiation logs, it is imperative to compensate for the influence of all factors other than the physical property being measured. Such factors include the following:

1. Distance between tool and borehole wall.
2. Type and size of casing (if any).
3. Properties of borehole fluid (if any).
4. Instrument drift.
5. Chemical characteristics of the formation.

Most of these factors can be filtered out of the record or compensated for by careful calibration procedures conducted in pits constructed from materials with known properties.

A more practical but potentially less precise calibration procedure is on-site borehole calibration. A frequently sampled and cored boring is used for this purpose, and correlations are established between the logs obtained in the boring and the physical properties determined by laboratory tests. The correlations are based on the following two empirical relationships between recorded count rates and physical properties being measured:

$$\text{Log } N_{\gamma\gamma} = a - b\gamma_t \quad \ldots \quad (2)$$

$$\text{Log } W_v = c - dN_{nn} \quad \ldots \quad (3)$$

in which $N_{\gamma\gamma}$ = gamma-gamma count rate; N_{nn} = neutron-neutron count rate; γ_t = total (bulk) density; W_v = water content per total volume (total porosity below the water table); and a, b, c, d, = constants established by calibration.

The calibration constants can be determined by selecting at least two sets of data points for each relationship. Other physical properties, including water content (by weight), total or partial porosity, void ratio, dry density, and degree of saturation, can be indirectly derived from the above relationships if the specific gravity of the earth materials and pore fluid is known.

The induced radiation logs are very sensitive to variations in borehole size. Therefore, it is imperative that a caliper log be obtained to determine the variation of borehole diameter. Zones with significant variations in borehole diameter should be excluded from quantitative analyses.

Induced radiation logs have been used by the writers in several siting studies to supplement the stratigraphic correlations generated by the natural gamma log. No express attempt was made during these studies to obtain geophysical logs for quantitative assessment of physical properties. However, review of the data obtained indicates that the logs contained information that could have been used for quantitative or semi-quantitative evaluations of physical properties.

At the site of the Palo Verde Nuclear Generating Station, subtle differences in porosity and density were detected by the geophysical logs. Fig. 6 displays the neutron-epithermal neutron (n-n) and neutron-gamma (n-γ) logs together

with plots of porosity and moisture content. The response of the Palo Verde clay is clearly recognizable on both the *n-n* and the *n-γ* logs but is more pronounced on the *n-n* log. The difference in response on the *n-γ* log is believed to be due to the influence of chloride ions in the soil.

Attention is also directed to the neutron log baseline shift associated with the Palo Verde clay section (depth range 200–280 ft). This shift is not as pronounced in laboratory porosity and moisture data and is illustrative of an important characteristic of the neutron response. The neutron tool responds to both free-water molecules and chemically-combined water molecules. In keeping with their chemically-combined and interstitial water, hydrous clay mineral structures will display neutron moisture or porosity responses. Therefore, two neutron calibrations would be required in boring U5-B43, one for the Palo Verde clay and one for the remainder of the section

Fig. 7 displays quantitative correlations between geophysical logs obtained in Boring U5-B43 and physical properties determined by laboratory tests on

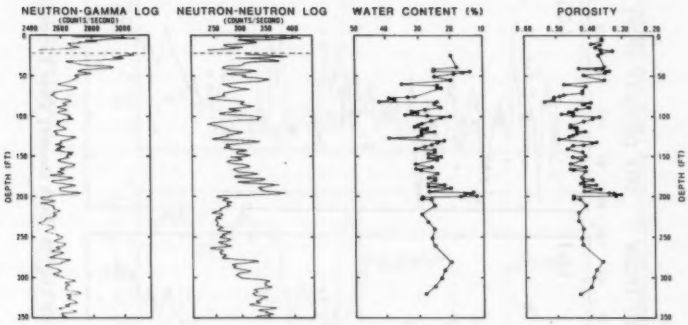

FIG. 6.—Comparison of Neutron Logs with Plots of Laboratory Water Content and Porosity Data (PVNGS Boring U5-B-43)

undisturbed samples from the same boring. Plot (*a*) displays the neutron-epithermal neutron (*n-n*) log with an overlay of porosity data, exponentiated in accordance with Eq. 3. The solid curve shows the log calibrated for the portion of the boring above the Palo Verde clay. The dashed curve represents a separate calibration for the Palo Verde clay that removes the baseline shift associated with the variation in hydrous clay minerals.

Plot (*b*) presents bulk density data from laboratory tests plotted over the gamma-gamma (γ-γ) log, exponentiated in accordance with Eq. 2. The log still contains the effect of all borehole irregularities. Plot (*c*) presents a plot of dry density data from laboratory tests over a hybrid log derived from the combination of the *n-n* log and the γ-γ log. The effect of moisture content, represented by the *n-n* log, has been subtracted from the bulk density, represented by the γ-γ log, to produce the dry density log.

The three overlays show excellent correspondence between physical parameters determined by laboratory tests and geophysical logs scaled to span the range

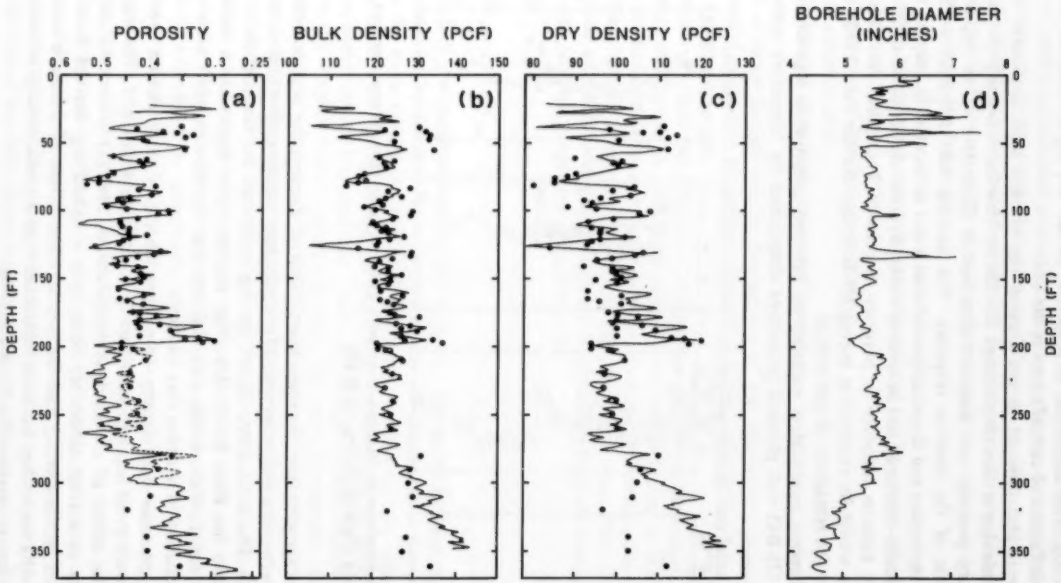

FIG. 7.—Overlays of: (*a*) Porosity Over Neutron-Neutron Log; (*b*) Bulk Density Over Exponentiated Gamma-Gamma Log; (*c*) Dry Density Over Composite Log; and (*d*) Caliper Log

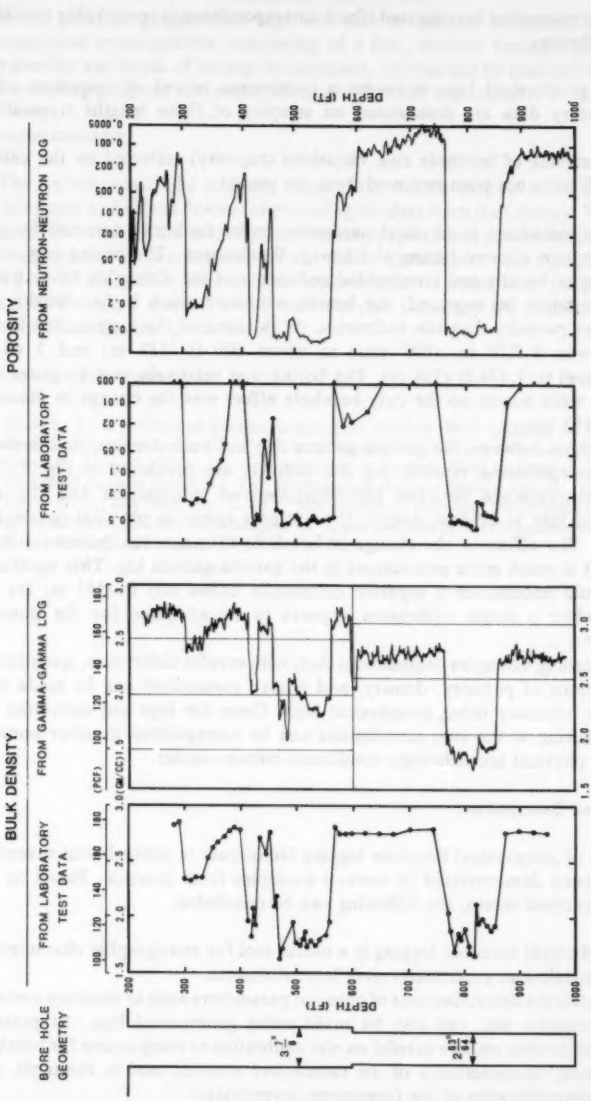

FIG. 8.—Correlations Between Physical Properties Measured by Laboratory Tests and Geophysical Logs (Data from Cheney, Washington)

of physical properties investigated. Such correspondence is remarkable considering the following:

1. The geophysical logs represent a continuous record of responses while the laboratory data are determined on samples of finite lengths (typically 6 in.).
2. The effects of borehole size variations (rugosity) reflected on the caliper log (Fig. 7) have not been removed from the record.

Extreme variations in physical parameters were faithfully detected by geophysical logs in a cored boring at Cheney, Washington. The boring penetrates a sequence of basalts and interbedded sediments of the Columbia River Basalt Group. As might be expected, the basalts exhibited much higher density and much lower porosity than the sediments. At the time of the logging, the boring diameter was 3 7/8 in. (NC size) to about 600 ft (183 m) and 2 63/64 in. (NX size) to 1,174 ft (358 m). The boring was relatively true to gauge and breakouts were minor, so the only borehole effect was the change in diameter at 600 ft (183 m).

Correlations between the gamma-gamma log and bulk density, and between the neutron-epithermal neutron log and porosity are presented in Fig. 8. The close correspondence between laboratory-derived information and the two geophysical logs is evident despite the extreme range in physical parameters displayed. The effect of the change in borehole diameter can be seen in both logs, but it is much more pronounced in the gamma-gamma log. This significant effect would necessitate a separate calibration below 600 ft (183 m) for the density, while a single calibration appears to be adequate for the porosity correlation.

The preceding examples demonstrate that, with careful calibration, quantitative determinations of porosity, density, and related parameters can be made with reasonable accuracy using geophysical logs. Once the logs are calibrated for a typical boring at the site, correlations can be extrapolated to other borings, as long as physical and lithologic conditions remain similar.

Summary and Conclusions

The use of geophysical borehole logging techniques in geotechnical investigations has been demonstrated by several examples from practice. Based on the studies described herein, the following can be concluded.

1. Geophysical borehole logging is a useful tool for stratigraphic characterization and correlation, particularly over large distances.
2. Quantitative determinations of physical parameters such as moisture content, density, porosity, etc. can also be made using geophysical logs. At present, such determinations require careful on-site calibration to compensate for borehole effects, decay characteristics of the radioactive sources used in the tools, and chemical characteristics of the formations investigated.
3. The methodology described herein has been used by the oil industry for over half a century. Tools used for such applications are more sophisticated and much costlier to operate than those used by the writers.

4. At present, geophysical logs are still of limited value for small-scale geotechnical investigations, consisting of a few, shallow borings. However, as the number and depth of borings is increased, savings can be realized by reducing the sampling program and substituting geophysical exploration.

Acknowledgments

The writers would like to thank Fugro, Inc., for its support in the preparation of this paper and Eileen Poeter for providing the data from the Cheney, Washington boring. The rest of the data reported in this paper were generated during siting investigations for two nuclear power plants (Sundesert and Palo Verde) and are part of the public record. The writers wish to thank San Diego Gas and Electric Company and Arizona Public Service Company for permitting the use of these data for this publication.

Appendix.—References

1. Czubek, J. A., "Gamma-gamma Logging in Nuclear Well Logging in Hydrology," *Technical Reports Series No. 126,* International Atomic Energy Agency, 1971.
2. Gray, D. A., and Preiss, K., "Introduction in Nuclear Well Logging in Hydrology," *Technical Reports Series No. 126,* International Atomic Energy Agency, 1971.
3. Keys, W. S., and MacCary, L. M., "Application of Borehole Geophysics to Water-Resources Investigations," Techniques of Water-Resources Investigations of the United States Geological Survey, 1971, Chapter E1.

FIELD AND LABORATORY DETERMINATION OF SOIL MODULI[a]

By William F. Marcuson III,[1] M. ASCE
and Joseph R. Curro, Jr.[2]

INTRODUCTION

The evaluation of the dynamic response of a soil or a structure founded on soil, requires knowledge of the stress-strain properties of the foundation material. When using current computer analysis techniques, the initial elastic moduli low strains, generally 10^{-4} cm/cm (or less) are required along with the variation in moduli as a function of strain.

These initial moduli (shear and Young's) can be determined in situ using various geophysical techniques. Or resonant column tests can be conducted in the laboratory on undisturbed samples to obtain moduli as functions of strain level.

Since the moduli previously mentioned would be needed for dynamic foundation design of four proposed buildings and a test loop structure (13), a test program was formulated that consisted of field and laboratory investigations to provide the required moduli. In addition, Poisson's ratios were determined from the investigations to aid in the dynamic design.

Therefore, the primary purpose of this project was to determine values of shear and Young's moduli for the foundation materials underlying the five proposed structures (designated as X-340-1 through X-340-4 and X-774), in Fig. 1. Additionally, building X-340-4 was arbitrarily selected as an example case to illustrate the procedure used for determining dynamic design values. The purpose of this paper is to compare dynamic soil properties determined in situ and in the laboratory and to examine the rationale used in obtaining design values.

Site Description.—The construction site is located in the vicinity of Portsmouth,

[1]Research Civ. Engr., Geotechnical Laboratory, U.S. Army Engineer Waterways Experiment Station, Vicksburg, Miss.

[2]Geophysicist, Geotechnical Laboratory, U.S. Army Engineer Waterways Experiment Station, Vicksburg, Miss.

Note.—Discussion open until March 1, 1982. Separate discussions should be submitted for the individual papers in this symposium. To extend the closing date one month, a written request must be filed with the Manager of Technical and Professional Publications, ASCE. Manuscript was submitted for review for possible publication on February 17, 1981. This paper is part of the Journal of the Geotechnical Engineering Division, Proceedings of the American Society of Civil Engineers, ©ASCE, Vol. 107, No. GT10, October, 1981.

Ohio, near the confluence of the Ohio and Scioto rivers. Overburden soils at the site were primarily Pleistocene river-bed and lake-bed deposits. Fig. 1 is a geologic map of the site (13). The map outlines the areal distribution of the glacial lake-bed deposits and early alluvial deposits. The lake-bed deposits, consisting of fat, thinly laminated clays, are largely confined to the old Scioto River channel.

The area outlined as lake deposits in Fig. 1 shows the occurrence of fat, laminated clay either at the surface or at some depth beneath the surface. Lean clays, silts (alluvium), and a fill material, which was placed during the period 1953–1955, lie above the fat clay in various thicknesses over a large portion of the outlined area. Early river alluvial silty clay and silt occupy that portion of the valley fill outside the fat clay boundaries.

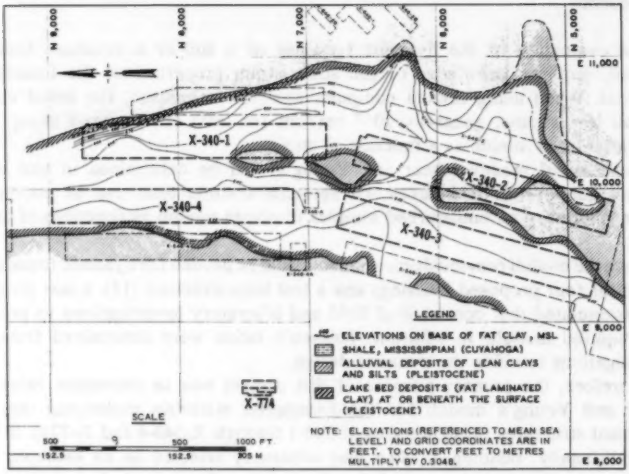

FIG. 1.—Proposed Building Locations and Geologic Map of the Site

Up to 60 ft (18 m) [averaging 35–40 ft (10.5–12.0 m)] of early river-bed and lake-bed deposits in the old valley still remain at the site. These deposits are mostly fat, laminated clays, lean clays, and fine silts, with a 2- to 10-ft (0.6- to 3-m) thick layer of weathered clayey gravel at the base. A 1- to 10-ft (0.3- to 3-m) thick layer of residual soil and colluvium mantles a large part of the valley. Rock, consisting of shale and sandstone, underlies the soil (13).

Field Investigation

The field investigation was comprised of two phases: (1) Drilling and sampling; and (2) geophysical investigation.

Drilling and Sampling.—During this phase of the field investigation, 27 holes were drilled at the site for in situ seismic test use and to obtain undisturbed

samples for laboratory testing. The holes were drilled in sets of three with one set near each end of the four proposed building locations and one set at the test loop location (X-774). The three holes were oriented to form an L-type configuration with the distance from the boring at the vertex of the L to the boring at the end of each leg being approximately 20 ft (6 m). Undisturbed samples were obtained from the boring at the vertex of the L for each set with a 5-in. (12.7-cm) Hvorslev fixed piston sampler. The remaining holes were drilled with a Waterways Experiment Station (WES) modified fishtail bit with upward baffles. After the holes had been drilled to the desired depth [2–5 ft (0.6–2 m) into rock], 3-in. (7.6-cm) ID PVC (polyvinyl chloride) pipe was

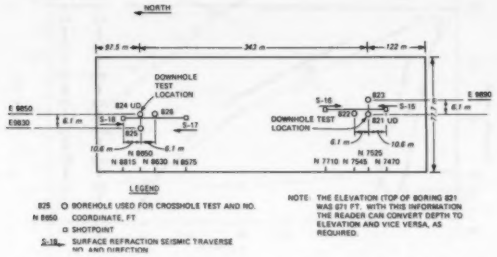

FIG. 2.—In Situ Seismic Test Layout; Proposed Building X-340-4 Location

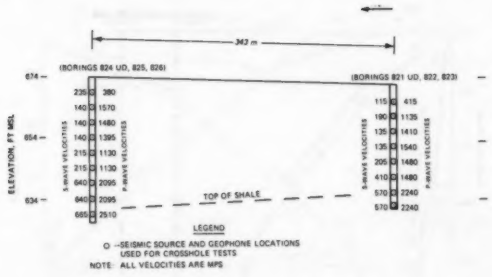

FIG. 3.—P- and S-Wave Velocities Determined from Crosshole Tests; Proposed Building X-340-4 Location

installed in the boreholes, and the annular space between the casing and walls of the borings was grouted with a mixture of cement, bentonite, and water that, after setting up, had the approximate consistency (modulus) of soil.

Geophysical Investigation

The geophysical investigation conducted at the site consisted of nine series of in situ seismic tests. Each series was comprised of crosshole, downhole, surface refraction seismic, and surface vibratory tests.

Crosshole Test Procedure.—The crosshole tests were conducted using a portable 24-channel refraction seismograph. A recorder displayed the data while operating at a paper speed of approx 35 in./sec (89 cm/s). Timing lines were displayed on the oscillogram at 10-msec intervals. Resolution time with this equipment and the above oscillograph speed was 0.5 msec. The test procedure to obtain shear wave (S-wave) data was a modified technique that used the same vibratory source and control package as that described by Ballard (1). The primary difference in the two procedures was concerned with the data acquisition package, i.e., no signal enhancement was used. Rather, the vibratory source was swept through

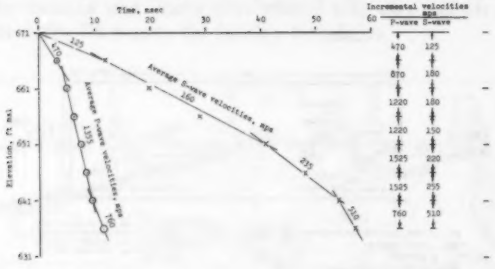

FIG. 4.—Arrival Time Versus Depth from Downhole Test; Boring 821; Proposed Building X-340-4 Location

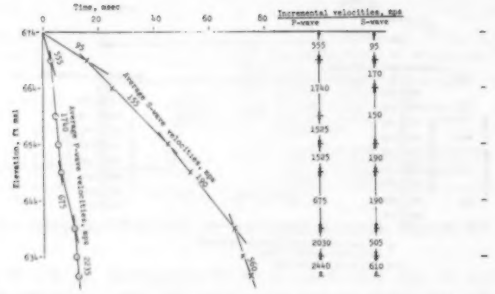

FIG. 5.—Arrival Time Versus Depth from Downhole Test; Boring 824; Proposed Building X-340-4 Location

a frequency range while monitoring the output of the two geophones placed at the same elevation in the receiver boreholes. (The vibrator was producing vertical oscillations, thereby transmitting a vertically polarized shear wave.) When an acceptable response was received at a specific frequency, this frequency was then interrupted by a tone-burst generator to send a specific number of cycles of that frequency to the receiver units. The source geophone was displayed simultaneously along with both receiver geophones on the oscillograph. In this manner, the origin of the source pulse could easily be recognized, and the

time difference between that pulse and the signal arrival at each of the two receivers could be determined.

The tests to obtain S-wave data were conducted by first placing the source and receivers at the same elevation near the top of the boreholes, then pulsing the source unit several times, recording both transmitted and received signals. After a satisfactory record had been obtained, the units were then repositioned 5 ft (1.5 m) deeper. The procedure above was repeated at this and each succeeding

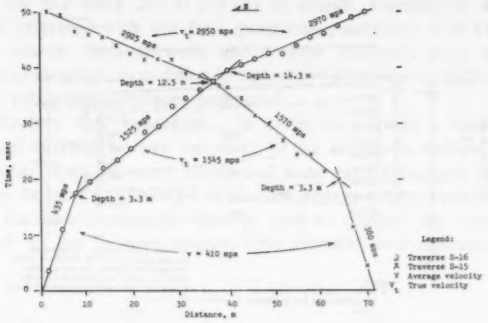

FIG. 6.—P-Wave Arrival Time Versus Distance; Proposed Building X-340-4 Location; S-15 and S-16

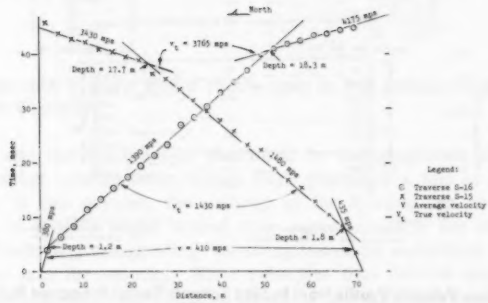

FIG. 7.—P-Wave Arrival Time Versus Distance; Proposed Building X-340-4 Location; S-17 and S-18

5-ft (1.5-m) depth until reaching the bottom of the boring. Since these holes were relatively shallow, their verticality could be checked by visual observation using either flashlight or mirror sources. In all cases, the boreholes were vertical within ±3 in. (±7.6 cm), thereby, eliminating the need for a formal deviation survey.

The compression wave (P-wave) data were obtained in a similar manner, except that the vibrator and its associated instrumentation were not used. Instead,

exploding bridgewire detonators (EBW's) were used at each 5-ft (1.5-m) increment as the P-wave source.

Data obtained from the crosshole tests were the times required for P- and S-waves to propagate from the source to a point of detection. These times were then divided into the distance between source and receiver geophones to provide apparent velocities. If a nearby higher velocity layer exists, the wave may refract and travel along that layer, thus, traveling along a faster path than the direct distance path. A computer program (2) for crosshole seismic

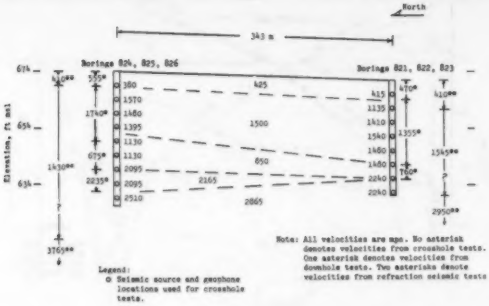
North
343 m
Borings 824, 825, 826
Borings 821, 822, 823
Elevation, ft msl
Note: All velocities are mps. No asterisk denotes velocities from crosshole tests. One asterisk denotes velocities from downhole tests. Two asterisks denote velocities from refraction seismic tests
Legend:
Seismic source and geophone locations used for crosshole tests.

FIG. 8.—S-Wave Velocity Profile from In Situ Seismic Tests; Proposed Building X-340-4 Location

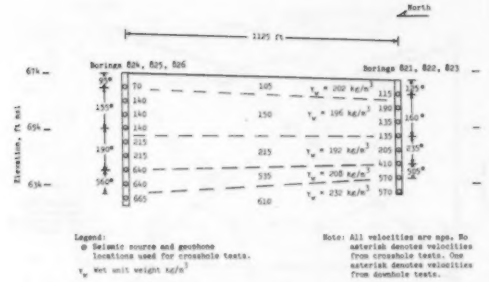
North
1125 ft
Borings 824, 825, 826
Borings 821, 822, 823
Elevation, ft msl
Legend:
Seismic source and geophone locations used for crosshole tests.
Note: All velocities are mps. No asterisk denotes velocities from crosshole tests. One asterisk denotes velocities from downhole tests.

FIG. 9.—S-Wave Velocity Profile from In Situ Seismic Tests; Proposed Building X-340-4 Location

interpretation, based on Snell's law of refraction, is used to determine true velocities by accounting for zones of high velocity contrast.

Downhole Test Procedure.—This test, designed to provide data for determination of vertically oriented P- and S-wave velocities, was conducted using the same seismograph and recorder as those used for the crosshole tests.

The receiver geophone was placed at a depth of 5 ft (1.5 m) in a borehole, and a vertical hammer blow to a steel plate positioned approx 1 ft (0.3 m) from the mouth of the boring on the ground surface was used as the P-wave source. A geophone adjacent to the hammer impact point provides the time

of seismic input. S-wave tests were then conducted by placing a large wooden plank on the ground surface and striking the plank at each end, thereby, reversing polarity of the horizontally polarized S-wave, which facilitates identification. The procedures for obtaining P- and S-wave data were then repeated with the receiver geophone at 5-ft (1.5-m) deeper increments until the bottom of the borehole was reached.

Surface Refraction Seismic Test Procedure.—Conventional surface refraction seismic tests were conducted at the site using the 24-channel unit. Refraction lines run at the site were 240 ft (73 m) in length. Geophones were spaced at 10-ft (3-m) intervals with the first geophone positioned 5 ft (1.5 m) from an explosive source. Both forward and reverse traverses were made at the site so that true velocities, in addition to apparent velocities, could be determined and depths to refracting interfaces computed.

Surface Vibratory Test Procedure.—In order to provide a necessary input parameter (near-surface S-wave velocity) to the crosshole computer program, surface vibratory tests (5) were conducted near each crosshole set. Rayleigh (R) waves may be generated using a controlled energy source such as a vibrator. In this case, the electromagnetic vibrator used to conduct the cross-hole tests was also used as the R-wave source. The vibrator was operated at several

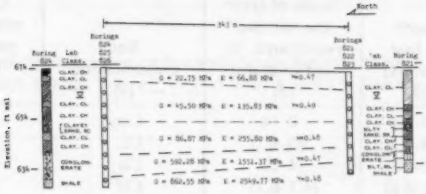

FIG. 10.—Shear and Young's Moduli Profile from In Situ Seismic Tests; Proposed Building X-340-4 Location

frequencies, and the R-wave was monitored by the geophones used for the surface refraction seismic tests, which were placed in a line at intervals of 1 ft (0.3 m). In this manner, the velocity of the R-wave can be determined from a plot of R-wave phase arrival time versus distance for each specific frequency. Then, a corresponding wavelength can be calculated by dividing the frequency into the velocity. Wave velocities thus derived are considered to be average values for an effective depth of one half the wavelength (10). S-waves, for practical purposes, can be considered to have the same velocity as R-waves.

Since the vibrator used at this site was of limited force output 50 lb (222 N), the depth of investigation was limited to approx 5 ft (1.5 m). These data could then be compared with those obtained for the shallow crosshole test position.

Elastic Moduli and Poisson's Ratio Determination

The P- and S-wave velocities determined from the previously mentioned test procedures should be converted to elastic parameters, such as shear modulus,

G, Young's modulus, E, and Poisson's ratio, ν, for use in foundation design. This conversion can be accomplished using theory of wave propagation in elastic media (8) and the total mass density, ρ, of the medium.

Field Test Results

The results determined from the in-situ seismic tests conducted at the proposed location of building X-340-4 are presented and examined below. It appeared feasible to the authors to select one location as "typical" and to examine the test results obtained there.

Proposed Building X-340-4 Location

Two series of in situ seismic tests were conducted at this location, one near each end of the proposed building location (Fig. 2).

TABLE 1.—Samples Obtained in Boring 821 UD from Which Resonant Column Test Specimens Were Obtained

Sample number (1)	Depth, in feet (meters) (2)	Depth of layer the sample represents, in feet (meters) (3)	Soil classification (4)	Mean effective consolidation stress, in pounds per square inch (kilopascals) (5)
2	2.7–4.2	0–14	Clay	1.7
	(0.8–1.3)	(0–4.3)	CL	(11.7)
9	20–21.8	14–22	Clay	6
	(6.1–6.6)	(4.3–6.7)	CH	(41.4)
11	24.5–26.6	22–27	Silt	9.5
	(7.5–8.1)	(6.7–8.3)	SM	(65.5)
13	29.2–30.5	27–31	Clay	10.75
	(8.9–9.3)	(8.3–9.4)	CL	(74)

Crosshole Tests.—These tests consisted of two crosshole sets. Borings 831, 822, and 823 comprised one set near the south end of the proposed building, whereas the second set, near the north end of the building, was made up of borings 824, 825, and 826 (Fig. 2).

Borings 821 and 824 were used as the seismic source boreholes for their respective sets, and borings 822, 823, 825, and 826 were employed as receiver holes for their respective sets. The seismic source and receiver (geophone) placements used in the performance of the crosshole tests are shown in Fig. 3. True P- and S-wave velocities determined from the crosshole data are presented alongside the receiver and source locations. Note that only one P- and S-wave velocity is shown for each test elevation although true P- and S-wave velocities were determined from the seismic source borehole to each of the receiver boreholes for each crosshole set. In comparing the velocities from the source to each receiver, the spread was so narrow, less than 10%, that it was thought advantageous to average the two P-wave velocities and, likewise, the two S-wave velocities.

Downhole Tests.—Two downhole tests located in Fig. 2 were conducted, one using boring 821 and the other using boring 824. The results of the downhole tests conducted in borings 821 and 824 are presented in Figs. 4 and 5, respectively. As shown, average and incremental P- and S-wave velocities were determined from the downhole data.

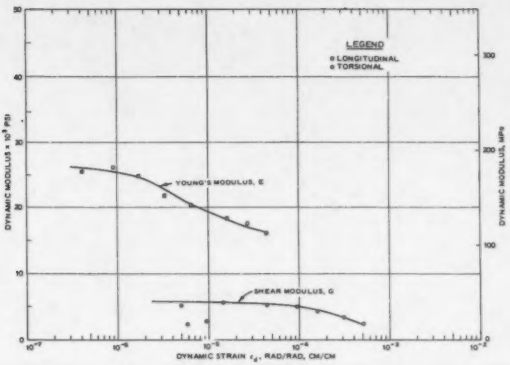

FIG. 11.—Dynamic Modulus Versus Dynamic Strain Amplitude from Resonant Column Tests; Sample: 821 UD No. 2-1; σ_{oct} = 11.7 kPa; B = 0.18; Nonsaturated

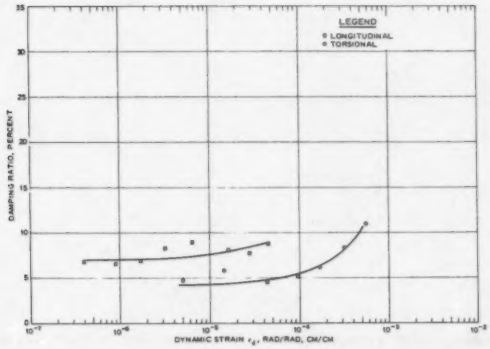

FIG. 12.—Damping Ratio Versus Dynamic Strain Amplitude from Resonant Column Tests; Sample: 821 UD No. 2-1; σ_{oct} = 11.7 kPa; B = 0.18; Nonsaturated

Surface Refraction Seismic Tests.—These tests consisted of four traverses (two lines), the orientation and location of which are shown in the test layout, in Fig. 2. The time versus distance plots for these traverses, designated as S-15–S-18, are shown in Fig. 6 and 7. These figures also present apparent velocities, true velocities, and associated depths to refracting layers.

Surface Vibratory Tests.—One surface vibratory test was conducted at boring 821 and another at boring 824. The results of these tests yielded average R-wave velocities of 375 and 235 fps (114 and 72 m/s) for the near-surface material, less than 5-ft (1.5-m) depth, at borings 821 and 824, respectively. These velocities

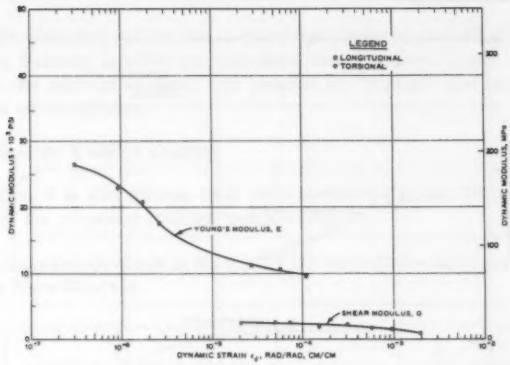

FIG. 13.—Dynamic Modulus Versus Dynamic Strain Amplitude from Resonant Column Tests; Sample: 821 UD No. 9-1; σ_{oct} = 41.4 kPa; B = 0.68

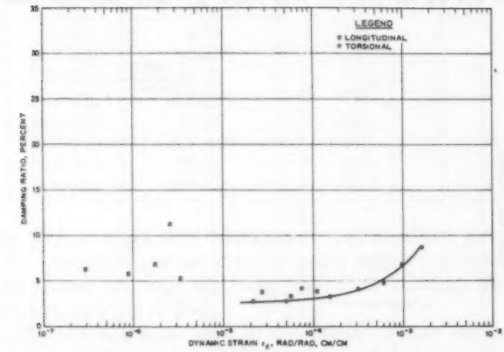

FIG. 14.—Damping Ratio Versus Dynamic Strain Amplitude from Resonant Column Tests; Sample: 821 UD No. 9-1; σ_{oct} = 41.4 kPa; B = 0.68

were used as true S-wave velocity inputs for the near surface to the crosshole computer program (2).

Data Interpretation

P- and S-Wave Velocity Zoning.—The P- and S-wave velocity results determined from the crosshole, downhole, surface refraction seismic, and surface vibratory

tests at this building location were analyzed and interpreted to produce the P- and S-wave velocity profiles shown in Figs. 8 and 9, respectively. The P- and S-wave zones will not necessarily align with one another. This is primarily due to a large increase in P-wave velocity as percent saturation of the soil reaches 99–100%, whereas S-wave velocity is not affected.

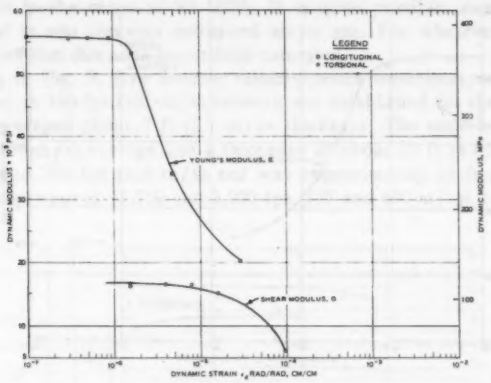

FIG. 15.—Dynamic Modulus Versus Dynamic Strain Amplitude from Resonant Column Tests; Sample: UD No. 11-1; σ_{oct} = 65.5 kPa; B = 0.83

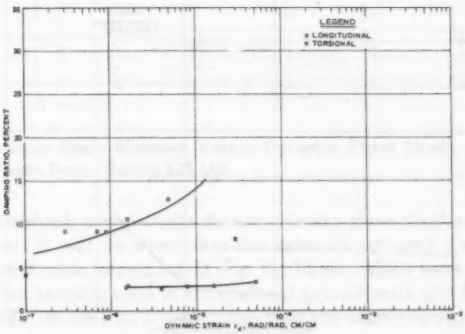

FIG. 16.—Damping Ratio Versus Dynamic Strain Amplitude from Resonant Column Tests; Sample: 821 UD No. 11-1; σ_{oct} = 65.5 kPa; B = 0.83

Referring to Fig. 8, five velocity zones were delineated from the P-wave data. The velocities presented for the zones were usually weighted averages based on data quality. A 1,400-fps (425-m/s) velocity was established for the near-surface zone, which averaged about 7 ft (2.1 m) in thickness. The second velocity zone averaged 4,900 fps (1,500 m/s) and was about 20 ft (6.1 m) thick.

This zone was underlain by a lower velocity layer [2,800 fps (850 m/s)], which ranged from 5–13 ft (1.5–4 m) in thickness and is best delineated by the uphole seismic data. The next two velocity zones [7,100 and 9,400 fps (2,165 and 2,865 m/s)] could be collapsed into one. However, since the top of the 9,400-fps (2,865-m/s) zone coincides with the top of shale, it was believed advantageous

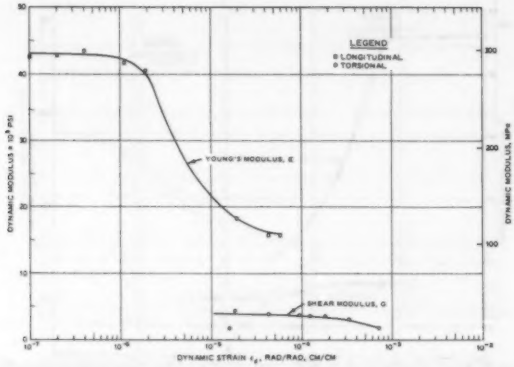

FIG. 17.—Dynamic Modulus Versus Dynamic Strain Amplitude from Resonant Column Tests; Sample: 821 UD No. 13-1; σ_{oct} = 74 kPa; B = 0.91

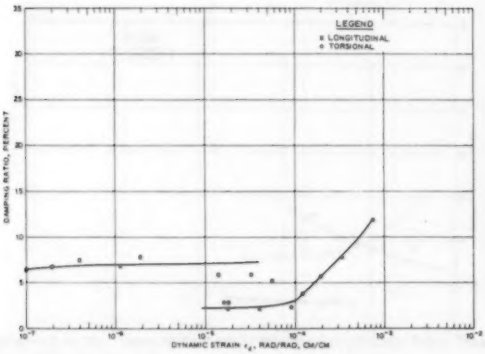

FIG. 18.—Damping Ratio Versus Dynamic Strain Amplitude from Resonant Column Tests; Sample: 821 UD No. 13-1; σ_{oct} = 74 kPa; B = 0.91

for analysis purposes to define top of rock and to keep the zones separate. The 7,100-fps (2,165-m/s) zone interpreted from the crosshole and downhole tests in borings 824–826 is probably indicative of a silt, sand, and gravel mixture cemented to form the conglomerate noted in the laboratory classifications of samples from boring 824 in this depth range.

Of particular interest is the data obtained for the third layer from the ground surface (Fig. 8). This layer is below the groundwater table, yet it has a P-wave velocity of 2,800 fps (850 m/s). One would expect a minimum P-wave velocity of approx 5,000 fps (1,530 m/s) which is the P-wave velocity of water. Since such a velocity was not obtained, the layer must be less than fully saturated. The P-wave velocity is very sensitive to percent saturation when the percent saturation is in the range of 98–100%. It is quite possible, even likely, that the material in situ contains entrapped air or gas. For whatever reason, the data indicates that this zone is not fully saturated.

Referring to Fig. 9, five S-wave velocity zones were interpreted from the S-wave data. A 350-fps (105-m/s) velocity was established for the near-surface zone and averaged about 7 ft (2.1 m) in thickness. The underlying zone had a 500-fps (150-m/s) average and a thickness of about 15 ft (4.6 m). The third zone averaged 700 fps (215 m/s) and was approximately 12 ft (2.7 m) thick. The two deeper zones [1,750 and 2,000 fps (535 and 610 m/s)] could probably

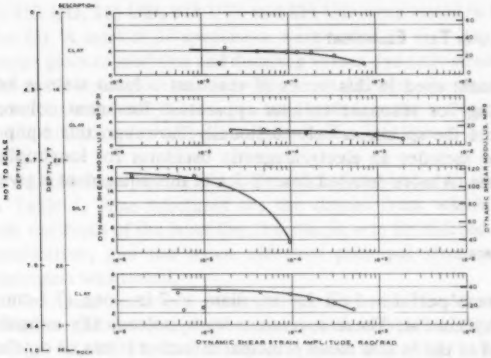

FIG. 19.—Dynamic Shear Modulus Versus Dynamic Shear Strain Amplitude from Resonant Column Tests; Boring 821 UD

have been combined; however, for the same reason given for the P-wave zoning, they were not. It will be noted that the value of wet unit weight applicable for each zone is also presented in Fig. 9. These values were obtained from the undisturbed samples used in the resonant column tests and from laboratory tests conducted on samples from borings near the in situ seismic test locations (13).

Shear and Young's Moduli and Poisson's Ratio (G, E, ν).—The interpretation of the data was continued by establishing zones from the velocity profiles and determining values of G, E, and ν for these zones. This was accomplished by overlaying the P- and S-wave velocity profiles (Figs. 8 and 9). This overlay produced seven zones. Then, values of G, E, and ν were computed for each zone using the P- and S-wave velocities and wet unit weights that fell into each zone. After analyzing G, E, and ν values for the various zones, it was evident that the controlling factor was the S-wave velocity zoning because the

P-wave velocity variations had little effect on E and ν values and of course, no effect on G values. Therefore, the seven newly established zones could be reduced to the five original zones shown on the S-wave profile (Fig. 9). The final field interpretation for this building location showing the five zones with their associated G, E, and ν values is presented in Fig. 10.

Laboratory Investigation

Undisturbed samples taken in the field were transported by truck to the WES. Once in the WES laboratory, the samples were opened and classified. The samples were evaluated to see which were representative of field conditions according to the boring logs and general knowledge of the site (13) and which samples could be tested in the laboratory based on lack of evidence of disturbance. Resonant column tests were performed on the representative samples found to be suitable for testing, i.e., those which did not contain particles of gravel or roots.

Resonant Column Test Equipment

The equipment used in this series of resonant column tests is known as the Drnevich Long-Tor resonant column apparatus. Resonant column apparatus normally excite the specimen only torsionally; however, this equipment differs in that it also includes an electromagnetic oscillator for longitudinal vibration of the specimen. A more detailed description of this equipment is given elsewhere (4).

Test Procedures

All tests were performed on 2.8 in. diam × 7-in. long (7.1-cm × 17.8-cm) undisturbed specimens. These specimens were isotropically consolidated so as to correspond to the in situ mean principal effective stress or octahedral stress, $\bar{\sigma}_{oct}$. The in situ mean principal effective stress was computed assuming normally consolidated conditions (13) and a coefficient of earth pressure at rest of 0.5.

After primary consolidation was complete, the drainage valve was closed and the B valve was checked and recorded (3). The specimen was subjected to sinusoidal excitation in both the longitudinal and torsional modes. Longitudinal and torsional vibrations were not conducted simultaneously. The frequency of vibration was varied until resonance was obtained and data were recorded such that the modulus and strain amplitude values could be computed. In order to obtain the variation of modulus as a function of strain amplitude, the driving force was increased, and the general test procedure was repeated.

Consolidation of all resonant column tests was started at the end of the working day and specimens were allowed to consolidate overnight. In general, primary consolidation was completed in less than 4 h. The specimen was subjected to sinusoidal excitation the following morning. This testing required approx 2 h. Thus, the data are plotted for a time of approx 12 h after primary consolidation was complete. Evaluation of the effects of time on the modulus and damping of the soil was beyond the scope of this study. It is recognized that time effects may be significant for the clay CH materials.

At the initiation of this investigation, it was decided that the data obtained during torsional excitation were of primary importance. These resonant column tests were not conducted on back pressure saturated specimens because: (1) Shear modulus and shear damping are more or less independent of percent saturation; and (2) the equipment does not lend itself to easy back pressure saturation. The top cap has no provision for vacuum or drainage which is needed for seepage saturation and an air fluid interface is required in the chamber; consequently, lower chamber pressures are desirable.

The procedure above is a brief description of that used by the WES. A more detailed testing procedure, along with a complete examination of the analysis and calculations required to obtain shear and Young's moduli from the raw data, is given elsewhere (4).

Resonant Column Test Results

Undisturbed samples from various depths in borings 800 UD, 803 UD, 806 UD, 809 UD, 812 UD, 815 UD, 818 UD, and 821 UD were tested in the resonant column device (3). A total of 37 specimens were tested.

Ref. 3 contains plots of modulus and damping versus dynamic strain amplitudes for all the resonant column tests. In order to familiarize the reader with the format of the resonant column data and its interpretation, the test results obtained from boring 821 UD samples will be reviewed. The location of boring 821 UD is shown in Fig. 2.

The samples taken from boring 821 UD, which were tested in the laboratory, are listed in Table 1. Also tabulated are the depths from which the samples were obtained, the depth of the layer that the sample was considered to represent, the soil classification, and the mean effective principal stress at which the laboratory specimen was tested.

The results of these tests are presented in Figs. 11–18. As expected, the modulus decreases and the damping increases with increasing strain (6,7,9,12). The data in Figs. 12, 14, 16, and 18 show a trend indicating that the damping obtained in the torsional vibration mode is on the order of one-half that determined in the longitudinal mode.

Below a depth of 31 ft (9.4 m), the soil is extremely gravelly. Samples obtained were disturbed to such an extent as to be considered unsatisfactory for testing. Rock was found at a depth of about 36 ft (11 m).

Laboratory Test Results

The resonant column data obtained from specimens trimmed from samples taken in boring 821 UD have been presented. A soil profile will be developed for this boring in terms of shear modulus, Young's modulus, and internal damping ratio.

Shear Modulus.—Fig. 19 summarizes the shear modulus data obtained from testing four specimens taken from samples of boring 821 UD. Also shown in Fig. 19 is a soil profile depicting the four layers that were observed in the boring. Note that the near-surface clay layer is 14 ft (4.3 m) thick and has a shear modulus at low strain levels of about 3.5×10^3 psi (24×10^3 kPa) (10^3 kPa = 1 MPa). As the shear strain is increased to a dynamic strain level

of about 10^{-3} rad/rad, the shear modulus decreases to about 1.7×10^3 psi (11.7 MPa). Immediately below this 14-ft (4.3-m) thick surficial layer is an 8-ft (2.4-m) thick layer of clay. From the resonant column test results, it appears that this material has a shear modulus of about 2.8×10^3 psi (19.3 MPa) at very low strains. This modulus decreases to about 1.0×10^3 psi (6.9 MPa) as the strain level increases to 10^{-3} rad/rad. Below a depth of 22 ft (6.7 m) there exists a 4-ft (1.2-m) thick silt layer. This material exhibits a shear modulus of 17×10^3 psi (117 MPa) at low strain levels. As the strain increases to

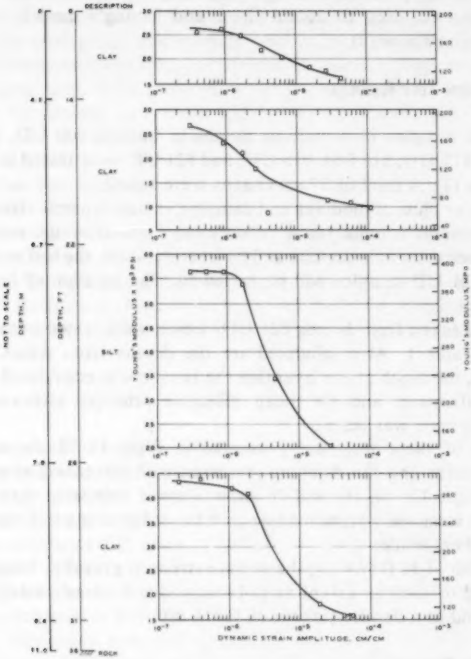

FIG. 20.—Dynamic Young's Moduli Versus Dynamic Strain Amplitude from Resonant Column Tests; Boring 821 UD

a dynamic strain amplitude of about 10^{-4} rad/rad, dynamic shear modulus decreases to a value of 5.6×10^3 psi (38.6 MPa). Below the 4-ft (1.2-m) thick silt layer there exists a 5-ft (1.5-m) thick clay layer between a depth of 26 and 31 ft (7.9 and 9.4 m). This layer exhibits a shear modulus of about 5.6×10^3 psi (38.6 MPa) at low strain levels. This modulus decreases to about 2.8×10^3 psi (19.3 MPa) as the strain level becomes greater than 10^{-4} rad/rad.

In reviewing Fig. 19 several specific items should be noted. These are

1. As the strain level increases from 10^{-5}–10^{-3} rad/rad, the shear modulus is generally reduced by about 50%, except in the silt layer at a depth of 22–26 ft (6.7–7.9 m). In this layer, the shear modulus is reduced to about one third of its original low strain value.

2. One would expect that the modulus would be a function of the mean principal effective stress. Thus, the modulus should increase as a function of depth, other things being equal. This is not the case in boring 821 UD. The clay layer at a depth of 14–22 ft (4.3–6.7 m) is not stiffer than the surficial clay.

3. The 5-ft (1.5-m) thick clay layer immediately below the silt has a modulus that is significantly lower than the silt layer at a depth of 22–26 ft (6.7–7.9 m). This is not unusual, but should be noted because it may be important in any future dynamic analyses or calculations.

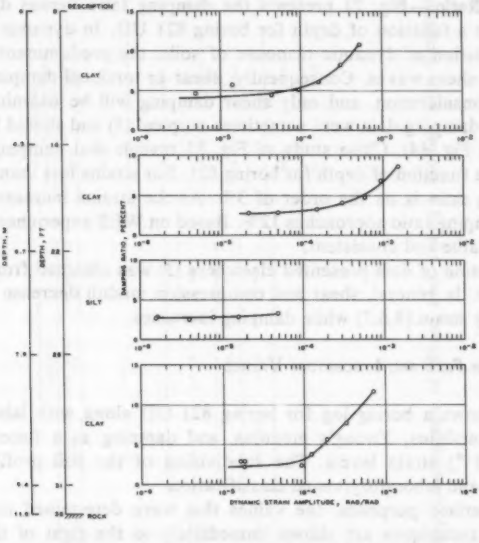

FIG. 21.—Damping Ratio Versus Dynamic Strain Amplitude from Resonant Column Tests; Boring 821 UD

Young's Modulus.—Fig. 20 shows Young's modulus (E) versus dynamic strain amplitude as a function of depth in boring 821 UD. The 14-ft (4.3-m) thick surficial layer has a Young's modulus at low strain levels of about 26×10^3 psi (179 MPa). This value decreases to approx 15×10^3 psi (103 MPa) when the strain level increases to 5×10^{-5} in./in. (cm/cm). The clay layer between a depth of 14 and 22 ft (4.3 and 6.7 m) is similar to the surficial layer. This 8-ft (2.4-m) thick clay layer has a Young's modulus of about 26×10^3 psi (197 MPa) at a strain level of 4×10^{-7} in./in. (cm/cm). As the strain increases to a level of approx 10^{-4} in./in. (cm/cm), the Young's modulus decreases

to 9.7×10^3 psi (66.9 MPa). The Young's modulus in the silt layer that lies at a depth of 22–26 ft (6.7–7.9 m) is approx 56×10^3 psi (386 MPa) at strain levels below 10^{-6} in./in. (cm/cm). As the strain level increases above 10^{-6} in./in. (cm/cm), this Young's modulus decreases to approx 20×10^3 psi (138 MPa) when the strain level is about 4×10^{-5} in./in. (cm/cm). The 5-ft (1.5-m) thick clay layer located at a depth of 26–31 ft (7.9–9.4 m) in boring 821 UD has a Young's modulus at low strain levels of about 43×10^3 psi (296 MPa). Again, as the strain increases from a level of around 10^{-6}–10^{-4} in./in. (cm/cm), the Young's moduli decrease to approx 16×10^3 psi (110 MPa).

As one looks at this collection of data, it is again apparent that the silt layer at a depth of 22–26 ft (6.7–7.9 m) is relatively stiff compared with the other layers. The two clay layers above 22 ft (6.7 m) have similar characteristics, with the layer located between 14 and 22 ft (4.3 and 6.7 m) being more sensitive to strain than the surficial layer.

Damping Ratio.—Fig. 21 presents the damping ratio versus dynamic strain amplitude as a function of depth for boring 821 UD. In dynamic analyses and in the calculation of dynamic response of soils, the predominant energy input comes from shear waves. Consequently, shear or torsional damping is the most important consideration, and only shear damping will be examined here. The longitudinal damping data were sometimes atypical (3) and should be considered suspect (see Fig. 14). Close study of Fig. 21 reveals that damping is relatively constant as a function of depth for boring 821. For strains less than 10^{-4} rad/rad the damping ratio is on the order of 3%. As the strains increase above 10^{-4}, then the damping ratio approaches 12%. Based on WES experience, this appears to be reasonable and consistent.

The collection of data presented elsewhere (3) was obtained from 35 resonant column tests. In general, shear and compression moduli decrease as a function of increasing strain (4,6,7) while damping increases.

Comparison of Field and Laboratory Values

Fig. 22 shows a boring log for boring 821 UD along with laboratory value *s* of shear modulus, Young's modulus, and damping as a function of depth at low ($\sim 10^{-6}$) strain levels. The subdivision of the soil profile was based on soil type and laboratory visual classification.

For comparison purposes, the values that were determined in the field by geophysical techniques are shown immediately to the right of the laboratory values. The reader is reminded that the subdivision of the soil profile is based on field techniques and results from changes in P- and S-wave velocities and is independent of material types or visual classification. Consequently, it is not surprising that the soil profile is not subdivided identically using data obtained in the laboratory and field.

Generally, moduli values obtained in the laboratory are less than in situ determined values. In fact, the values obtained for laboratory tests may be as low as one half the field values (11). The fact that the laboratory data obtained during this investigation exhibit so much scatter was surprising. No consistent trend can be obtained from a comparison of the data presented in Fig. 22. For some zones (soil layers) the laboratory values are approximately equal to the field values. For other zones the laboratory values are greater than the

FIG. 22.—Field and Laboratory Comparison of Shear and Young's Moduli with Resultant Design Values for Boring 821 UD

field values and vice versa. Because of the scatter in the data, data comparison and the selection of design values are presented below.

Shear and Young's Moduli

Near-Surface Material.—In comparing the laboratory and field values, the thickness of the near-surface layer was determined to be 14 ft (4.3 m) in the laboratory. This was based primarily on the boring logs; however, in the field, using velocity data, the near-surface layer was chosen to be only 8 ft (2.4 m) thick. The laboratory-determined shear modulus of 3.5×10^3 psi (24 MPa) compares very favorably with the field-determined value of 3.3×10^3 psi (22.7 MPa). For practical purposes, these numbers are the same. The Young's modulus computed from the field data was determined to be 9.7×10^3 psi (67 MPa). This value seems reasonable; however, it is about one third of the laboratory-determined value, which is 26×10^3 psi (180 MPa). This value is judged to be too high. For the top layer, values of shear and Young's moduli selected for design were 3.4×10^3 psi and 10×10^3 psi (23.4 and 69 MPa), respectively.

Second Layer.—Immediately below the near-surface layer is a second clay layer that ends at 20–22 ft (6–6.7 m) depending on whether the field seismic data or the laboratory classifications of samples obtained from the boring are accepted. The shear modulus as determined in the laboratory for this layer is 2.8×10^3 psi (19.3 MPa). This value is slightly less than half of the shear modulus 6.6×10^3 psi (45 MPa) that was determined in the field. Because the soil is predominantly clay to a depth of 20 ft (6 m), and because the shear modulus should increase with increasing depth, a design shear modulus of about 5×10^3 psi (34 MPa) was selected. The values of Young's modulus range from $19.7–24.4 \times 10^3$ psi (136–168 MPa) depending on whether one chooses the field or laboratory values. These values are relatively close (within about 20% of each other), and this is considered good agreement. A value of 20×10^3 psi (138 MPa) has been selected for design purposes.

Third Layer.—The third layer selected for design purposes combines the two layers within the depth interval of 22–31 ft (6.7–9.4 m) in the laboratory-determined values and is assumed to be at a depth of 20–30 ft (6–9.1 m). If one averages the shear modulus values of 16.7×10^3 and 5.56×10^3 psi (115 and 38 MPa), one obtains 11.1×10^3 psi (76.5 MPa). This value is in close agreement with 12.6×10^3 psi (87 MPa) that was obtained in the field, and consequently a value of 12×10^3 psi (83 MPa) was assigned for design purposes. In the laboratory, averaging the Young's moduli for the two layers between 22 and 31 ft (6.7 and 9.4 m) yields a value of about 50×10^3 psi (344 MPa). This is considerably higher than Young's modulus of 37.1×10^3 psi (256 MPa) as determined by geophysical methods. Based on engineering judgment, a value of 40×10^3 psi (276 MPa) has been selected for design purposes.

Fourth Layer.—From a depth of 30–36 ft (9.1–11 m), the soil consisted of sandy silts with gravels and consequently was not suitable for laboratory testing. Shear and Young's moduli of 86×10^3 and 225×10^3 psi (593 and 1,550 MPa), respectively, were assumed for design purposes. These values are based on the field information.

Foundation Rock.—Finally, the shear and Young's moduli of the foundation rock were determined to be 125×10^3 and 370×10^3 psi (860 and 2,550 MPa), respectively. These values are based solely on the field geophysical data.

Synopsis

The data presented in Fig. 22 show that the shear modulus determined in the laboratory is approximately equal to or less than the shear modulus obtained by in situ geophysical techniques. This trend has been reported by others (10) and can be attributed to the following: (1) The data obtained in the laboratory are influenced by such things as sample disturbance, equipment limitations, and boundary conditions; (2) the geophysical techniques produce data at a much smaller strain than the laboratory tests; and (3) time effects that tend to increase the laboratory determined shear modulus have not been included.

On the other hand, the Young's modulus obtained in the laboratory is higher than that obtained in the field (Fig. 22). This was not expected. It is believed that soil anisotropy is responsible for the laboratory values being greater than the field values. In the resonant column technique, Young's modulus is measured perpendicular to the bedding planes. The geophysical tests measure Young's modulus both parallel and perpendicular to the sample bedding planes. The crosshole tests and the surface refraction seismic tests provide P-wave velocities for travel paths parallel to the bedding planes. The downhole tests provide P-wave velocities perpendicular to the bedding planes. Comparison of the P-wave velocity data obtained by the three geophysical techniques does not substantiate the hypothesis of the soil being anisotropic (Fig. 8). On the other hand, these materials are glacial lake-bed deposits, and the geology and mode of deposition support the hypothesis that the soil is anisotropic. This cross-anisotropy is believed to be responsible for the data obtained in the laboratory being higher than that obtained in the field.

An additional explanation for the laboratory determined Young's moduli being higher than the field values is the possibility that the laboratory specimens did not adequately represent the entire in situ soil layer. The geophysical techniques evaluate several cubic meters of soil while the laboratory technique is limited to several cubic centimeters of soil. As a result, the specimens tested in the laboratory may or may not adequately represent in situ conditions.

A third possible explanation for the laboratory determined Young's moduli being greater than the field values could be the difference in percent saturation. As mentioned previously the third layer from the ground surface which has a P-wave velocity of 2,800 fps (850 m/s) is not believed to be fully saturated, and the resonant column test specimens were not back-pressure saturated. Consequently, it is difficult to say whether the laboratory specimens were more or less saturated than the in situ soil. Nevertheless as the percent saturation approaches 100%, a change in percent saturation of 0.1 or 0.2% can cause a change in P-wave velocity of several hundred feet per second. One cannot isolate the determined cause of the high laboratory Young's moduli, but it could be one of the hypotheses mentioned above or a combination of these hypotheses.

Damping Values

If analytical calculations are to be conducted, a damping value of 3–5% should be used for low strain calculations. This value is based on resonant column data and is valid only to a depth of 31 ft (9.4 m) because the soil below that depth was not tested. However, because the damping appears to be uniform

with depth, extrapolation to the bottom layer [30–36 ft (9.1–11 m) in depth] does not seem unreasonable.

Summary

Based on the data and the analysis presented, the soil at boring 821 UD can be subdivided and zoned for the purpose of dynamic analysis of building or machine foundations Fig. 22. This figure shows four soil layers above rock. The near-surface layer is 8 ft (2.4 m) thick, the second layer is 12 ft (3.6 m) thick, the third layer is 10 ft (3 m) thick, and there is a 6-ft (1.8-m) thick layer immediately overlying the rock. This is an idealized soil profile that would be suitable for design calculations. The values of shear modulus, Young's modulus, and damping ratio for each of these layers to be used in design are listed in the right hand three columns of Fig. 22.

When there exists considerable scatter in the laboratory and field data obtained for a specific soil layer, WES usually places more emphasis on the field data. The reasons for this are

1. The field investigation usually involves the use of several procedures (such as the crosshole, downhole, surface refraction, and vibratory techniques), which produce redundant data.
2. The laboratory investigation is usually limited to resonant column testing.
3. The data obtained in the laboratory are influenced by such things as sample disturbance, equipment limitations, and boundary conditions.
4. Furthermore, the laboratory data are only as valid as the specimen tested is representative of the soil layer. In this regard the field investigation is influenced by a volume of soil measured in terms of cubic meters not cubic centimeters as in the laboratory.

Acknowledgments

Grateful appreciation is expressed to those colleagues at WES who assisted in the data acquisition phase of this study and to those who offered constructive criticism during the documentation stage. The support of the Energy Research and Development Administration (ERDA) and their permission to publish this paper are gratefully acknowledged.

Appendix.—References

1. Ballard, R. F., Jr., "A Method for Crosshole Seismic Testing," *Journal of the Geotechnical Engineering Division*, ASCE, Vol. 102, No. GT12, Dec., 1976, pp. 1261–1273.
2. Butler, D. K., Skoglund, G. R., and Landers, G. B., "CROSSHOLE: An Interpretive Computer Code for Crosshole Seismic Test Results, Documentation, and Examples," Miscellaneous Paper S-78-8, U.S. Army Engineer Waterways Experiment Station, Viscksburg, Miss., July, 1978.
3. Curro, J. R., and Marcuson, W. F., III, "In Situ and Laboratory Determinations of Shear and Young's Moduli for the Portsmouth, Ohio Gaseous Diffusion Add-On Site," Miscellaneous Paper S-78-12, U.S. Army Engineer Waterways Experiment Station, Vicksburg, Miss., Aug., 1978.
4. Drnevich, V. P., Hardin, B. O., and Shippy, D. J., "Modulus and Damping of Soils

by the Resonant Column Method," *Dynamic Geotechnical Testing*, American Society for Testing and Materials, STP 654, Philadelphia, Pa., Sept., 1978, pp. 91–125.
5. Fry, Z. B., "A Procedure for Determining Elastic Moduli of Soils by Field Vibratory Techniques," Miscellaneous Paper No. 4-577, U.S. Army Engineer Waterways Experiment Station, Vicksburg, Miss., June, 1963.
6. Hardin, B. O., and Drnevich, V. P., "Shear Modulus and Damping in Soils: Measurement and Parameter Effects," *Journal of the Soil Mechanics and Foundations Division*, ASCE, Vol. 98, No. SM6, June, 1972, pp. 603–624.
7. Hardin, B. O., and Drnevich, V. P., "Shear Modulus and Damping in Soils: Design Equations and Curves," *Journal of the Soil Mechanics and Foundations Division*, ASCE, Vol. 98, No. SM7, July, 1972, pp. 667–692.
8. Kolsky, H., "Stress Waves in Solids," Dover Publications, Inc., New York, N.Y., 1963.
9. Marcuson, W. F., III, and Wahls, H. E., "Effects of Time on the Damping Ratio of Clays," *Dynamic Geotechnical Testing*, American Society for Testing and Materials, STP 654, Philadelphia, Pa., Sept., 1978, pp. 126–147.
10. Maxwell, A. A., and Fry, Z. B., "A Procedure for Determining Elastic Moduli of In Situ Soils by Dynamic Techniques," Miscellaneous Paper No. 4-933, U.S. Army Engineer Waterways Experiment Station, Vicksburg, Miss., Oct., 1967.
11. Richart, F. E., Jr., Anderson, D. G., and Stokoe, K. H., II, "Predicting in Situ Strain-Dependent Shear Moduli of Soil," *Proceedings, Sixth World Conference on Earthquake Engineering*, New Delhi, Vol. 6, Jan., 1977, pp. 6–159–6–164.
12. Seed, H. B., and Idriss, I. M., "Soil Moduli and Damping Factors for Dynamic Response Analyses," Report No. EERC 70-10, Earthquake Engineering Research Center, University of California, Berkeley, Calif., Dec., 1970.
13. Taylor, H. M., Jr., et al., "Title I Design Foundation Investigation for Static Loading, Gaseous Diffusion Add-On Plant, Portsmouth, Ohio," Miscellaneous Paper S-77-20, U.S. Army Engineer Waterways Experiment Station, Vicksburg, Miss., Nov., 1977.

SAND WAVES IN LOWER COOK INLET, ALASKA[a]

By Arshud Mahmood,[1] Clarence J. Ehlers,[2] and Blase A. Cilweck,[3]
Members, ASCE

INTRODUCTION

Geophysical methods are sometimes used in soil investigations on land to supplement borehole data and other site investigation information. In studies of soil conditions offshore, high-resolution geophysical tools and methods are used on a nearly routine basis in conjunction with bottom sampling and soil borings. Although the water at an offshore site inhibits the familiar and reassuring experience of a visual reconnaissance. Since water is a medium in which acoustical energy can be easily propagated, its presence offers greater opportunities for a rapid and comprehensive geophysical investigation.

In 1973, acoustic (geophysical) methods were used to investigate the seafloor geological conditions, particularly sand waves, in an area of potential offshore development, lower Cook Inlet, Alaska. The bedform aspects of the survey results are reviewed here. The term "sand waves" is generally used for wave-shaped bedforms composed of granular material and formed at the boundary between flowing water and a mobile bed of unconsolidated sediment. Sand waves are a potential foundation hazard, particularly to submarine pipelines, due to the possibility of their movement.

Regional Setting.—Cook Inlet is a 190 mile (300 km) long basin, a topographical expression of a structural trough bounded by mountain ranges. The portion of Cook Inlet south of Kalgin Inland, generally known as lower Cook Inlet, is underlain by a sequence of thick sedimentary rocks that extend across much of southern Alaska. Several quaternary glacial episodes prior to about 15,000 years ago have affected lower Cook Inlet and resulted in the deposition of considerable thicknesses of granular sediments, which subsequently have been subjected to marine erosion processes.

Geophysical Survey.—The acoustic data were acquired in 1973 and consist

[a]Presented at the October 22–26, 1979, ASCE Annual Convention and Exposition, held at Atlanta, Ga.

[1]Engr. Mgr., McClelland Engrs., Inc., Houston, Tex.
[2]Sr. Engr. Mgr., McClelland Engrs., Inc., Houston, Tex.
[3]Sr. Engrg. Geologist, McClelland Engrs., Inc., Ventura, Calif.

Note.—Discussion open until March 1, 1982. Separate discussions should be submitted for the individual papers in this symposium. To extend the closing date one month, a written request must be filed with the Manager of Technical and Professional Publications, ASCE. Manuscript was submitted for review for possible publication on February 17, 1981. This paper is part of the Journal of the Geotechnical Engineering Division, Proceedings of the American Society of Civil Engineers, ©ASCE, Vol. 107, No. GT10, October, 1981. ISSN 0093-6405/81/0010-1293/$01.00.

of 3,400 line-miles (5,440 line-kilometers) of multisystem, high-resolution, marine acoustic survey data collected on a variable grid shown in Fig. 1. The survey was performed using a 4 kilojoule sparker, as acoustipulse, a tuned transducer, fathometer and dual side-scan sonar. In each system, a sound source in water produces sound energy, and this energy is transmitted down to the seafloor. When this sound energy strikes the seafloor (or any other object having acoustic properties different from water) a part of it is reflected back to a sound receiver as an echo. This sound energy then is reconverted to electric energy, amplified, and recorded on a graphic recorder. The amount of time that lapses between

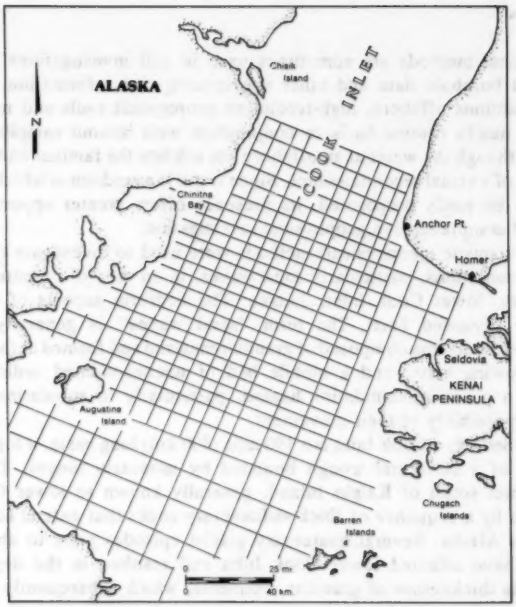

FIG. 1.—Multisensor Acoustic Survey (1973) Lines in Lower Cook Inlet, Alaska

the pulse transmission and the echo reception is a measure of the distance traveled.

Generally, several acoustic devices can be deployed simultaneously from a sufficiently large boat. A typical equipment layout is shown in Fig. 2. The three systems most useful in interpreting sand waves were acoustipulse, fathometer and side-scan sonar. Specific features of these three systems are summarized in the section entitled Geophysical Systems. Characteristics of all five systems are summarized in Table 1.

All of the acoustic systems used in this study operate on the principle whereby transmitted sound energy, incident upon an acoustic interface, is reflected from

the interface. An acoustic interface can be defined as any interface across which there is a contrast in acoustic properties. Such contrast is dependent on the acoustic impedance of the materials on each side of the interface. The characteristic acoustic impedance of a soil layer is $I = \rho_s V$, in which ρ_s = the soil bulk density and V = the velocity of a compressional wave, such as a sound wave traveling in the soil layer.

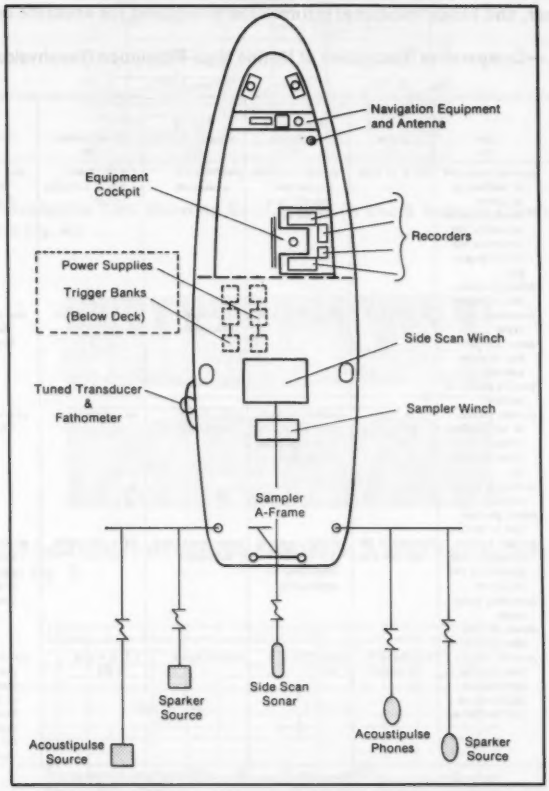

FIG. 2.—Geophysical Equipment Layout

The amount of energy that is transmitted to the next interface depends on the contrast in acoustic impedance between the two materials. The contrast is symbolized by the Rayleigh reflection coefficient, R, which at normal incidence is expressed as $R = I_2 - I_1/I_2 + I_1$, in which I_1 and I_2 = impedance values for two layers on either side of an interface. Thus, the boundary between a very dense sand with a large acoustic impedance and an overlying soft clay

with a small impedance will act as a strong reflector. The energy attenuation within each layer is frequency-dependent, and the relationship is generally expressed as $\alpha = kf^n$ in which α = attenuation in db/m, k = a constant, f = frequency in kHz and n = the exponent of frequency.

The velocity of seismic waves is complex and depends on the properties of the materials. However, the velocity generally increases as the density increases. For this reason, the depth scale on the profiles cannot be considered truly linear, and hence additional information is required for accurate calibration.

TABLE 1.—Comparative Description of Marine High-Resolution Geophysical Systems

System (1)	Use (2)	Frequency of output pulse (3)	Operational resolution (4)	Type of acoustic source (5)	Power output (6)	Comments (7)
Side Scan Sonar	provide map view of seafloor to (a) locate wrecks, pipelines/debris, (b) determine seafloor topography. detect gas bubbles in water.	105 ± 10 kHz	variable; typically 1 to several feet (0.3 to a few meters)	piezoelectric transducer	128 db (Peak) Ref. 1 microbar at 1 m	also referred to as "Side-Looking Sonar"
Fathometer	determine water depth detect gas bubbles in water column provide profile of seafloor	40–200 kHz	about 2 ft (0.6 m)	piezoelectric transducer	about 0.5 joules	also referred to as "Depth-Sounder"
Tuned Transducer	provide profiles of very shallow subseafloor to about 100 ft (30 m) determine water depth. detect gas bubbles in water.	3.5 or 7 kHz	variable; typically 2 to 3 ft (0.6 to 1 m) depending on application	piezoelectric transducer	up to 2 joules	also referred to as "RTT-1000"*
Acoustipulse*	provide profiles of shallow subseafloor to 500 ft (150 m) determine water depth. detect gas bubbles in water.	broadband 200 Hz to 4 kHz	variable; typically 2 ft (0.6 m) depending on application	electromechanical transducer	200–1,500 joules	provides excellent resolution of shallow faults, bedding, gas zones, etc.
Sparker	provide subseafloor profiles to intermediate depths about 3,000 ft (900 m)	broadband 10 Hz to 500 Hz	about 25 ft (7.6 m)	electric Spark	3.3, 4, 6.6 or 10-KJ	provides most penetration but least resolution of the subseafloor profiling systems used for site surveys.

*Tradename.

Alternatively, a close approximation of shallow subseafloor depths can be made by assuming a velocity previously determined for other similar materials.

All of the acoustic systems except the side-scan sonar system are designed to provide data essentially from beneath each sound source; no data is received from either side of the line of profile, except for occasional spurious side reflections. In contrast, the side-scan sonar system provides data from several tens or hundreds of meters on both sides of the ship's trackline. The three geophysical systems from which data are used in studying sandwaves,

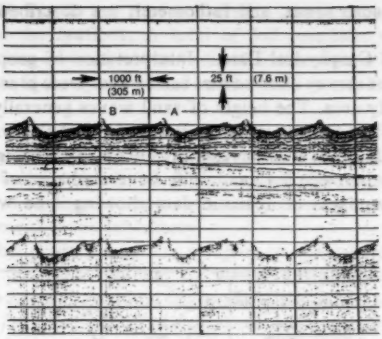

FIG. 3.—Acoustipulse Data Showing Sand Waves (A and B Refer to Corresponding Locations on Fig. 4.)

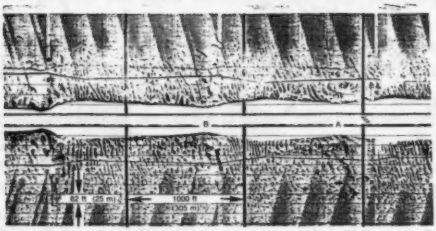

FIG. 4.—Side-Scan Sonar Data Showing Sand Waves (A and B Refer to Corresponding Locations on Fig. 3)

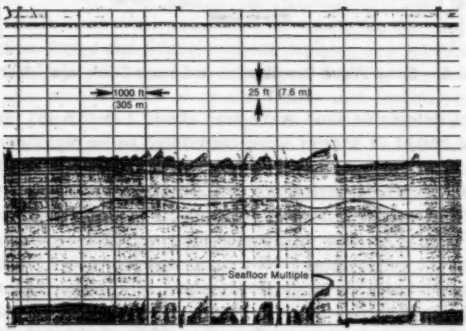

FIG. 5.—Acoustipulse Data Showing Sand Waves and Old Erosion Surface (Dashed Line)

acoustipulse, side-scan sonar, and fathometer, are described briefly in a later section.

Interpretation of Geophysical Data.—Interpretation of geophysical data from the lower Cook Inlet survey showed that sand waves were present in the northern portion of the study area. The height of sand waves generally observed ranged from less than 2 ft (0.6 m) to over 50 ft (15 m), and the wave length ranged from less than 20 ft (6 m) to over 1,000 ft (305 m). The height to wave-length ratio was generally between 1:15 and 1:50. Several shapes of ripples and dunes were observed. Examples of acoustic data showing sand waves are given in Figs. 3, 4, and 5.

FIG. 6.—Sand Wave Distribution in Lower Cook Inlet, Alaska

The smallest detectable sand wave was about 2 ft (0.6 m). Sand waves of 5 ft (1.5 m) in height or greater were considered to be significant, since local seafloor elevation changes exceeding 5 ft (1.5 m) over a short distance could affect the installation and performance of seafloor-supported structures. Sand waves with a height of 5 ft (1.5 m) or greater were mapped, and their distribution is shown in Fig. 6. The area of most numerous sand waves contained waves in over 80% of the geophysical profile lines, and is about 1,200 sq mile (3,100 sq km) in size. The area of moderate numbers of sand waves had about 50% of profile line lengths covered with waves higher than 5 ft (1.5 m). In the remainder of the sand wave area, less than 20% of the survey line lengths were covered with significant sand waves.

Seafloor Sampling.—Seafloor materials were sampled using a grab sampler

weighing about 100 lb (45 kg) that achieved a penetration of about 6–8 in. (152–203 mm) into the seafloor. A total of 362 locations were concentrated in five sampling areas selected on the basis of features seen on the geophysical data. Some of the 65 sample sites of area No. 3 were in the area of sand waves.

The survey vessel was located over each sample site by means of an electronic positioning system. The grab sampler was lowered to the seafloor and recovered by means of a winch onboard the survey vessel. Each sample was visually observed, logged, and then a representative portion placed in a water-tight container for shipment to the laboratory.

To determine the gradation of the samples in the laboratory, the samples were mixed with an equal amount of water, stirred thoroughly, and then centrifuged. The water was decanted and, using a 10 power binocular microscope, the apparent clay/silt and silt/sand interfaces were visually determined. The clay, silt, and sand volumes were expressed as percentages of the total sample volume.

All of the 64 samples analyzed from sampling area No. 3 were predominantly sand. About 50 of the 64 samples contained more than 90% sand by volume. Visual examination placed the sand mostly in the fine to medium grain size range with a 50 percentile size, D_{50}, of about 0.04 in. (1.0 mm).

Sand Waves—Terminology.—A variety of terms and definitions have been used in the literature to describe the various shapes and origins of sand waves. The two disciplines that study sand waves are sedimentology and hydraulics. There is no general agreement on terms and definitions between the two areas of study, nor even within each discipline. Many comprehensive publications present an *ad hoc* set of definitions to establish a basis for examination. One of the main causes of confusion is indiscriminate mixing of terms based on origin, shape, or size. No attempt is made here to resolve all the differences, as some of them result from different geologic settings or other specific study aspects.

In this paper, the term "sand waves" is applied in a generic sense to all wave-shaped bedforms composed of granular materials. The description of seafloor features in lower Cook Inlet is mainly confined to their size. A variety of shapes and sizes were observed, some of which fit the shapes and sizes implied by ripples, dunes and ridges, without implying any specific origin.

In the theoretical analysis on sediment transport flow regime, a clear classification can be made on the basis of origin. Dunes and ripples are asymmetric sand waves that are formed under tranquil flow conditions (Froude number, F, is less than 1). The symmetrical wave forms termed "antidunes" are formed under shooting flow conditions (F greater than 1).

Influence of Sand Wave Movement on Offshore Facilities.—Because of the possibility of their movement, submarine sand waves constitute a potentially hazardous foundation condition and place constraints on offshore exploratory drilling and construction. The movement of bedforms is of primary concern to the construction and performance of offshore pipelines. As extreme sand waves with side slopes representing over 50 ft (15 m) height change in a horizontal distance of 200–300 ft (60–90 m) were observed in the study area, burial of pipelines below the potential depth of scour would be impractical. Movement of sand under a pipeline will result in loss of support (8). Routing of pipelines

around areas of numerous sand waves, provision of alternate pipelines, use of heavier pipe and periodic monitoring of the seafloor may be required. Movement of sand waves in the upper Cook Inlet has caused several pipeline failures, and vigilance is maintained by means of yearly side-scan sonar surveys to identify areas of bedding support loss (16).

For pile-supported structures, partial loss of lateral support would result due to sand movement away from the structure, analogous to deep scour. Such a loss of support would have to be anticipated in lateral load design of the structure piles. For gravity structures, local relief associated with sand waves would influence site selection. Such relief would also influence the siting of mat-supported mobile jack-up rigs. For leg-supported mobile rigs used in oil exploration, leg penetrations are expected to be shallow if the seafloor soils consist of sands. Thus, scour due to possible sand wave movement could undermine the leg footings and present a serious threat to rig stability.

Evaluation of Sand Wave Movement

The presence of sand waves in an area generally implies that some sediment movement may be occurring. However, the rate and frequency of movement cannot be inferred by observing wave forms. All sand waves are in a dynamic condition during formation, and the movement continues as long as similar conditions prevail. The absence or presence of sand wave movement under the prevailing conditions in lower Cook Inlet is difficult to assess. An indication of movement has been sought through an approach using the following steps:

1. Examination of the two phase (water-sand) flow regime from a knowledge of grain size and current data.
2. Direct observations (diver or TV) to ascertain bed movement.
3. Repeated geophysical surveys to examine the bedforms for changes.

Flow Regime.—The 64 bottom samples described earlier showed that the shallow seafloor materials consist predominantly of fine to medium sand, with an approximate mean grain size of 0.04 in. (1 mm). Data on bottom current observations is quite limited, and shows a mean velocity at maximum flood tide of 1.0 knot (0.5 m/sec) at one location, although some measurements exceeding 1.4 knots (0.7 m/sec) were also recorded (16). These velocity measurements were not taken during a storm.

Based on relationships between flow velocity, bed shear, and grain size, a 1.0-knot (0.5 m/sec) current imparts a bottom shear stress of 0.25 lb/ft^2 (1.2 N/m^2 or 12 $dynes/cm^2$) as computed from Hjulstrom's and Shield's diagrams (1). This shear stress value can be used to assess whether the flow regime is conducive to the formation of sand waves, which would imply movement. By computing grain size, Reynolds number, and the mobility number for 0.04 in. (1.0 mm) size sand sampled in lower Cook Inlet, and assuming a 1.0 knot (0.5 m/sec) current, the lower Cook Inlet flow regime can be compared with data obtained under controlled conditions. A plot of Reynolds number and mobility number in Fig. 7 (17) shows that the lower Cook Inlet data fall in a zone where the simultaneous formation of ripples and dunes is likely.

The sand wave formation is also a function of time, and the full development

duration can be as long as several days at small flow velocities (17). Flow velocities of 1.0 knot (0.5 m/sec) acting for short periods and equally in both directions of tidal flow, are probably insufficient to form significant sand waves. Under these conditions, bedform development might take place only during severe storms when current velocities are high. The complex seafloor and shoreline topography could also affect current velocities during storms and periods of wide tidal ranges. The applicability of the laboratory-based relationships given in Fig. 7 to field conditions such as those found in lower Cook Inlet is uncertain. However, sediment transport concepts have been applied to the examination of phenomena ranging from desert dunes to sand waves (17). Detailed computations of flow regime appears in a later section.

Direct Observations.—TV camera observations of the seafloor at the end of a flood tide by a U.S. Geological Survey (USGS) study team (2,3), showed bed load transport occurring in the form of rolling and saltating grains. This led to the conclusion that active transport takes place in lower Cook Inlet. As only a limited area could be observed for a brief time period, movement of bedforms larger than the smallest ripples could not be ascertained by direct observation.

Repeat Geophysical Surveys.—During the 1973 survey reported in this paper, duplicate fathometer coverage of portions of the survey grid was obtained while performing separate sparker and acoustipulse profiling. The fathometer records

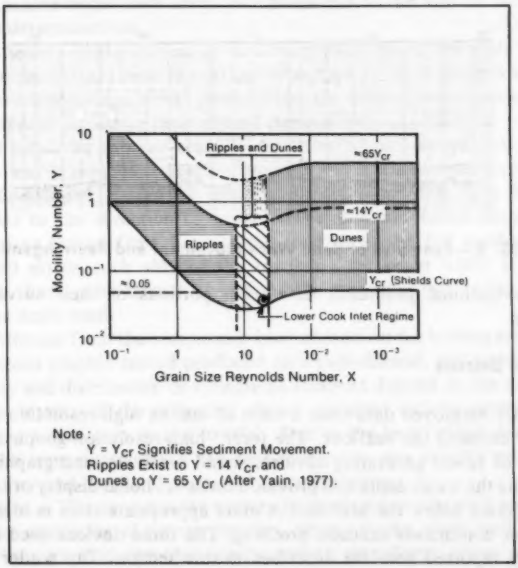

FIG. 7.—Flow Regime Showing Conditions Suitable for Initiating Formation of Sand Waves

were obtained during two surveys anywhere from 3–52 days apart. A comparison of fathometer profiles provides information concerning the short-term movement of sand waves.

Comparison of these repeat fathometer records shows that the seafloor configuration is generally stable, but locally there are differences in the seafloor profile. Each limited area of possible movement is bounded by other areas that did not appear to move during the survey span. An example of possible movement is shown in Fig. 8. About a dozen such isolated instances of sand wave movement were found in which postplots indicated that the later and earlier survey lines coincided. Thus, navigation errors can be ruled out.

An assessment of long-term movement was attempted in 1977 and 1978 by USGS teams who resurveyed six lines from the 1973 survey reported here (2,3,4,16). They concluded that the sand-wave fields in lower Cook Inlet appear to be stable with very limited changes in bed-forms over five years. However,

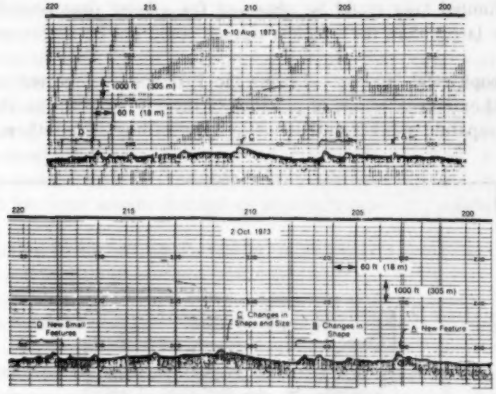

FIG. 8.—Examples of Sand Wave Movement and Rearrangement

due to navigational problems, data from portions of their survey was not conclusive.

Geophysical Systems

This study employed data from a suite of marine high-resolution geophysical devices to examine the seafloor. The term "high-resolution geophysics" refers to the use of sound generating devices, sound receivers, and graphic recorders which define the water depth and provide a cross-sectional display of the sediment and rock layers below the seafloor. A more appropriate term is high-resolution acoustics or continuous acoustic profiling. The three devices used in the sand wave study reported here are described in this section. The reader is referred to other publications for a more complete description of the systems (12,13), for details of data processing techniques (14), for application of methods (9,10,11,12,15), and for marine sediment properties that affect the propagation

and attenuation of sound energy (5,7). The following descriptions are adapted from an earlier paper that describes the geophysical systems used in this study (12).

Fathometer or Depth-Sounder.—The depth-sounder system consists of a power supply, a transducer (a transceiver that alternately transmits and receives sound), and a graphic recorder. The depth-sounder transducer usually is installed in the hull of the vessel, midship, and 6–10 ft (2–3 m) below the water surface. The transducer converts electric energy to sound energy, and the sound energy is transmitted downward to the seafloor. When this energy strikes the seafloor, or any other object having acoustic properties different from water, a part of it is reflected back to the transducer (transceiver) as an echo. This sound energy then is reconverted to electric energy, then recorded on a graphic recorder. Assuming that the speed of sound in water is nearly constant, the amount of time which lapses between the pulse transmission and the echo reception is a measure of the distance traveled.

Because of the high frequency of the fathometer, virtually no subbottom penetration is obtained. This system is suitable for operating in water depths of a few meters to several hundred meters, and also can be used to detect gas bubbles.

The accuracy of a depth-sounder system is largely dependent on two variables: (1) The velocity of sound in water, which can vary with changes in temperature and salinity; and (2) the precision of the electronic timing circuits used. Both of these variables necessitate frequent calibration of the system for accurate bathymetric determinations.

Side-Scan Sonar.—Side-scan sonar systems provide graphic records that show a two-dimensional (map) view of seafloor topography. These records are closely analogous to a low-oblique aerial photo. Features shown on the side-scan sonar commonly appear similar to their natural perspective.

A typical side-scan system consists of a towfish containing two arrays of transducers and a shipboard graphic recorder. The transducers emit 105-kHz pulses as fan-shaped beams on each side of the towfish. The beams are perpendicular to the direction of vessel travel and are broad enough in the vertical plan to extend from beneath the towfish to the full system range of 1,500 ft (450 m) to each side of the towfish. The beam width is only 1.2° in plan view. Each pulse lasts 0.1 msec and the repetition rate varies depending on the range scale used.

Signals reflected from the bottom and from objects on the bottom are displayed on a continuous graphic record produced on a two-channel, wet paper recorder. The intensity and distribution of reflections received depend on the composition and surface texture of the reflecting object, its size, and its orientation with respect to the transducers in the towfish. Due to the beam shape and the short length of the transmitted pulse, the side-scan sonar can resolve small objects on the seafloor and details of topographic irregularities.

Acoustipulse.—The acoustipulse system is an electromechanical acoustic profiling system consisting of power supplies, trigger banks, shipboard electronics package, filter graphic recorder, and a towed transducer array with an accompanying towed hydrophone. Acoustipulse is a single channel, high resolution, marine reflection seismic system developed to provide both high resolution and penetration up to 300 ft (90 m) in areas underlain by soils and soft-rock strata.

Typical seafloor penetration is about 250–300 ft (70–90 m). Penetration of as much as 500 ft (150 m) can be obtained under the most ideal acoustic conditions (where the material being profiled is soft).

The acoustipulse waveform is produced by discharging stored electrical energy into a potted wire coil. Eddy currents set up in the coil repel an adjacent aluminum plate. A partial vacuum created by the flexed plate returns the plate to its original position. The return motion is highly dampened by a rubber diaphragm, thereby minimizing source reverberations. The source is driven by a capacitive-discharge power supply capable of producing up to 1,000 joules per transducer.

Normally, a source consists of three electromechanical transducers, all of which are fired simultaneously every 0.5 sec. Energy output of each transducer is variable, all of which are mounted on a 8 ft (2.5 m) long catamaran and towed at or near the water surface 100 ft (30 m) behind the survey vessel. Reflected signals are received by a 10 element linear hydrophone array towed at or near the water surface and abeam of the source transducers. Signals outside the desired frequency range are removed by frequency filtering. The data are displayed graphically on a 0.25 sec record. Vertical exaggeration of the subbottom profiles is typically 10–20 times. Signals also can be recorded on an analog tape recorder for laboratory playback.

Flow Regime

Experiments indicate that a mobile granular sediment bed acquires sand wave shapes for certain intervals of the dimensionless variables of two-phase motion (17). If the set of variables expressed as Froude number reduces to a value less than unity, then the flow is considered tranquil, and sand waves formed take the asymmetrical shapes of ripples and dunes. These may be stationary or move along the current path. If the Froude number is greater than 1, then the flow is shooting, and symmetrical sand waves termed antidunes are formed. These may be stationary or move upstream against the current path. The Froude number, F_r, is expressed as:

$$F_r = \frac{u}{\sqrt{(gh)}} \quad \ldots\ldots\ldots\

To assess whether the present flow regime is capable of moving, or forming, the bedforms observed in acoustic profiling data, the field measurement data can be plotted on the X-Y plot in Fig. 7 (17), in which X = grain size Reynolds number and Y = mobility number, as defined below: Grain size Reynolds number, $X = vD/\nu$ in which D = grain size; ν = kinematic viscosity; v = shear velocity $= \sqrt{(\tau_o/\rho)}$. In which τ_o = shear stress interacting between the flow and bed surface; ρ = density of fluid = γ/g; in which γ = specific unit weight of fluid; g = acceleration due to gravity.

$$\text{Mobility number } Y = \frac{\rho v^2}{\gamma_s D} \quad \ldots\ldots\ldots\ldots\ldots\ldots\ldots\ldots\ldots\ldots\ldots\ldots (2)$$

in which γ_s = specific unit weight of grains, and ρ, v and D are as defined above. For conditions in the lower Cook Inlet, the following data are available:

1. $D = 3.3 \times 10^{-3}$ ft (1.0 mm)
2. $\rho = \gamma/g = 64/32 = 2$ slugs (1.03 gf)
3. γ_s (quartz) = 165 lb/ft^3 (2.64 g/cm^3)

Current velocity = 1.0 knot (0.5 m/sec), which, according to Hjulstrom's and Shield's diagrams (1), imparts a bed shear stress $\tau_o = 0.025$ lb/ft^2 (1.2 N/m^2 or 12 dynes/cm^2). Therefore, shear velocity $v = \sqrt{(\tau_o/\rho)} = \sqrt{(0.025/2)} = 0.11$ ft/sec (3.4 cm/sec). For water at 39.2° F (4° C), which is close to the prevailing temperature in lower Cook Inlet, kinematic viscosity $\nu = 0.00001687$ ft^2/sec (0.0159 cm^2/sec) from tabulated values given by King and Brater (7).

$$X = \frac{vD}{\nu} = 0.11 \times 3.3 \times \frac{10^{-3}}{0.00001687} = 21.6 \quad \ldots\ldots\ldots\ldots\ldots\ldots (3)$$

$$Y = \frac{\rho v^2}{\gamma_s D} = 2 \times \frac{0.11^2}{165} \times 3.3 \times 10^{-3} = 0.044 \quad \ldots\ldots\ldots\ldots\ldots\ldots (4)$$

Considering Fig. 7 with the above values of X and Y, the conditions are suitable for simultaneous formation of ripples and dunes.

Summary and Conclusions

Geophysical methods are an integral part of offshore site investigations. Selected high-resolution geophysical systems can be used to study the seafloor and shallow subseafloor zones to identify the bedforms. A portion of the seafloor in lower Cook Inlet is covered with waveshaped bedforms composed of granular materials, ranging in height from less than 2 ft (0.6 m) to over 50 ft (15 m), with wave lengths from less than 20 ft (6 m) to over 1,000 ft (305 m), and with height to wave-length ratios generally between 1:15 and 1:50.

Wave-shaped bedforms are generally associated with sediment movement in strong current areas. Since sand wave movement could put constraints on offshore construction, a multiplicity of techniques was applied to assess the movement of these bedforms in lower Cook Inlet. An examination of the flow regime shows that the prevalent currents in lower Cook Inlet are capable of initiating some movement, but apparently the tidal durations are too short to form the

large sand waves. Bed form development might take place only during severe storms when current velocities are high. Reported direct TV observations support the view that there is some localized sediment movement. Repeat geophysical surveys, however, showed the sand waves to be generally stable over large areas with some movement in localized areas. Further investigations, including post-storm inspection of actual construction sites, is required for more definite conclusions.

In siting offshore facilities in an area of sand waves, a map similar to Fig. 6 presenting sand wave distribution will be very helpful in the preliminary selection of the most suitable or feasible site(s) or route(s) for which the incidence of sand waves is lowest. Final selection and evaluation of a structure site or pipeline route will require consideration of the potential for sand wave movement and the depth of scour associated with the movement. The geophysical surveys conducted in lower Cook Inlet have demonstrated that high-resolution geophysical systems can be used to identify bedforms, determine the size, shape, and distribution of bedforms, and evaluate the movement of bedforms.

Acknowledgments

McClelland Engineers, Inc. permitted use of proprietary data originally acquired by former BBN-Geomarine Services Co., now a part of McClelland Engineers. An unnamed client permitted publication of Fig. 6, which is based on exclusive interpretive work. Phyllis Swinney typed the manuscript and Keith Dick prepared the illustrations.

Appendix I.—References

1. Blatt, H., Middleton, G., and Murray, R., *Origin of Sedimentary Rocks*, Prentice-Hall, Englewood Cliffs, 1972, pp. 91–93.
2. Bouma, A. H., Hampton, M. A., and Orlando, R. C., "Sand Waves and Other Bedforms in Lower Cook Inlet, Alaska," *Marine Geotechnology*, Vol. 2, 1977, pp. 291–308.
3. Bouma, A. H., Hampton, M. A., and Wennekens, M. P., "Large Dunes and Other Bedforms in Lower Cook Inlet, Alaska," *Offshore Technology Conference*, Paper No. OTC 2737, Vol. 1, 1977, pp. 79–90.
4. Bouma, A. H., Hampton, M. A., Rappeport, M. L., Whitney, J. W., Teleki, P. G., Orlando, R. C., and Torresan, M. E., "Movement of Sand Waves in Lower Cook Inlet, Alaska," *Offshore Technology Conference*, Paper No. OTC 3311, Vol. 4, 1978, pp. 2271–2284.
5. Hamilton, E. L., "Sound Velocity and Related Properties of Marine Sediments, North Pacific," *Journal of Geophysical Research*, Vol. 75, No. 23, Aug. 10, 1970, pp. 4423–4446.
6. Hamilton, E. L., "Sound Attenuation as a Function of Depth in the Sea Floor," *Journal of Acoustical Society of America*, Vol. 59, No. 3, Mar., 1976, pp. 528–535.
7. King, H. W., and Brater, E. F., *Handbook of Hydraulics*, McGraw-Hill, New York, N.Y., 1963, Table 1-2.
8. Machemehl, J. L., "Pipelines in The Coastal Ocean," *Pipelines in Adverse Environments, Procs. ASCE Pipeline Division Specialty Conference*, New Orleans, Vol. 1, 1979, pp. 204–221.
9. Mahmood, A., and Hough, J. C., "Seabottom Soil Properties and Acoustic Characteristics," *Offshore Technology Conference*, Paper No. OTC 3208, Vol. 3, 1978, pp. 1353–1360.
10. Mahmood, A., and Reifel, M. D., "Foundation Conditions in Outer Banks Area Offshore Southern California," *Offshore Technology Conference*, Paper No. OTC 3213, Vol. 3, 1978, pp. 1401–1408.

11. Porter, W. J., and Bell, D. L., "Development of Quantitative Remote Acoustic Indices for Location and Mapping of Sea Floor Soil Deposits," *Offshore Technology Conference*, Paper No. OTC 2288, Vol. 2, 1975, pp. 411–418.
12. Sieck, H. C., and Self, G. W., "Analysis of High Resolution Seismic Data," *American Association of Petroleum Geologists*, Memoir 26, 1977, pp. 353–385.
13. Tyce, R. C., "Toward a Quantitative Near Bottom Seismic Profiler," *Ocean Engineering*, Vol. 4, No. 3, 1977, pp. 113–140.
14. Watters, B. G., Harter, R., and Hough, J. C., "Wavelet Control—The Key to High Resolution Sparker Data and Interpretation," *Offshore Technology Conference*, Paper No. OTC 2987, Vol. 4, 1977, pp. 211–216.
15. Westneat, A. S., and Porter, W. J., "Acoustic Sediment Classification Involving Gas-Laden Soils," *Offshore Technology Conference*, Paper No. OTC 2613, Vol. 2, 1976, pp. 961–966.
16. Whitney, J. W., Noonan, W. G., Bouma, A. H., Hampton, M. A., and Thurston, D., "Lower Cook Inlet, Alaska: Do those Large Sand Waves Migrate?," *Offshore Technology Conference*, Paper No. OTC 3484, Vol. 2, 1979, pp. 1071–1082.
17. Yalin, M. S., *Mechanics of Sediment Transport*, Pergamon Press, Oxford, 1977, Chapter 7, pp. 209–267.

Appendix II.—Notation

The following symbols are used in this paper:

D = grain diameter;
F_r = Froude number = $u/\sqrt{(gh)}$;
g = acceleration due to gravity;
h = flow depth;
I, I_1, I_2 = characteristic acoustic impedance;
k = a constant relating acoustic attenuation to frequency;
n = exponent of acoustic frequency;
R = Rayleigh reflection coefficient;
u = average velocity of flow;
V = compressional wave velocity;
v = shear velocity = $\sqrt{(\tau_o/\rho)}$;
X = grain size Reynolds number = vD/ν;
Y = mobility number = $\rho v^2/\gamma_s D$;
Y_{cr} = Shields function. The value $Y = Y_{cr}$ signifies sediment motion;
α = acoustic attenuation;
γ = specific unit weight of fluid;
γ_s = specific unit weight of grains;
ν = kinematic viscosity;
ρ = density of fluid = γ/g;
ρ_s = sediment bulk density; and
τ_o = shear stress interacting between flow and bed surface.

SEISMIC TECHNIQUES IN THE LABORATORY[a]

By Richard D. Woods,[1] M. ASCE and Robert Henke[2]

INTRODUCTION

Several seismic exploration techniques are used routinely in geotechnical engineering to characterize earth materials at field sites. Some of these seismic techniques can be used to advantage at a laboratory scale. While the principles remain the same, some of the details of performing scaled down tests are different. Four applications of seismic techniques in the laboratory will be described with an emphasis on differences between the normal field application of each technique and the adaptation of each for laboratory use.

MODEL HALF-SPACE FACILITY

A facility was built by Woods (13) to perform steady-state elastic wave screening studies. This facility, in Fig. 1, was about 7 m in diameter and 2 m deep and was constructed with an absorbing perimeter of wet sawdust to minimize reflection of wave energy. The central testing zone consisted of well graded sand (common mortar sand) at a void ratio of about 0.5. The moisture content of the sand was maintained at between 2.5% and 6% to provide apparent cohesion and to permit excavation of open trenches and holes for wave screening studies.

It was necessary to know the shear wave velocity profile in the half-space facility to analyze adequately dynamic model footing and screening studies. Woods (13) used the steady-state Rayleigh wave method described in Richart, Hall, and Woods (8) to determine shear wave velocity as a function of depth. The solid circles in Fig. 2 represent the shear wave velocity profile.

The electromagnetic vibrator, shown in Fig. 1, was used to generate Rayleigh waves, and the distance to in-phase points was determined by comparing, on a dual beam oscilloscope, the signal from a transducer built into the vibrator with the signal from a geophone moved along the sand surface at increasing

[a]Presented at the October 22–26, 1979, ASCE Annual Convention and Exposition, held at Atlanta, Ga. (Preprint 3794).

[1]Prof. of Civ. Engrg., Univ. of Michigan, Ann Arbor, Mich.

[2]Research Engr., Exxon Production Research, Houston, Tex. (formerly Grad. Student, Univ. of Michigan, Ann Arbor, Mich.).

Note.—Discussion open until March 1, 1982. Separate discussions should be submitted for the individual papers in this symposium. To extend the closing date one month, a written request must be filed with the Manager of Technical and Professional Publications, ASCE. Manuscript was submitted for review for possible publication on February 17, 1981. This paper is part of the Journal of the Geotechnical Engineering Division, Proceedings of the American Society of Civil Engineers, ©ASCE, Vol. 107, No. GT10, October, 1981. ISSN 0093-6405/81/0010-1309/$01.00.

radial distances from the exciter. Varying the frequency of the exciter provided energy with different wavelengths which sampled different depths, as described in Richart et al., (8).

FIG. 1.—Model Half-Space Facility (13)

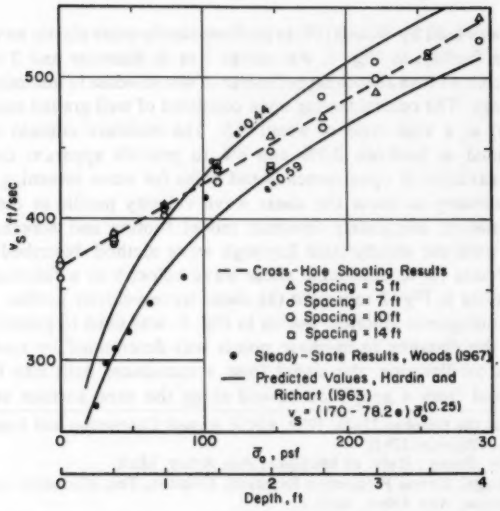

FIG. 2.—Shear Wave Velocity Profile in Half-Space Facility (10)

The major difference between these steady-state tests and those normally performed in the field (2,3,5) was the size of the exciter and geophone. In both instances smaller units were used in the half-space facility. The exciter was an M-B Electronics, Model C-31 with a maximum force capacity of 112

N while field units usually have at least 1.4 kN capacity. The geophone was an Electro-Tech, 8.5-Hz unit which was chosen because its base size, 40-mm diameter, was small compared to the wavelength of the shortest Rayleigh wave, about 225 mm. In addition, because the wavelengths were short, more care was used in matching phase and measuring distances.

Stokoe (10) also performed small scale cross-hole seismic tests to determine the shear wave velocity profile in the same half-space facility. The cross-hole method employed by Stokoe was that described in Stokoe and Woods (11). Results of Stokoe's tests are also plotted on Fig. 2. The cross-hole velocities are consistent with the earlier steady-state velocities and with empirical equations proposed by Hardin and Richart (6) at depths greater than about 0.3 m. The effective confining pressure $\bar{\sigma}_o$ used in the Hardin equation, as noted in Fig. 2, was computed from

$$\bar{\sigma}_o = \frac{1}{3}(\bar{\sigma}_v + 2K_o\bar{\sigma}_v) \quad \ldots \ldots \ldots

To determine the dynamic shear modulus of the sand medium, interferograms were made for various frequencies of excitation and the wavelength of the Rayleigh wave was scaled directly from the interferogram. From the measured wavelengths and known excitation frequency, the Rayleigh wave velocity could be computed. Using frequencies from 575 Hz–1700 Hz, wavelengths ranged from 75 mm–165 mm. Using the half-wavelength effective depth as described in Richart, et al., (8), the Rayleigh wave velocity versus depth was plotted (Fig. 5). Note that the depth sampled in these tests was very shallow, less than 85 mm, but, more importantly, the velocity decreased with depth rather

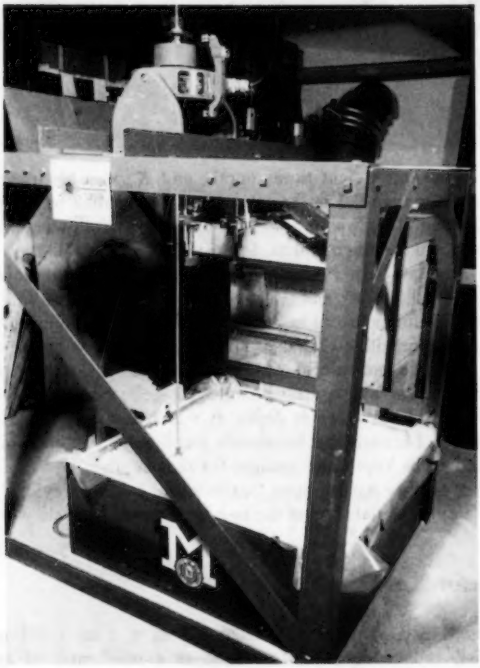

FIG. 3.—Holography Model Facility (14)

than the opposite as would be expected. A possible explanation for this behavior is based on the relationships developed between water content and apparent cohesion in the fine sand. Table 1 shows the results of direct shear tests on this sand at different water contents. The sand in the box was placed at a water content of about 5%, and the surface was covered with a plastic sheet to retain the moisture. However, the plastic had to be removed during some parts of the testing so surface drying occured. According to Table 1, as the water content decreased near the surface, the apparent cohesion increased;

therefore, near the surface apparent cohesion became the dominant force providing confinement. Using the cohesion intercept as effective confining pressure to compute shear wave velocity by the Hardin equation, the shear

FIG. 4.—Interferogram of Traveling Surface Waves (14)

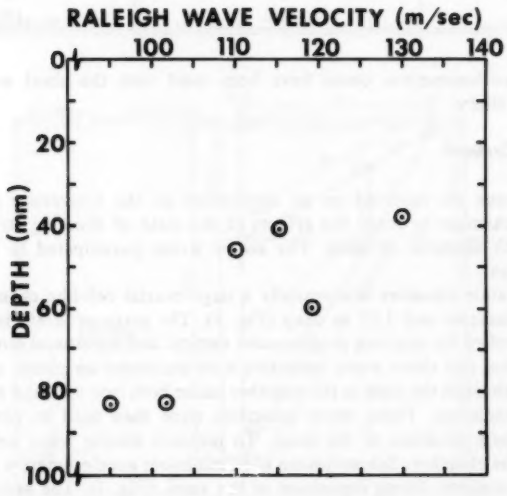

FIG. 5.—Rayleigh Wave Velocity Profile in Holography Facility

wave velocities in the right column of Table 1 were obtained. At a water content near 4% the empirical shear wave velocity was close to the measured Rayleigh wave velocity and a water content of 4% near the surface was very probable.

Because of the shallow depth of the box, the small size of the footing, and

the properties of the soil, it was not possible to produce interferograms at lower frequencies which would have sampled deeper into the sand. It is expected, however, that the wave velocity would have started to increase with depth again when confinement from geostatic pressure became large compared with apparent cohesion.

The major difference in these steady-state tests and those in the field was that no transducers were needed to determine in-phase points for wavelength determination. Wavelengths were scaled directly from contours on the interferograms and could be determined very accurately. No transducers, except possibly

TABLE 1.—Direct Shear Tests on Crushed Quartz Fine Sand

Water content, as a percentage (1)	Cohesion intercept, in pounds per square inch (kilopascals) (2)	Shear wave velocity, in feet per second (meters per second) (3)
2.4	2.5	500
	(17)	(152)
4.3	1.0	420
	(7)	(128)
6.0	0	0
	(0)	(0)

miniature accelerometers, could have been used with the short wavelengths used in this study.

Calibration Chamber

Schmertmann (9) reported on an application of the University of Florida calibration chamber to study the effects of the state of shearing stress on the dynamic bulk modulus of sand. The senior writer participated in that study as a consultant.

The calibration chamber is essentially a large triaxial cell-like chamber about 1.25 m in diameter and 1.25 m deep (Fig. 6). The state of stress in the sand can be controlled by applying programmed vertical and horizontal stresses.

Compression and shear wave velocities were measured on planes at selected orientations through the sand in the chamber under both isotropic and anisotropic confining conditions. These wave velocities were then used to compute the low-strain, bulk modulus of the sand. To measure elastic wave velocities in the sand in the chamber, Schmertmann used miniature accelerometers embedded at selected locations during deposition of the sand, (Fig. 7). The accelerometer locations were selected based on the position of access ports in the top platen of the chamber, the direction of planes of interest, and the dimensions and configuration of the chamber. Seismic energy sources were operated through the ports in the top platen of the chamber. Using four accelerometers and three source locations, wave propagation was studied along four planes through the sand (Fig. 7).

Wave velocities were determined by finding the time for a pulse to travel

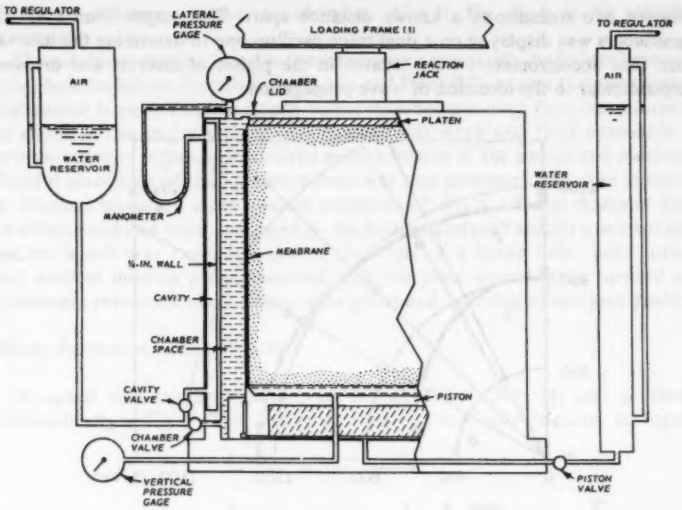

FIG. 6.—Schematic of University of Florida Calibration Chamber and Loading System (9)

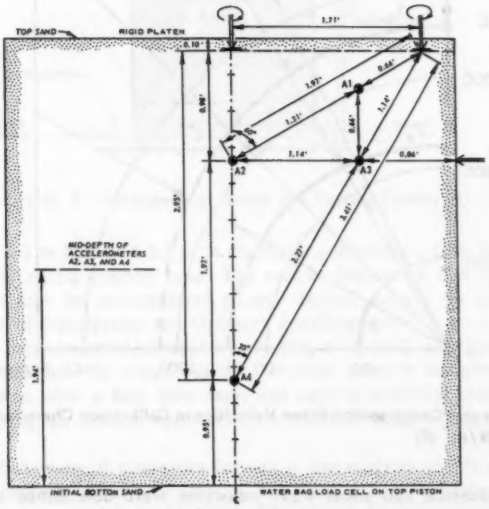

FIG. 7.—Location of Accelerometers and Seismic Sources in Calibration Chamber (9)

between two transducers a known distance apart. The output from a set of transducers was displayed on a dual trace oscilloscope to determine the interval time. The accelerometers were located in the planes of interest and oriented perpendicular to the direction of wave propagation.

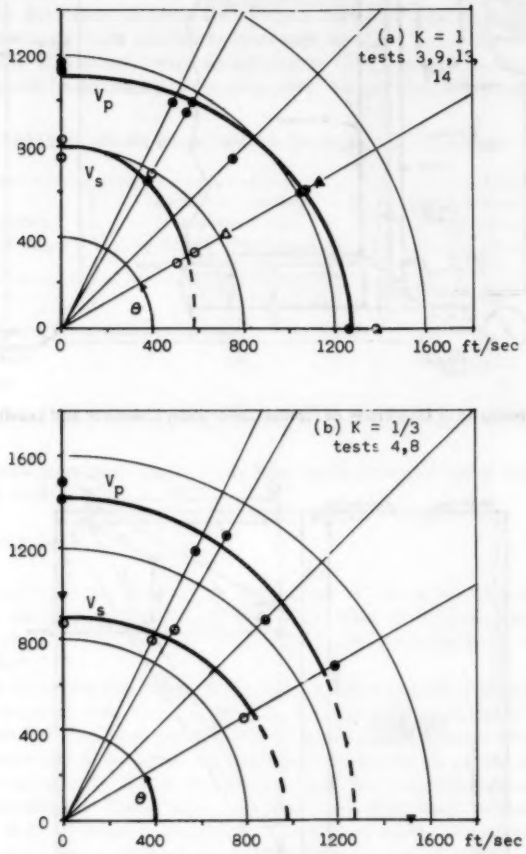

FIG. 8.—Shear and Compression Wave Velocities in Calibration Chamber, Octahedral Stress = 35 kN/m² (9)

Both compression and shear wave velocities were determined in planes at various orientations through the sand. An example of the results is plotted in Fig. 8 in polar coordinates. In Fig. 8, velocity is measured radially from the origin and the angle from the horizontal, θ, represents the orientation of

the plane of interest in the test chamber. Also in Fig. 8, K is the principal stress ratio, σ_3/σ_1.

The seismic techniques used in these tests were essentially the interval velocity cross-hole technique described by Stokoe and Hoar (12), expect that the receiver and source were at fixed locations rather than being moved from one elevation to another. The major differences between this work and field cross-hole or interval velocity techniques involved minaturization of the source and receivers. Careful placement of the accelerometers was also necessary to assure accuracy in spacing. Miniature input sources consisted of: (1) A 100-mm diameter plate to which sand had been cemented to the bottom surface; and (2) a scissor-jack packer which was expanded against the walls of a bored hole. Both torsion and vertical impacts were generated with the plate source while upward and downward reversible shear pulses were generated with the scissor-jack packer.

Model Foundation Testing Facility

A model pile testing facility was described by Chon (4) and is shown schematically in Fig. 9. This facility consists of a vertically oriented, corrugated

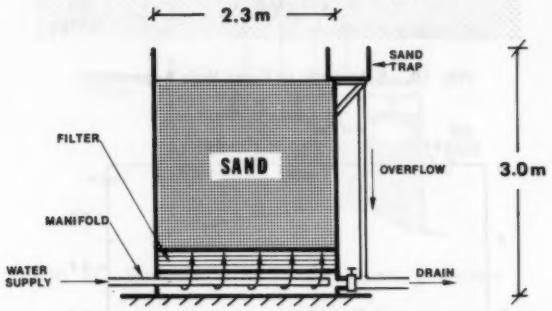

FIG. 9.—Schematic of Model Pile Testing Facility (4)

steel culvert, 3 m high and 2.3 m in diameter, containing a fine, poorly graded, cohesionless, round grained sand. The unique feature of this facility is that its contents may be reconstituted to any desired density by an appropriate combination of liquefaction and vibratory densification.

Test bed preparation is initiated by creating a "quick" condition in the sand by an upward flow of water. Sand in a loose state is achieved by gradual flow reduction after a high flow rate, and sand in a denser condition can be achieved using an electric spud concrete vibrator at preselected depths and patterns.

To establish material properties for use in the analysis of pile studies, Chon performed seismic cross-hole tests in the facility to determine the variation of dynamic shear modulus with depth. The crosshole apparatus used is shown in Fig. 10. The state of the sand as developed by a liquefaction and vibration process was relatively dense with $D_r = 76\%$ and $e = 0.6$. Spacing between

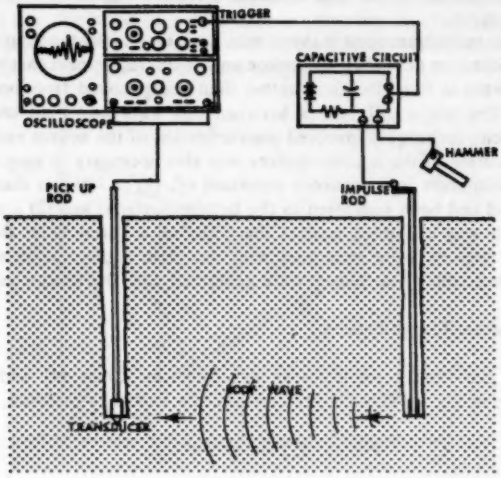

FIG. 10.—Schematic of Cross Hole Apparatus

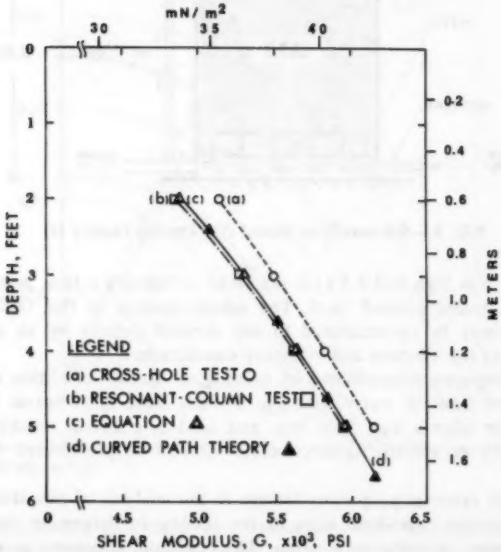

FIG. 11.—Shear Modulus Versus Depth in Model Pile Facility (4)

the impulse and receiver rods was 1.22 m and data were obtained from depths of 0.61 m, 0.91 m, 1.22 m, and 1.52 m. The seismic source consisted of an impulse rod coupled to an open-ended pipe. At each depth, the direction of the impulse was reversed to facilitate identification of the shear wave arrival.

Shear wave velocities from the cross-hole tests were converted to shear moduli using

$$G = \rho V_s^2 \quad \ldots \ldots \ldots

manometer. It has been found that at least 35 kPa may be safely used, resulting in a force of approx. 217 MN distributed uniformly over the area.

A new set of seismic cross-hole tests was performed by the junior writer with improved cross-hole apparatus and techniques to establish shear wave velocity as a function of both applied surface pressure and depth. The objective was to determine the surcharge pressure that produced the most favorable elastic property distribution for model footing tests. A schematic of the apparatus and its arrangement is presented (Fig. 13).

The impulse source for the crosshole tests (Fig. 14) consists of a freely rotating hammer supported by wooden bearings in a 64-mm diameter pipe. Attached to the upper end of the pipe is a target arm. The lower end couples to a rod, which in turn attaches to a Shelby tube. The rod is 25 mm in diameter and 2.44 m long while the Shelby tube is 355 mm long and 51 mm in diameter. Impact of the hammer onto the target arm applies a pure torque to the tube.

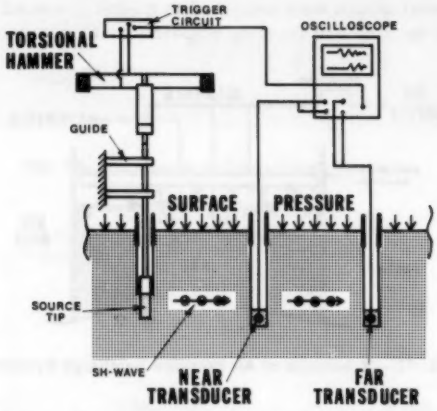

FIG. 13.—Schematic of Torsional Cross Hole Apparatus

In an actual test, the Shelby tube is embedded 152 mm into the soil below the borehole, and its rotation generates a horizontally polarized (SH) shear wave field.

Two horizontal velocity transducers, placed at the same depth as the Shelby tube and along a straight line from the source, were used as receivers. These geophones were oriented perpendicular to the array line for maximum response to the SH wave field.

The components of the electronic instrumentation system are shown (Fig. 13). The hammer and the target arm of the torsional device are separated by a wooden bearing which, in addition to its structural function, serves as an electric insulator between the two. As in Chon's (4) tests, hammer-target impact initiates triggering of the oscilloscope sweep by closing an RC trigger circuit. The torsional device was excited in both the clockwise and counterclockwise directions, and clear shear-wave reversals were noted. No distinct trend, however,

was detected for the compression wave because of its low amplitude and the presence of boundary interference.

Tests were conducted at depths of 0.15 m, 0.31 m, 0.61 m, 0.91 m, 1.22 m, and 1.52 m. For each of these depths the tank water level was slowly raised and lowered prior to testing in order to maintain a consistent water content. The source and transducers were then placed and the pressure was raised to 35 kPa to seat the air bags. Testing at a given depth consisted of obtaining cross-hole data at each surface pressure of the following unloading-loading sequence: 35 kPa, 28 kPa, 21 kPa, 14 kPa, 7 kPa, 14 kPa, 21 kPa, 28 kPa, and 35 kPa. A 15-min delay was adhered to after every surcharge change to allow for the minor time effects characteristic of cohesionless soils.

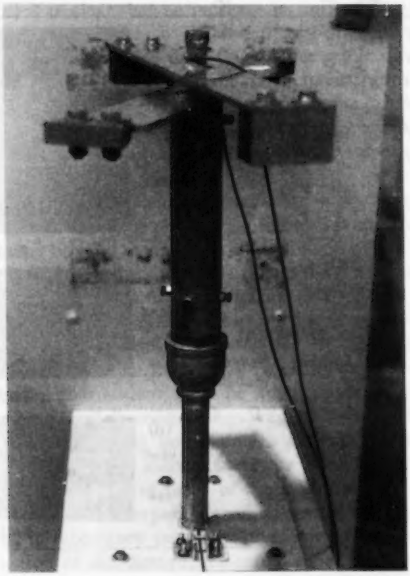

FIG. 14.—Photograph of Torsional Hammer

To calculate shear wave velocity, the straight path distance between receivers was divided by the time taken for a wave to travel from the near to the far transducer. Trigger error was found to be significant for the computation of velocity based on the first arrival at the near transducer; consequently, velocities were based upon interval timing only. Several points on the wave train were considered for wave arrival identification, and the results for a given impulse were averaged to arrive at the shear-wave velocity for that test.

Fig. 15(*a*) shows the results of these cross-hole tests as a family of shear wave velocity versus depth curves with surface pressure as a third parameter. Figs. 15(*b*), (*c*), and (*d*) present a representative group of photographic records

that demonstrate test reproducibility and the variation of the wave form with surcharge pressure at a depth of 152 mm. At this depth a pronounced trend of decreasing shear wave velocity with decreasing pressure may readily be observed by comparison among the records. Also apparent with decreasing pressure is the degradation of wave form believed to be associated with the inability of the material to transmit shear disturbances at low levels of confinement.

Also of interest is the quality of the reproducibility indicated in Fig. 15(*b*) and the preservation of the wave form shape between receivers, especially at the larger pressures where the medium is most receptive to shear wave transmission and transducer coupling is maximized. Inspection of the records

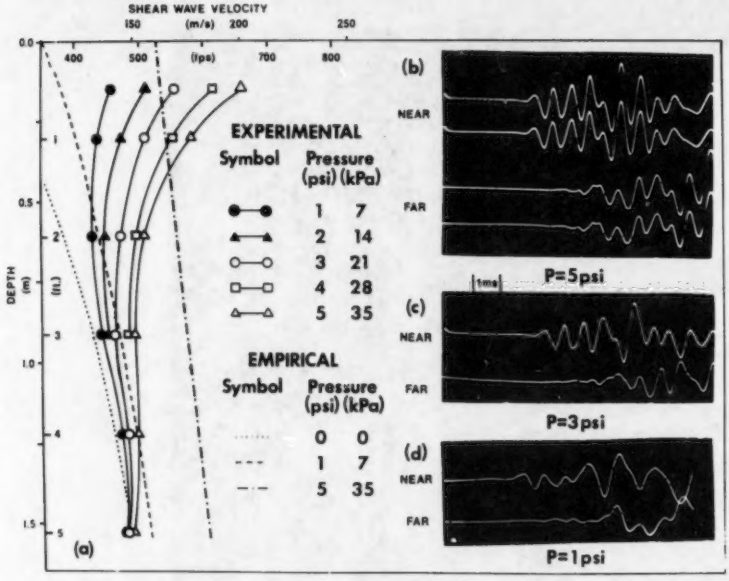

FIG. 15.—(*a*) Shear Wave Velocity Versus Depth for Model Foundation Testing Facility; (*b,c,d*) Representative Photographs at 152 mm Depth for Indicated Pressures

reveals a wave-form separation, which is evident in each of the far transducer traces by a low amplitude disturbance, which is not present in the near transducer records and precedes the major vibration. This initial segment is believed to be composed of compression waves that travel at a greater rate than shear waves, and reflections and refraction from a high wave speed surface or boundary. A final characteristic noted was a slight decrease in wave velocity with later points on the wave train implying effects of either material nonlinearity, wave dispersion, or reflection-refraction interference. This trend, however, did not persist with depth. The greatest velocity variation among individual computations based upon different wave points for any one record was 10.7% of the average

velocity for the record and occurred for the shallowest test depth of 0.15 m at which influence of boundary phenomena may be expected to be large. At each depth, the maximum velocity variation was determined and the smallest, 4.6%, occurred at the level of 1.22 m, well removed from disruptive boundaries.

To compare with these experimental results, shear-wave velocity profiles as a function of surface pressure were calculated by use of the Hardin equation. The void ratio was taken as 0.69. It was assumed that the air bags produced a uniform vertical pressure equal to the applied pressure throughout the facility and K_o was assumed to be 0.4. The confining stress distribution due to the surcharge was superimposed on that caused by geostatic stress. The results of calculations for surcharges of 7 kPa and 35 kPa and for geostatic confining stress only are also plotted on Fig. 15(*a*).

From Fig. 15(*a*) it is clear that an increase in the surcharge pressure results in an increase in shear-wave velocity at all depths. For each pressure the theory underestimates the wave velocity near the surface while overestimating wave velocity at the base. This indicates an apparent concentration of the surcharge induced stress in the vicinity of the surface, implying the existence of an arching effect created by the tank walls. Studies which tend to confirm this idea are currently being conducted in an effort to explain the experimentally observed phenomena.

Additionally, these cross-hole tests results are now being used as a basis for redesign of the facility to avoid arching under the application of surcharge and further tests may be used to study the effectiveness of any future alterations. The demonstrated ability of the cross-hole test in the detection of small changes in stress, as well as its potential for identification of a regional stress distribution which may have otherwise been difficult to obtain, is noteworthy and suggests solution of the inverse problem, the estimation of the confining stress or a change in confining stress that produces an existing or a change in an existing shear wave velocity distribution. Possible applications include the evaluation of damage to earth masses following earthquakes, monitoring of the stress transfer from pore water to soil during consolidation following construction, and the study of any process, which is associated with a change in confining stress.

By virtue of its scale, the execution of the laboratory cross-hole test differs somewhat from its field counterpart. For short source to receiver spacings such as those required in laboratory testing, a given triggering delay may represent a significant fraction of the disturbance travel time, leading to large errors in shear-wave velocity computations. To avoid this difficulty, the use of multiple transducers permitting transducer-to-transducer-based shear-wave velocities is considered essential. Because receiver-to-receiver distances are small, wave form spreading, which has been observed in the field by Stokoe and Hoar (12), is not particularly significant in the laboratory. This permits shear-wave velocities to be based upon the average of velocities obtained from different wave points appearing within the initial portion of the wave train. The advantage of this procedure is that random shifting of peaks, due in part to boundary reflections and refractions and in part to compression wave separation, may be averaged out.

Conclusions

Seismic techniques which are usually used in the field can be successfully

applied in laboratory size facilities. The major changes required are associated with: (1) Size and energy content of seismic source; (2) receiver size and sensitivity; (3) wave speed timing; (4) electronic triggering; and (5) precision of distance or spacing measurements, or both.

The same advantages that make seismic techniques attractive in the field are equally advantageous in the laboratory, namely; the tests are nondestructive and can be performed on materials in situ.

The seismic cross-hole tests proved to be very effective means for determining the spacial variation of elastic soil properties in large scale laboratory facilities. This technique was also demonstrated to be quite sensitive to relatively small confining pressure changes, a characteristic of considerable practical value for estimating effects of facility modification, and for the preparation of the most favorable material property distribution for foundation testing. Furthermore, its sensitivity suggests potential applications for the investigation of any process associated with confining pressure changes.

Acknowledgments

The writers wish to acknowledge and express appreciation to the National Science Foundation for support of some of these studies through several grants, including GI-344771 and ENG-01277. Also the writers express their appreciation for the support and encouragement of Professors F. E. Richart and E. B. Wylie.

Appendix I.—References

1. Auld, B., "Cross-Hole and Down-Hole V_s by Mechanical Impulse," *Proceedings of the Geotechnical Engineering Division*, ASCE, Vol. 103, No. GT12, Dec., 1977, pp. 1381–1398.
2. Ballard, R. F., Jr. and Casagrande, D. R., "Dynamic Foundation Investigations," TAA-2A Radar Site, Cape Kennedy, Florida, WES, *Misc. Paper No. 4-878*, Feb., 1967.
3. Ballard, R. F., Jr., and McLean, F. G., "Seismic Field Methods for In Situ Moduli," *Proceedings of the Conference on In Situ Measurement of Soil Properties*, ASCE, Geotechnical Engineering Division Specialty Conference, Raleigh, N.C., June 1–4, 1975, Vol. 1, pp. 121–150.
4. Chon, C.-S., "Dynamic Response of Friction Piles," thesis presented to the University of Michigan, at Ann Arbor, Mich., in 1977, in partial fulfillment of the requirements for the degree of Doctor of Philosophy.
5. Fry, Z. B., "Dynamic Soils Investigations Project Buggy," Buckboard Mesa Nevada Test Site, Mercury, Nev., WES, *Misc. Paper No. 4-666*, Jan., 1965.
6. Hardin, B. O., and Richart, F. E., Jr., "Elastic Wave Velocities in Granular Soils," *Journal of the Soil Mechanics and Foundation Division*, ASCE, Vol. 99, No. SM1, Feb., 1963, pp. 224–228.
7. Haupt, W. A., "Discussion of In Situ Shear Wave Velocity by Cross-Hole Method," *Journal of the Soil Mechanics and Foundation Division*, ASCE, Vol. 99, No. SM2, Feb., 1973, pp. 224–228.
8. Richart, F. E., Jr., Hall, J. R., Jr. and Woods, R. D., *Vibrations of Soils and Foundations*, Prentice-Hall, Inc., Englewood Cliffs, N.J., 1970, 414 pp.
9. Schmertmann, J. H., "Effect of Shear Stress on Dynamic Bulk Modulus of Sand," *Technical Report S-78-16*, WES, Oct., 1978, 27 pp.
10. Stokoe, K. H., II, "Dynamic Response of Embedded Foundations," thesis presented to the University of Michigan, at Ann Arbor, Mich., in 1972, in partial fulfillment of the requirements for the degree of Doctor of Philosophy.
11. Stokoe, K. H., II, and Woods, R. D., "In Situ Shear Wave Velocity by Cross-Hole

Method," *Journal of the Soil Mechanics and Foundations Division*, ASCE, Vol. 98, No. SM5, May, 1972, pp. 443–460.
12. Stokoe, K. H., II, and Hoar, R. J., "Variables Affecting In Situ Seismic Measurements," *Proceedings of the Conference on Earthquake Engineering and Soil Dynamics*, ASCE, Geotechnical Engineering Division Specialty Conference, Pasadena, Calif., June 19–21, 1978, Vol. 2, pp. 919–939.
13. Woods, R. D., "Screening of Elastic Surface Waves by Trenches," thesis presented to the University of Michigan, at Ann Arbor, Mich., in 1967, in partial fulfillment of the requirements for the degree of Doctor of Philosophy.
14. Woods, R. D., Barnett, N. E. and Sagesser, R., "Holography—A New Tool for Soil Dynamics," *Journal of the Geotechnical Engineering Division*, ASCE, Vol. 100, No. GT11, Nov., 1974, pp. 1231–1247.

Appendix II.—Notation

The following symbols are used in this paper:

G = shear modulus;
K = principal stress ratio;
K_o = coefficient of lateral earth pressure;
V_s = shear wave velocity;
θ = angle measured from horizontal;
ρ = mass density of soil;
σ_1 = major principal stress;
σ_3 = minor principal stress;
$\bar{\sigma}_0$ = average effective confining pressure; and
$\bar{\sigma}_v$ = effective vertical pressure.

DRILLED-SHAFT INTEGRITY BY WAVE PROPAGATION METHOD[a]

By Thomas M. Hearne, Jr.,[1] Kenneth H. Stokoe, II,[2] Associate Members, ASCE, and Lyndon C. Reese,[3] F. ASCE

INTRODUCTION

The increasing use of cast-in-place concrete shafts and the difficult soil conditions under which many of these deep foundations are constructed, uncertainty often arises concerning the integrity of the cast members (3,19). Foundation performance may be greatly impaired if defects or irregularities exist in these shafts. Defects and irregularities such as voids, soil inclusions, separations, enlarged regions, or necked regions may occur during construction (6,13,14). Therefore, definitive and economical test procedures are needed that can be used shortly after construction to evaluate the structural integrity of drilled shafts. Then construction can proceed with confidence, or the appropriate corrections can be made.

As a recent example of the kinds of problems that come to the attention of the writers, a drilled shaft that was supporting a bridge pier was found to have settled about 4 in. (100 mm), even though the full load had not been applied to the structure. While there were some unusual features in the construction procedures that led to the likelihood that there was excessive settlement in end bearing, there was no way to prove that the settlement did not occur because of a void or soil inclusion. The question was critical in relation to the possible lack of integrity of the other drilled shafts at the site. It is not being proposed, of course, that every drilled shaft be instrumented, but it is suggested that strong consideration be given to instrumenting routinely a certain fraction of the drilled shafts on many construction projects. Had instrumentation been used at the bridge site, valuable and instructive information could have been gained at a small cost.

[a]Presented at the October 22–26, 1979, ASCE Annual Convention and Exposition, held at Atlanta, Ga.

[1]Research Asst., Dept. of Civ. Engrg., Univ. of Texas, Austin, Tex. 78712.
[2]Assoc. Prof., Dept. of Civ. Engrg., Univ. of Texas, Austin, Tex. 78712.
[3]Prof., Dept. of Civ. Engrg., Univ. of Texas, Austin, Tex. 78712.

Note.—Discussion open until March 1, 1982. Separate discussions should be submitted for the individual papers in this symposium. To extend the closing date one month, a written request must be filed with the Manager of Technical and Professional Publications, ASCE. Manuscript was submitted for review for possible publication on February 17, 1981. This paper is part of the Journal of the Geotechnical Engineering Division, Proceedings of the American Society of Civil Engineers, ©ASCE, Vol. 107, No. GT10, October, 1981. ISSN 0093-6405/81/0010-1327/$01.00.

In the past, several nondestructive methods have been employed to evaluate the structural integrity of drilled shaft foundations. These methods include nuclear radiation, sonic, stress wave propagation, and vibration methods (1,4,5,7,11,12, 16,17,18,20). Their application has met with varying degrees of success. During the last 2 yr, the writers have successfully adapted and employed the stress wave propagation method to evaluate drilled-shaft integrity. In theory, this method is quite simple; that is, one just measures the time for compression waves to propagate vertically through the shaft from a source to one or more receivers. In reality, the method requires a viable field technique, which is described herein, and well-trained, conscientious field personnel.

Background

Of the many different source-receiver configurations that can be employed with the compression wave propagation method, two basic configurations have been used in this study. In the simpler of the two configurations [which has been used with limited success in the past (1,11,12,17,18)], both the source and receiver are installed on the top of the shaft. The time required for the compression wave, P-wave, to propagate from the top of the shaft to the bottom and then return to the top again is measured. This test configuration is referred to herein as *compression wave propagation with surface receiver.*

In the second source-receiver configuration, which was developed in this study, the source is installed at the top of the shaft, and the receiver is mounted within the shaft. The receiver is usually mounted on the steel reinforcing cage at a predetermined elevation. With the receiver position known, the source-to-receiver travel distance is also known. Therefore, P-wave propagation velocity can be determined directly once the source-to-receiver travel time is measured. This test procedure is referred to herein as *compression wave propagation with embedded receivers.*

Regardless of the source-receiver configuration employed, successful use of the method requires identification of reflected wave arrivals so that travel times of reflected waves can be used with propagation velocity to determine elevations of reflection points. Reflection points for sound, straight-sided shafts are the concrete-air interface at the top of the shaft and the concrete-soil interface at the bottom of the shaft. For shafts with discontinuities and irregularities, additional reflection points occur, and it is the monitoring of reflections from these additional points which permits identification of defective or irregular shafts. The amplitudes of any monitored reflections depend upon many factors including the input signal amplitude, concrete quality, surrounding soil conditions, the size and nature of the discontinuity or irregularity, and the location of the receiver relative to the elevation of the discontinuity or irregularity.

The following formulae are used in the compression wave propagation method to calculate the P-wave velocity, V_C, and Young's modulus in a rod, E, for the concrete:

$$V_C = \frac{d}{t} \quad \ldots\ldots\ldots\

in which d = travel distance; t = travel time; γ = unit weight of concrete; and g = acceleration of gravity.

Young's modulus determined by this procedure is the modulus of concrete at low strain levels. Strain levels resulting from P-waves propagating down the shaft are typically less than 10^{-6} mm/mm. As a result, Young's modulus determined by this method represents the maximum value of E, and moduli measured at higher strain levels, such as those determined in standard compression tests, will likely be much lower.

Compression Wave Propagation with Embedded Receivers

The most successful application of the compression wave propagation method in this study has resulted from the use of embedded receivers. The receivers

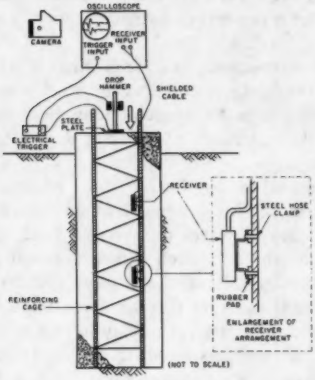

FIG. 1.—Compression Wave Propagation Method with Embedded Receivers

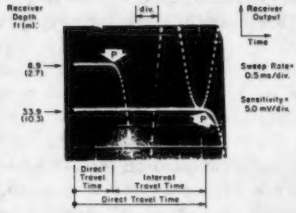

FIG. 2.—Determination of Direct and Interval Travel Times with Embedded Receivers

are cast in place in the shaft at preselected depths during the construction operation. Each receiver consists of a vertical velocity transducer sealed in an epoxy-coated aluminum case. An electrical cable extends from the aluminum case to about 10 ft (3 m) beyond the top of the shaft. The receiver cable is usually taped to the reinforcing steel along the shaft length to permit ease of placement during construction. The receiver case is joined to a metal bracket which is in turn attached to the reinforcing steel with steel hose clamps. A silicon rubber pad is used to isolate the bracket from the reinforcing steel. In these tests, isolation of the receiver from the reinforcing steel is an important consideration because the compression wave velocity in steel is greater than in concrete. If significant levels of compression wave energy are generated within the reinforcing steel and isolation is not provided, then monitored travel times may correspond to the compression wave velocity in steel rather than in concrete.

Fig. 1 shows the testing equipment employed and source-receiver configuration

used in recording P-wave propagation with embedded receivers. The equipment includes: (1) A compression wave source (a drop hammer with steel plate or hand-held hammer and chisel); (2) an electrical trigger; (3) a vertical receiver(s); (4) a storage oscilloscope (or digital oscilloscope); and (5) a Polaroid camera.

Compression waves are generated at the top of the shaft by releasing the drop hammer from a predetermined level. Hammers used in this study weighted from 10 lb–32 lb (4.5 kg–14.5 kg) and drop heights ranged from 6 in.–30 in. (150 mm–760 mm). An alternative approach for generating P-waves is to replace the drop hammer arrangement with a hand-held hammer and pointed chisel. However, the drop hammer technique provides a constant input amplitude which is desirable when analyzing the amplitude of monitored P-waves.

When the falling hammer contacts the steel plate, the oscilloscope is triggered, and recording of the receiver output commences. The time for the compression wave to travel from the top of the shaft to the receiver is then recorded. This time is called the direct travel time, and, with the travel distance known, one can compute the direct P-wave velocity.

For accurate timing measurements, it is essential that triggering of the oscilloscope occurs at a known time after the hammer contacts the steel plate. If triggering is delayed some unknown amount, then the direct velocity measurement will be in error on the high side, with the magnitude of the error dependent upon the delay time and the travel distance.

One means of eliminating triggering problems is to install two or more receivers with a vertical spacing of 10 ft (3 m) or more. Measurement of an interval travel time can then be performed. The interval travel time is the time for the wave to propagate from one receiver to another. Such a measurement is shown in Fig. 2 and is based on the initial arrivals of the P-wave, denoted by the P's in the figure. The output of both receivers for the same impulse has been captured on the oscilloscope record, and any time delay in triggering did not affect the interval travel time measurement illustrated. Use of a vertical spacing of 10 ft (3 m) or more between receivers minimizes the influence of slight variations in interpretations of the initial P-wave arrival times. However, any time delay or variations in interpretations of P-wave arrivals would affect the direct travel times shown in Fig. 2.

The hammer impact used to generate P-waves also generates other waves which can complicate interpretation of P-wave arrivals. Rayleigh waves (surface waves) are also generated by the hammer impact. These surface waves produce a very noisy environment in the upper portion of the shaft [most severe in the upper 10 ft (3 m) in this study]. Therefore, embedded receivers are placed at a depth of 10 ft (3 m) or more to minimize any unwanted monitoring of Rayleigh waves. The noise generated by surface waves constitutes a major problem when using a surface receiver (8).

To monitor wave arrivals accurately, receivers must be used which track closely wave particle motion. Frequencies generated in concrete by mechanical sources vary from several hundred to several thousand Hz (cycles per second). Receiver packages utilizing small velocity transducers with natural frequencies between 4.5 Hz and 40 Hz are economical (about $40 each, including cable) and can be used satisfactorily in concrete.

Vertical velocity transducers are utilized to sense the vertical particle motion generated by the propagating P-wave. Verticality of the receivers must be

maintained to prevent reduction and distortion of signal output. When using these receivers, one must ensure a good bond between the concrete and receiver. Also, isolation of the receiver from reinforcing steel must be provided as mentioned previously.

A storage oscilloscope and Polaroid camera are well suited for monitoring receiver output and obtaining a permanent record at a reasonable cost. More precision and greater ease in data analysis can be obtained by using a digital oscilloscope with magnetic recording capabilities. However, the digital oscilloscope is about two to three times more expensive. An electrical trigger is used to initiate timing with either oscilloscope. The trigger is essentially instantaneous when properly used and typically delays the oscilloscope sweep by less than 0.01 ms. A complete description of the trigger and possible triggering problems is given by Hoar and Stokoe (9).

Compression Wave Propagation with Surface Receiver

The equipment required for this testing procedure includes the following: (1) A compression wave source (a drop hammer with steel plate or hand-held hammer and chisel); (2) an electrical trigger; (3) an accelerometer; (4) a charge conditioner (used to amplify the accelerometer signal); (5) a filter (used with accelerometer signal); (6) a storage oscilloscope (or digital oscilloscope); and (7) a Polaroid camera.

Fig. 3 shows the testing equipment employed and the source-receiver configuration. The procedure involved in generating and recording the compression wave is the same as that described for compression wave propagation with embedded receivers.

The monitoring equipment and testing configuration in this test procedure differ from that when testing with embedded receivers in several respects: (1) The receiver is bonded to the top of the shaft with epoxy rather than being embedded at some depth within the shaft; (2) a small accelerometer is used as the surface receiver instead of a velocity transducer because reflections are more easily monitored with the accelerometers (velocity transducers are used as embedded receivers because they are much less expensive; and (3) the receiver output is typically filtered to reduce noise generated at the top of the shaft.

In terms of convenience, economy, and ease of testing, the procedure using a surface receiver has obvious advantages over testing with embedded receivers. One receiver can be used to test all shafts, and no instrumentation need be installed before or during shaft construction. However, these advantages are overshadowed by several severe limitations.

1. The success of the method requires that the reflection from the bottom of the shaft (or a defect or irregularity) be monitored. If a reflection cannot be monitored or identified, the results of the test are inconclusive, and no accurate information can be obtained to judge the concrete quality or integrity.
2. P-wave velocity cannot be measured directly. A method exists for estimating the P-wave velocity by monitoring the frequency of the surface wave reflecting back and forth across the top of the shaft (18). By determining this frequency, measuring the shaft diameter, and assuming a Poisson's ratio, one can make an estimate of the compression wave velocity in the shaft. However, at best

this is a crude estimate. Drilled shafts encountered in practice often have highly irregular surface shapes, thus rendering this procedure questionable and many times erroneous.

3. The most important limitation of testing with a surface receiver is that any impact at the top of the shaft generates surface waves which reflect back and forth across the top of the shaft for a time period that extends well beyond P-wave reflection arrivals for most shafts. These surface waves act as noise, which complicates and many times precludes identification of the arrival of the reflected P-wave. This noise problem is further compounded by any reinforcing cage or steel dowels which extend above the shaft surface.

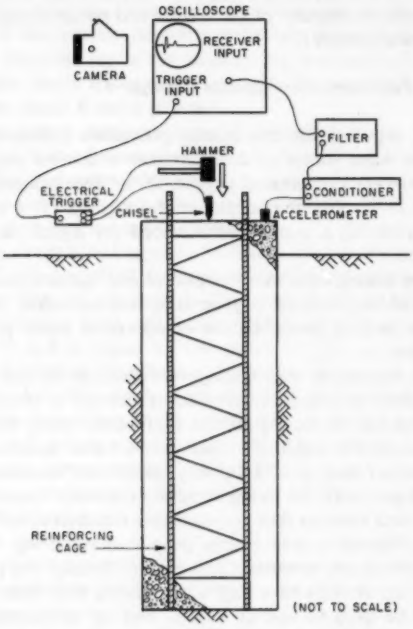

FIG. 3.—Compression Wave Propagation Method with Surface Receiver

Filtering may be used to minimize surface noise. However, filtering may cause additional problems, many times unrecognized problems, by altering amplitudes and travel times of reflections, and one must be very careful when filtering receiver output. If the generated P-wave frequency is close to the surface wave frequency, filtering will not be advantageous because the P-wave will be attenuated along with the surface noise, resulting in no improvement in the monitored receiver output. As the diameter of the shaft decreases, the frequency of noise created by the surface waves increases. Filtering is most helpful for shafts less than 2 ft (0.6 m) in diameter. When using most mechanical

sources on shafts of this diameter or smaller, the generated compression wave frequency differs from the frequency of noise generated by the surface wave, and a filter can be used effectively.

Compression Wave Velocity

In this study, P-wave velocities in 3,000 psi–4,000 psi (20,700 kPa–27,600 kPa) concrete have ranged from 12,000 fps to almost 15,000 fps (3,600 m/s–4,570 m/s) for measurements made 2 or more days after casting. Compression wave velocity cannot be directly related to concrete strength due to mix design variations. However, for a given mix design, measured P-wave velocity gives a relative indication of concrete quality, and, therefore, direct wave velocity measurements as made with embedded receivers are very worthwhile.

A suggested rating of concrete quality based on P-wave velocity is given in Table 1 (10). This rating is based on ultrasonic pulse tests (high-frequency tests) which were used to measure P-wave velocity through a concrete medium. In wave propagation testing, the compression wave velocity in a rod differs

TABLE 1.—Suggested Compression Wave Velocity Ratings for Concrete from Ultrasonic Tests (10)

Compression wave velocity, in feet per second (meters per second) (1)	General condition (2)
above 15,000 (4,570)	excellent
12,000–15,000 (3,660–4,570)	good
10,000–12,000 (3,050–3,660)	questionable
7,000–10,000 (2,130–3,050)	poor
below 7,000 (2,130)	very poor

from the compression wave velocity in a continuous medium of the same material if the wavelength is greater than the rod diameter. Because a drilled shaft is a rodlike structure, the wave propagation velocity as determined herein will be less than the velocity measured in a concrete medium at ultrasonic frequencies (15). This velocity reduction is approximately 10% for a Poisson ratio of 0.25. Therefore, velocities shown in Table 1 should be reduced by 10% if they are to be compared with velocities determined by the methods presented here.

Reflected Waves

Shaft lengths can be computed from reflection arrival times for measurements with embedded receivers. These lengths should correspond closely to the actual shaft lengths for sound shafts without irregularities. The success of this technique is, however, based upon the ability to measure or estimate P-wave velocity and to identify at least one reflection arrival.

When the P-wave encounters the concrete-soil interface at the bottom of the shaft, some of the incident wave energy will be reflected and some of

the wave energy will be transmitted into the soil beneath the shaft. If a significant portion of the energy is reflected, the P-wave will be detectable at the embedded receiver. Under these circumstances, the possibility also exists of identifying an additional reflection from the top of the shaft where essentially total reflection of the energy occurs. In this case, the 2L travel time can be determined as shown in Fig. 4, and an estimate of the effective shaft length, L, can be made without knowing the receiver depth.

A typical record showing the propagation of the compression wave as outlined in Fig. 4 is shown in Fig. 5. The oscilloscope record in Fig. 5 was obtained with three receivers embedded in a large [48-in. (1,120-mm) diam] shaft at the depths indicated. The 2L travel time for each of the receivers is the time interval from the initial compression wave arrival to the second reflection arrival,

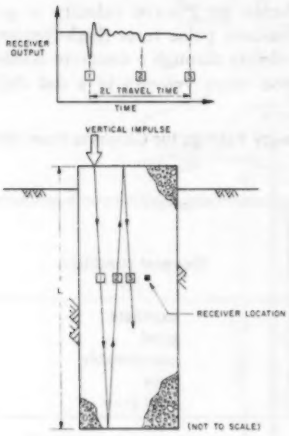

FIG. 4.—Reflection Analysis with Embedded Receiver

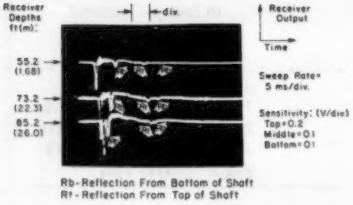

FIG. 5.—Reflection Record for 92-ft (28-m) Long Shaft with Three Embedded Receivers

Rt, which is from the top of the shaft. In this record, the 2L travel time could also be determined from successive reflection from the base, Rb's.

It is interesting to note in Fig. 5 that the first reflection has the same polarity as the initial arrival, indicating that the compression wave is reflected as a tensile wave from the base of the shaft. This tensile wave is then reflected as a compression wave from the top of the shaft, and the process repeats. This represents a typical reflection pattern for sound drilled shafts.

Typical shaft length computations based on reflection travel times for tests with embedded receivers are shown in Table 2. The listed shafts are representative examples from three different sites in Texas. An example of a record from a shaft with a known defect is shown in Fig. 6(*a*). During construction, a 2-ft (0.6-m) thick clay seam was added near the middle of the 39-ft (11.9-m) long shaft to simulate possible defects such as a soil inclusion or slurry entrapment

TABLE 2.—Calculated Shaft Lengths Based on Reflection Travel Times

Shaft number (1)	Measured* shaft length, in feet (meters) (2)	Shaft length based on reflections, in feet (meters) (3)	Percent difference (4)
1	105.1 (32.0)	103.6 (31.6)	−1.4
2	91.9 (28.0)	93.1 (28.4)	+1.3
3	98.1 (29.9)	102.0 (31.1)	+4.0
4	100.0 (30.8)	101.9 (31.1)	+1.0
5	94.4 (28.8)	94.7 (28.9)	+0.3
6	82.9 (25.3)	83.4 (25.4)	+0.6
7	111.9 (34.1)	113.5 (34.6)	+1.4
8	47.5 (14.5)	44.7 (13.6)	−5.9
9	46.5 (14.2)	46.3 (14.1)	−0.4
10	25.1 (7.7)	25.0 (7.6)	−0.4
11	25.2 (7.7)	25.2 (7.7)	0
12	106.0 (32.3)	104.9 (32.0)	−1.0

*Determined by taping hole before concrete placement.

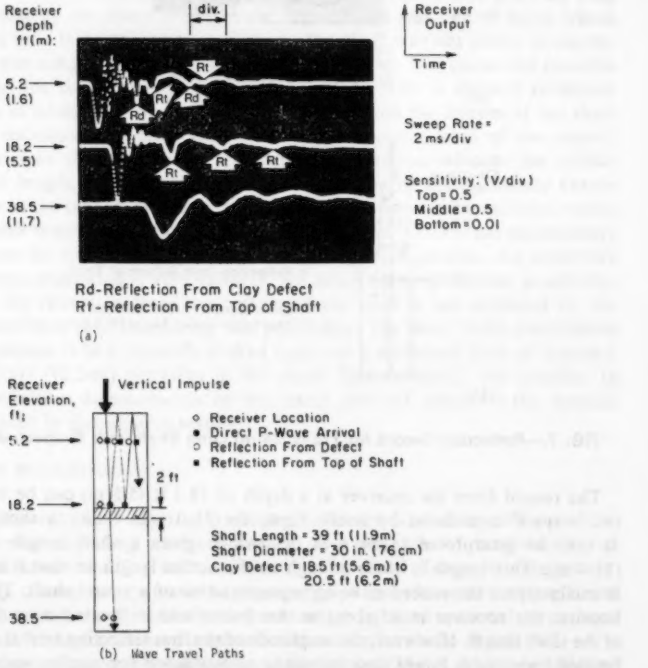

FIG. 6.—Reflection Record for 39-ft (12-m) Long Shaft with a Planned Defect

covering the entire cross section of the shaft (1). The shaft was instrumented with three embedded vertical velocity transducers, as shown in Fig. 6(*b*).

Several important points that highlight inherent strengths and limitations of P-wave propagation testing are shown in this record. The receiver located at a depth of 5.2 ft (1.5 m) monitored two distinct reflection arrivals much earlier than would be anticipated for a sound, 39-ft (11.9-m) long shaft. By using the 2L travel time determined from this receiver and a P-wave velocity of 12,200 ft/sec (3,719 m/s) determined from the interval travel time between the top two receivers, the effective shaft length, *L*, is 18.3 ft (5.6 m), indicating a defect at that depth.

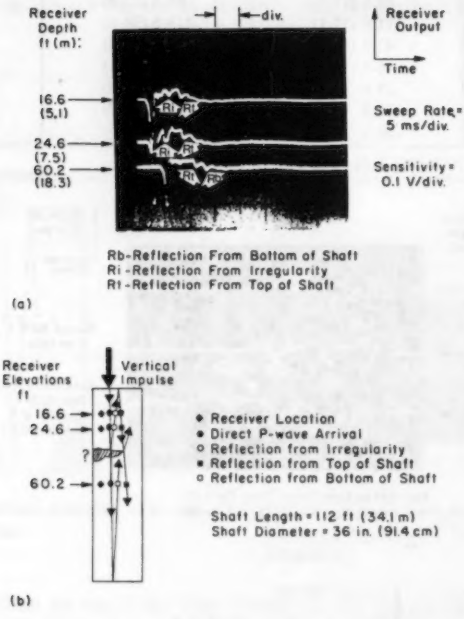

FIG. 7.—Reflection Record for 112-ft (34-m) Long Shaft with Suspected Defect

The record from the receiver at a depth of 18.2 ft (5.5 m) can be interpreted two ways if considered by itself. First, the 2L travel time (as shown in Fig. 4) may be interpreted to be 6.14 ms, which gives a shaft length of 37.5 ft (11.4 m). This length is close enough to the actual length so that it is possible to misinterpret the record as being representative of a sound shaft. This occurs because the receiver is adjacent to the defect and is located near the middle of the shaft length. However, the amplitude of the first reflection arrival monitored by this receiver is larger than normally encountered for similar sound shafts, which indicates a possible discrepancy with the first interpretation. Because

the receiver is located adjacent to the upper surface of the defect, which is a reflection point, there is only one reflection arrival (from the top of the shaft) for each 2L travel distance of the P-wave. Therefore, the second interpretation is that the 2L travel time is 3.00 ms, which is represented by the time interval between successive troughs on the record. This interpretation gives a length of 18.3 ft (5.6 m), which correctly identifies the location of the defect. This second interpretation would automatically occur when the output from this receiver is analyzed with the other embedded receivers.

The bottom receiver located at an elevation of 38.5 ft (11.7 m) recorded a very weak P-wave arrival, and it is obvious that some type of defect covering a large percentage of the cross section is present. (The sensitivity setting for the bottom trace is 50 times greater than that of the upper two traces.) Additionally, the measured interval P-wave velocity from 18.2 ft–38.5 ft (5.5 m–11.7 m) is reduced by almost 2,000 ft/sec (610 m/s) from the interval velocity measurement between 5.2 ft (1.6 m) and 18.2 ft (5.5 m). This observation further indicates a defective zone exists within the shaft. However, essentially no information is present in the bottom trace, which can be used to determine exactly where the defect exists.

An example of a record from a shaft with a possible defect which was discovered during routine field testing is shown in Fig. 7(*a*). This 112-ft (34.1-m) long shaft was cast by the slurry displacement method and was one of many which were tested on a large construction project. The shaft was not cored, however, because it was not going to be used in the structure. Fig. 7(*b*) shows the possible travel paths for the P-wave record shown in Fig. 7(*a*). A distinct reflection (Ri) occurs in addition to the reflection monitored from the bottom of the shaft (Rb). The reflections are most easily seen on the bottom trace of the record. This output was obtained from a receiver which was located near the middle of the shaft length, and reflection arrival times should be approximately evenly spaced across the record. However, two distinct reflections are monitored within a very narrow time frame. Because the direct wave amplitude is not significantly reduced from the monitored amplitude above the region in question, the possibility of a complete separation is very unlikely. An enlargement is another possibility. However, the reflection from the bottom of the shaft is not recorded by the top two receivers, thus minimizing this possibility. The most likely possibilities were determined to be a severely necked region or a weakened zone of concrete near the 40-ft (12.2-m) elevation in the shaft. Unfortunately, the inability to make a definitive determination of the exact type of defect is the present state-of-the-art in propagation testing.

Compression Wave Attenuation

Attenuation of the P-wave as it propagates down a shaft is influenced by several factors including concrete quality, the presence of irregularities or discontinuities, surrounding soil conditions, and method of concrete placement. Free-falling concrete may result in segregation which decreases strength and increases attenuation. Drilled shafts surrounded by hard material have been found to exhibit higher P-wave attenuation than similar shafts in soft soil.

Fig. 8 shows P-wave attenuation in a 92-ft long (28-m), 48-in. (1,120-mm) diameter drilled shaft founded in clay and cast by the slurry displacement method.

The shaft was in 8 ft (2.4 m) of water with the top 10 ft (3.0 m) of the shaft above the mean water line. At the bottom of this shaft a portion of the compression wave energy was transmitted into the underlying soil. Theoretically, for a plane wave, the ratio of reflected-to-incident compression wave amplitude depends on the density, and P-wave velocity contrasts between the concrete and soil at the base of the shaft (15). This ratio is expressed as follows:

$$\frac{C}{A} = \frac{\frac{\rho_1}{\rho_2}\frac{V_{C1}}{V_{C2}} - 1}{\frac{\rho_1}{\rho_2}\frac{V_{C1}}{V_{C2}} + 1} \quad \ldots\ldots\ldots\

following items: (1) Structural importance of shaft to be instrumented; (2) receiver costs; (3) existing soil conditions; (4) construction method; and (5) anticipated construction problems.

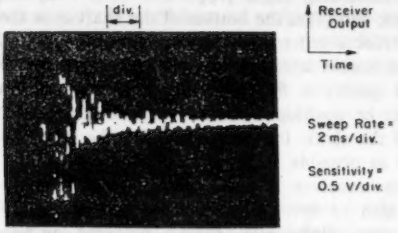

a. Unfiltered Output From Surface Accelerometer

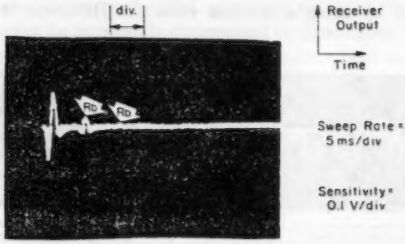

Rb-Reflection From Bottom of Shaft
b. Filtered Output From Surface Accelerometer

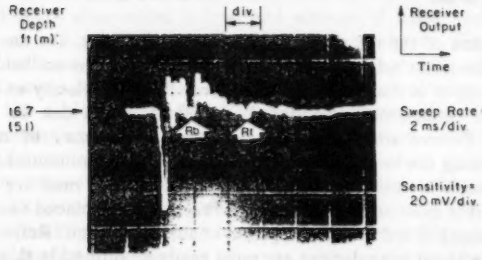

Rb-Reflection From Bottom of Shaft
Rt-Reflection From Top of Shaft
c. Unfiltered Output From Embedded Velocity Transducer

FIG. 10.—Surface and Embedded Receiver Records for 25.2-ft (7.7-m) Long, 18-in. (460-mm) Diameter Shaft

Likely problem regions where embedded receivers should *not* be placed include the following (based on wavelengths generated in this study): (1) Within 10

ft (3.0 m) of the top of the shaft because noise is a major problem; (2) near the elevation of the bottom of the casing if the casing method of construction is employed because this seems many times to be a location of irregularities; (3) on short reinforcing cages [approx 10 ft (3.0 m) long or less] because of noise problems; and (4) at the bottom of the shaft or in the proximity of possible locations of defects or irregularities because wave arrivals and reflections will overlap, which makes interpretation difficult if not impossible.

If concrete quality is the major concern at a job site, it is recommended that a receiver be positioned about 1 wavelength [approx 15 ft (4.6 m)] from the bottom of the shaft. It is important that the receiver elevation be recorded as accurately as possible. Direct velocity measurements can then be made to the depth of the receiver. A relationship between P-wave velocity and concrete strength can also be developed for a given mix design. Then, by maintaining a log of velocities, shafts with problem concrete can be easily identified based on direct P-wave velocities and no coring is required.

Shafts less than 2 ft (0.6 m) in diameter that are not founded in hard material can be tested by using a surface receiver. However, even under favorable

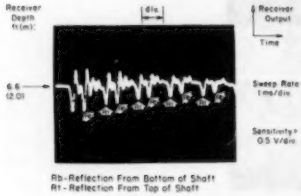

FIG. 11.—Reflection Record for 10-ft (3-m) Long, 12-in. (300-mm) Diameter, Free-Standing Shaft

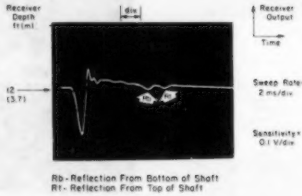

FIG. 12.—Reflection Record for 58-ft (17.7-m) Long, 24-in. (610-mm) Diameter Drilled Shaft

conditions, some of the tests are likely to be inconclusive. On the other hand, even under the most adverse conditions, testing with an embedded receiver near the bottom of a shaft will give the direct P-wave velocity as a minimum. If the bottom reflection is monitored, the shaft length can be determined. Additionally, P-wave amplitudes and other reflections may be monitored to aid in determining the locations of irregularities and discontinuities.

If defects such as soil cave-ins and entrapped drilling mud are likely to be encountered, it is most advantageous for a receiver to be placed near the middle of the shaft length if soil and construction conditions permit. Reflections within sound shafts without irregularities are most easily monitored in this region.

Three oscilloscope records obtained from a 25.2-ft (7.7-m) long, 18-in. (460-mm) diam shaft tested with both a surface receiver and an embedded receiver are shown in Fig. 10 to show the difference between the two methods. The unfiltered oscilloscope record obtained from the surface receiver (acclerometer) is shown in Fig. 10(*a*). This record is typical for drilled shafts with irregular surface shapes and with reinforcing steel extending above the top of the shaft. As Fig. 10(*a*) shows, surface noise masks any reflection arrivals. The filtered output (low pass filter set at 900 Hz) obtained from the same surface accelerometer

is shown in Fig. 10(*b*). Filtering eliminated the surface noise, and two reflection arrivals can be identified. By knowing the shaft length, the P-wave velocity in the shaft can be determined by dividing twice the shaft length by the time between reflection arrivals.

The unfiltered receiver output obtained from an embedded receiver at a depth of 16.5 ft (5.0 m) is shown in Fig. 10(*c*). Some noise is present, but two reflection arrivals can be identified from this record. With the direct travel time measurement, the compression wave velocity in the shaft can also be accurately determined, and the shaft length can easily be calculated.

Testing Limitations

Currently, several testing limiations exist for the compression wave propagation procedures described herein. For a shaft with several defects or irregularities, it is very likely that by using a surface receiver, only the elevation of the uppermost defect will be determined and defects at lower elevations will not be identified. Also, even when embedded receivers are used, the extent and severity of defects cannot be accurately determined in most cases. For example, a thin soil seam across the entire shaft cross section might have the same reflection characteristics as a soil inclusion covering about half the shaft cross section. However, if an embedded receiver is located beneath the soil defect, an indication of the seriousness of the defect might be determined from reductions in the monitored P-wave amplitude and direct P-wave velocity.

The success of both methods requires reflections to be monitored and identified. If reflections are not identified, shaft lengths or depths to defects cannot be calculated.

Often testing techniques are developed under conditions which do not represent field conditions, such as on model piles or precast concrete piles lying in construction yards for the techniques presented herein. Results under these unrealistic conditions are falsely encouraging because reflection arrivals are easily monitored, P-wave attenuation is low, and sources of noise such as irregular surface shapes and protruding reinforcing steel are absent. Fig. 11 shows a record obtained from a receiver embedded in a 10-ft (3.0-m) long, 12-in. (300-mm) diam free-standing concrete shaft. Reflection arrival amplitudes are high and damping is low which results in an incorrect prototype test. Fig. 12 shows a more representative record. This record was obtained from a receiver embedded in a 58-ft (17.7-m) long, 24-in. (610-mm) diam drilled shaft founded in a clay deposit. Only two reflection arrivals are monitored, and reflection amplitudes are strongly attenuated and are easily masked by noise. Of the many factors affecting compression wave attenuation, the surrounding soil is a major contributor to the attenuation process.

Using the methods described herein, generated wavelengths are approx 10 ft–25 ft (3.0 m–7.6 m). With these wavelengths, defects on the order of a small portion of the wavelength will be undetected. One improvement in the technique would be to generate higher frequency P-waves (thus shorter wavelengths) to sample effectively smaller regions of concrete. However, wavelengths cannot be allowed to decrease to much less than the shaft diameter or the shaft will no longer represent a rod-like structure. Instead the shaft will behave as an elastic medium, and P-wave reflections will originate at all shaft boundaries.

Conclusions

Although inherent weaknesses exist in the compression wave propagation techniques outlined herein, the tests provide an economical and rapid means of assessing the overall structural integrity of drilled shafts. When embedded receivers are used, sound shafts without irregularities are easily identified as are shafts with discontinuities such as complete separations and large voids that span a major portion of the cross-sectional area of the shaft. However, testing procedures and interpretation methods need to be improved so that the full potential of the methods presented herein can be utilized.

Of the two compression wave propagation techniques reviewed herein, the most successful application has resulted from the use of embedded receivers. The advantages of using one or more embedded receivers instead of a surface receiver include the following: (1) Direct and interval P-wave velocity measurements are performed; (2) two reflection arrivals occur for each 2L travel distance; (3) lower noise levels are encountered; and (4) attenuation is measured directly. The major disadvantages are costs of the embedded receivers and the installation required prior to and during construction.

Advantages of using a surface receiver instead of embedded receivers include economy and ease of placement since only one receiver is required for all testing and no instrumentation needs to be installed during the construction phase. The disadvantages of using a surface receiver include the following: (1) Direct P-wave velocity measurements are not possible; (2) testing is inconclusive if reflections are not monitored and only one reflection arrival is measured for each 2L travel distance; (3) high noise levels complicate interpretation; and (4) P-wave attenuation cannot be monitored.

The value of wave propagation testing as a diagnostic tool has been clearly demonstrated to the writers during the performance of this study. With only one exception, drilled shafts that have exhibited irregularities in testing with embedded receivers have given no indication by visual inspection during construction that any problems existed. In addition, many shafts which were cast under difficult conditions in which delays and other construction problems occurred have proven to be sound.

Acknowledgments

This work represents part of the first writer's doctoral dissertation. The work was supported by the Bureau of Engineering Research at The University of Texas, the Texas State Department of Highways and Public Transportation, the University of Texas System, and the Henry C. Beck Company. Thanks are extended to these organizations for their financial support. The writers would like to thank H. D. Butler and C. R. Rea of the Texas State Department of Highways and Public Transportation; B. Broaddus and F. J. Meyer of the University of Texas System, J. S. Farr and G. Farmer of the Farmer Foundation Company, and D. C. Osborne of the Henry C. Beck Company for their encouragement and assistance in developing and implementing the testing procedures. Thanks are also extended to R. J. Hoar for his assistance and suggestions to field testing and to J. R. Stewart for his technical assistance.

Appendix I.—References

1. Arias, R. P., "Evaluation of Drilled Shaft Integrity by Non-Destructive Methods," thesis presented to The University of Texas, at Austin, Tex., in 1977, in partial fulfillment of the requirements for the degree of Master of Science.
2. Baker, C. N., Jr., and Khan, F., "Caisson Construction Problems and Correction in Chicago," *Journal of the Soil Mechanics and Foundation Division*, ASCE, Vol. 97, No. SM2, Proc. Paper 7934, Feb., 1971, pp. 417–440.
3. "Caisson Trouble Hits Chicago," *Engineering News Record*, Sept., 29, 1966, p. 14.
4. Davis, A. G., and Dunn, C. S., "From Theory to Field Experience with the Non-Destructive Vibration Testing of Piles," *Proceedings, Institution of Civil Engineers*, Part 2, Dec., 1974, pp. 571–593.
5. Davis, A. G., and Robertson, S. A., "Vibration Testing of Piles," *The Structural Engineer*, Vol. 54, No. 6, June, 1976, pp. A7–A10.
6. Feld, J., *Construction Failure*, John Wiley and Sons, Inc., New York, N.Y., 1968, p. 78.
7. Gardner, R. P. M., and Moses, G. W., "Testing Bored Piles Formed in Laminated Clays," *Civil Engineering and Public Works Review*, Vol. 68, No. 198, Jan., 1973, pp. 60–63.
8. Hearne, T. M., Jr., "Evaluation of Drilled-Shaft Integrity by Stress Wave Propagation Method," thesis presented to The University of Texas, at Austin, Tex., in 1981, in partial fulfillment of the requirements for the degree of Doctor of Philosophy.
9. Hoar, R. J., and Stokoe, K. H., II, "Generation and Measurement of Shear Waves in Situ," *Dynamic Geotechnical Testing, American Society for Testing and Materials STP 654*, American Society for Testing and Materials, 1977, pp. 3–29.
10. Malhotra, V. M., *Testing Hardened Concrete: Nondestructive Methods*, Iowa State University Press, Ames, Iowa, and American Concrete Institute, Detroit, Mich., 1976, p. 87.
11. Mitchell, J. M., "Assessing Large Diameter Piles," *The Consulting Engineer*, Vol. 51, No. 6, Dec., 1978, pp. 37–39.
12. Preiss, K., Weber, H., and Caiserman, A., "Integrity Testing of Bored Piles and Diaphragm Walls," *The Civil Engineer in South Africa*, Johannesburg, South Africa, Vol. 20, No. 8, Aug., 1978, pp. 191–196.
13. Reese, L. C., "Design and Construction of Drilled Shafts," presented at the Sept., 1976, Twelfth Terzaghi Lecture, National Meeting, ASCE, held at Philadelphia, Pa.
14. Reese, L. C., and Wright, S. J., "Construction of Drilled Shafts and Design for Axial Loading," *Drilled Shaft Design and Construction Guidelines Manual*, Vol. 1, United States Dept. of Transportation, Washington, D.C., July, 1977.
15. Richart, F. E., Jr., Hall, J. R., Jr., and Woods, R. D., *Vibration of Soils and Foundations*, Prentice-Hall, Inc., Englewood Cliffs, N.J., 1970.
16. Robertson, S. A., "Vibration Testing," *The Consulting Engineer*, Vol. 46, No. 1, Jan., 1976, pp. 36–39.
17. Steinbach, J., "Caisson Evaluation by the Stress Propagation Method," thesis presented to the Illinois Institute of Technology, at Chicago, Ill., in 1971, in partial fulfillment of the requirements for the degree of Doctor of Philosophy.
18. Steinbach, J., and Vey, E., "Caisson Evaluation by Stress Wave Propagation Method," *Journal of the Geotechnical Engineering Division*, ASCE, Vol. 101, No. GT4, Proc. Paper 11245, Apr., 1975, pp. 361–378.
19. "Testing Halts John Hancock Work," *Engineering News Record*, Vol. 202, No. 5236, Aug., 19, 1966, p. 18.
20. Whitaker, T., "Structural Integrity of Piles," *Civil Engineering*, Vol. 44, No. 6, London, England, June, 1974, pp. 20–23.

Appendix II.—Notation

The following symbols are used in this paper:

A = incident compression wave amplitude;
C = reflected compression wave amplitude;

d = travel distance;
E = Young's modulus;
g = acceleration of gravity;
L = effective shaft length;
P-wave = compression wave;
Rb = reflection from bottom of shaft;
Rd = reflection from defect;
Ri = reflection from irregularity;
Rt = reflection from top of shaft;
V_C = compression wave velocity;
V_{C1} = compression wave velocity in concrete;
V_{C2} = compression wave velocity in underlying soil;
γ = unit weight of concrete;
ρ_1 = mass density of concrete; and
ρ_2 = mass density of underlying soil.

ESTIMATION OF SPT-N AND RELATIVE DENSITY

By Michael N. Fardis,[1] A. M. ASCE, and Daniele Veneziano,[2]
Associate Members, ASCE

INTRODUCTION

The Standard Penetration Test (SPT) has been employed for a number of years as a method of indirect evaluation of subsurface soils. The test is particularly useful for granular cohesionless soils, e.g., sands, for which it provides a measure of denseness. In fact, laboratory experiments indicate that for a given sand and vertical effective stress $\bar{\sigma}_v$, the blowcount number N is highly correlated with relative density D_r; N is a measure of strength and for a given sand, strength increases with D_r and $\bar{\sigma}_v$. The fact that measuring N in the field is less expensive than measuring D_r has encouraged development of relationships between N, D_r, and $\bar{\sigma}_v$ (3,4,5,8,10). These relationships are dependable under laboratory-controlled conditions but their validity in the field is reduced due to the effect of factors, such as soil structure (fabric), consolidation history, and, possibly, sand type (9).

It is the objective of this paper to develop a consistent set of models for inference of D_r from N under both laboratory and field conditions. The model in the laboratory ("reference model") is somewhat more sophisticated than those presently available in that it accounts for errors that have been previously neglected, specifically, those in the determination of D_r; it is also based on a more comprehensive set of data. Finally, the log-linear form of the proposed relationship offers computational advantages, especially when one considers N and D_r as random variables and wants to derive probabilistic characteristics of one quantity from those of the other.

Only some of the features of the laboratory model are assumed to hold in the field; other properties, such as trends and probabilistic correlation in space, are site-specific and must be inferred from site data.

Once a site-specific relationship has been constructed by appropriately modifying the reference laboratory model, one can infer properties of in-situ D_r from field measurements of N. One such relationship has been used in Ref. 2 to

[1] Asst. Prof. of Civ. Engrg., Massachusetts Inst. of Technology, Cambridge, Mass.
[2] Assoc. Prof. of Civ. Engrg., Massachusetts Inst. of Technology, Cambridge, Mass.

Note.—Discussion open until March 1, 1982. Separate discussions should be submitted for the individual papers in this symposium. To extend the closing date one month, a written request must be filed with the Manager of Technical and Professional Publications, ASCE. Manuscript was submitted for review for possible publication on September 24, 1980. This paper is part of the Journal of the Geotechnical Engineering Division, Proceedings of the American Society of Civil Engineers, ©ASCE, Vol. 107, No. GT10, October, 1981. ISSN 0093-6405/81/0010-1345/$01.00.

infer probabilistic characteristics of D_r as a random field in space from characteristics of the random field, N, and to evaluate the hazard of liquefaction of a soil deposit. Another area of application is that of fill compaction.

Presence of measurement errors makes it necessary to distinguish between actual values of N, D_r, etc., and measurements or estimates in the Laboratory (N_L, D_{r_L} ...) or in the field (N_F, D_{r_F} ...). Some of these quantities, e.g., N, do not exist prior to the experiment that measures them; others, e.g., D_r, are defined in terms of a mathematical idealization of the soil material. In both cases, one must clearly (although somewhat arbitrarily) define what one means by "actual value." We propose the following definition: For a generic parameter θ, let the series of outcomes of independent measurements in the lab or in the field be θ_1, θ_2, ... (here θ_i stands for either θ_{L_i} or θ_{F_i} with subscripts, L and F, denoting "laboratory" and "field," respectively) and let $\hat{\theta}_n$ by a point estimator of θ from θ_1, ..., θ_n e.g., $\hat{\theta}_n = 1/n \, \Sigma_i \, \theta_i$. Then by the *actual value* of θ we mean the limit

$$\theta = \lim_{n \to \infty} \hat{\theta}_n \quad \ldots \ldots \ldots

to be correlated for small variations of D_r and $\bar{\sigma}_v$.

Uncertainty on D_{r_L} given D_r is caused by variability of the estimators of the limiting dry densities γ_{max} and γ_{min} in the laboratory, and poses more severe problems. One can quantify uncertainty on D_{r_L} by using: (1) the definition of D_r in terms of γ_D, dry unit weight, γ_{max} and γ_{min}:

$$D_r = \frac{\gamma_{max}}{\gamma_D} \frac{\gamma_D - \gamma_{min}}{\gamma_{max} - \gamma_{min}} \quad \ldots\ldots\ldots\ldots\ldots\ldots\ldots\ldots\ldots\ldots\ldots\ldots (5)$$

and (2) results from the comparative tests (11) in which several laboratories performed maximum and minimum dry density determinations for the same cohesionless soil. Using data in this last reference one can separately infer the variance of limiting density values reported by the same lab, s^2, a measure of within-lab variability, and the variance of the *average* value determined by

TABLE 1.—Probability Distributions of Uncertain Soil Parameters

Symbol (1)	Uncertain parameter or property (2)	Distribution (3)	Mean (4)	Second central moments (5)
γ_{max}	maximum dry density determined by ASTM[1] procedure	Normal	—	within lab: $s^2 = 0.46^2$ pcf[2a]; interlab: $s_m^2 = 2.7^2$ pcf^2
	maximum dry density determined by non-ASTM[2] procedure	Normal	—	within lab: $s^2 = 0.54^2$ pcf^2; interlab: $s_m^2 = 8.2^2$ pcf^2
γ_{min}	minimum dry density determined by ASTM[1] procedure	Normal	—	within lab: $s^2 = 0.39^2$ pcf^2; interlab: $s_m^2 = 1.5^2$ pcf^2
γ_{min}	minimum dry density determined by non-ASTM[2] procedure	Normal	—	within lab: $s^2 = 0.46^2$ pcf^2; interlab: $s^2 = 1.9^2$ pcf^2
$\begin{bmatrix} a_1 \\ a_2 \\ a_3 \end{bmatrix}$	vector of parameters in reference $N - D_r$ relationship in equation 2	Normal	$\begin{bmatrix} 2.67 \\ 2.06 \\ 0.442 \end{bmatrix}$	$\begin{bmatrix} 0.024 & 0.0073 & -0.0025 \\ & 0.034 & 0.0009 \\ & \text{symmetric} & 0.00092 \end{bmatrix}$
ϵ	lack of fit term, equation 2	Normal	0	0.057
ϵ_L	residual term, equation 4	Normal	0	0.095
$\epsilon_{\ln N_L}$	measurement error in the lab	Normal	0	0.028
$\epsilon_{\ln N_F}$	measurement error in the field	Normal	0	0.028

[a]1 pcf = 0.016 g/cm^3.
[1]American Society for Testing Materials.
[2]Non-American Society for Testing Materials.

different labs, s_m^2, a measure of interlab variability. Values of s^2 and s_m^2 are given in Table 1. They are for a particular sand but they can be considered representative of all uniform medium sands. The distributions of γ_{max_L} given γ_{max} and of γ_{min_L} given γ_{min}, both within and across laboratories, are nearly normal. Although s and s_m are small compared to the average values of the limiting densities, the sensitivity of D_r to γ_{max} and γ_{min} is such that these errors could not be neglected when regressing N against D_r and $\bar{\sigma}_v$.

Inaccuracy of relative density data can be accounted for in the regression of N_L on D_r by substituting for D_r in Eq. 4 in terms of γ_D, γ_{max} and γ_{min}. This gives the *nonlinear* regression model

$$\ln N_L = a_1 + a_2 \ln \left(\frac{\gamma_{max}}{\gamma_D} \frac{\gamma_D - \gamma_{min}}{\gamma_{max} - \gamma_{min}} \right) + a_3 \ln \bar{\sigma}_v + \epsilon_L \quad \ldots\ldots\ldots\ldots (6)$$

in which γ_D and $\bar{\sigma}_v$ are control variables and a_1, a_2, a_3, γ_{max}, γ_{min} are uncertain regression parameters. An additional complication of the model is that data are from sands of different types for which γ_{max} and γ_{min} are different and the parameters a_1, a_2, and a_3 may or may not be the same. Due to these features, the following special procedure has been devised for parameter estimation.

Analysis of Regression Model in Equation 6.—Let the index $k(k = 1, 2, \ldots n_s)$ identify the type of sand and suppose that for the kth sand type, M laboratories provide limiting density data. If $(\gamma^k_{r_1}, \ldots, \gamma^k_{r_{n_r}})$ denote the n_r values of γ^k_{max} from the rth laboratory, then *before* regression analysis, γ^k_{max} may be considered to be a normal random variable with mean value

$$m'_{\gamma^k_{max}} = \sigma^{2\prime}_{\gamma^k_{max}} \sum_{r=1}^{M} \frac{\sum_{j=1}^{n_r} \gamma_{r_j}}{n_r s_m^2 + s^2} \quad \ldots\ldots\ldots\ldots\ldots\ldots\ldots\ldots\ldots\ldots (7)$$

and variance

$$\sigma^{2\prime}_{\gamma^k_{max}} = \left(\sum_{r=1}^{M} \frac{n_r}{n_r s_m^2 + s^2} \right)^{-1} \quad \ldots\ldots\ldots\ldots\ldots\ldots\ldots\ldots\ldots\ldots (8)$$

The above expressions are obtained by specializing results of the linear Gaussian model with noninformative flat prior (12). If $n_r = n$ for all laboratories, then Eqs. 7 and 8 take on the simple forms

$$m'_{\gamma^k_{max}} = \frac{1}{Mn} \sum_{r=1}^{M} \sum_{j=1}^{n} \gamma_{r_j} \quad \ldots\ldots\ldots\ldots\ldots\ldots\ldots\ldots\ldots\ldots (9)$$

and $$\sigma^{2\prime}_{\gamma^k_{max}} = \frac{1}{M} \left(s_m^2 + \frac{s^2}{n} \right) \quad \ldots\ldots\ldots\ldots\ldots\ldots\ldots\ldots\ldots\ldots (10)$$

Similarly for $m'_{\gamma^k_{min}}$ and $\sigma^{2\prime}_{\gamma^k_{min}}$. In the course of regression analysis, the distributions of γ^k_{max} and γ^k_{min} are updated in the same way as the distributions of the parameters a_1, a_2, and a_3. This is achieved by including the quantities

$$\Delta\gamma^k_{max} = \gamma^k_{max} - m'_{\gamma^k_{max}} \quad \ldots\ldots\ldots\ldots\ldots\ldots\ldots\ldots\ldots\ldots (11)$$

and $$\Delta\gamma^k_{min} = \gamma^k_{min} - m'_{\gamma^k_{min}} \quad \ldots\ldots\ldots\ldots\ldots\ldots\ldots\ldots\ldots\ldots (12)$$

among the components of the parameter vector $\boldsymbol{\beta}$, in which

$$\boldsymbol{\beta} = (a_1, a_2, a_3, \Delta\gamma^1_{max}, \Delta\gamma^1_{min}, \ldots, \Delta\gamma^{n_s}_{max}, \Delta\gamma^{n_s}_{min})^T \quad \ldots\ldots\ldots\ldots\ldots\ldots (13)$$

Bayesian analysis can be used for the estimation of the vector $\boldsymbol{\beta}$, provided one knows its prior distribution. This distribution can be taken to be multivariate normal, $\boldsymbol{\beta} \sim N(\mathbf{m}'_{\beta}, \boldsymbol{\Sigma}'_{\beta})$. The inverse of the prior covariance matrix, $(\boldsymbol{\Sigma}'_{\beta})^{-1}$, is diagonal with the first three diagonal coefficients equal to zero, to express complete ignorance of a_1, a_2, and a_3. By definition, $\Delta\gamma^k_{max}$ and $\Delta\gamma^k_{min}$ have zero prior mean, and prior variance in Eq. 8 or 10.

The estimation procedure is much simplified if the right-hand side of Eq. 6 is replaced with a linear function of $\boldsymbol{\beta}$, e.g., with the linear Taylor series expansion about the prior mean values of γ^k_{max} and γ^k_{min} and the posterior mean

value of a_2, m''_{a_2}. (Notice that the more common procedure of linearizing about the prior mean of $\boldsymbol{\beta}$ does not apply here, because the prior mean of a_2 is not defined.) One can then write, for the ith measurement of sand k,

$$\ln N_{L,i} = a_1 + a_2 \overline{\ln D_{r,i}} + m''_{a_2}(\alpha^k \Delta\gamma^k_{\max} + \beta^k_i \Delta\gamma^k_{\min}) + a_3 \ln \bar{\sigma}_{v,i} + \epsilon_{L,i} \quad (14)$$

In the expression above, the quantity

$$\overline{\ln D_{r,i}} = \ln\left(\frac{m'_{\gamma^k_{\max}}}{\gamma_{D,i}} \frac{\gamma_{D,i} - m'_{\gamma^k_{\min}}}{m'_{\gamma^k_{\max}} - m'_{\gamma^k_{\min}}}\right) \quad (15)$$

is in approximation the prior mean value of $\ln D_{r,i}$,

$$\alpha^k = -\frac{m'_{\gamma^k_{\min}}}{m'_{\gamma^k_{\max}}(m'_{\gamma^k_{\max}} - m'_{\gamma^k_{\min}})} \quad (16)$$

is a constant independent of i, and β^k_i is given by

$$\beta^k_i = -\frac{m'_{\gamma^k_{\max}} - \gamma_{D,i}}{(\gamma_{D,i} - m'_{\gamma^k_{\min}})(m'_{\gamma^k_{\max}} - m'_{\gamma^k_{\min}})} \quad (17)$$

One may rewrite Eq. 14 as

$$\mathbf{z} = \mathbf{H}\boldsymbol{\beta} + \boldsymbol{\epsilon}_L \quad (18)$$

in which vector $\mathbf{z}$ contains all the observations $\ln N_{L,i}$, $\mathbf{H}$ is a matrix with ith row

$$\mathbf{H}_i = [1, \overline{\ln D_{r,i}}, \ln \bar{\sigma}_{v,i}, 0, ..., 0, m''_{a_2}\alpha^k, m''_{a_2}\beta^k_i, 0, ..., 0] \quad (19)$$

and $\boldsymbol{\epsilon}_L$ is a vector of independent normal errors with zero mean and unknown variance σ^2_L.

Bayesian regression with unknown residual variance is feasible and reasonably simple only in the case when $\boldsymbol{\beta}$ and σ^2_L have conjugate prior distribution (6). Unfortunately, our prior information is not of this form and we have to resort to an approximate procedure. (Modification of standard Bayesian regression would have been needed even in the case of conjugate prior, because the matrix $\mathbf{H}$ depends on the a priori unknown quantity m''_{a_2}). The procedure is iterative. First one assumes some values for m''_{a_2} and σ^2_L. With these parameters given, the matrix $\mathbf{H}$ is known and the prior normal distribution of $\boldsymbol{\beta}$ is in conjugate form. Under the same condition, the posterior distribution of $\boldsymbol{\beta}$ is normal, with mean value (1)

$$\mathbf{m}''_{\boldsymbol{\beta}}|_{m''_{a_2},\sigma^2_L} = \mathbf{m}'_{\boldsymbol{\beta}} + \frac{1}{\sigma^2_L}\boldsymbol{\Sigma}''_{\boldsymbol{\beta}}\mathbf{H}^T(\mathbf{z} - \mathbf{H}\,\mathbf{m}'_{\boldsymbol{\beta}}) \quad (20)$$

and covariance matrix

$$\boldsymbol{\Sigma}''_{\boldsymbol{\beta}} = \left(\boldsymbol{\Sigma}'^{-1}_{\boldsymbol{\beta}} + \frac{1}{\sigma^2_L}\mathbf{H}^T\mathbf{H}\right)^{-1} \quad (21)$$

An estimator of the variance, σ^2_L, is

$$\hat{\sigma}^2_L = \frac{1}{n_z - n_{\boldsymbol{\beta}}}(\mathbf{z} - \mathbf{H}\boldsymbol{\beta})^T(\mathbf{z} - \mathbf{H}\boldsymbol{\beta}) \quad (22)$$

in which n_z and n_β are the dimensions of $\mathbf{z}$ and $\boldsymbol{\beta}$, respectively.

The vector $\mathbf{m}''_\beta$ in Eq. 20 includes m''_{a_2} as one of its components. If m''_{a_2} from Eq. 20 and the estimate of σ_L^2 from Eq. 22 are not close to the values initially assumed, then these values are modified and Eqs. 20, 21, and 22 are used repeatedly until reasonable agreement between assumed and calculated value is attained. Convergence is usually fast.

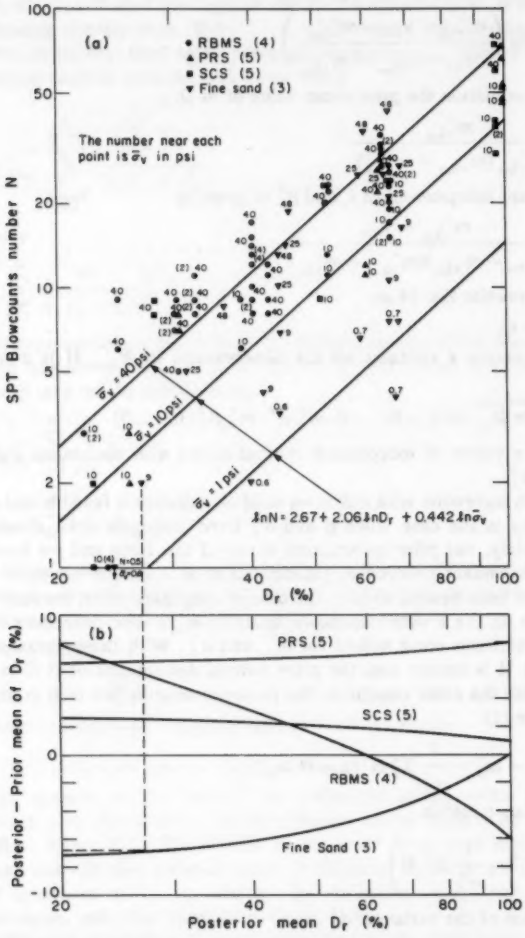

FIG. 1.—Reference Model between SPT-N and D_r: (*a*) Laboratory Data and Fitted Relationship; (*b*) Initial and Revised Estimates of D_r (1 psi = 6.89 kN/m²)

The regression procedure described above has been applied to 117 data points and four clean sands with different grain size distributions: the fine sand noted in Ref. 3, the Reid Bedford model sand (RBMS) in Ref. 4, and the standard concrete sand (SCS) and the Plate River sand (PRS) in Ref. 5. Analysis was performed in two stages. At first, the four sands were assumed to have different coefficients a_1, a_2, and a_3. Because the posterior mean values of these coefficients were nearly the same for all sands (in consideration of their posterior standard deviations), it was assumed, in the second stage of analysis, that the regression of Eq. 2 is identical for all sand types. Under this condition, the best estimates of the limiting densities changed from their prior values by only small amounts. The regression variance from the final analysis, $\sigma_L^2 = 0.094$, is not appreciably larger than any of the four variances from the first stage of the analysis. This means that the final model fits the data almost as well as the four separate models while having the advantages of using fewer parameters and reducing estimation errors by pooling together information for all sands. The mean value vector and the covariance matrix of $[a_1, a_2, a_3]^T$ are given in Table 1 for D_r expressed as a fraction and $\bar{\sigma}_v$ in psi. The covariance matrix includes the effect of uncertainty on the limiting dry densities of the four sands. The variances of the residual terms, ϵ, in Eq. 2 and, ϵ_L, in Eqs. 4 and 6 are given in the same table.

Eq. 2 with parameters a_i and residual ϵ distributed according to Table 1 is called here the *reference relationship* between N and D_r for normally consolidated sands. This relationship applies for $\bar{\sigma}_v$ in the range of 1–50 psi (6.9–344 kPa) and refers to actual values of N and D_r under laboratory conditions, i.e., to N and D_r determined from a large number of laboratory measurements (D_r is calculated from Eq. 5 with average limiting densities from a large number of laboratory measurements according to the American Society for Testing Materials procedure). Eq. 2 is shown in Fig. 1(*a*) after setting the a_i equal to their posterior mean values, $\hat{a}_1 = m''_{a_1} = 2.67$, $\hat{a}_2 = m''_{a_2} = 2.06$, $\hat{a}_3 = m''_{a_3} = 0.442$ and for $\epsilon = 0$. Also shown in Fig. 1 are data points used in the analysis. The horizontal axis gives values of D_r calculated from Eq. 5 using the *posterior* mean values of $\gamma^k_{\max}$ and $\gamma^k_{\min}$. Fig. 1(*b*) shows the difference between posterior and prior mean values of D_r for each of the four sands, as a function of the posterior mean of relative density. For example, consider the point with coordinates $D_r = 27\%$ and $N = 2(\bar{\sigma}_v = 9$ psi) in Fig. 1(*a*). This point corresponds to a measurement of fine sand. The associated difference between posterior and prior mean of D_r is, from Fig. 1(*b*), 7%. This means that a priori the mean value of D_r was 27% + 7% = 34%. Updating of D_r is a consequence of updating the estimates of the limiting densities.

The reference relationship between N and D_r cannot be used directly in the field, because of factors, such as fabric, fines content, and consolidation history, and because of different ways in which the Standard Penetration Test is conducted (9). The next section shows how one can generate site-specific models through modification of Eq. 2.

Correction of Equation 2 for Field Conditions

Visual display and formal analysis of data from 17 different sites confirms existence of a log-linear trend of N versus D_r. In none of the 17 cases was

it needed to modify the slope parameter a_2, but significant and sometimes very important differences were found in the dependence of ln N on depth, h. The physical explanation is that factors such as fines content, fabric, consolidation history, etc., may vary considerably in-situ, thus distorting the dependence of $E(\ln N)$ on h as predicted from Eq. 2 with $\bar{\sigma}_v$ a function of depth. For this reason it is more realistic, in the field, to replace the parameter, a_1, with a

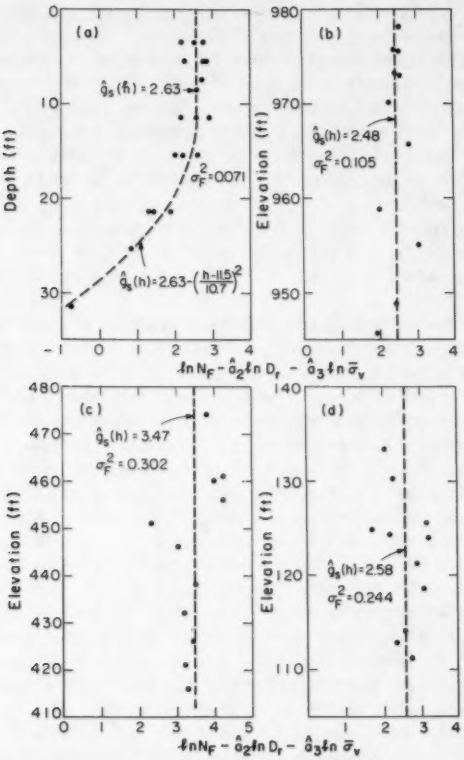

FIG. 2.—Relationships between N and D_r at Four Different Sites (1 ft = 0.305 m)

generic function of depth, $g_s(h)$, variable from site to site. For field measurements we shall therefore write

$$\ln N_F = g_s(h) + a_2 \ln D_r + a_3 \ln \bar{\sigma}_v + \epsilon_F \quad \ldots\ldots\ldots\ldots\ldots\ldots \quad (23)$$

The residual term ϵ_F has a structure similar to ϵ_L in Eq. 4, i.e., $\epsilon_F = \epsilon_s + \epsilon_{\ln N_F}$ in which $\epsilon_{\ln N_F}$ is measurement error with the same probability distribution as $\epsilon_{\ln N_L}$ in Eq. 3, and ϵ_s represents lack-of-fit at the site.

Eq. 23 assumes that the deposit has horizontal stratification. If percent fines, fabric, degree of consolidation, etc., vary also horizontally, then clearly $g_s(h)$ should be replaced with a more general function of location.

Estimation of Parameters in Eq. 23.—We take as our objective in the field to estimate parameters of $\ln D_r$ (D_r = actual relative density in situ) as a random function of spatial location. Data consists of field measurements of N and D_r. Because measuring D_r is more costly than measuring N, it is typical that measurements of only blow-count number are taken at many more locations than joint measurements of (N, D_r) and that the latter are at discrete points along one or very few vertical borings.

As a first step, the differences $\ln N_F - \hat{a}_2 \ln D_r - \hat{a}_3 \ln \bar{\sigma}_v$ are calculated at the locations in which N and D_r are stimultaneously measured and plotted versus depth, h, to estimate the vertical trend $g_s(h)$ at the site. Plots of this type and fitted trends at four sites are shown in Fig. 2. Data from the first site (these were used in Ref. 7 to conclude that "no usable correlation exists between density and SPT values at the site") show a strong dependence of g_s on h, at least below a depth of 11.5 ft (3.5 m). The other three cases, all drawn from nuclear power plant foundation studies, show no significant variation of g_s with depth. Although in these cases one can take $g_s(h)$ as a constant, the fitted values differ significantly from the laboratory estimate, $\hat{a}_1 = 2.67$. Analysis of data from 13 other sites gave similar results: considerable site-to-site variability of $g_s(h)$ and sometimes significant variation of g_s with depth. As an indication of this site-to-site variability, if one considers $g_s(h)$ to be independent of depth at each site, then its variance over 17 sites equals 0.77^2 with an associated mean value of 3.01 (2). Analyses of this type indicate the importance of obtaining a few joint measurements of N and D_r at the site, in order to estimate $g_s(h)$ and remove bias from the relationship between N and D_r.

The function $\hat{g}_s$ provides information about in situ fabric, overconsolidation, etc., as a function of depth. For example, a value of $\hat{g}_s(h)$ much larger than the laboratory estimate $\hat{a}_1 = 2.67$ indicates overconsolidation or in situ structure with considerable stability under undrained cyclic loading, such as that induced during the SPT. One may also expect, that the larger the difference $\hat{g}_s(h) - \hat{a}_1$, the higher the liquefaction resistance of in situ soil compared to a sample prepared in the laboratory to the same D_r.

Once $g_s(h)$ has been estimated, the—in general depth-dependent—variance of ϵ_F, σ^2_F, can be calculated as the average squared deviation of $\ln N_F - \hat{a}_2 \ln D_r - \hat{a}_3 \ln \bar{\sigma}_v$ from $\hat{g}_s(h)$. As examplified in Fig. 2(a), fitting a depth-dependent trend g_s reduces the variance of the lack-of-fit term ϵ_s, $\sigma_s^2 = \sigma^2_F - \sigma^2_{\epsilon_{\ln N_F}}$.

Spatial Variation of N and D_r

Estimation of the mean value, variance and correlation function of $\ln D_r$ is pursued conditionally on given $g_s(h)$, a_2, and a_3. If this function and parameters cannot be assumed known, (e.g., equal to $\hat{g}_s(h)$, $\hat{a}_2$, and $\hat{a}_3$), then a viable procedure is to simulate them numerically and each time estimate the parameters of the random field $\ln D_r$. This simulation approach was used in Ref. 2 to probabilistically characterize liquefaction resistance of a soil deposit.

Given $g_s(h)$, a_2 and a_3, one can calculate, for each measurement N_F of N,

the residual quantity

$$(\ln N_F)' \equiv \ln N_F - g_z(h) - a_3 \ln \bar{\sigma}_v = a_2 \ln D_r + \epsilon_F \quad \ldots\ldots\ldots\ldots (24)$$

and group these residuals according to depth. The sample mean and variance of the residuals at discrete depth, h_i, are estimators of the mean $m_{(\ln N_F)'}(h_i)$ and the variance $\sigma^2_{(\ln N_F)'}(h_i)$ of $(\ln N_F)'$. The same quantities are estimators of $a_2 E[\ln D_r(h_i)]$ and $a_2^2 \sigma^2_{\ln D_r}(h_i) + \sigma^2_F$. Notice that the lack-of-fit term ϵ_z does not contribute significantly to the sample mean of the residuals because ϵ_z varies on each horizontal plane around its zero mean. Thus, one may estimate the first two moments of $\ln D_r(h_i)$ as

$$\hat{m}_{\ln D_r}(h_i) \approx \frac{1}{a_2} \hat{m}_{(\ln N_F)'}(h_i) \quad \ldots\ldots\ldots\ldots\ldots\ldots\ldots\ldots (25)$$

and $$\hat{\sigma}^2_{\ln D_r}(h_i) = \max\left\{0, \frac{1}{a_2^2}[\sigma^2_{(\ln N_F)'}(h_i) - \sigma^2_F]\right\} \quad \ldots\ldots\ldots\ldots (26)$$

In some cases it is useful to know the degree of correlation in space of the blowcount number and of relative density. A realistic and relatively simple model for the covariance function of $(\ln N_F)'$ is one of the following type. First one writes

$$B_{(\ln N_F)'}(x_1, y_1, h_1, x_2, y_2, h_2) \equiv \mathrm{Cov}\,[(\ln N_F(x_1, y_1, h_1))', (\ln N_F(x_2, y_2, h_2))']$$

$$= B_1(r_H, h_1, h_2) + B_2(r_H, r_v) + B_3(r_H, r_v) \quad \ldots\ldots\ldots\ldots\ldots\ldots (27)$$

in which $r_H = [(x_1 - x_2)^2 + (y_1 - y_2)^2]^{1/2}$ is horizontal distance, $r_v = |h_1 - h_2|$ is vertical distance, and B_1, B_2, B_3 are the covariance functions of $a_2 \ln D_r$, ϵ_z, and $\epsilon_{\ln N_F}$, respectively. The additive form of Eq. 27 holds under the plausible condition that these three terms are mutually uncorrelated. The covariance functions B_1 and B_2 are further assumed to have similar "separable" form:

$$B_1(r_H, h_1, h_2) = a_2^2 \sigma_{\ln D_r}(h_1)\, \sigma_{\ln D_r}(h_2)\, \rho_H(r_H)\, \rho_v(r_v) \quad \ldots\ldots\ldots\ldots (28)$$

$$B_2(r_H, r_v) = \sigma^2_{\epsilon_z}\, \rho_H(r_H)\, \rho_v(r_v) \quad \ldots\ldots\ldots\ldots\ldots\ldots (29)$$

whereas B_3 is given by

$$B_3(r_H, r_v) = \begin{cases} \sigma^2_{\epsilon_{\ln N_F}}, & \text{if } r_H = r_v = 0 \\ 0, & \text{otherwise} \end{cases} \quad \ldots\ldots\ldots\ldots (30)$$

to express the fact that $\epsilon_{\ln N_F}$ is not correlated. The term $\sigma^2_{\epsilon_{\ln N_F}}$ equals the variance of the measurement error in the laboratory (0.028) and $\sigma^2_{\epsilon_z} = \sigma^2_F - \sigma^2_{\epsilon_{\ln N_F}}$, with σ^2_F estimated by the procedure at the end of the last section.

As a special case, one may set $r_H = 0$ to obtain the vertical covariance function of $(\ln N_F)$,

$$B_{(\ln N_F)'}(h_1, h_2) = [a_2^2 \sigma_{\ln D_r}(h_1)\, \sigma_{\ln D_r}(h_2) + \sigma^2_{\epsilon_z}]\, \rho_v(r_v) + \sigma^2_{\epsilon_{\ln N_F}} I(r_v) \quad \ldots\ldots (31)$$

in which $I(r_v) = 1$ if $r_v = 0$ and $I(r_v) = 0$ otherwise. Similarly, by setting $h_1 = h_2 = h (r_v = 0)$ one obtains the horizontal covariance function

$$B_{(\ln N_F)'}(r_H, h) = [a_2^2 \sigma^2_{\ln D_r}(h) + \sigma^2_{\epsilon_z}]\, \rho_H(r_H) + \sigma^2_{\epsilon_{\ln N_F}} I(r_H) \quad \ldots\ldots\ldots (32)$$

From observations of N on a regular (e.g., rectangular) network of points it is possible to form estimators of the covariance functions in Eqs. 29 and 30. For example,

$$\hat{B}_{(\ln N_F)'}(h_1, h_2) = \frac{1}{n_{h_1 h_2} - 1} \sum [(\ln N_F(h_1))' - \hat{m}_{(\ln N_F)'}(h_1)] [(\ln N_F(h_2))' - \hat{m}_{(\ln N_F)'}(h_2)] \quad \ldots \quad (33)$$

in which the summation is over all measurement pairs at depths h_1 and h_2 and at the same horizontal location, and $n_{h_1 h_2}$ is the number of such pairs.

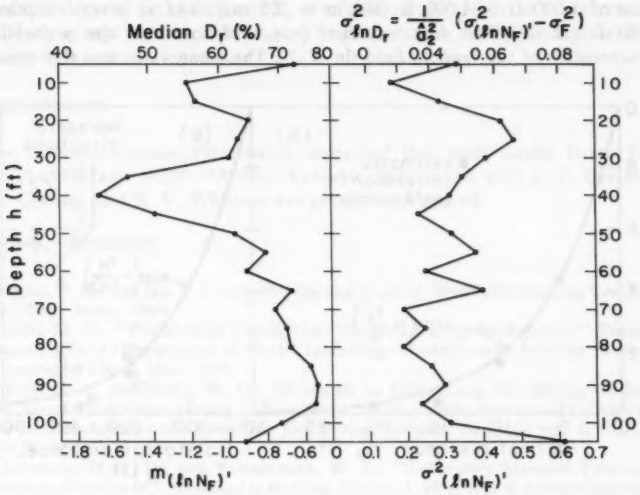

FIG. 3.—First Two Moments of $(\ln N_F)'$ and D_r for the Site Analyzed in Ref. 2: (*a*) Mean Value; (*b*) Variance (1 ft = 0.305 m)

Similarly, for the covariance function on the horizontal plane at depth, h,

$$\hat{B}_{(\ln N_F)'_H}(r_H, h) = \frac{1}{n_{r_H h} - 1} \sum [(\ln N_F(x_1, y_1, h))' - \hat{m}_{(\ln N_F)'}(h)] [(\ln N_F)(x_2, y_2, h))' - \hat{m}_{(\ln N_F)'}(h)] \quad \ldots \quad (34)$$

in which summation is over all measurement pairs at locations with horizontal distance $[(x_1 - x_2)^2 + (y_1 - y_2)^2]^{1/2} = r_H$ and depth, h. The number of such pairs is denoted by $n_{r_H h}$.

From knowledge of $B_{(\ln N_F)'_H}$ and $B_{(\ln N_F)'_V}$ it is possible to estimate the vertical and horizontal correlation functions, ρ_v and ρ_H. Convenient estimators are

$$\hat{\rho}_v(r_v) = \frac{1}{n_{r_v}} \sum_{h_1} \frac{\hat{B}_{(\ln N_F)'_V}(h_1, h_1 + r_v) - \sigma^2_{\epsilon_{\ln N_F}} I(r_v)}{\sigma_{(\ln N_F)'}(h_1)\, \sigma_{(\ln N_F)'}(h_1 + r_v) + \sigma^2_{\epsilon_s}} \quad \ldots \quad (35)$$

and $$\hat{\rho}_H(r_H) = \frac{1}{n_{r_H}} \sum_h \frac{\hat{B}_{(\ln N_F)'Y_H}(r_H, h) - \sigma^2_{\epsilon_{\ln N_F}} I(r_H)}{\sigma^2_{(\ln N_F)'}(h) + \sigma^2_{\epsilon_s}} \quad \ldots\ldots\ldots\ldots (36)$$

Summations are over the values of h_1 for which $\hat{B}_{(\ln N_F)'Y_V}(h_1, h_1 + r_v)$ exists (n_{r_v} terms) and over the values of h at which $\hat{B}_{(\ln N_F)'Y_H}(r_H, h)$ exists (n_{r_H} terms).

Notice that the functions in Eqs. 35 and 36 do not depend on the form of $g_s(h)$ or on the parameters a_2 and a_3. Therefore, even if $g_s(h)$ and a_2, a_3 are simulated numerically, these functions need to be calculated only once.

To exemplify the analysis, data on N has been processed from an actual sand deposit. In situ measurements were made on a 6 × 6 horizontal square grid of points, with regular spacing of 200 ft (61 m) [hence over a horizontal region of 1,000 ft × 1,000 ft (305 m × 305 m)], and at several depths up to 105 ft (32 m). This data was first processed to obtain the probabilistic characteristics of the random field $(\ln N_F)'$. The mean value and the variance

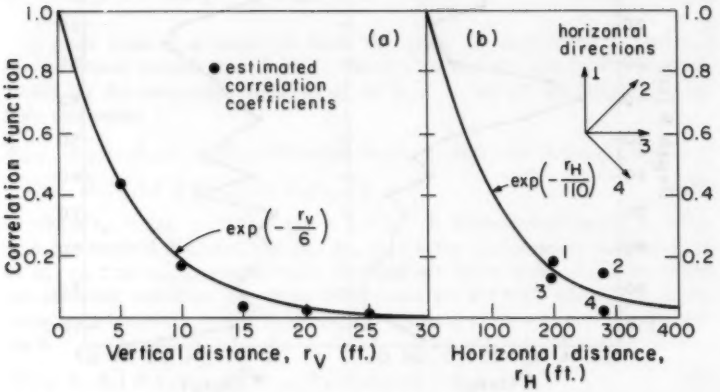

FIG. 4.—Correlation Function of ln D_r for the Site Analyzed in Ref. 2: (*a*) Vertical Correlation; (*b*) Horizontal Correlation (1 ft = 0.305 m)

of the field are shown in Fig. 3 as functions of depth. The same figure shows the median of D_r [equal to exp $(1/\hat{a}_2\ m_{(\ln N_F)'})$] and the variance of ln D_r, $\sigma^2_{\ln D_r}$. The standard deviation of ln D_r, $\sigma_{\ln D_r}$, equals in approximation the coefficient of variation of D_r. Fig. 4(*a*) shows the sample horizontal correlation function $\hat{\rho}_v(r_v)$ and a fitted parametric model of the simple exponential type. As shown in Fig. 4(*b*), data on horizontal correlation is scanty. Assuming that the correlation function is exponential also on horizontal planes, the model in Fig. 4(*b*) can be fitted. It is worth mentioning that very similar correlation results were obtained at the same deposit for other soil properties, e.g., grain size distribution characteristics (2). This fact gives support to the correlation results in Fig. 4.

Conclusions

A consistent set of models is developed for inference of D_r from N under

both laboratory and field conditions. The model in the laboratory (reference model) is based on a large data set, which consists of essentially all available laboratory information on joint measurements of N, D_r and $\bar{\sigma}_v$. It takes explicitly into account errors in the laboratory determination of D_r and is of a form that makes its use particularly simple. The reference model is not directly applicable in situ, because of the effects of factors such as in situ structure, consolidation history, fines content and variations in the way the SPT is performed. However, the model can be applied in the field after a simple, but sometimes depth dependent, modification, which requires a few joint measurements of N and D_r at the site. Once constructed, the site-specific model can be used to infer D_r from N at individual locations and more importantly to determine the mean value and the variance of D_r as a function of depth from measurements of N along a large number of borings. The procedure is exemplified numerically by using data from an actual site.

Acknowledgments

The National Science Foundation supported this study under Grant Nos. ENG-75-19400 and AEN 78-09626. Valuable discussions with J. T. Christian, C. A. Cornell, and R. V. Whitman are greatly appreciated.

Appendix I.—References

1. Bryson, A. E., and Ho, Y. C., *Applied Optimal Control*, Blaisdell Publishing Company, Waltham, Mass., 1969.
2. Fardis, M. N., "Probabilistic Liquefaction of Sands During Earthquakes," Research Report R79-14, Department of Civil Engineering, Massachusetts Institute of Tech., Cambridge, Mass., Mar., 1979.
3. Gibbs, H. J., and Holtz, W. G., "Research on Determining the Density of Sands by Spoon Penetration Testing," *Proceedings of the Fourth International Conference on Soil Mechanics and Foundation Engineering*, London, England, Vol. 1, 1957, pp. 35–39.
4. Marcuson, W. G. III, and Bieganousky, W. A., "Laboratory Standard Penetration Tests on Fine Sands," presented at the Sept. 27–Oct. 1, 1976, ASCE Annual Convention and Exposition, held at Philadelphia, Pa.
5. Marcuson, W. F. III, and Bieganousky, W. A., "SPT and Relative Density in Coarse Sands," *Journal of the Geotechnical Engineering Division*, ASCE, Vol. 103, No. GT11, Proc. Paper 13350, Nov., 1977, pp. 1295–1309.
6. Raiffa, H., and Schlaiffer, R., "Applied Statistical Decision Theory," Graduate School of Business Administration, Harvard University, Cambridge, Mass., 1961.
7. Schmertmann, J. H., discussion of "Standard Penetration Test: Its Uses and Abuses" by G. F. A. Fletcher, *Journal of the Soil Mechanics and Foundations Division*, ASCE, Vol. 92, No. SM5, Proc. Paper 4890, Sept., 1966, pp. 130–133.
8. Schultze, E., and Melzer, K. J., "the Determination of the Density and the Modulus of Compressibility of Noncohesive Soils by Soundings," *Proceedings of the Sixth International Conference on Soil Mechanics and Foundation Engineering*, Vol. 1, Montreal, 1965, pp. 354–358.
9. Seed, H. B., "Soil Liquefaction and Cyclic Mobility Evaluation for Level Ground during Earthquakes," *Journal of the Geotechnical Division*, ASCE, Vol. 105, No. GT2, Proc. Paper 14380, Feb., 1979, pp. 201–255.
10. Tag, E. A. G., "Standard Penetration Resistance in Cohesionless Soils," *Soils and Foundations*, Vol. 16, No. 4, Dec., 1976, pp. 47–60.
11. Tavenas, F. A., Ladd, R. S., and LaRochelle, P., "Accuracy of Relative Density Measurements: Results of a Comparative Test Program," *Evaluation of Relative Density and Its Role in Geotechnical Projects Involving Cohesionless Soils*, ASTM STP 523,

American Society for Testing and Materials, 1973, pp. 61–73.
12. Veneziano, D., "Statistical Estimation and Prediction in Probabilistic Models, with Application to Structural Reliability," thesis presented to the Massachusetts Institute of Technology, at Cambridge, Mass., in 1974, in partial fulfillment for the degree of Doctor of Philosophy.

Appendix II.—Notation

The following symbols are used in this paper:

a_i = parameter in N-D_r relationship, Eq. 2 ($i = 1, 3$);
$B_X(\cdot)$ = covariance function of random field X;
$B_1(\cdot), B_2(1), B_3(\cdot)$ = covariance functions of $a_2 \ln D_r$, ϵ_s and $\epsilon_{\ln N_F}$ (Eqs. 28, 29, 30);
D_r = relative density;
F = subscript indicating a quantity measured in the field;
$g_s(h)$ = depth- and site-dependent intercept in N-D_r relationship in the field, Eq. 23;
$\mathbf{H}$ = observation matrix with ith row given by Eq. 19;
h, h_i = depth, with continuous or discrete values;
$I(x)$ = function of x, equal to 1 for $x = 0$ and equal to 0 otherwise;
i = index for measurement;
j = index for limiting density measurement from rth laboratory, ($j = 1, n_r$);
k = index for sand type ($k = 1, n_s$);
L = subscript indicating a quantity measured in the lab;
$\ln D_{r,i}$ = quantity defined by Eq. 15, for ith measurement on sand k;
$(\ln N_F)'$ = residual quantity defined by Eq. 24;
M = number of laboratories providing values for $\gamma^k_{\max}$, $\gamma^k_{\min}$;
$m_x, \mathbf{m}_x$ = mean value of variable x or mean value vector of vector $\mathbf{x}$;
$m'_x, m''_x, m'_{\mathbf{x}}, m''_{\mathbf{x}}$ = prior and posterior mean values of x or $\mathbf{x}$;
N = blowcount number of the SPT;
n = number of measurements;
n_r = number of limiting density measurements from rth laboratory;
n_s = number of sand types in the data;
n_z, n_β = dimension of vector $\mathbf{z}$ or $\boldsymbol{\beta}$, respectively;
$n_{h_1h_2}, n_{r_Hh}, n_{r_v}, n_{r_H}$ = number of terms in summation of Eqs. 33, 34, 35, 36;
r = index for laboratory providing limiting density data ($r = 1, M$);
r_H, r_v = horizontal and vertical distance between two points;
s^2, s^2_m = within lab and interlab variance of measurements of $\gamma_{\max}$ and $\gamma_{\min}$;
x, y = horizontal coordinates;
$\mathbf{z}$ = vector containing observations of $\ln N_{L,i}$;
α^k = coefficient defined by Eq. 16 for sand k;
β^k_i = coefficient defined by Eq. 17 for observation i, on sand k;

$\boldsymbol{\beta}$ = vector of parameters to be estimated, Eq. 13;
γ_D = dry unit weight;
$\gamma_{max}, \gamma_{min}$ = maximum and minimum dry densities;
γ_{rj}^k = jth measurement of limiting density of sand, k, from rth laboratory;
$\Delta\gamma_{max}^k, \Delta\gamma_{min}^k$ = deviations of γ_{max}^k, γ_{min}^k from their prior mean values;
ϵ, ϵ_s = lack-of-fit terms in $N - D_r$ relationships in the lab or in the field;
ϵ_F, ϵ_L = residual term in Eqs. 4 and 23;
$\boldsymbol{\epsilon}_L$ = vector of values of ϵ_L for observations of ln $N_{L,i}$;
$\epsilon_{\ln N_F}, \epsilon_{\ln N_L}$ = error in measurement of ln N in the field or in the lab;
θ, θ_i = measured parameter and the outcome of its ith measurement;
$\rho_H(r_H), \rho_v(r_v)$ = horizontal and vertical correlation function of ln D_r and ϵ_s;
$\boldsymbol{\Sigma}_{\mathbf{x}}$ = covariance matrix of random vector $\mathbf{x}$;
$\boldsymbol{\Sigma}_{\mathbf{x}}', \boldsymbol{\Sigma}_{\mathbf{x}}''$ = prior and posterior covariance matrix of $\mathbf{x}$;
$\sigma_F^2, \sigma_L^2, \sigma_s^2$ = variance of $\epsilon_F, \epsilon_L, \epsilon_s$, respectively;
σ_x^2 = variance of random variable, x;
$\sigma_x^{2\prime}, \sigma_x^{2\prime\prime}$ = prior and posterior variance of x;
$\bar{\sigma}_v$ = vertical effective stress; and
$\hat{\ }$ = mean value or sample average as an estimator of a random variable.

STATISTICAL ANALYSIS OF SAND LIQUEFACTION

Michael N. Fardis[1] and Daniele Veneziano,[2] Associate Members, ASCE

INTRODUCTION

Because of the large damage potential of liquefaction failures, the profession has made a major effort to understand and design against this phenomenon, particularly, under earthquake conditions. Although explanation of the physical mechanism and extrapolation from laboratory experiments to field conditions still pose controversial problems, a number of useful design methods are now available. The simpler procedures are empirical; they consist of comparing Standard Penetration Test results at the site and a design earthquake acceleration with similar data from sites of known performance during historical earthquakes. More sophisticated "fundamental" approaches require calculation of the shear stresses at various depths in the soil deposit and comparison with laboratory test data on undisturbed or reconstituted samples.

Most design methods are deterministic, but some empirical procedures have been extended to estimate the liquefaction probability from given, Standard Penetration Test, SPT, blowcounts number, N, and peak ground acceleration or other earthquake intensity parameter (5,34). Probabilistic versions of the fundamental approach have been proposed by Donovan (6), Faccioli (7), Haldar and Tang (13), and McGuire, et al. (20).

The cornerstone of any probabilistic fundamental approach is a stochastic model of liquefaction resistance for a soil mass with uniform properties, either a laboratory sample, or a small volume of in-place material. Models of this type are developed here.

In early studies (18,19,29), relative density was considered as the main sand parameter governing liquefaction, but more recent experimental work (16,17,24) has emphasized the importance of sample preparation method and soil structure so that present design practice relies on tests of "undisturbed" samples. Validity of this procedure is seriously diminished by the inability of sampling techniques to preserve in-place density of cohesionless material (except for medium-dense

[1]Asst. Prof. of Civ. Engrg., Massachusetts Inst. of Technology, Cambridge, Mass.
[2]Assoc. Prof. of Civ. Engrg., Massachusetts Inst. of Technology, Cambridge, Mass.

Note.—Discussion open until March 1, 1982. Separate discussions should be submitted for the individual papers in this symposium. To extend the closing date one month, a written request must be filed with the Manager of Technical and Professional Publications, ASCE. Manuscript was submitted for review for possible publication on September 25, 1980. This paper is part of the Journal of the Geotechnical Engineering Division, Proceedings of the American Society of Civil Engineers, ©ASCE, Vol. 107, No. GT10, October, 1981. ISSN 0093-6405/81/0010-1361/$01.00.

sands) (3), in situ structure, and the effects of previous stress history (23). As a result, laboratory testing of undisturbed samples seems to offer little or no advantage over testing of reconstituted samples, provided that in situ D_r can be reliably estimated and appropriate corrections made for the effect of soil structure.

A probabilistic model of liquefaction in the lab for undrained simple shear tests is developed first. The model gives the probability distribution of the number of cycles to liquefaction as a function of uniform shear stress amplitude, mean initial effective stress, and relative density. It also accounts for sample preparation method, system compliance, stress nonuniformities, and errors inherent in the laboratory determination of relative density. Parameters of the model are estimated from a large number of test results obtained by several researchers.

Information in the literature on the difference between liquefaction behavior of undisturbed medium dense sands and reconstituted samples and on the effects of motion bidirectionality are used to convert the laboratory liquefaction model into one applicable in the field. Finally, the model is generalized to load cycles with nonuniform shear stress amplitude.

Number of Stress Cycles to Liquefaction in Laboratory

For given cyclic shear stress and initial effective stresses (vertical and lateral) the in situ liquefaction behavior of a sand depends on grain size characteristics, relative density, soil structure, and previous static and dynamic stress history (28). Because of the complexity of these effects, a liquefaction model based on tests of undisturbed samples would be most desirable. Unfortunately, the limitation of current sampling techniques and of available data forces one into using indirect approaches, such as that proposed here. First, a probabilistic model is developed for liquefaction in the laboratory as a function of relative density, D_r; initial mean effective stress, $\bar{\sigma}_m^o$; and sample preparation method. Then the model is transformed for in situ conditions by incorporating the effect of in place structure and multidirectionality of motion.

Analysis of Simple Shear Test Results.—Undrained cyclic simple-shear tests provide the closest laboratory approximation to in situ stress conditions under vertically propagating shear waves. A relatively large data set (192 tests) can be assembled using published results (1,9–12,23,26,32,35–37) and classified into eight groups depending on testing devices. Characteristics of each group are given in Table 1, including sand type (all sands are uniform, medium and clean), initial vertical effective stress $\bar{\sigma}_v^o$, and sample preparation method. The following log-linear model fits the data of all groups well with k a group index

$$\ln N_l = a_1^k + a_2 \ln \frac{\tau}{\bar{\sigma}_m^o} + a_3 \ln D_r + \epsilon \quad \ldots \ldots \ldots

Preliminary analysis with a_2 and a_3 in Eq. 1 indexed by k showed that these parameters are practically the same for all groups. The zero-mean Gaussian scatter term, ϵ, in the same equation reflects minor differences in soil structure for given sample preparation method and has the same variance for all groups. Thus, group dependence in Eq. 1 is limited to the intercept parameter a_1.

Standard regression techniques cannot be used to estimate the coefficients (a_1^k, a_2, a_3) from observed values of $(N_l, \tau/\bar{\sigma}_m^o, D_r)$ because of unreliability of laboratory determinations of D_r. This problem was previously encountered by these authors in the analysis of regression relationships between SPT-N and D_r; it can be solved here by the same technique. In short, the technique consists

TABLE 1.—Test Groups Used in Analysis

Group (1)	Testing device (2)	Sand (3)	$\bar{\sigma}_v$, in pounds per square inch (4)	Preparation method (5)	References (6)
1	Ring-torsional with rigid walls	Bandaijima, Niigata	14.22	pluviation through water	35,36,37
2	Ring-torsional with rigid walls	Ottawa, American Society for Testing Materials, C-109	20	pluviation through water	14,32
3	Constant volume	Ottawa, American Society for Testing Materials, C-109	28.44	dry vibrations	12
4	Large shaking table	Monterey, Number 0	8	pluviation through air	1,23
5	Roscoe-type	Ottawa, American Society for Testing Materials, C-109	28.44	pluviation through water	9,11
6	Roscoe-type	Monterey, Number 20–30	28.44–113.76	pluviation through water	26
7	Ring-torsional with flexible walls	Fuji River	14.22	pluviation through water	15
8	Roscoe-type	crystal silica, No. 20	unspecified	pluviation through water	10

of the following: (1) Replacing D_r in Eq. 1 in terms of dry unit weight and limiting dry densities, γ_{max} and γ_{min}; (2) calculating the variances of within-lab and across-lab errors in the determination of the limiting densities and using these variances to form a prior distribution of γ_{max} and γ_{min} for each sand; (3) linearizing the model with respect to γ_{max} and γ_{min}; and (4) using Bayesian regression in an iterative mode to revise the initial (laboratory) estimates of γ_{max} and γ_{min}, while also estimating the parameters a_1^k, a_2, and a_3. The prior distribution of these last parameters is assumed to be noninformative flat.

The 192 data points and the fitted regressions are shown in Fig. 1(*a*)–1(*h*), for $k = 1, \ldots, 8$. For each experimental point, two values of D_r are given:

the estimate from laboratory determinations of the limiting densities (value in parenthesis) and the estimate using the updated values of γ_{max} and γ_{min} for the appropriate group after regression analysis. The latter estimate is, in approximation, the posterior mean of D_r. Due to large sensitivity of D_r to the limiting densities, prior and posterior values are sometimes different. For groups that include tests at a single value of relative density, updating of γ_{max} and γ_{min} is not possible (due to non-informativeness of the prior distribution of a_1^k) so that in this case prior and posterior mean value of D_r coincide.

The posterior mean ($\hat{a}_1^k$) and variance of a_1^k are also given (Fig. 1). The

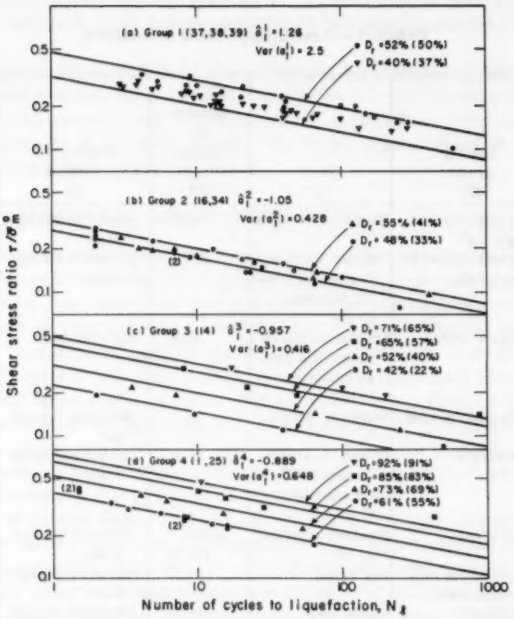

FIG. 1.—Laboratory Liquefaction Data and Fitted Relationships

large fluctuation of Var $[a_1^k]$ from group to group is due in part to differences in sample size but primarily to differences in the posterior variance of the limiting dry densities. The latter variances are especially large when the limiting densities are not updated (groups 7 and 8) or when one starts with large prior variances because information on γ_{max} and γ_{min} is from one laboratory only (groups 1, 7 and 8) or is obtained from non-American Society for Testing and Materials procedures. First and second moments of a_2, a_3, and ϵ are in Table 2.

In the past, it has often been found convenient to assume that the shear

stress ratio $\tau/\bar{\sigma}_v^o$ that causes liquefaction in a given number of cycles varies proportionally to D_r (15). This assumption has been based on early cyclic triaxial tests by Seed and Lee (19,29). In terms of the present model, Eq. 1, the implication is $a_2 = -a_3$. Based on more recent simple shear testing, Seed and his co-workers (1,28) have presented in a graphical form a relationship between shear stress ratio and relative density (for given N) which suggests that $\tau/\bar{\sigma}_v^o$ varies as D_r^n with n approx 1.35. The model proposed herein, which is based on a more comprehensive set of data and accounts for uncertainty in D_r, suggests a similar relationship, but with a slightly modified value of n; $n = -a_3/a_2 \approx 1.5$.

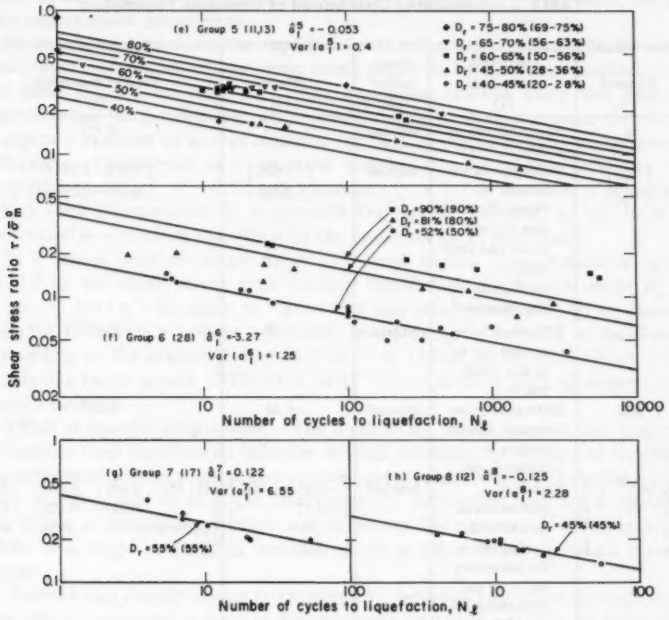
(e) Group 5 (11,13) $\hat{a}_1^5 = -0.053$
Var $(a_1^5) = 0.4$
D_r = 75-80% (69-75%)
D_r = 65-70% (56-63%)
D_r = 60-65% (50-56%)
D_r = 45-50% (28-36%)
D_r = 40-45% (20-28%)
80%
70%
60%
50%
40%
D_r = 90% (90%)
D_r = 81% (80%)
D_r = 52% (50%)
(f) Group 6 (28) $\hat{a}_1^6 = -3.27$
Var $(a_1^6) = 1.25$
Shear stress ratio $\tau/\bar{\sigma}_m^o$
Number of cycles to liquefaction, N_ℓ
(g) Group 7 (17) $\hat{a}_1^7 = 0.122$
Var $(a_1^7) = 6.55$
D_r = 55% (55%)
(h) Group 8 (12) $\hat{a}_1^8 = -0.125$
Var $(a_1^8) = 2.28$
D_r = 45% (45%)
Number of cycles to liquefaction, N_ℓ

FIG. 1.—*Continued*

The remainder of this section aims at resolving differences among the estimated intercepts $\hat{a}_1^k$. These differences are due to many factors: (1) Preparation method; (2) initial mean effective stress $\bar{\sigma}_m^o$; (3) system compliance and stress nonuniformity; (4) sand type; and (5) testing devices. After calculating the effect of the first three factors, it will be found that the corrected intercepts differ little from one another, thus, that a general model for liquefaction in the lab needs not explicitly recognize sand type (within the present class of sands) or testing device.

Experimental results suggest that preparation method, system compliance and

stress nonuniformity can be accounted for through additive constants whereas dependence on $\bar{\sigma}^{o}_{m}$ should be included by considering mean effective stress as an additional regression variable. After doing so, the intercepts a_1^k will be expressed as

$$a_1^k = a_1 - \Delta_{pr}^k - \Delta_{\text{comp}}^k - \Delta_{\text{rough}}^k + a_4 \ln \frac{\bar{\sigma}^{o}_{m}}{\sigma_{\text{ref}}} \quad \ldots\ldots\ldots\ldots\ldots\ldots\ldots (2)$$

in which Δ_{pr}^k, Δ_{comp}^k and Δ_{rough}^k are corrections for the preparation method of group k (relative to a reference method), system compliance, and platten

TABLE 2.—Probability Distribution of Uncertain Parameters

Symbol (1)	Uncertain parameter (2)	Distribution (3)	Mean (4)	Second moments (5)
ϵ	Residual term in Eqs. 1, 9, 13	Normal	0	0.45^2
$\begin{bmatrix}\Delta_{pr}^1\\ \Delta_{pr}^2\end{bmatrix}$	Difference in intercept between pluviation through water and pluviation through air[1] or dry vibration[2]	Normal	$\begin{bmatrix}0.430\\ -0.840\end{bmatrix}$	$\begin{bmatrix}0.038 & 0.031\\ 0.031 & 0.054\end{bmatrix}$
$\Delta_{\text{in situ}}$	Difference in intercept due to in situ structure	Normal	2.58	0.65^2
Δ_{2D}	Difference in intercept due to motion bidirectionality	Normal	−0.44	0.25^2
$\begin{bmatrix}a_1, (a^{\text{in situ}})^{\text{I}}\\ a_2\\ a_3\\ a_4\end{bmatrix}$	Vector of parameters in model for liquefaction in the laboratory, Eq. 9, or (in parenthesis) in situ, Eq. 13	Normal	$\begin{bmatrix}-0.66, (1.48)^{\text{I}}\\ -5.17\\ 7.8\\ -0.72\end{bmatrix}$	$\begin{bmatrix}(1.48)^{\text{I}} & 0.001 & 0.086 & 0\\ & 0.015 & -0.021 & 0\\ \text{Symmetric} & & 0.36 & 0\\ & & & 0.59\end{bmatrix}$

[1] Values in parentheses refer to $a_1^{\text{in situ}}$.

roughness, respectively; σ_{ref} is a reference value of initial mean effective stress, and a_1 is the group-independent coefficient, that replaces a_1^k in Eq. 1 under reference testing conditions (when all the correction factors are zero and $\bar{\sigma}^{o}_{m} = \sigma_{\text{ref}}$). These reference conditions are taken to be: sample preparation by pluviation through water, testing at constant volume (no system compliance), uniform stress, and $\bar{\sigma}^{o}_{m} = \sigma_{\text{ref}} = 4.8$ psi (33 kN/m^2). This value of σ_{ref} corresponds to $\bar{\sigma}^{o}_{m} = 8$ psi (55 kN/m^2) and a coefficient of lateral stress at rest, $K_o = 0.4$. Details are given next.

Effect of $\bar{\sigma}^{o}_{m}$.—There is enough experimental evidence that liquefaction behavior

does not depend only on $\tau/\bar{\sigma}^o_m$, but rather on τ and $\bar{\sigma}^o_m$, separately. Therefore, a better model should result from adding to the right-hand-side of Eq. 1 a term that depends on $\bar{\sigma}^o_m$. Available experimental data suggests the following model:

$$\ln N_l = a^k_1 + a_2 \ln \frac{\tau}{\bar{\sigma}^o_m} + a_3 \ln D_r + a_4 \ln \frac{\bar{\sigma}^o_m}{\sigma_{ref}} + \epsilon \quad \ldots \ldots \ldots \ldots \ldots \ldots \quad (3)$$

With only one exception (26), tests within each group were made using a single value of vertical effective stress $\bar{\sigma}^o_v$. Therefore, simple shear test data cannot be used to estimate the coefficient a_4. A viable alternative is to estimate a_4 from cyclic triaxial tests, assuming that this parameter is the same for the two experimental procedures.

Some of the triaxial tests reported in the literature (4,11,19,24,26) were performed on samples of the same sand, prepared by the same method, with the same D_r, but different $\bar{\sigma}^o_m$. From regression analysis using this data (8) one finds that the parameter a_4 differs significantly from sand to sand; therefore, a separate estimate of a_4 was obtained for each of the five sands in the quoted references. Considered as a statistical sample, this set of five estimates has empirical mean $m_{a_4} = -0.72$ and variance $\sigma^2_{a_4} = 0.77^2$. Because it is unclear which sand characteristic is responsible for this dependence, a_4 will have to be treated as a random variable with the moments given previously.

In a recent state-of-the-art paper (28) Seed applied a multiplicative factor of 0.9 to the shear stress ratio causing liquefaction in the lab under $\bar{\sigma}^o_v =$ 8 psi (55 kN/m^2) in order to "allow for increased pressures, up to about 1 tons/sq ft, which would be applicable in the range of interest in the field." According to the present model and for 1 tsf (2,000 psf or 95.7 kN/m^2) this correction factor equals $[2000/(8 \times 144)]^{-a_4/a_2} \approx 0.92$, in good agreement with Seed's estimate.

Effect of Sample Preparation.—The method by which samples are prepared influences their liquefaction behavior through modification of the soil structure. Experimental results suggest that sample preparation method affects the regression in Eq. 1 only through the coefficient a^k_1. Objectives here are to quantify the effect of sample preparation and to correct the parameters a^k_1 by referring them to a single preparation method, which is taken to be pluviation through water.

Assume that the difference in intercept Δ^i_{pr} between pluviation through water and the ith preparation method depends only on i (and not also on sand type, testing procedure, etc.). Then the parameter Δ^i_{pr} can be estimated for all i by performing a regression analysis of the model

$$\ln N_l = \alpha - \sum_i I_i \Delta^i_{pr} + a_2 \ln \frac{\tau}{\bar{\sigma}^o_m} + \epsilon \quad \ldots \ldots \ldots \ldots \ldots \ldots \quad (4)$$

in which I_i is a (0, 1) indicator variable with value 1 if preparation method i is used, and the intercept $\alpha = a_1 + a_3 \ln D_r + a_4 \ln \bar{\sigma}^o_m/\sigma_{ref}$ is a constant, if preparation method is all that is being changed (in addition to $\tau/\bar{\sigma}^o_m$) during the experiment. Refs. 12 and 24 provide the data one needs for this analysis. The resulting mean value and covariance matrix of the vector with components Δ^i_{pr} for the methods used in the 8 test groups have been calculated in Ref. 8 and are reproduced here in Table 2.

In the next section, a correction of the type Δ^i_{pr} will be introduced to convert the lab model with samples prepared by pluviation through water, to a model applicable in situ, i.e., to "undisturbed" samples.

Effect of System Compliance and Stress Nonuniformity.—Membrane stretching in the corners, expansion of the confining frame and compliance of the pore-pressure measurement system (these phenomena are collectively called "system compliance") have an effect on the liquefaction of undrained samples tested by simple shear devices with relatively rigid walls (21). Such devices were used in test groups 1, 2, 5, 6 and 8. Quantification of the compliance effect is possible if one assumes that only the coefficient a^k_1 in Eq. 1 is affected. For analysis, one can use data in Ref. 12 from experiments under constant volume (uncompliant) and undrained (compliant) conditions. In this set of experiments, sand type and all other testing parameters except $\tau/\bar{\sigma}^o_m$ were kept the same; therefore, the effect of compliance can be determined from a regression model of the type

$$\ln N_l = \alpha - I_c \Delta^k_{\text{comp}} + a_2 \ln \frac{\tau}{\bar{\sigma}^o_m} + \epsilon \quad \ldots \ldots \ldots \ldots \ldots \ldots \ldots \ldots \quad (5)$$

in which I_c is a (0, 1) indicator variable with value 0 for uncompliant conditions, and k takes on the values 1, 2, 5, 6. Analysis gives Δ^k_{comp} as a normal variable with mean -0.99 and variance 0.5^2. This means that the parameters a^k_1 of groups 1, 2, 5, 6 and 8 should be decreased by 0.99 in order to remove bias from system compliance.

Simple shear tests of specimens covered in part by flexible membranes, such as those in group 7, suffer from complaince due to reduced membrane penetration into peripheral voids. Following the procedure suggested in Ref. 21, it is found that in this case $\Delta^7_{\text{comp}} \sim N(1.3, 0.6^2)$, thus, that a^k_1 for test group 7 should be decreased by 1.3 to remove this source of bias. Results in group 4 are already corrected for compliance, whereas tests in group 3 are free of compliance effects.

For group 6 the effect of stress non-uniformities due to inadequate platten roughness can be corrected by adding 0.61 to a_1; the correction $\Delta_{\text{rough}} \sim N(0.61, 0.8^2)$ has been found through analysis of a model of the type in Eq. 5, using data for rough and smooth plattens in Ref. 11.

Model of Liquefaction in Laboratory.—Previous results allow one to correct the coefficients a^k_1 for system compliance and platten roughness and to refer them to the same preparation method (pluviation through water) and to a given value σ_{ref} of initial mean effective stress. The corrected coefficients, denoted by a'^k_1, are estimated as

$$\hat{a}'^k_1 = \hat{a}^k_1 + \hat{\Delta}^k_{pr} + \hat{\Delta}^k_{\text{comp}} + \hat{\Delta}^k_{\text{rough}} - \hat{a}_4 \ln \frac{\bar{\sigma}^o_m}{\sigma_{\text{ref}}} \quad \ldots \ldots \ldots \ldots \ldots \ldots \quad (6)$$

Values of all the terms in the right hand side of Eq. 6 are listed in Table 3. Uncorrected and corrected coefficients are compared in the same Table. Residual differences among the corrected values reflect variations in sand type and testing procedure, as well as possible statistical error in the determination of the correction terms. (See variances of the quantities for Δ given previously.)

The variance of the corrected parameters $\hat{a}'^k_1$ (0.74^2) is three times smaller

than the variance of the uncorrected estimates (1.31^2), and is of the same order as the estimation variances of a_1^k in Fig. 1. We shall take advantage of this fact to replace the eight parameters $a_1'^k$ with a single uncertain parameter a_1 (this is the first term in the righthand side of Eq. 2), which can be written

$$a_1 = m_{a_1} + \epsilon_s \quad \ldots \quad (7)$$

Since it is not clear which of the testing procedures represents best the in situ stress conditions, and since the model applies to the generic sand, the variation of a_1 due to sand type and testing procedure, modeled by ϵ_s, will be included in the final in situ model.

The objective here is to estimate m_{a_1} and the variance of ϵ_s in Eq. 7. The latter can be computed as the sample variance of the quantities $\hat{a}_1'^k$, i.e., $\sigma^2_{\epsilon_s}$

TABLE 3.—Correction of Intercept Parameters, a_1^k, for Preparation Method, Effect of $\bar{\sigma}_v^o$, and System Compliance

Group (1)	Uncorrected intercept, $\hat{a}_1^k$ (2)	$-\hat{a}_4 \ln \frac{\bar{\sigma}_m^o}{\sigma_{ref}}$ (3)	$\hat{\Delta}_{pr}^k$ (4)	$\hat{\Delta}_{comp}^k + \hat{\Delta}_{rough}^k$ (5)	Corrected intercept, $\hat{a}_1'^k$ (6)
1	1.26	0.42	0	−0.99	0.69
2	−1.05	0.95	0	−0.99	−1.09
3	−0.96	0.92	−0.84	0	−0.88
4	−0.89	0	0.43	0	−0.46
5	−0.05	0.92	0	−0.99	−0.12
6	−3.27	1.58	0	−0.38	−2.07
7	0.12	0.42	0	−1.3	−0.76
8	−0.12	0.71	0	−0.99	−0.40
Mean	−0.62				−0.64
Variance	1.31^2				0.74^2

$= 0.74^2$. For estimation of m_{a_1} one may use the average of the quantities $\hat{a}_1'^k$ in Eq. 6

$$\hat{m}_{a_1} = \frac{1}{8} \sum_{k=1}^{8} \hat{a}_1'^k \quad \ldots \quad (8)$$

or more efficient Bayesian or linear-minimum-variance estimation which give different weights to the quantities $\hat{a}_1'^k$, depending on their estimation variance. From Eq. 8, $\hat{m}_{a_1} = -0.64$, whereas from Bayesian estimation, which is the procedure used in Ref. 8, one finds that m_{a_1} is a normal variable with mean -0.66 and variance 0.67^2. This last variance accounts for statistical variability of the estimator in Eq. 6, and, therefore, for uncertainty on the correction terms Δ. It is large in comparison to $\sigma^2_{\epsilon_s}$ because of the strong positive correlation of the corrected coefficients, $\hat{a}_1'^k$. By adding the estimation variance of m_{a_1} to the variance of ϵ_s, which is due to sand type and testing procedure, one obtains a total variance of $0.74^2 + 0.67^2 = 1.0$ for a_1.

For $\sigma_{ref} = 4.8$ psi, D_r expressed as a fraction, sample preparation by pluviation through water, and an uncompliant testing device, the final model of liquefaction in the laboratory has the form,

$$\ln N_l = a_1 + a_2 \ln \frac{\tau}{\bar{\sigma}'^{o}_{m}} + a_2 \ln D_r + a_4 \ln \frac{\bar{\sigma}'^{o}_{m}}{\sigma_{ref}} + \epsilon \quad \ldots\ldots\ldots\ldots\ldots\ldots (9)$$

in which the vector of parameters $[a_1, a_2, a_3, a_4]^T$ has normal distribution with mean $[-0.66, -5.17, 7.8, -0.72]^T$ and covariance matrix

$$\text{Cov} \begin{bmatrix} a_1 \\ a_2 \\ a_3 \\ a_4 \end{bmatrix} = \begin{bmatrix} 1 & 0.01 & 0.086 & 0 \\ & 0.015 & -0.021 & 0 \\ & & 0.36 & 0 \\ \text{Symmetric} & & & 0.59 \end{bmatrix} \quad \ldots\ldots\ldots\ldots (10)$$

The residual term ϵ has normal distribution with zero mean and variance 0.45^2.

Number of Stress Cycles to Liquefaction in Field

The previous model for liquefaction in the laboratory, Eq. 9, refers to a sample of uniform medium clean sand prepared by pluviation through water and subjected to unidirectional simple shear cycles of uniform amplitude. In order to obtain a model applicable in situ to a small volume of the same sand, with the same D_r, subjected to a known time history of horizontally propagating seismic S-waves, one must account for three factors: (1) The effect of difference in soil structure and age between in-place material and laboratory samples; (2) the effect of bidirectionality of the stress time history; and (3) the nonuniformity of stress cycle amplitudes in the field. The first two factors are considered next to produce a model for liquefaction in the field under uniform shear stress cycling. A procedure to incorporate cycle nonuniformity will be given in the next section.

Effect of In Situ Soil Structure.—On the basis of experimental evidence in Ref. 25, it appears reasonable to confine the effect of soil structure and aging to the parameter a_1 in Eq. 9. If $a_1^{\text{in situ}}$ is the corrected value of a_1, then the difference $\Delta_{\text{in situ}} = a_1^{\text{in situ}} - a_1$ will vary from site to site depending on local soil structure and age. One can obviously write

$$\Delta_{\text{in situ}} = \Delta'_{\text{in situ}} - \Delta'_{pr} \quad \ldots\ldots\ldots\ldots\ldots\ldots\ldots\ldots\ldots\ldots (11)$$

in which $\Delta'_{\text{in situ}}$ is the difference between the values of a_1 for undisturbed samples and samples remolded to the same D_r by the ith procedure, and Δ'_{pr} is the correction in the lab calculated in the previous section. Eq. 11 is the instrument by which $\Delta_{\text{in situ}}$ can be evaluated using information in Refs. 24, 33 on the liquefaction behavior of undisturbed samples and samples reconstituted by five different procedures. Nineteen values of $\Delta_{\text{in situ}}$ have been calculated in this way, from 19 different natural deposits. The variance of these values is due to site-to-site differences in soil structure and age and equals 0.63^2.

An estimate of the mean value of $\Delta_{\text{in situ}}$ in Eq. 11 can be obtained by various procedures. Perhaps the simplest estimator is

$$\hat{\Delta}_{\text{in situ}} = \frac{1}{19} \sum_{j=1}^{19} (\Delta'_{\text{in situ}} - \hat{\Delta}'_{pr}) = 2.51 \quad \ldots\ldots\ldots\ldots\ldots\ldots\ldots (12)$$

in which the index, i, is for preparation method and depends on the deposit,

j. More efficient estimators (Bayesian, linear-minimum-variance) recognize that Δ'_{pr} have different estimation variances for different i, and, therefore, should receive different weighting in a formula of the type in Eq. 12. The Bayesian approach was pursued in Ref. 8, with the result that the mean value of $\Delta_{\text{in situ}}$ has distribution $N(2.58, 0.17^2)$. By adding the estimation variance, 0.17^2, to the variance for within-group fluctuation one obtains a total variance of 0.65^2. Thus, the distribution of the correction term in Eq. 11 can be taken to be $N(2.58, 0.65^2)$.

In Ref. 28, Seed has applied a multiplicative factor of 1.8 to the shear stress ratio which causes liquefaction of a sample prepared by pluviation through air, in order to correct for in situ structure and long-term loading effects. According to the present model, this correction factor equals $\exp\,[-(\hat{\Delta}'_{\text{in situ}}/\hat{a}_2)]$ with $\hat{\Delta}'_{\text{in situ}} = \hat{\Delta}_{\text{in situ}} + \hat{\Delta}'_{pr} = 2.58 + 0.43 = 3.01$, for i that corresponds to pluviation through air. Therefore, the correction factor according to the present model is $\exp\,[-(3.01)/(-5.17)] = 1.79$, in excellent agreement with the value suggested by Seed.

Although $\Delta_{\text{in situ}}$ varies across sites according to the distribution above, indirect information on its value at a site can be obtained from a few joint measurements of SPT-blowcounts number N and D_r, on the basis of the fact that factors such as soil-structure, time under pressure, stress history, etc. affect in the same direction both the liquefaction resistance (through $\Delta_{\text{in situ}}$) and the value of N for given D_r and $\bar{\sigma}_v$ (28). If a high positive correlation coefficient is assumed between $\Delta_{\text{in situ}}$ and the average difference of measured N from that predicted by a laboratory relationship between N and $(D_r, \bar{\sigma}_v)$, then one can use a few measurements of $(N, D_r, \bar{\sigma}_v)$ to limit uncertainty on $\Delta_{\text{in situ}}$ at the site (8).

Multidirectionality of Motion.—In the analysis of seismic response it is common practice to attribute all horizontal components of ground motion to shear waves propagating vertically in a single plane (unidirectional plane strain model). We shall assume that this model is used and that the unidirectional input motion is selected with frequency content and intensity (e.g., peak acceleration) equal to the average frequency content and intensity along two orthogonal horizontal directions at rock outcrop. The effect of bidirectionality of motion (more pronounced rearrangement of the grains and smaller liquefaction resistance) is found in approximation as follows.

Let RD be the factor by which the densification rate of dry sand under vertically propagating multidirectional S-waves exceeds the same rate under a unidirectional input motion of average intensity. The value of RD depends on details of the ground motion. Its probabilistic characteristics can be estimated from experimental results in Ref. 27 on the densification caused by artificial acceleration time-histories applied to dry samples, separately or simultaneously in two orthogonal directions. The latter condition realistically simulates actual bidirectional ground motions: when averaged over a sample of 8 simulation pairs, the ratio of the smaller to the larger peak acceleration is 0.87, which is close to the value 0.82 estimated from actual records (22). From the same 8 motion pairs, the sample values of the mean and variance of RD are 1.7 and 0.3^2, respectively. These statistics are taken as the true mean and the true variance of RD and denoted by $\hat{\text{RD}}$ and Var (RD).

Analytical results in Ref. 31 suggest that for a given sand the ratio RD affects only the intercept a_1 in Eq. 9. From the same reference one can estimate the

two moments of the change in a_1, Δ_{2D}, conditionally on RD = 2. They are $\hat{\Delta}_{2D}$ (RD = 2) = −0.63 and Var $[\Delta_{2D}(\text{RD} = 2)] = 0.25^2$. If $\hat{\Delta}_{\text{RD}}$ is linear in RD, then Δ_{2D} has unconditional mean $\hat{\Delta}_{2D} = -0.63 \times 1.7/2.0 = -0.44$, and if Var $[\Delta_{2D}(\text{RD})]$ is quadratic in RD, then Var $(\Delta_{2D}) = 0.24^2$.

Seed suggested to apply a multiplicative factor of 0.9 to the shear stress ratio which causes liquefaction in unidirectional simple shear testing, in order to correct for the effect of bidirectionality of the actual motion (28). According to the model proposed herein this correction factor equals $\exp(\hat{\Delta}_{2D}/\hat{a}_2) = \exp(-0.44/5.17) = 0.92$, in good agreement with the value suggested by Seed.

In summary, multidirectionality of shear waves reduces liquefaction resistance. This reduction can be accounted for by adding a motion-dependent random quantity Δ_{2D} with mean −0.44 and variance 0.24^2 to the right hand side of Eq. 11.

Field Liquefaction Model.—For bidirectional, constant amplitude shear waves, the number of cycles to liquefaction in the field satisfies

$$\ln N_l = a_1^{\text{in situ}} + a_2 \ln \frac{\tau}{\bar{\sigma}_m^o} + a_3 \ln D_r + a_4 \ln \frac{\bar{\sigma}_m^o}{\sigma_{\text{ref}}} + \epsilon \quad \ldots\ldots\ldots\ldots \quad (13)$$

in which $a_1^{\text{in situ}} = a_1 + \Delta_{\text{in situ}} + \Delta_{2D}$ has distribution, $N(-0.66 + 2.58 - 0.44 = 1.48, 1.0^2 + 0.65^2 + 0.24^2 = 1.22^2)$.

In this final model for field conditions and for given τ, D_r and $\bar{\sigma}_m^o$, statistical uncertainty on the coefficients a_2 and a_3 and variability of a_4 due to sand type contribute little to uncertainty on N_l. Uncertainty on Δ_{2D}, which is due to details of the ground motion, is also relatively unimportant. The major contributions to uncertainty on N_l come from site-to-site variations of in place soil structure, the effect of sand type, uncertainty on $\gamma_{\max}$ and $\gamma_{\min}$ for the sands that provided data for the laboratory model, and uncertainty on the corrections of the laboratory data for preparation method, system compliance, etc. All these more important sources of uncertainty are included in the variance of $a_1^{\text{in situ}}$.

The term ϵ, which represents the effect of minor differences in soil structure for the same sample preparation method, is retained in the model for liquefaction in the field as an uncorrelated random function of location. Eq. 13 is used next to develop a model of pore pressure evolution under non-uniform stress cycles.

Undrained Pore Pressure Evolution under Nonuniform Simple Shear Cycles

The model of Ref. 32 predicts that after a number n of uniform shear stress cycles, the undrained excess pore pressure u_e is related to $\bar{\sigma}_v^o$ and N_l as

$$\frac{u_e}{\bar{\sigma}_v^o} = \frac{2}{\pi} \arcsin\left(\frac{n}{N_l}\right)^{1/2\theta} \quad \ldots\ldots\ldots\ldots\ldots\ldots\ldots\ldots \quad (14)$$

with θ as a parameter. Information in Refs. 1, 9, 10, 15, 26, 35, 36 on simple shear testing of different sands with different values of D_r provides 22 sample values of the parameter θ. The relationship

$$\theta = 0.96\, D_r^{0.83}\, \epsilon_\theta \quad \ldots\ldots\ldots\ldots\ldots\ldots\ldots\ldots\ldots\ldots \quad (15)$$

with D_r as a fraction, ϵ_0 a log normal scatter term, and $\ln \epsilon_0 \sim N(0, 0.1^2)$ fits the data well.

In order to obtain the undrained evolution of u_e under nonuniform stress cycles, the assumption is made that, given $\bar{\sigma}_v^o$, θ, D_r and the parameters a_i in Eq. 13, the quantity u_e is a *state variable* of the evolution of undrained pore pressure, i.e., future values of u_e depend only on its present value and on future shear stress amplitudes. Then, if the effect of any individual stress cycle on u_e is small so that one can consider n as a continuous "time" variable, the firstorder differential equation that governs the evolution of u_e in time is of the type

$$\frac{du_e}{dn} = f[u_e(n), \tau_n, n)] \quad \ldots\ldots\ldots\ldots\ldots\ldots\ldots\ldots \quad (16)$$

in which τ_n is stress amplitude at time n. The function $f(.,.,.)$ should be such that Eq. 14 is the solution of the differential equation, Eq. 16, in the particular case of uniform stress cycles. Differentiation of Eq. 14 with respect to n gives:

$$\frac{du_e}{dn} = f[u_e(n), \tau_n, n] = \frac{\bar{\sigma}_v^o}{\theta \pi N_l} \frac{1}{\sin^{2\theta-1}\left(\frac{\pi}{2}\frac{u_e}{\bar{\sigma}_v^o}\right)\cos\left(\frac{\pi}{2}\frac{u_e}{\bar{\sigma}_v^o}\right)} \quad \ldots\ldots \quad (17)$$

in which τ_n appears implicitly through N_l. Eq. 17 can be integrated analytically from 0–n to give

$$\frac{u_e(n)}{\bar{\sigma}_v^o} = \frac{2}{\pi} \arcsin\left[e^{-(a|^{\beta \pm 1}+4)} D_r^{-a_3}\left(\frac{\bar{\sigma}_m^o}{\sigma_{ref}}\right)^{-a_4} \sum_o^n \left(\frac{\tau_n}{\bar{\sigma}_m^o}\right)^{-a_2}\right]^{1/2\theta} \quad \ldots\ldots \quad (18)$$

In essence, Eq. 18 gives an expression of the equivalent uniform cycle concept described by Seed (28). In Ref. 8 it is shown that Eq. 18 corresponds to the quantification of this concept proposed by Annaki and Lee (2).

Conclusions

The present paper develops a consistent set of stochastic models of liquefaction resistance of a homogeneous mass of sand, such as a laboratory sample or a small element of in situ material. A probabilistic model for liquefaction in the laboratory for undrained simple shear tests is developed first. This model gives the probability distribution of the number of cycles to liquefaction as a function of uniform shear stress amplitude, mean initial effective stress and relative density and accounts for errors inherent in the laboratory determination of relative density. Corrections for sample preparation method, system compliance and stress nonuniformities are calculated and incorporated into the model. Parameters are estimated from a large number of simple shear test results obtained by eight different groups of researchers using several sands and testing techniques. Because of the type of sands in the data set, the model is applicable only to uniform, medium clean sand, which is the most liquefiable class of sand. Information in the literature on the difference between liquefaction behavior of undisturbed and reconstituted samples and on the effects of motion bidirectionality is used to convert the laboratory liquefaction model into one applicable

in the field. Finally, the model is generalized to load cycles with nonuniform shear stress amplitude.

The major contributions to uncertainty on the number of cycles to liquefaction, for given stress amplitude, relative density and confining stress come from site-to-site variations of in-place soil structure, the effect of sand type, uncertainty on the limiting densities of the sands that provided data for the laboratory model, and uncertainty on the corrections of the laboratory data for preparation method, system compliance, etc. The model developed here is used to predict the liquefaction potential of sand deposits (8).

Acknowledgments

The National Science Foundation Supported this study under Grant Nos. ENG 75-19400 and AEN 78-09626. Valuable conversations with J. T. Christian, C. A. Cornell, and R. V. Whitman are greatly appreciated.

Appendix I.—Reference

1. Alba, P., Chan, C. K., and Seed, H. B., "Determination of Soil Liquefaction Characteristics by Large-Scale Laboratory Tests," Report No. EERC 75-14, Earthquake Engineering Research Center, University of California, Berkeley, Calif., May, 1975.
2. Annaki, M., and Lee, K. L., "Equivalent Uniform Cycle Concept for Soil Dynamics," *Journal of the Geotechnical Engineering Division*, ASCE, Vol. 103, No. GT6, Proc. Paper 12991, June, 1977, pp. 549–564.
3. Castro, G., "Liquefaction and Cyclic Mobility of Saturated Sands," *Journal of the Geotechnical Engineering Division*, ASCE, Vol. 101, No. GT6, Proc. Paper 11388, June, 1975, pp. 551–569.
4. Castro, G., and Poulos, S. J., "Factors Affecting Liquefaction and Cyclic Mobility," *Journal of the Geotechnical Engineering Division*, ASCE, Vol. 103, No. GT6, Proc. Paper 12994, June, 1977, pp. 501–516.
5. Christian, J. T., and Swiger, W. G., "Statistics of Liquefaction and SPT Results," *Journal of the Geotechnical Engineering Division*, ASCE, Vol. 101, No. GT11, Proc. Paper 11701, Nov., 1975, pp. 1135–1150.
6. Donovan, N. C., "A Stochastic Approach to the Seismic Liquefaction Problem," *Proceedings of the First International Conference on Applications of Statistics and Probability to Soil and Structural Engineering*, Hong Kong, Sept., 1971, pp. 513–535.
7. Faccioli, E., "A Stochastic Model for Predicting Seismic Failure in a Soil Deposit," *Earthquake Engineering and Structural Dynamics*, Vol. 1, No. 3, Jan.–Mar., 1973, pp. 293–307.
8. Fardis, M. N., "Probabilistic Liquefaction of Sands During Earthquakes," Research Report R79-14, Dept. of Civ. Engrg., Massachusetts Institute of Technology, Cambridge, Mass., Mar., 1979.
9. Finn, W. D. L., Bransby, P. L., and Pickering, D. J., "Effect of Strain History on Liquefaction of Sand," *Journal of the Soil Mechanics and Foundations Division*, ASCE, Vol. 96, No. SM6, Proc. Paper 7670, Nov., 1970, pp. 1917–1933.
10. Finn, W. D. L., Lee, K. W., and Martin, R. G., "An Effective Stress Model for Liquefaction," *Journal of the Geotechnical Engineering Division*, ASCE, Vol. 103, No. GT6, Proc. Paper 13008, June, 1977, pp. 517–533.
11. Finn, W. D. L., Pickering, D. J., and Bransby, P. L., "Sand Liquefaction in Triaxial and Simple Shear Tests," *Journal of the Soil Mechanics and Foundations Division*, ASCE, Vol. 97, No. SM4, Proc. Paper 8039, Apr., 1971, pp. 639–659.
12. Finn, W. D. L., and Vaid, Y. P., "Liquefaction Potential from Drained Constant Volume Cyclic Simple Shear Tests," *Proceedings of the Sixth World Conference of Earthquake Engineering*, Vol. 6, New Delhi, India, Jan., 1977, pp. 7–12.
13. Haldar, A., and Tang, W. H., "Probabilistic Evaluation of Liquefaction Potential,"

Journal of the Geotechnical Engineering Division, ASCE, Vol. 105, No. GT2, Proc. Paper 14374, Feb., 1979, pp. 145–163.
14. Ishibashi, I., and Sherif, M. A., "Soil Liquefaction by Torsional Simple Shear Device," *Journal of the Geotechnical Engineering Division*, ASCE, Vol. 100, No. GT8, Proc. Paper 10752, Aug., 1974, pp. 871–888.
15. Ishihara, K., and Yasuda, S., "Sand Liquefaction in Hollow Cylinder Torsion under Irregular Excitation," *Soils and Foundations*, Vol. 15, No. 1, Mar., 1975, pp. 45–59.
16. Ladd, R. S., "Specimen Preparation and Liquefaction of Sands," *Journal of the Geotechnical Engineering Division*, ASCE, Vol. 100, No. GT10, Proc. Paper 10857, Oct., 1974, pp. 1180–1184.
17. Ladd, R. S., "Specimen Preparation and Cyclic Stability of Sands," *Journal of the Geotechnical Engineering Division*, ASCE, Vol. 103, No. GT6, Proc. Paper 13014, June, 1977, pp. 535–547.
18. Lee, K. L., and Fitton, J. A., "Factors Affecting the Cyclic Loading Strength of Soil," *Vibration Effects of Earthquakes on Soils and Foundations*, ASTM STP 450, American Society for Testing and Materials, 1969, pp. 71–95.
19. Lee, K. L., and Seed, H. B., "Cyclic Stress Conditions Causing Liquefaction of Sand," *Journal of the Soil Mechanics and Foundations Division*, ASCE, Vol. 93, No. SM1, Proc. Paper 5058, Jan., 1967, pp. 47–70.
20. McGuire, R. K., Tatsuoka, F., Iwasaki, T., and Tokida, K., "Assessment of the Probability of Liquefaction of Water-Saturated Reclaimed Land," *Proceedings of the 3rd International Conference on Applications of Statistics and Probability in Soil and Structural Engineering*, Sydney, Australia, Jan., 1979, pp. 786–801.
21. Martin, G. R., Finn, W. D. L., and Seed, H. B., "Effects of System Compliance on Liquefaction Tests," *Journal of the Geotechnical Engineering Division*, ASCE, Vol. 104, No. GT4, Proc. Paper 13667, Apr., 1978, pp. 463–479.
22. Mohraz, B., "A Study of Earthquake Response Spectra for Different Geological Conditions," *Bulletin of the Seismological Society of America*, Vol. 66, No. 3, June, 1976, pp. 915–935.
23. Mori, K., Seed, H. B., and Chan, C. K., "Influence of Sample Disturbance on Sand Response to Cyclic Loading," Report No. EERC 77-03, Earthquake Engrg. Research Center, Univ. of California, Berkeley, Calif., Jan., 1977.
24. Mulilis, J. P., Chan, C. K., and Seed, H. B., "The Effects of Method of Sample Preparation on the Cyclic Stress-Strain Behavior of Sands," Report No. EERC 75-18, Earthquake Engineering Research Center, University of California, Berkeley, Calif., July, 1975.
25. Mulilis, J. P., Mori, K., Seed, H. B., and Chan, C. K., "Resistance to Liquefaction Due to Sustained Pressure," *Journal of the Geotechnical Engineering Division*, ASCE, Vol. 103, No. GT7, Proc. Paper 13031, July, 1977, pp. 793–797.
26. Peacock, W. H., and Seed, H. B., "Sand Liquefaction Under Cyclic Loading Simple Shear Conditions," *Journal of the Soil Mechanics and Foundations Division*, ASCE, Vol. 94, No. SM3, Proc. Paper 5957, May, 1968, pp. 689–708.
27. Pyke, R., Seed, H. B., and Chan, C. K., "Settlement and Liquefaction of Sands Under Multidirectional Shaking," Report No. EERC 74-2, Earthquake Engineering Research Center, University of California, Berkeley, Calif., Feb., 1974.
28. Seed, H. B., "Soil Liquefaction and Cyclic Mobility Evaluation for Level Ground during Earthquakes," *Journal of the Geotechnical Engineering Division*, ASCE, Vol. 105, No. GT2, Proc. Paper 14380, Feb., 1979, pp. 201–255.
29. Seed, H. B., and Lee, K. L., "Liquefaction of Saturated Sands During Cyclic Loading," *Journal of the Soil Mechanics and Foundations Division*, ASCE, Vol. 92, No. SM6, Proc. Paper 4942, Nov., 1966, pp. 105–134.
30. Seed, H. B., Martin, P. P., and Lysmer, J., "Pore-Water Pressure Changes During Soil Liquefaction," *Journal of the Geotechnical Engineering Division*, ASCE, Vol. 102, No. GT4, Proc. Paper 12074, Apr., 1976, pp. 323–346.
31. Seed, H. B., Pyke, R. M., and Martin, G. R., "Effect of Multidirectional Shaking on Pore Pressure Development in Sands," *Journal of the Geotechnical Engineering Division*, ASCE, Vol. 104, No. GT1, Proc. Paper 13485, Jan., 1978, pp. 27–44.
32. Sherif, M. A., Ishibashi, I., and Tsuchiya, C., "Saturation Effects on Initial Soil Liquefaction," *Journal of the Geotechnical Engineering Division*, ASCE, Vol. 103,

No. GT8, Proc. Paper 13101, Aug., 1977, pp. 914–917.
33. Tatsuoka, F., Iwasaki, T., Tokida, K., Yasuda, S., Hirose, M., Imai, T., and Kon-no, M., "A Method for Estimating Undrained Cyclic Strength of Sandy Soils Using Standard Penetration Resistances," *Soils and Foundations*, Vol. 18, No. 3, Sept., 1978, pp. 43–58.
34. Yegian, M., "Risk Analysis for Earthquake Induced Failure by Liquefaction," Research Report No. R76-22, Department of Civil Engineering, Massachusetts Institute of Technology, Cambridge, Mass., May, 1976.
35. Yoshimi, Y., and Oh-Oka, H., "A Ring Torsion Apparatus for Simple Shear Tests," *Proceedings of the Eighth International Conference on Soil Mechanics and Foundation Engineering*, Vol. 1.2, Moscow, USSR, 1973, pp. 501–506.
36. Yoshimi, Y., and Oh-Oka, H., "Influence of Degree of Shear Stress Reversal on the Liquefaction Potential of Saturated Sand," *Soils and Foundations*, Vol. 15, No. 3, Sept., 1975, pp. 27–40.
37. Yoshimi, Y., and Tokimatsu, K., "Settlement of Buildings on Saturated Sand During Earthquakes," *Soils and Foundations*, Vol. 17, No. 1, Mar., 1977, pp. 23–38.

Appendix II.—Notation

The following symbols are used in this paper:

a_1, a_2, a_3, a_4 = parameters of laboratory liquefaction model, Eq. 9;
a_1^k = intercept parameter for group k in Eq. 1;
$a_1'^k$ = value of a_1^k after correction for preparation method, compliance, etc.
$a_1^{\text{in situ}}$ = intercept parameter for liquefaction in the field, Eq. 13;
D_r = relative density;
I_c = (0, 1) indicator variable, equal to 0 for uncompliant conditions;
I_i = (0, 1) indicator variable equal to 1 for preparation method, i;
i = index for sample preparation method;
j = index;
K_o = coefficient of lateral stress at rest;
k = index for test group ($k = 1,8$);
m_X = mean value of random variable X;
n = number of shear stress cycles;
N = blow-count number of the Standard Penetration Test;
N_l = number of uniform shear stress cycles to liquefaction;
RD = factor by which densification rate of dry sand under bidirectional shaking exceeds same rate under unidirectional shaking;
u_e = excess pore pressure;
α = $a_1 + a_3 \ln D_r + a_4 \ln \bar{\sigma}'_m/\sigma_{\text{ref}}$ in Eqs. 4 and 5;
$\gamma_{\max}, \gamma_{\min}$ = maximum and minimum dry density;
$\Delta_{\text{in situ}}, \Delta^i_{\text{in situ}}$ = difference in intercept of liquefaction model for in situ soil and for samples prepared by pluviation through water or by preparation method i, respectively;
$\Delta^k_{pr}, \Delta^k_{\text{comp}}, \Delta^k_{\text{rough}}$ = corrections of intercept parameter for the preparation method of group k (relative to a reference method), system compliance, and platten roughness;

Δ_{2D} = change in intercept parameter due to multidirectionality of shaking;
ϵ = residual term in Eq. 1;
ϵ_s = variation of a_1 due to sand type and testing device;
ϵ_θ = scatter factor in Eq. 15;
θ = exponent parameter in Eq. 14;
$\bar{\sigma}^o_m, \bar{\sigma}^o_v$ = initial mean and vertical effective stress;
σ_{ref} = reference value of $\bar{\sigma}^o_m$, equal to 4.8 psi (33 kN/m^2);
$\sigma^2_X = \text{Var}(X)$ = variance of random variable X;
τ, τ_n = shear stress amplitude, constant or dependent on cycle number n; and
$\hat{}$ = mean value of sample average as an estimator of a random variable.

TIME-DEPENDENT BEHAVIOR OF SOLUTION CAVERNS IN SALT

By Jamshid Ghaboussi,[1] M. ASCE, Randall E. Ranken,[2] and Alfred J. Hendron, Jr.,[3] M. ASCE

INTRODUCTION

The creeping of salt surrounding solution caverns over long periods of time causes continuing changes in the state of stress and deformation around the caverns. The long-term behavior of solution caverns is dependent on many factors. For caverns which are located at sufficient distances from the boundaries of salt domes and other caverns, the main factors affecting their long term behavior are cavern shape, cavern depth and in-situ stress, material properties of rock salt, and internal pressure. The emphasis in this study is on the influence of the cavern shape and the internal pressure history on the long-term behavior of caverns. The caverns studied are at approximately the same depth, and only one set of creep material properties was used throughout this study.

A number of creep finite element analyses were performed on three caverns. The cavern geometries were selected so as to cover a wide range of height-to-diameter ratios, varying from a disc shaped cavern to a long cylindrical cavern. These caverns were analyzed under several different internal pressures. In addition, analyses were performed to study the following: (1) The effect on cavern behavior of a sudden drop in internal pressure; (2) the response of a single cavern versus that of a cavern in an array of regularly spaced caverns; (3) the influence of creep deformations in a cavern tightness pressure test; and (4) the effect on analysis results of the way in which the leaching process is simulated in the analysis—instantaneous versus gradual simulation of the leaching process.

In the following sections, the creep material model and the finite element creep analysis are discussed briefly, followed by the description of the caverns and the method of analysis. In the remainder of the paper, various aspects of results of the analyses are presented and examined.

[1]Assoc. Prof., Dept. of Civ. Engrg., Univ. of Illinois at Urbana-Champaign, Urbana, Ill.
[2]Stone and Webster Engrg., Denver, Colo.
[3]Prof., Dept. of Civ. Engrg., Univ., of Illinois at Urbana-Champaign, Urbana, Ill.

Note.—Discussion open until March 1, 1982. To extend the closing date one month, a written request must be filed with the Manager of Technical and Professional Publications, ASCE. Manuscript was submitted for review for possible publication on July 1, 1980. This paper is part of the Journal of the Geotechnical Engineering Division, Proceedings of the American Society of Civil Engineers, ©ASCE, Vol. 107, No. GT10, October, 1981. ISSN 0093-6405/81/0010-1379/$01.00.

THEORY

Material Model.—The strains are assumed to consist of elastic strains, ϵ_{ij}^e and creep strains, ϵ_{ij}^c:

$$\epsilon_{ij} = \epsilon_{ij}^e + \epsilon_{ij}^c \quad \ldots \ldots \ldots

0.25% elastic strain which was estimated from the test results. It can be seen from Fig. 1 that the power law reasonably well approximates the test results, except at a very early time where the creep strains are underestimated.

Finite Element Solution Scheme.—The creep finite element analysis is carried out in a time marching scheme and the solution is obtained at discrete times, t_i, $i = 1, \ldots$, with time steps Δt_i:

$$\Delta t_i = t_i - t_{i-1} \quad \ldots \quad (7)$$

The stress vector, $\boldsymbol{\sigma}_i$, at time t_i, is written as the sum of the known stress vector, $\boldsymbol{\sigma}_{i-1}$, at time t_{i-1} plus the incremental stress vector, $\Delta\boldsymbol{\sigma}_i$:

$$\boldsymbol{\sigma}_i = \boldsymbol{\sigma}_{i-1} + \Delta\boldsymbol{\sigma}_i \quad \ldots \quad (8)$$

The incremental stress vector, $\Delta\boldsymbol{\sigma}_i$, is related to the increment of the total strain vector, $\Delta\boldsymbol{\varepsilon}_i$, and the increment of the creep strain vector, $\Delta\boldsymbol{\varepsilon}_i^c$, through

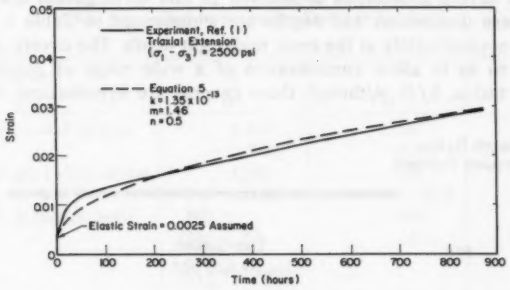

FIG. 1.—Strain Versus Time—Comparison of Test Data and Creep Properties Used in Study (1 psi = 6.89 kPa)

the elastic material property matrix, **c**:

$$\Delta\boldsymbol{\sigma}_i = \mathbf{C}(\Delta\boldsymbol{\epsilon}_i - \Delta\boldsymbol{\epsilon}_i^c) \quad \ldots \quad (9)$$

The creep strain increment $\Delta\boldsymbol{\epsilon}_i^c$ at time t_i is computed by the following equation:

$$\Delta\boldsymbol{\epsilon}_i^c = nk\,(J_2)_{i-1}^m \left(t_{i-1} + \frac{1}{2}\Delta t_i\right)^{n-1} \Delta t_i \left(\frac{\mathbf{S}}{|\mathbf{S}|}\right)_{i-1} \quad \ldots \quad (10)$$

in which **S** = the vector of deviatoric stresses; and $|\mathbf{S}| = (\mathbf{S}^T\mathbf{S})^{1/2}$.

The finite-element equation can be written as follows:

$$\sum_k \mathbf{L}^k \int \mathbf{B}^{k^T} \boldsymbol{\sigma}_i^k \, dv = \mathbf{P}_i \quad \ldots \quad (11)$$

in which **L** = element Boolean incidence matrix; **B** = element strain-displacement matrix; $\Delta\boldsymbol{\epsilon} = \mathbf{B}\Delta\mathbf{u}$; $\Delta\mathbf{u}$ = incremental vector of nodal displacements; $\mathbf{P}_i$ = nodal load vector at time, t_i; k = superscript denoting the element number; and T = superscript denoting the transpose of a matrix. In Eq. 11 the integration is over the volume of each element and the summation is over all the elements

in the system. Substituting Eqs. 8–10 into Eq. 11 results in the following incremental finite element equation:

$$\mathbf{K}\Delta\mathbf{u}_i = \mathbf{P}_i - \mathbf{R}_i \quad \ldots \ldots \ldots

depth and dimensions are similar to many existing caverns in salt domes.

Axisymmetric finite element meshes for each of the three caverns are shown in Figs. 3, 4, and 5. The meshes given in Figs. 3, 4, and 5 are for single caverns; i.e., it was assumed that there were no other caverns nearby that would influence the behavior of the cavern being analyzed. Cavern 2, however, was also analyzed for the multiple cavern case. As shown in Fig. 4, a hexagonal array of identical caverns was assumed. For such an array, the vertical planes of symmetry form, in plane view, a hexagon around each cavern. Thus, due to symmetry, the multiple cavern case can be analyzed by considering just one of the caverns and that portion of the surrounding medium that is located within the hexagon. An axisymmetric finite element mesh was generated for the cavern 2 multiple cavern case, with a radius corresponding to that of the circle in Fig. 4 (area of circle = area of hexagon). This type of analysis is a reasonable approximation to the much more expensive three-dimensional

TABLE 1.—Geometry of the Caverns Studied

Cavern (1)	1 (2)	2 (3)	3 (4)
Depth to cavern roof, in feet (meters)	3,240 (988)	2,700 (824)	2,950 (900)
Thickness of salt cover, in feet (meters)	1,240 (378)	700 (214)	950 (290)
Diameter, D, in feet (meters)	840 (256) (top) 696 (212) (bottom)	270 (82)	350 (107)
Height, h, in feet (meters)	150 (46)	2,000 (610)	700 (214)
h/D	0.2	7.4	2.0
Initial volume, in cubic feet (cubic meters)	69,700,000 (1,980,000)	114,500,000 (3,260,000)	67,400,000 (1,920,000)
Initial volume, in barrels (cubic meters)	12,400,000 (1,980,000)	20,400,000 (3,260,000)	12,000,000 (1,920,000)

analysis that would be required to analyze the actual hexagon configuration. It should be noted that this approach to the analysis of the multiple cavern case yields results that are applicable only to the caverns located in the interior of a large array of identically shaped caverns that are all leached at the same time.

Each analysis can be divided into three phases as the basis of the various solution steps. These phases are the in-situ phase, the leaching phase, and the operation phase. The in-situ phase corresponds to solution step 1 in which the in-situ stress state in the salt mass is simulated. The left boundary, mesh center line, and the bottom boundary, are assigned displacement boundary conditions (no displacements normal to boundary). The top boundary is assigned a force boundary condition corresponding to the weight of the overburden and cap rock. The right boundary is assigned a force boundary condition corresponding to the vertical distribution of horizontal in-situ stresses. The vertical stresses

resulting from the self-weight of the salt are introduced by body forces applied to the *salt* elements.

The leaching phase consists of one or more solution steps during which the leaching out of the cavern is simulated. The majority of analyses performed

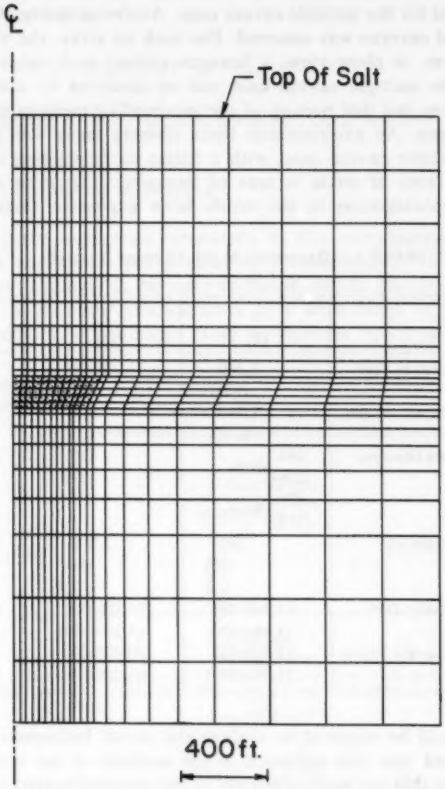

FIG. 3.—Finite-Element Mesh for Cavern 1

assumed the cavern to be formed instantaneously at time, $t = 0$. Thus, in solution step 2 the force boundary condition at the right boundary is replaced by a displacement boundary condition, the salt elements within the perimeter of the cavern are deactivated to simulate creation of the cavern, and forces are applied to the roof, floor, and wall of the newly created cavern to simulate the internal pressure exerted by the fluid within the cavern. In one analysis

of cavern 1, the gradual leaching out of the cavern over a period of time was simulated. This multistage leaching analysis will be explained in detail in a later section.

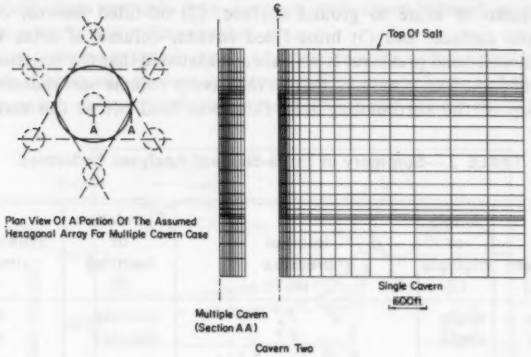

FIG. 4.—Finite-Element Meshes for Cavern 2—Single and Multiple Cavern Cases

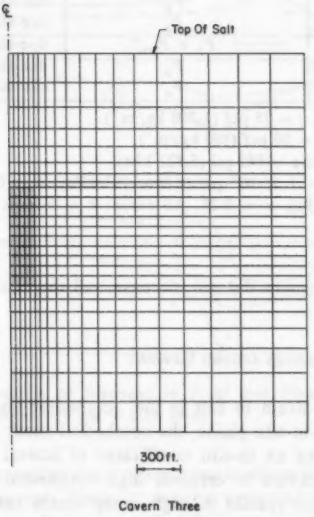

FIG. 5.—Finite-Element Mesh for Cavern 3

The operation phase consists of all solution steps after completion of the leaching phase. Because the mesh geometry remains unchanged during this phase of the analysis, the main variable, is the cavern internal pressure. Some analyses

assumed that after a certain length of time the brine is replaced by oil, or that a pressure test is performed. These changes were simulated by altering the force distributions applied to the roof, floor, and wall of the simulated cavern. Basically, three force distributions were considered: (1) Brine-filled cavern, column of brine to ground surface; (2) oil-filled cavern, column of oil to ground surface; and (3) brine-filled cavern, column of brine to ground surface plus well-head pressure. It was always assumed that the internal pressure remained constant with time, i.e., that as the cavern volume was reduced through inward creep of the surrounding salt, fluid was bled off at the surface such

TABLE 2.—Summary of Finite-Element Analyses Performed

Case (1)	Cavern (2)	Single or multiple (3)	Internal pressure (4)	Simulation of leaching (5)	Pressure test simulated (6)
1	one	single	P_B[a]	one-step	no
2	one	single	P_o[b]	one-step	no
3	one	single	P_B, $0 \le t \le 7.5$ yr P_O, 7.5 yr $\le t \le$ 15 yr	one-step	no
4	one	single	P_B	multistage	no
5	one	single	P_B	multistage	yes
6	two	single	P_B	one-step	no
7	two	single	$P_B + P_{WH}$[c]	one-step	no
8	two	multiple	P_B	one-step	no
9	three	single	P_B	one-step	no

[a] P_B = column of brine, γ = 75 pcf (1,200 kg/m^3).
[b] P_O = column of oil, γ = 50 pcf (800 kg/m^3).
[c] P_{WH} = wellhead pressure = 845 psi (5,822 kPa).
Notes: Cases 1–5: $E = 1 \times 10^6$ psi (6.9×10^6 kPa), $\nu = 0.25$. Cases 6–9: $E = 4 \times 10^6$ psi (27.6×10^7 kPa), $\nu = 0.25$. All cases: $k = 1.36 \times 10^{-13}$, $m = 1.45$, $n = 0.5$.

that cavern internal pressure did not increase. All the analyses are summerized in Table 2.

Creep-Induced Stress Changes around Caverns

The cause of creep strain in salt is the octahedral shear stress, as can be seen from Eq. 5. In the in-situ phase, the octahedral shear stresses are negligible since in all the analyses an in-situ coefficient of lateral stress of $K_0 = 1.02$ was used. When the cavern is created, high octahedral shear stresses occur around the cavern. This results in high creep strain rates. As time elapses, the octahedral shear stresses around the caverns generally decrease, resulting in decreasing creep strain rates. If this process is allowed to continue for a very long period of time, the octahedral shear stresses will vanish in the limit, and the state-of-stress around the cavern will approach a hydrostatic stress condition.

Of the individual stress components, the one acting normal to the cavern

surface must remain constant and equal to internal fluid pressure. The magnitude of the other two normal stresses generally approach the value the internal pressure, and the shear stresses approach zero. This pattern of stress changes is the dominant aspect of the creep behavior of the medium around the cavern. Any method which does not take into account such creep-induced stress changes can lead to grossly misleading results.

The above arguments strictly apply to single caverns within very large masses of salt rock. During the process of creep, arching takes place, and the effective zone of creeping medium tends to extend further from the cavern. This process

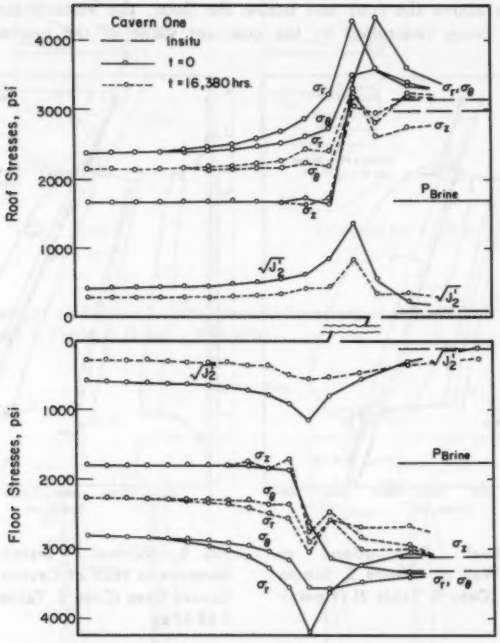

FIG. 6.—Radial Distribution of Stresses in Roof and Floor of Cavern 1 at t = 0 and 1.87 yr (Case 1, Table 2) (1 psi = 6.89 kPa)

will continue if the extending zone of creeping medium does not intersect similar zones from other caverns. Thus, it can be expected that the behavior of a cavern within an array of caverns will differ somewhat from that of a single cavern. In a multiple cavern situation, arching is not possible and the average vertical stress in the salt between the caverns must remain constant and equal to the overburden stress. Therefore, the limiting value of the octahedral shear stress is determined by the difference between the average vertical stress and the internal fluid pressure.

To illustrate the main aspects of the creep-induced stress changes, the stresses around the three caverns plus multiple case of cavern 2, under constant fluid pressure due to column of brine, are explained (cases 1, 6, 8, and 9 of Table 2).

The distribution of stresses in the roof and floor of cavern one are shown in Fig. 6. There is little variation of stress magnitude with radial distance from the center line except around the corners. It can be seen that, upon instantaneous creation of the brine-filled cavern, the vertical stress, σ_z, immediately drops to a value equal to the internal pressure. In response to this stress reduction, the radial and circumferential stresses also drop to values less than their in-situ magnitudes. There is a general stress reduction with the passage of time. However, immediately above the roof and below the floor, the vertical stress remains unchanged, being controlled by the constant value of the internal pressure.

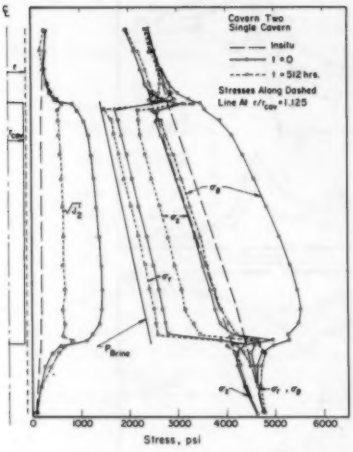

FIG. 7.—Vertical Distribution of Stresses in Wall of Cavern 2, Single Cavern Case (Case 6, Table 2) (1 psi = 6.89 kPa)

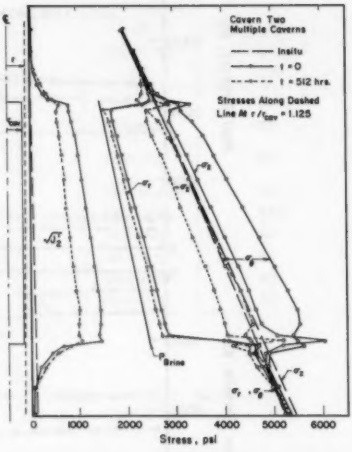

FIG. 8.—Vertical Distribution of Stresses in Wall of Cavern 2, Multiple Cavern Case (Case 8, Table 2) (1 psi = 6.89 kPa)

With time, the magnitudes of the radial and circumferential stresses tend to approach that of the internal pressure, and $\sqrt{J_2}$ approaches zero.

The vertical distributions of stresses in the salt just beyond the cavern wall are given in Figs. 7 and 8, for cavern 2 and the cavern 2-multiple cavern case, respectively. Upon the instantaneous creation of these brine-filled caverns, the radial stress drops from its in-situ magnitude to that of the internal pressure. For a single cavern, the vertical stresses near the wall essentially remain at their in-situ magnitudes because the effect of arching is concentrated away from the cavern wall and over a large area. However, for the multiple cavern case, the vertical stress initially carried by the salt removed to form the caverns must now be carried by the salt remaining between the caverns, thus resulting in an increase of vertical stress magnitude from the in-situ conditions. With

the passage of time, the radial and circumferential stresses tend to approach the magnitude of the internal pressure. The vertical stress in the salt adjacent

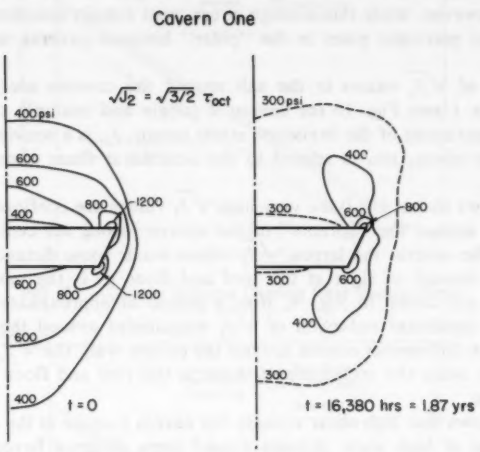

FIG. 9.—Contours of Square Root of Second Invariant of Deviatoric Stress Around Cavern 1 (Case 1, Table 2) (1 psi = 6.89 kPa)

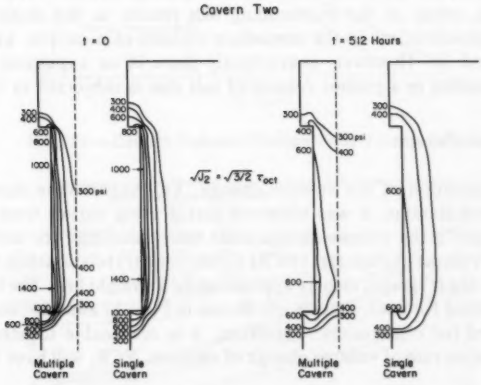

FIG. 10.—Contours of Square Root of Second Invariant of Deviatoric Stress for Cavern 2 (Cases 6 and 8, Table 2) (1 psi = 6.89 kPa)

to a single cavern also tends to approach the internal pressure. Additional arching of vertical stress to the salt farther away from the cavern compensates for this reduction of vertical stress.

Such additional arching is not possible for the multiple cacern case. For this case, it is required that the average vertical stress in the salt between caverns remain constant with time and equal to the weight of all material above the caverns. However, while this average stress must remain constant, the vertical stress at any particular point in the "pillar" between caverns may vary with time.

Contours of $\sqrt{J_2}$ values in the salt around the caverns are given in Fig. 9 for cavern 1 and Fig. 10 for cavern 2 (single and multiple cavern cases). The second invariant of the deviatoric stress tensor, J_2, is a convienent measure of the shear stress, and is related to the octahedral shear stress as follows: $J_2 = 1.5\,\tau_{oct}^2$.

Fig. 9 shows that at $t = 0$ the very high $\sqrt{J_2}$ values are confined to relatively small zones around the "corners" of the cavern. Along the center line above and below the cavern, the largest $\sqrt{J_2}$ values occur some distance away from the cavern, instead of right at the roof and floor as is the case for cavern 2 (Fig. 10). As shown in Fig. 9, after a period of approximately 2 yr there has been a significant reduction of $\sqrt{J_2}$ magnitudes around the cavern. The highest stress differences remain around the cavern wall, the $\sqrt{J_2}$ values there being almost twice the magnitude of those in the roof and floor at the center of the cavern.

Fig. 10 shows that high shear stresses for cavern 2 occur at the cavern walls, and the zone of high shear stresses extend some distance beyond the walls. As shown in Fig. 10, the $\sqrt{J_2}$ contours for the multiple cavern case do not differ at all that much from those for the single cavern, although it is obvious that the differences do exist. Stresses around the caverns for the multiple cavern case, of course, are quite dependent on the spacing between caverns.

In general, creep of the surrounding salt results in the dissipation of the high $\sqrt{J_2}$ concentrations in the immediate vicinity of a cavern, as can be seen in Figs. 9 and 10. However, concurrently there is an expansion of the zone of creep, resulting in a greater volume of salt that is subjected to creep.

Cavern Volume Changes

Upon examination of the volume change, VC, versus time curves obtained from these calculations, it was observed that if these curves were divided into increments, and if the volume change rates were calculated for each increment, the resulting volume change rate (VCR) versus time (t) relationship, when plotted on a log VCR-log (t) graph, closely approximated a straight line. The log (VCR)-log (t) plots obtained for several cases are shown in Figs. 11 and 12. Similar relations were obtained for other cases. Therefore, it is reasonable to assume that the equation for time rate of volume change of caverns, VCR, will have the following form:

$$\text{VCR} = (\text{VCR})_1\, t^{-S} \quad \ldots\ldots\ldots\

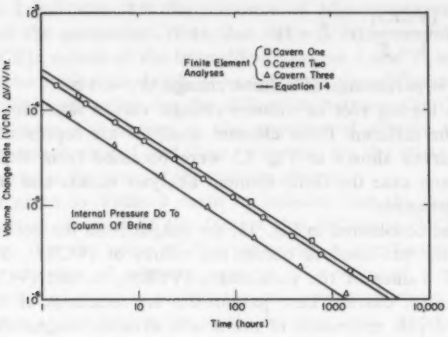

FIG. 11.—Cavern Volume Change Rate Versus Time

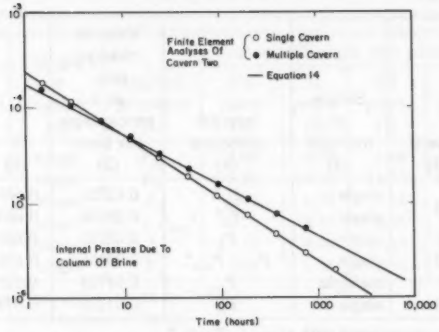

FIG. 12.—Cavern Volume Change Rate Versus Time

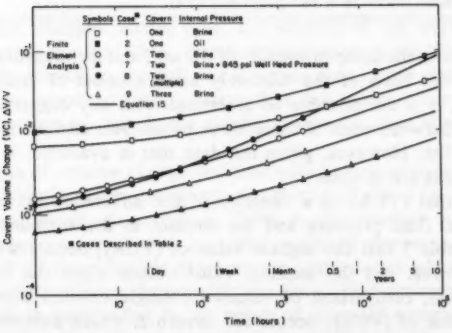

FIG. 13.—Cavern Volume Change Versus Time

$$VC = (VC)_1 + \frac{(VCR)_1}{1 - S}(t^{1-S} - 1) \quad \ldots\ldots\ldots\ldots\ldots\ldots\ldots\ldots\ldots\ldots (15)$$

in which VC_1 = percentage of volume change at $t = 1$ h.

Fig. 13 is a log-log plot of volume change versus time. In this figure, the results from the different finite element analyses are represented by the data points. The curves shown in Fig. 13 were obtained from Eq. 15. It can be seen that in each case the finite-element analysis results and the equation are in excellent agreement.

For each case considered in Fig. 13, the output from the corresponding finite element analysis was used to obtain the values of $(VCR)_1$, S, and VC_1 for use in Eq. 15. Values of the parameters $(VCR)_1$, S, and $(VC)_1$ are given in Table 3 for the six cases. These parameters are functions of cavern size and shape, cavern depth, magnitude of the in-situ stresses, magnitude of the cavern

TABLE 3.—Values of Parameters for Eq. 15 as Determined from Finite-Element Results

Cases[a] (1)	Cavern (2)	Single or multiple (3)	Internal pressure (4)	Volume change rate, as a percentage per hour (5)	S (6)	Volume change as a percentage, at $t = 1$ h (7)
1	1	single	P_B[b]	0.02720	0.660	0.67063
2	1	single	P_O[c]	0.05830	0.660	0.98939
6	2	single	P_B	0.02285	0.660	0.15132
7	2	single	$P_B + P_{WH}$[d]	0.00565	0.670	0.05910
8	2	multiple	P_B	0.01725	0.525	0.12553
9	3	single	P_B	0.01275	0.670	0.10320

[a] Case numbers correspond with those in Table 2.
[b] P_B = pressure due to a column of brine.
[c] P_O = pressure due to a column of oil.
[d] P_{WH} = wellhead pressure = 845 psi (5,822 kPa).

internal pressure, the creep properties of the salt, and the presence of surrounding caverns. On the basis of the relatively small number of analyses performed in this study, it is not possible to determine with any degree of certainty the relationships between each of these three parameters and the individual factors in the above list. However, given the data that is available, it does seem that a few comments are in order.

It appears that $(VCR)_1$ is a function of the difference between magnitudes of the internal fluid pressure and the stresses in the surrounding salt. It can be seen in Table 3 that the highest value of $(VCR)_1$ occurs when the internal pressure is lowest and the smallest value occurs when the internal pressure is highest. Also, comparison of values for single caverns 2 and 3 show that the higher value of $(VCR)_1$ occurs for cavern 2, which extends to the greater depth and therefore is subjected to the larger $\sigma_{salt} - P_i$ stress difference. Comparison of the $(VCR)_1$ values for the single cavern and multiple cavern

cases of cavern 2 indicates that the presence of adjacent caverns influences the magnitude of the parameter. Note that there is a considerable difference between the $(VCR)_1$ values of the brine-filled caverns 1 and 3, which are both located at the same midheight depth. It would seem that differences of cavern shape are primarily responsible for the difference between the $(VCR)_1$ values of these two caverns. For cavern 1, the majority of volume change is due to inward displacement of roof and floor, whereas, for the other caverns, wall displacements account for most of the volume change.

The S values given in Table 3 seem to indicate that the parameter, S, is relatively insensitive to most of the factors that influence $(VCR)_1$. It would appear, however, that the value of this parameter is significantly affected by the presence or absence of adjacent caverns. The value of S may be linked to the redistribution of stresses around the cavern during creep. There are no obstacles to stress redistribution for single caverns, and, therefore, the creep rate (and thus the volume change rate) is allowed to reduce relatively rapidly.

TABLE 4.—Volume Changes (Closures), as a Percentage

Case[a] (1)	Cavern (2)	Single or multiple (3)	Internal pressure (4)	Volume Change, as a percentage, after 7.5 years (5)	15 years (6)	20 years (7)	30 years (8)	40 years (9)
1	1	single	P_B[b]	4.06	4.99	5.44	6.16	6.73
2	1	single	P_O[c]	8.26	10.25	11.22	12.75	13.98
6	2	single	P_B	3.00	3.78	4.16	4.76	5.24
7	2	single	$P_B + P_{WH}$[d]	0.71	0.88	0.96	1.09	1.20
8	2	multiple	P_B	7.13	9.89	11.33	13.72	15.71
9	3	single	P_B	1.57	1.95	2.14	2.44	2.67

[a] Case numbers correspond to those in Table 2.
[b] P_B = pressure due to column of brine.
[c] P_O = pressure due to column of oil.
[d] P_{WH} = wellhead pressure = 845 psi (5,822 kPa).

However, for the multiple cavern case, the amount of salt surrounding any one cavern is rather limited. Thus, stress redistribution is hindered, and large stress differences remain in the salt for a longer time. This would cause the volume creep rate to reduce more slowly than for a single cavern; i.e., the log (VCR) versus log (t) line has a smaller slope, S, than that of a single cavern.

The percentages of volume change (volume reduction or closure), as obtained from Eq. 15 for the six cases considered, are given in Table 4 for five different times from 7.5 yr–40 yr. As shown in Table 4, the smallest volume change occurs for the single cavern 2 with an added wellhead pressure. These values are less than 25% of those for the same cavern without this additional internal pressure. The largest volume changes (for the brine-filled caverns) occur when this same cavern is surrounded by an array of identical caverns. At 7.5 yr, $(\Delta V/V)\%$ for the multiple cavern case is about 140% larger than that for the single cavern. In addition, this difference increases with time, for at 40 yr

the difference is 200%. Comparison of cases 9 and 6 shows that $(\Delta V/V)\%$ for cavern 3 is approximately 50% of that for cavern 2 which has almost three times the height, h_{cav}, of cavern 3 and therefore extends to a much greater depth.

Cavern Response to Sudden Decrease of Internal Pressure

A sudden decrease in the internal pressure of a cavern would cause instantaneous elastic changes in the state of stress around the cavern. Generally, the octahedral shear stresses are suddenly increased and as a result the rate of creep increases. Presented in this section are the results of analysis of simulation of pressure decrease in cavern 1 (case 3 of Table 2). In this analysis the cavern was subjected to the following history of internal pressure.

1. $t = 0$: Leaching of the cavern (one-step simulation-assumes leaching is instantaneous).
2. $0 \leq t \leq 7.5$ yr: The surrounding salt is allowed to creep, the cavern internal pressure is maintained constant, equal to the cavern filled with brine plus a column of brine to ground surface.
3. $t = 7.5$ h: Instantaneous reduction of the cavern internal pressure from that in 2 to that for the cavern filled with oil, plus a column of oil to the ground surface.
4. 7.5 yr $\leq t \leq$ 15 yr: The surrounding salt is allowed to creep in accordance with the new internal pressure which is constant.

At the time of the pressure drop, the magnitudes of the stresses in the surrounding salt change so as to be in equilibrium with the new internal pressure. After, as before, the pressure change all stresses are compressive.

In the salt comprising the central portions of the cavern roof and floor i.e., away from the "corners," the vertical stresses, σ_z, undergo a decrease of magnitude that is identical to the internal pressure change. In these same locations the radial and circumferential stresses, σ_r and σ_θ, also decrease in magnitude, but not to the extent that σ_z does. Although there is a general stress reduction in these locations in response to the pressure drop, because σ_z decreases more than do σ_r and σ_θ, there is a resultant increase of the stress differences. Thus, the magnitude of $\sqrt{J_2}$ immediately after the pressure drop is greater than that just before the pressure drop. The magnitudes of $\sqrt{J_2}$ in the cavern wall also increase immediately following the pressure drop. Here, however, this is to a great extent due to the large increase of the shear stress, τ_{rz}, rather than the changes of the normal stresses. In general, it can be said that in response to a reduction of cavern internal pressure the magnitude of the octahedral shear stress, $\sqrt{J_2}$, is increased everywhere in the salt surrounding the cavern. As a consequence, the rate of creep is also everywhere increased.

Results from this analysis are shown, in terms of cavern volume change (closure), by the lower curve in the log $(\Delta V/V)$ versus log (t) plot of Fig. 14. For $0 \leq t \leq 7.5$ yr, the volume change values are identical to those obtained from the analysis of cavern one with brine pressure which was mentioned earlier. Extension of the solid-line curve beyond $t = 7.5$ yr shows the cavern volume changes that would have resulted if the cavern internal pressure had been

maintained at that for brine. The upper curve in Fig. 14 represents the cavern volume changes that would result if cavern 1 were subjected to an internal pressure corresponding to that for oil throughout the entire time span illustrated (case 2, Table 2). It can be seen in Fig. 14 that, simultaneously with the pressure drop, the salt around the cavern experiences a certain amount of elastic inward displacement which results in an elastic component of volume change of approximately $\Delta V/V = 0.35\%$. Following the pressure drop, the increased stress differences in the salt result in a higher rate of creep and, thus, a higher rate of cavern volume change.

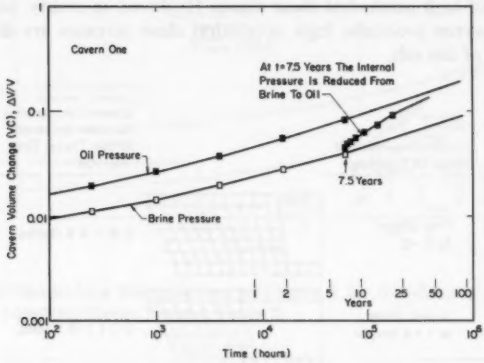

FIG. 14.—Cavern Volume Change Due to Internal Pressure Drop

The following qualitative observations can be made regarding the cavern behavior following a sudden internal pressure drop.

1. Following the internal pressure decrease, a sudden increase in the creep rate occurs, resulting from the increase of octahedral stresses around the cavern.
2. A period of high creep rate follows, and gradually the creep behavior approaches that of a cavern which has been under the lower internal pressure from the beginning. In effect, the "memory" of earlier higher internal pressure gradually disappears. This behavior is evident from cavern volume changes shown in Fig. 14.

An important practical implication of these observations is that in the analysis of cavern behavior, the recent past history plays an important role and must be simulated. However, the distant past history need not be considered since, for all practical purposes, their influence has disappeared.

Multistage Versus Single-Step Simulation of Leaching Phase

The actual leaching out of caverns takes a relatively long period of time before a final configuration is reached. During this period of time the salt creeps, resulting in considerable redistribution of stresses around the cavern. In a

single-step excavation analysis, the creation of the cavern is simulated in one step, representing instantaneous formation of the cavern. Thus, in this type of analysis, the creep deformations start taking place after the cavern has reached its final configuration. In order to allow creep during the leaching period, it is necessary to simulate the leaching process. In this method of analysis, the leaching of the cavern is simulated in a number of stages with real time intervals between subsequent stages of excavation.

In a single-step excavation analysis, immediately after the simulation of leaching, large octahedral shear stresses can be expected to occur around the cavern, which may suggest yielding and possible failure of the rock salt in these zones of high octahedral shear stress. However, in reality, as the leaching out of the cavern proceeds, high octahedral shear stresses are dissipated due to the creep of the salt.

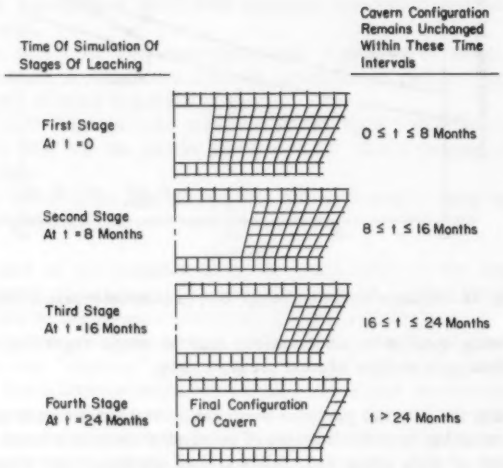
Time Of Simulation Of Stages Of Leaching
Cavern Configuration Remains Unchanged Within These Time Intervals
First Stage At t =0
0 ≤ t ≤ 8 Months
Second Stage At t = 8 Months
8 ≤ t ≤ 16 Months
Third Stage At t = 16 Months
16 ≤ t ≤ 24 Months
Fourth Stage At t = 24 Months
Final Configuration Of Cavern
t > 24 Months

FIG. 15.—Detail of Finite Element Mesh Around Cavern 1 at Various Stages of Simulation of Leaching (Case 4, Table 2)

Here the simulation of the leaching process in cavern 1 was performed in four stages as shown in Fig. 15. The fourth stage leaching, which completed the formation of the final configuration of the cavern, occurred two years after the leaching of the first stage. Between each of the leaching stages, 8 months of elapsed time was allowed. The results of this analysis are compared with the results of the single-step analysis in Figs. 16, 17, and 18. The vertical displacements of the center of the cavern roof as shown in Fig. 16. The second invariant of the deviatoric stress at the same point versus time is shown in Fig. 17 for the two types of analyses. The sudden jumps in the displacements and stresses at the beginning of each stage of excavation are due to elastic instantaneous response. In reality, the leaching out of the cavern is gradual

and continuous, similar to very small steps of excavation. In such a case, at each instant of time the deformations will consist of an elastic and a creep component, and thus the portions of the curves in Figs. 16 and 17 which consist of elastic jumps followed by creep should be replaced by continuous curves. However, during the leaching-out period, the rate of deformation will be higher than the rate deformation resulting from the single-step analysis. This should

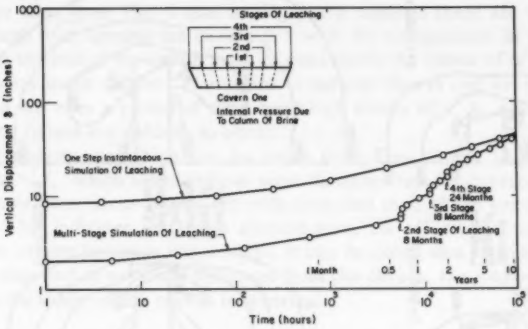

FIG. 16.—Roof Center-Line Displacement of Cavern 1 for One-Step and Multistage Simulation of Leaching (Cases 1 and 4, Table 2)

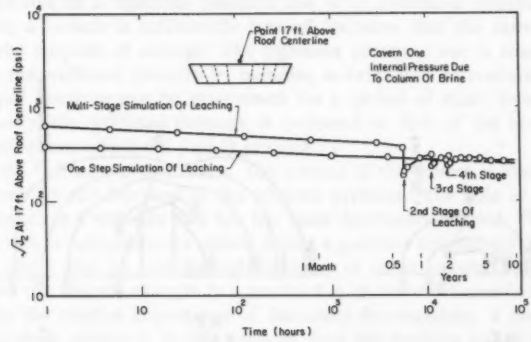

FIG. 17.—Square Root of Second Invariant of Deviatoric Stress at Roof Center Line of Cavern 1 for One-Step and Multistage Simulation of Leaching (Cases 1 and 4, Table 2) (1 psi = 6.89 kPa)

be expected, since in a single-step analysis all the elastic deformation occur at time $t = 0$ when the formation of the cavern is simulated.

After the leaching phase, the displacements and stresses from the multistage analysis approach those of the single-step analysis. This indicates that for the study of the long-term >10 yr effects the single-step excavation analysis will provide reasonable results.

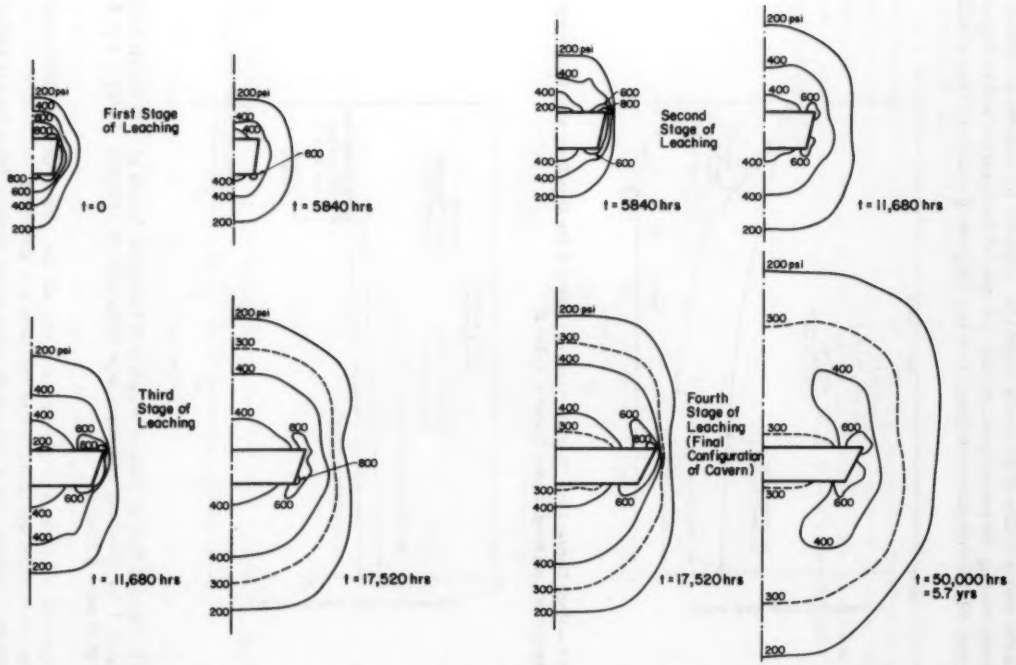
First Stage of Leaching
t = 0
t = 5840 hrs
Second Stage of Leaching
t = 5840 hrs
t = 11,680 hrs
Third Stage of Leaching
t = 11,680 hrs
t = 17,520 hrs
Fourth Stage of Leaching (Final Configuration of Cavern)
t = 17,520 hrs
t = 50,000 hrs = 5.7 yrs
200 psi

FIG. 18.—Contours of Square Root of Invariant of Deviatoric Stress Around Cavern 1 during Multistage Simulation of Leaching, (Case 4, Table 2) (1 psi = 6.89 kPa)

The contours of the square root of the second invariant of deviatoric stresses $\sqrt{J_2}$ for the single-step analysis and the multistage analysis are shown in Figs. 9 and 18, respectively. For the single step analysis, $\sqrt{J_2}$ for times $t = 0$ (instantaneous formation of the cavern) and $\sqrt{J_2}$ for $t = 1.87$ yr are shown in Fig. 9. For the multistage leaching analysis, the contours of $\sqrt{J_2}$ for $t = 0$, after the first stage of leaching, before and after each of the leaching stages 2, 3, and 4, and at time $t = 5.7$ yr, are shown in Fig. 18.

It can be seen from Fig. 9 that in single-step analysis there are very large zones of high $\sqrt{J_2}$ around the cavern at $t = 0$. By comparison, in multistage analysis, at the end of the fourth stage of excavation the values of $\sqrt{J_2}$ around the cavern are much smaller. This seems to indicate that in real caverns which are leached out over a period of time, very high values of $\sqrt{J_2}$, and therefore yielding and failure are unlikely to occur.

Another observation which can be made from Figs. 9 and 18 is that the contours of $\sqrt{J_2}$, which are initially at some distance from the cavern, generally tend to move away from the cavern with time and their shape becomes more spherical. This indicates that, with elapsed time, the effective zone of creep around the cavern becomes larger. Also, it can be noted that after a sufficient period of time and at sufficient distances from the cavern, the medium behaves as though the shape of the cavern is spherical.

Simulation of Tightness Pressure Test

The objective of a tightness pressure test is to determine whether the salt surrounding a cavern is sufficiently free of fractures that the cavern can be used for the purpose of storage. The tightness pressure test is conducted by increasing the wellhead pressure by pumping in brine and determining whether the wellhead pressure can be maintained for a period of time, usually a few days. Usually, the wellhead pressure is increased to 90% of the in-situ stress at the depth above which the pipe is grouted.

During the tightness pressure test, the volume of the cavern is also changing due to creep by the increase in the internal pressure. The role of the creep volume change in a pressure test has not been thoroughly studied. The amount of brine which is pumped into a cavern during a pressure test not only represents the brine which may be lost through fractures or other causes, but must also compensate the volume changes in a cavern due to creep deformations.

To study the relative importance of the creep deformations, a pressure test was simulated in cavern 1. In this analysis, first the leaching out of the cavern was simulated in four stages over 2 yr, as described in the previous section, and then the cavern was allowed to creep for five and one half additional years, with an internal pressure resulting from a column of brine. At $t = 7.5$ yr, the tightness pressure test was simulated by instantaneously increasing the internal pressure by 713 psi (4,913 kPa). This increased pressure was maintained for 60 days.

The increased internal pressure caused an instantaneous elastic volume increase of the cavern of about 55,000 bbl (8,800 m^3). This was followed by a gradual outward displacement of cavern roof, floor, and walls. Due to creep of the salt, the cavern roof and floor continue to move outward for about 10 days,

and then they reverse direction and start moving inward, as they would under normal conditions.

The creep volume increase of the cavern with elapsed time is shown in Fig. 19. It can be seen that maximum volume increase is about 960 bbl (151 m^3). However, 800 bbl (126 m^3) of this volume increase occurs within 1 h. The various volume changes are tabulated below.

$$\left.\begin{array}{l}\text{wellhead pressure increase} = 713 \text{ psi } (4{,}913 \text{ kPa}) \\ \text{volume decrease of the brine in the cavern} = 3{,}900 \text{ bbl } (624 \text{ m}^3) \\ \text{instantaneous elastic volume increase} = 55{,}000 \text{ bbl } (8{,}600 \text{ m}^3) \\ \text{maximum creep volume increase} = 960 \text{ bbl } (154 \text{ m}^3) \\ \text{creep volume increase in 1 h} = 800 \text{ bbl } (128 \text{ m}^3)\end{array}\right\} \quad \ldots . \quad (16)$$

In reality, to increase the wellhead pressure by 713 psi (4,913 kPa), sufficient brine must be pumped in to overcome a 3,900 bbl (624 m^3) volume decrease of the brine and 55,000 bbl (8,800 m^3) instantaneous elastic volume increase of the cavern. Obviously, it will take more than 1 h to pump in that much brine. Thus, at least the first hour creep volume change must be included in the volume of brine required to raise the wellhead pressure by 713 psi (4,913 kPa). The remaining creep volume change of 960 − 800 = 160 bbl (26 m^3) would cause pressure changes if the valves were closed and no additional brine

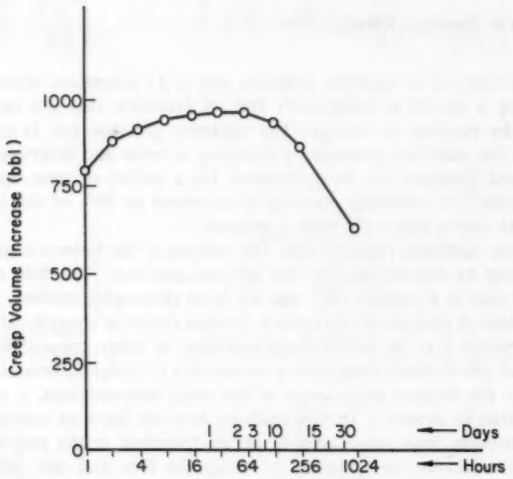

FIG. 19.—Volume Change of Cavern 1 During Pressure Test (1 barrel = 0.16 m^3)

was allowed in or out of the cavern. This would correspond to a volumetric strain of $160/12{,}400{,}000 = 1.3 \times 10^{-5}$ in the brine. Assuming the bulk modulus of brine to be 4×10^5 psi (2.8×10^6 kPa), the maximum pressure change during a 10 day pressure test due to creep would be $1.3 \times 10^{-5} \times 400{,}000 = 5.2$ psi (35.8 kPa), or less than 1% of the test pressure. This analysis seems to indicate that creep deformations have no significant influence on the results of the tightness pressure test for the cavern analyzed.

However, it must be emphasized that the above conclusion is only valid for the cavern which was analyzed. In general, the following factors will have a significant influence on the results of the simulation analyses of the tightness pressure test.

1. Cavern shape; mainly the height-to-diameter ratio.
2. Cavern depth.
3. Recent past pressure history; whether the cavern has been subjected to significant pressure changes in the recent past.

In order to arrive at a more general conclusion regarding the influence of the creep deformations on the tightness pressure test results, these factors must be systematically analyzed.

Acknowledgment

The financial support of the Solution Mining Research Institute, Inc., Flossmoor, Ill., is gratefully acknowledged.

Appendix.—References

1. Boresi, A. P., and Deere, D. U., "Creep Closure of a Spherical Cavity in an Infinite Medium," Report to Homes and Narver, Inc., May, 1963.
2. Bradshaw, R. L., Boegly, W. J., and Empson, F. M., "Correlation of Convergence Measurements in Salt Mines with Laboratory Creep-Test Data," *Proceedings of the Sixth Symposium on Rock Mechanics*, Rolla, Mo., Aug., 1964.
3. Hermann, W., Wawersik, W. R., and Lauson, H. S., "Creep Curves and Fitting Parameters for Southeastern New Mexico Bedded Salt," *Report SAND-80-0087*, Sandia Laboratories, Albuquerque, N.M., Mar., 1980.
4. Lomenick, T. F., and Bradshaw, R. L., "Deformation of Rock Salt in Openings Mined for the Disposal of Radioactive Wastes," *Rock Mechanics*, Vol. 1, No. 3, 1969, pp. 5–30.
5. Maxwell, D. E., Wahi, K. K., Reaugh, J. E., and Hofmann, R., "A Time-Dependent Creep Model for Salt," *The Fifth International Symposium on Salt*, Hamburg, Germany, May, 1978.
6. Nickell, R. E., "Rock Salt Constitutive Modelling," *Report UCRL-15207*, Lawrence Livermore National Laboratory, Livermore, Calif., Mar., 1980.
7. Obert, L. E., "Deformational Behavior of Model Pillars Made from Salt, Trona and Potash Ore," *Proceedings of the Sixth Symposium on Rock Mechanics*, Rolla, Mo., Aug., 1964.

ROAD ON PEAT: OBSERVATIONS AND DESIGN

By Edward T. Hanrahan,[1] and Martin G. Rogers[2]

INTRODUCTION

A road in County Offaly, Ireland, from Edenderry to Rathangan, located on a peat bog of average depth 25 ft (7.6 m) was reconstructed during the period between August 1953 and March, 1954. The thickness of gravel base, originally 12 in. (305 mm) was to be increased to 2.5 ft (0.8 m). The control of the thickness of gravel proved to be difficult, and excessive quantities were used in certain locations resulting in serious consequences in the form of settlement, upheaval, and lateral spread. Over three lengths in particular, 3,630–3,820 ft (1,107–1,165 m); 3,905–4,090 ft (1,191–1,247 m), and 4,630–4,783 ft (1,412–1,459 m), the rate of deformation was of such magnitude that it was decided to adopt the expedient of preconsolidation (5) i.e., to remove part of the gravel and replace it with light-weight bales of compressed horticultural peat.

The bales, each 3.28 ft × 2.19 ft × 1.64 ft (1 m × 0.67 m × 0.5 m) were placed in one, two, or three layers respectively, as shown in Figs. 1 and 2. Remedial measures were complete before November 1954. Road levels were taken during the ensuing period of nearly 26 years, and there is now an excellent opportunity to compare predicted and observed values of settlement.

An investigation by means of ten trial holes was undertaken in July, 1962 to determine the thickness of gravel base and the condition of the peat bales after eight years of submergence. At the same time, a comprehensive laboratory investigation was carried out to make a general study of the behavior of peat under load. A simple method of predicting settlements was formulated and a comparison was made with the settlements which had occurred up to that date. This study was published (6).

It was observed that in the baled sections which, during construction, had proved to be the weakest sections, the road was stable and in good shape. Elsewhere, it was badly distorted, and has since required continuous addition of material to maintain its surface. A further investigation was made in March,

[1]Assoc. Prof. of Civ. Engrg., University College, Dublin, Ireland.
[2]Research Student, University College, Dublin, Ireland.

Note.—Discussion open until March 1, 1982. To extend the closing date one month, a written request must be filed with the Manager of Technical and Professional Publications, ASCE. Manuscript was submitted for review for possible publication on September 4, 1980. This paper is part of the Journal of the Geotechnical Engineering Division, Proceedings of the American Society of Civil Engineers, ©ASCE, Vol. 107, No. GT10, October, 1981. ISSN 0093-6405/81/0010-1403/$01.00.

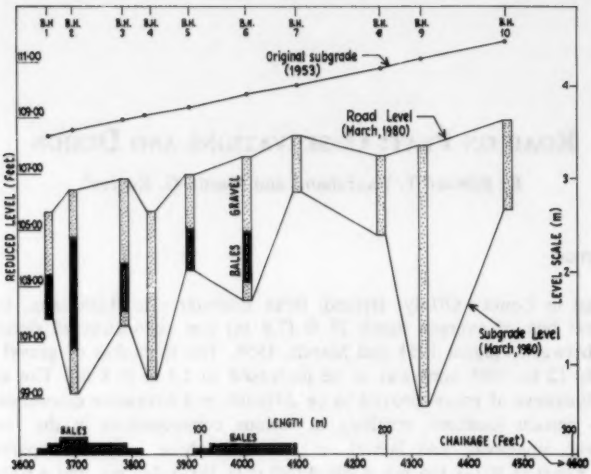

FIG. 1.—Longitudinal Section

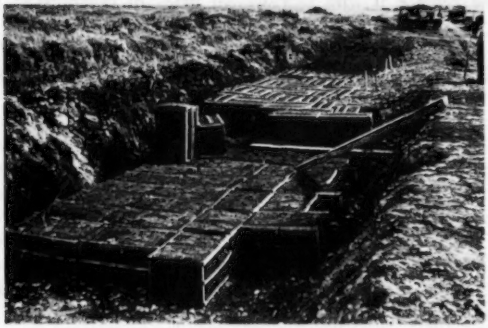

FIG. 2.—Method of Placing Bales

1980, mainly for the purpose of determining the thickness of construction at each of the ten previous locations.

Simple Design Method

A simple design method was proposed in 1964, and this has since been used successfully on a wide range of compressible soils (11). Briefly, it requires settlement to be separately evaluated under three headings and the results combined to give total settlements.

Elastic Settlement.—Various formulas and charts based on Young's modulus

and Poisson's ratio, are available for elastic analysis. Direct measurement of elastic settlement was made during the 1964 investigation using plane strain deformation in a model tank. If it is assumed that the elastic properties are proportional to the shear strength, the elastic settlement (stiff strip) may then be computed from the simple formula

$$y_e = \frac{0.02\,B\,q}{s} \quad \ldots\ldots\ldots\

Consolidation Settlement.—Consolidation settlement is measured with the oedometer apparatus and requires that a number of similar specimens be tested under a range of loadings. Each load is applied as a single increment. The wellknown H^2 time-scaling method, based on the Terzaghi equation of one-dimensional consolidation, proposed by Hanrahan (5,6), is used for forecasting field settlements. The method is especially useful for soils such as peat, the properties of which change significantly under load and time.

Firstly, the laboratory curve relating vertical strain and time is established (Fig. 3). For forecasting field behavior, the time scale is then altered in the ratio $(D/d)^2$ in which D = maximum length of drainage path in field; and d = maximum length of drainage in laboratory. It is generally understood that this method is not applicable in the so-called secondary phase of consolidation. This does not correlate with this author's experience.

If the loading does not remain constant, a simple method of curve-hopping is used, as illustrated in the following example. Suppose it is required to forecast the field settlement of a stratum (D) under a unit load x for a time t, subsequent to which the loading is to be increased to y for a time interval Δt. Two single-increment oedometer curves (d) ABC and DEF, (Fig. 4), are required. The field-time scale is established by correcting the laboratory scale by the ratio $(D/d)^2$. The strain produced by the load x at time t is then shown at the point B. The total strain produced at time $t + \Delta t$ by the loading sequence is given by the point F. The method of curve-hopping is valid both for increasing and decreasing loads.

Creep Settlement.—This important type of settlement is taken into account in the formula

$$y_p = 10^{-4}\left[21\left(\frac{q}{s}\right)^3 + 39\left(\frac{q}{s}\right)^{1.78} \log t\right]\frac{B}{s} \quad \ldots\ldots\ldots\ldots\ldots\ldots (2)$$

in which y_p = creep settlement (m); B = width of loaded strip (m); q = unit load on strip (kPa); and s = undrained shear strength (kPa).

This equation is the result of a regression analysis of a family of curves (6). Eq. 2 may also be used when either the loading or the time is a variable. For example, suppose that the creep settlement is known at the start of a time increment Δt, during which a load x is in operation. Clearly, this settlement may have developed under a succession of previous loads of different values. Eq. 2 is then used to find an *equivalent time*, t_{eq}. This is the time it would take for the known creep settlement to develop under the single load x. The required settlement at the end of the time interval, Δt, is then found by putting $t = t_{eq} + \Delta t$, and again solving Eq. 2 for a new value of y_p.

Design Data

Design data are used for the application of the simple method to the County Offaly road.

In-Situ Characteristics.—These were previously described (6). The average undrained shear strength was 0.75 psi (5.81 kPa) and the moisture content 1,150%. A relationship between undrained shear strength and moisture content was also

established. To allow for the strengthening which takes place on consolidation, the simple assumption was made that there was a uniform vertical strain, a reduction of moisture content, and an increase of strength throughout the full depth of the stratum. This is the basis of Fig. 5.

Oedometer Settlement Curves.—Fig. 6 shows three curves relating vertical strain in the oedometer with time, obtained using a standard 76 mm diam specimen, over a time period of 1,000 min, for three different loads. Curves for other loads may be interpolated, as shown (6).

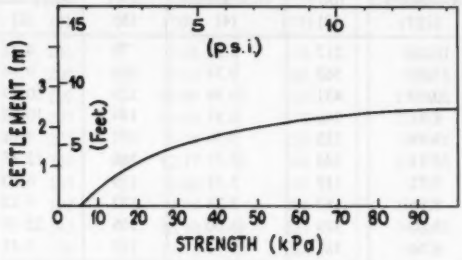

FIG. 5.—Relationship Between Settlement and Average Strength of Peat

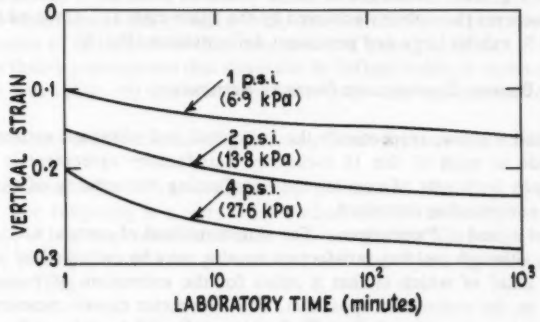

FIG. 6.—Oedometer Curves Showing Effect of Varying Loads

Width of Loaded Strip.—(assumed stiff) = 6.4 m.

Thickness of Peat Layer.—= 25 ft (7.6 m). The peat stratum was underlain by impermeable glacial till, and the maximum drainage path was, therefore, taken equal to the thickness of the peat stratum. Thus, 1 min laboratory time was equivalent to 438 days field time.

Loading.—Table 1 shows the loadings which were in operation since construction, between 3,500 and 9,500 days. Any change in loading was assumed to be caused by periodic maintenance, and observed increases in thickness were applied in four equal increments at 3,500, 5,000, 6,500, and 8,000 days respectively.

TABLE 1.—Loadings in

Location (1)	LOADS					
	0–100 days		100–3,500 days		3,500–5,000 days	
	In kilopascals (2)	In pounds per square foot (3)	In kilopascals (4)	In pounds per square foot (5)	In kilopascals (6)	In pounds per square foot (7)
1	10.18	212	3.36	70	4.22	88
2	27.02	563	9.74	203	9.74	203
3	20.69	431	10.99	229	10.99	229
4	6.91	144	6.91	144	10.56	220
5	15.98	333	9.74	203	9.74	203
6	26.11	544	12.77	266	12.77	266
7	5.71	119	5.71	119	6.10	127
8	8.74	182	8.74	182	9.12	190
9	18.00	375	18.00	375	22.08	460
10	8.74	182	8.74	182	9.41	196

The changes in loading at 100 days was due to the substitution of the lightweight bales for the gravel. Reference to baled sections, such as at trial holes 2, 3, 5, and 6, confirms the stability achieved by the lightweight fill. Unbaled sections, e.g., 4 and 9, exhibit large and persistent deformations (Fig. 8).

Comparison Between Computed and Observed Settlements

Figs. 7 and 8 show, respectively the computed and observed settlements of the subgrade at each of the 10 locations. Satisfactory agreement is seen to exist between both sets of curves, thus confirming the validity of the simple method of computation described.

Method of e_g and e_k Parameters.—The simple method of computation outlined previously, although yielding satisfactory results, may be criticized on a number of counts, chief of which is that it relies for the estimation of consolidation settlement on the oedometer apparatus. The oedometer cannot measure lateral strains, and does not give essential information on the lateral stresses. These were shown (10,11) to vary with time, size of specimen, and location of element in a stratum. The importance of varying stresses was clearly demonstrated by Biot (1) in his equation

$$\frac{\partial u}{\partial t} = C \nabla^2 u + \frac{1}{3} \frac{\partial \theta}{\partial t} \quad \ldots\ldots\ldots\ldots\ldots\ldots\ldots\ldots\ldots\ldots\ldots\ldots\ldots\ldots (3)$$

in which u = excess pore pressure; c = coefficient of consolidation; ∇ = La Place operator; and $\theta = \sigma_1 + \sigma_2 + \sigma_3$.

Unfortunately, Biot's equation is also unsatisfactory, for the following reasons:

1. Solutions are available for only a few cases, Gibson and McNamee 1957,

Operation since Construction

5,000–6,500 days		6,500–8,000 days		8,000–9,500 days	
In kilopascals (8)	In pounds per square foot (9)	In kilopascals (10)	In pounds per square foot (11)	In kilopascals (12)	In pounds per square foot (13)
5.09	106	5.95	124	6.82	142
9.74	203	9.74	203	9.74	203
10.99	229	10.99	229	10.99	229
14.26	297	17.90	373	21.60	450
9.74	203	9.74	203	9.74	203
12.77	266	12.77	266	12.77	266
6.48	135	6.86	143	7.20	150
9.50	198	9.89	206	10.27	214
26.06	543	30.10	627	34.18	712
10.08	210	10.75	224	11.42	238

De Jong 1957, Davis and Poulos 1972, Smith and Hobbs 1976.

2. The theory is confined to ideally elastic materials of constant properties.
3. The equations do not permit a ready conversion of pore pressure necessary for estimates of settlement to the components of principal strain.
4. The theory presupposes that strain can be defined solely in terms of effective stress. It was shown (9) that this is possible only with an equal all-round stress system.
5. The theory is defective in its ignorance of time-dependent distortional strain.

Most of these defects are eliminated by the method of the e_g, e_k parameters (7,9,11). The following is a very brief outline of this method: Total principal strains e_1, e_2, e_3 are subdivided into two categories. These are termed the e_g and e_k principal strains (or parameters) and are separately measured in the laboratory. Thus

$$\begin{vmatrix} e_1 & 0 & 0 \\ 0 & e_2 & 0 \\ 0 & 0 & e_3 \end{vmatrix} = \begin{vmatrix} e_{g1} & 0 & 0 \\ 0 & e_{g2} & 0 \\ 0 & 0 & e_{g3} \end{vmatrix} + \begin{vmatrix} e_{k1} & 0 & 0 \\ 0 & e_{k2} & 0 \\ 0 & 0 & e_{k3} \end{vmatrix} \quad \ldots\ldots\ldots\ldots (4)$$

Both categories are time-dependent, but have different time rates. Essentially, the e_k strains are those which can develop only under drained conditions. Their rate is determined by the consolidation (diffusion) process. The e_g strains can occur in both drained and undrained conditions. Only in saturated and non-dilatant soils are the e_g strains synonymous with distortional strains. In other soils they include a component of volumetric strain, although in soft compressible soils the latter is usually negligible. The rate at which the e_g strains develop is governed by the rheological properties of the soil. Unlike the e_k strains, this rate is

independent of the size or drainage path of the specimen or element.

Fig. 9 shows a diagrammatic representation of both types of strain for a system of axisymmetric principal stresses. To illustrate the important continuous interaction of both types of strain, the special condition of one-dimensional

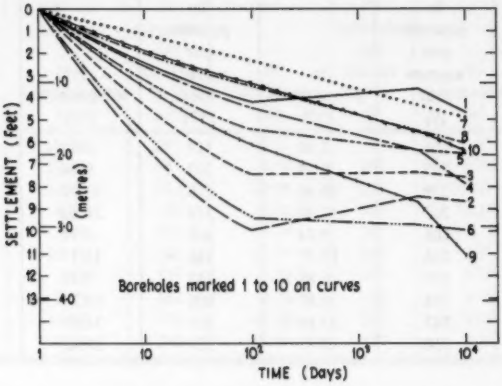

FIG. 7.—Computed Settlements at Ten Locations Using Simple Method

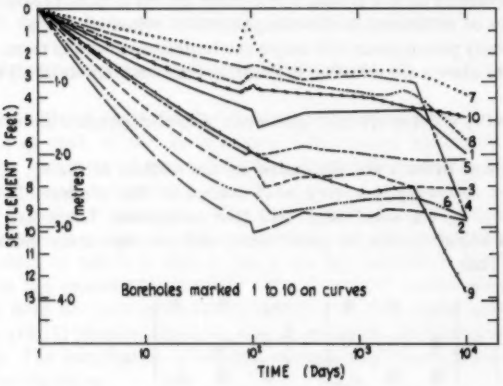

FIG. 8.—Observed Settlements at Ten Locations

consolidation may be examined. This is expressed

$$\sigma_1 > \sigma_2 = \sigma_3 \quad \ldots\ldots (5)$$

$$e_1 > e_2 = e_3 = 0 \quad \ldots\ldots (6)$$

The equality $e_3 = 0$ is better described (Fig. 9) by

$$e_{g3} = e_{k3} \quad \text{for all} \quad t, z \quad \ldots\ldots\ldots\ldots\ldots\ldots\ldots\ldots\ldots\ldots\ldots\ldots\ldots\ldots\ldots\ldots (7)$$

in which t = time; and z = depth.

Eq. 7 implies a continuous equality between two types of strain of opposite sign. But, under a constant stress system, the two types are known to develop at different rates. Therefore, in circumstances where the strains cannot develop in full freedom, the stress system is subject to continuous change. This has been demonstrated experimentally (10). The lateral stress has also been shown to vary with size of specimen and location of element in a stratum. The special advantage of the method is that it permits a continuous evaluation of the lateral stress, σ_3 (11). For one-dimensional consolidation, essentially two laboratory-measured relationships, F_1, F_2 are required.

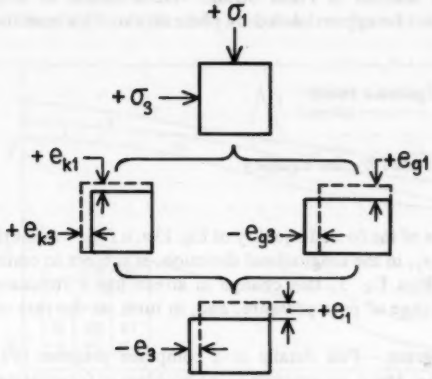

FIG. 9.—Diagrammatic Representation of e_g, e_k Principal Strains

The first, F_1, is based, using an undrained triaxial specimen, on observation with time of the e_{g3} strain for a range of values of principal stress-difference. It may be written

$$e_{g3} = F_1 [(\sigma_1 - \sigma_3), t] \quad \ldots\ldots\ldots\ldots\ldots\ldots\ldots\ldots\ldots\ldots\ldots\ldots\ldots\ldots\ldots\ldots (8)$$

The second relationship, F_2, is based on the observation, with time of the volume change of a radially drained triaxial specimen under a range of values of effective stress. Equal all-round stresses are employed, thereby avoiding the complication of distortional strain. For applying the measurements, if the stress is equal in the three principal directions, the e_k strain may be taken to be one-third the volumetric strain. If unequal, correction factors σ_1/σ_{oct}, σ_2/σ_{oct}, σ_3/σ_{oct} are applied for each of the three principal directions, respectively (8).

Field rates of strain may be computed from the laboratory rates by applying consolidation theory. It is then possible to write

$$e_{k3} = F_2(\sigma_{oct}, \sigma_3, t) \quad \ldots\ldots\ldots\ldots\ldots\ldots\ldots\ldots\ldots\ldots\ldots\ldots\ldots\ldots\ldots\ldots (9)$$

In a typical example of one-dimensional consolidation, the following are usually known or specified quantities: (1) Vertical pressure, σ_1; (2) time, t; and (3) pore pressure, u. The latter is a dependent variable of the specified time. Hence, combining Eqs. 8 and 9 in the equality

$$e_{g3} = e_{k3} \quad \ldots \quad (10)$$

the lateral stress, σ_3, may be solved at all values of time and depth below surface.

Having thus fully defined the stress, it is possible to solve all the remaining e_g and e_k strain components by using relationships similar to Eqs. 8 and 9. Finally, using Eq. 4, the total strains may be determined and the settlement evaluated.

Application of Method to Plane Strain.—Deformation of soil under a long strip load may best be approximated by plane strain. This condition is described

$$e_1 = e_{g1} + e_{k1} \quad \ldots \quad (11)$$

$$e_3 = e_{g3} + e_{k3} \text{ (algebraic sum)} \quad \ldots \quad (12)$$

$$e_2 = 0 \quad \ldots \quad (13)$$

Eq. 13 is better stated by the equality

$$e_{g2} = e_{k2} \quad \ldots \quad (13a)$$

As a consequence of the forced equality of Eq. 13*a*, it follows that the intermediate principal stress, σ_2, in the longitudinal direction, is subject to continuous change. As seen in the Biot Eq. 3, this change in stress has a fundamental influence on the rate of change of pore pressure, and, in turn, on the rate of consolidation settlement.

Computer Program.—Full details of a computer program (PLANE) for the application of the e_g and e_k parameters to the problem of forecasting the settlement of a road are available (12). A few comments may be made:

1. Initial stresses and pore pressures are determined from elastic theory and the equation by Scott, (13) (Eqs. 6–62, p. 272), respectively.
2. The time is subdivided into intervals, during each of which the pore pressure is assumed to dissipate while the applied stresses remain constant. The term $\partial\theta/\partial t$ in Eq. 3 is, therefore, zero.
3. At the end of each interval, the change in total stress which is required to satisfy Eq. 13*a*, is estimated, and a corresponding correction made to the pore pressure in accordance with the equation of Scott, (13).

Computer Data for County Offaly Road

The following are the data used for the application of the program (PLANE) to the Offaly road.

e_g Data.—A regression analysis of a family of curves, obtained by testing undrained triaxial specimens under an axisymmetric stress system, yielded the relationship

$$e_{g1} = 14.85\left(\frac{\tau}{\tau_f}\right)^{1.43} + 2.35\left(\frac{\tau}{\tau_f}\right)^{0.9} \cdot \log t \quad \ldots \quad (14)$$

It will be noted that the principal stress-difference $(\sigma_1 - \sigma_3)$ is here expressed in the dimensionless form, τ/τ_f (8), in which $2\tau = (\sigma_1 - \sigma_3)$; and $2\tau_f = (\sigma_1 - \sigma_3)$ at failure. The assumption of constant volume during undrained shear is reasonably valid for peat. Hence

$$e_{g3} = \frac{1}{2} e_{g1} \quad \ldots \quad (15)$$

The variation in shear strength with moisture-content is expressed by the relationship

$$\tau_f = 3.5\left(10\frac{\Delta v}{649}\right) \quad \ldots \quad (16)$$

in which τ_f = shearing strength (kPa); and Δv = loss in volume, in cc of

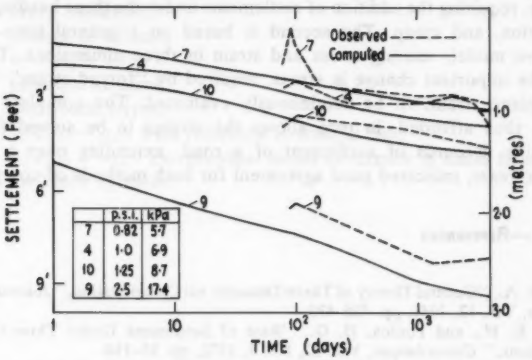

FIG. 10.—Comparison Between Observed and Computed Settlements Based on Method of e_g and e_k Parameters at Four Locations

triaxial specimen initially 76 mm by 38 mm diameter, at initial moisture-content, 1,150%. For convenience, the e_g parameters are measured in the laboratory using an axisymmetric system of stresses. For use with a nonequal system they must be corrected. The factor to be used is obtained by comparing the extended form of both the axisymmetric and three-dimensional stress tensors. For example

$$e_{g2} = e_{g3(a)} \frac{2\sigma_2 - \sigma_3 - \sigma_1}{\sigma_3 - \sigma_1} \quad \ldots \quad (17)$$

in which e_{g2} = required value for nonequal three-dimensional stress system; and $e_{g3(a)}$ = value of e_{g3} from Eq. 15.

e_k Data.—Data can be expressed by the formula

$$\Delta v = 3.01\,(\bar{\sigma}_{oct})^{0.768} \quad \ldots \quad (18)$$

in which Δv = loss in volume (cc) of triaxial specimen, initially 76 mm by 38 mm diameter at initial moisture-content, 1,150%. And, $c_v = 38$ in which c_v = coefficient of consolidation (mm^2/min).

Comparison Between Observed and Computed Settlements.—Fig. 10 shows a comparison between the observed values of settlement and values obtained using the e_g and e_k parameters, from four locations. The level of agreement is not noticeably better than that shown in Figs. 7 and 8, which is based on the simple method. Nevertheless, the agreement is satisfactory. The availability of the computer program PLANE makes the application of this method simple and convenient.

Summary and Conclusions

Two methods of evaluating settlement are described. The first is a simple procedure, requiring the addition of settlements under the three headings, elastic, consolidation, and creep. The second is based on a general time-dependent constitutive model, relating stress and strain in three dimensions. This model permits the important change in stress, required by "forced strain" conditions such as plane strain, to be continuously evaluated. The complete definition of stress, thus afforded, in turn allows the strains to be solved from basic relationships. Records of settlement of a road, extending over a period of twenty-six years, indicated good agreement for both methods of computation.

Appendix I.—References

1. Biot, M. A., "General Theory of Three-Dimensional Consolidation," *Journal of Applied Physics*, Vol. 12, 1941, pp. 426–430.
2. Davis, E. H., and Poulos, H. G., "Rate of Settlement Under Three-Dimensional Conditions," *Geotechnique*, Vol. 22, No. 1, 1972, pp. 95–114.
3. de Jong, G., de J., "Application of Stress Functions to Consolidation Problems," *Proceedings of the Fourth International Conference SMFE*, 1957, pp. 320–323.
4. Gibson, R. E., and McNamee, J. J., "Consolidation of a Load Uniformly Distributed on a Rectangular Area," *Proceedings of the Fourth International Conference SMFE*, Vol. 1, 1957, pp. 297–300.
5. Hanrahan, E. T., "Roads on Soft Soils," *Proceedings of the Ninth International Roads Congress*, 1951, Lisbon, Spain.
6. Hanrahan, E. T., "A Road Failure on Peat," *Geotechnique*, Vol. 14, 1964, pp. 185–202.
7. Hanrahan, E. T., "Analyzing Strain in a Real Solid," *Civil Engineering Public Works Review*, March, 1968, London, England.
8. Hanrahan, E. T., "The e_g and e_k Parameters," *Proceedings of the Roscoe Symposium*, Foulis & Co. Ltd., Cambridge University, 1971.
9. Hanrahan, E. T., "The Stress-Strain-Time Relationship in Soil," An Foras Forbartha St. Martin's House, Waterloo Road, Dublin 4, 1974.
10. Hanrahan, E. T., "Lateral Stress in One-Dimensional Consolidation," *Proceedings of the Ninth International Conference SMFE*, Tokyo, 1977.
11. Hanrahan, E. T., "Irish Compressible Soils," An Foras Forbarths, St. Martin's House, Waterloo Road, Dublin 4, 1979.
12. Rogers, M. G., "Analysis of Consolidation Problems," thesis presented to the University College, Dublin 2, 1980.
13. Scott, R. F., "Principles of Soil Mechanics," Addison-Wesley, 1963, Reading, Mass.
14. Smith, I. M., and Hobbs, R., "Biot Analysis of Consolidation," *Geotechnique*, Vol. 26, No. 1, 1976, pp. 149–171.

Appendix II.—Notation

The following symbols have been used in this paper:

B = width of strip load;
c_v = coefficient of consolidation;
D = maximum length of drainage path in field;
d = maximum length of drainage path in laboratory;
$e_{1,2,3}$ = principal strains;
e_g, e_k = principal strain parameters;
q = unit load on strip;
s = undrained shear strength of soil;
t = time;
u = excess pore pressure;
y_e = elastic settlement;
y_p = creep settlement;
Δv = change in volume;
θ = $\sigma_1 + \sigma_2 + \sigma_3$;
$\sigma_{1,2,3}$ = principal stresses;
σ_{oct} = octahedral stress;
τ = $1/2(\sigma_1 - \sigma_3)$, with reference to triaxial test;
τ_f = $1/2(\sigma_1 - \sigma_3)_f$, i.e. principal stress difference at shear failure; and
∇ = La Place operator.

TECHNICAL NOTES

Note.—Discussion open until March 1, 1982. To extend the closing date one month, a written request must be filed with the Manager of Technical and Professional Publications, ASCE. This paper is part of the Journal of the Geotechnical Engineering Division, Proceedings of the American Society of Civil Engineers, ©ASCE, Vol. 107, No. GT10, October, 1981.

Technical Notes

To provide a place within ASCE for publication of technical ideas that have not advanced, as yet, to the point where they warrant publication as a Proceedings paper in a *Journal*, the publication of Technical Notes was authorized by the Board of Direction on October 16–18, 1967, under the following guidelines:

1. An original manuscript and two copies are to be submitted to the Manager of Technical and Professional Publications, ASCE, 345 East 47th Street, New York, N.Y., 10017, along with a request by the author that it be considered as a Technical Note.
2. The two copies will be sent to an appropriate Technical Division or Council for review.
3. If the Division or Council approves the contribution for publication, it shall be returned to Society Headquarters with appropriate comments.
4. The technical publications staff will prepare the material for use in the earliest possible issue of the *Journal*, after proper coordination with the author.
5. Each Technical Note is not to exceed 4 pages in the *Journal*. As an approximation, each full manuscript page of text, tables, or figures is the equivalent of one-half a *Journal* page.
6. The Technical Notes will be grouped in a special section of each *Journal*.
7. Information retrieval abstracts and key words will be unnecessary for Technical Notes.
8. The final date on which a Discussion should reach the Society is given as a footnote with each Technical Note.
9. Technical Notes will not be included in *Transactions*.
10. Technical Notes will be included in ASCE's annual and cumulative subject and author indexes.

The manuscripts for Technical Notes must meet the following requirements:

1. Titles must have a length not exceeding 50 characters and spaces.
2. The author's full name, Society membership grade, and a footnote reference stating present employment must appear on the first page of the manuscript. Authors need not be Society members.
3. The manuscript is to be submitted as an original copy (with two duplicates) that is typed double-spaced on one side of 8-1/2-in. (220-mm) by 11-in. (280-mm) white bond paper.
4. All mathematics must be typewritten and special symbols must be properly identified. The letter symbols used must be defined where they first appear, in figures or text, and arranged alphabetically in an Appendix.—Notation.
5. Standard definitions and symbols must be used. Reference must be made to the lists published by the American National Standards Institute and to the *Authors' Guide to the Publications of ASCE*.
6. Tables must be typed double-spaced (an original ribbon copy and two duplicate copies) on one side of 8-1/2-in. (220-mm) by 11-in. (280-mm) paper. An explanation of each table must appear in the text.
7. Figures must be drawn in black ink on one side of 8-1/2-in. (220-mm) by 11-in. (280-mm) paper. Because figures will be reproduced with a width of between 3 in. (76 mm) to 4-1/2 in. (110 mm), the lettering must be large enough to be legible at this width. Photographs must be submitted as glossy prints. Explanations and descriptions must be made within the text for each figure.
8. References cited in text must be typed at the end of the Technical Note in alphabetical order in an Appendix.—References.
9. Dual units, i.e., U.S. Customary followed by SI (International System) units in parentheses, should be used throughout the paper.

Instrumentation Corrections to Wave Velocity Data

By John R. Hall, Jr.,[1] M. ASCE, John T. Christian,[2] F. ASCE, Eduardo Kausel,[3] A. M. ASCE, and James L. Wolfgang[4]

The detection of the arrival of seismic stress waves for a field measurement of wave velocity requires that the incoming signal be recorded and displayed by an instrument such as a seismograph. Filters, introduced into recording circuits to limit noise or to prevent aliasing in digital recording, can have significant effects on the observed arrival times and on the computation of wave velocity. Such filtration is often not taken into account in processing the data, but the example that follows indicates how the effects can be evaluated and the data corrected by simple techniques. The properties of electronic filters are, of course, well known to electrical engineers, and the following comments are concerned with an application in which their importance has not always been appreciated by those trained in other disciplines.

Filter Characteristics and Effects

One widely used recorder is the Bison Model 1580, the filter of which is composed of two first-order, low-pass, Butterworth filters cascaded in series, having cutoff frequencies of 160 Hz and 89 Hz, respectively. The ratio of the output voltage to the input voltage for a unit gain first-order, low-pass, Butterworth filter is

$$\frac{E_o}{E_i} = \frac{1}{\sqrt{1 + \left(\frac{f}{f_c}\right)^2}} \quad \ldots\ldots\ldots\ldots\ldots\ldots\ldots\ldots\ldots\ldots\ldots\ldots\ldots\ldots (1)$$

in which E_o = output voltage amplitude; E_i = input voltage amplitude; f = signal frequency in Hertz, f_c = filter cutoff frequency in Hertz. The phase angle, θ, is given by:

[1]Sr. Consulting Engr., Stone & Webster Engrg. Corp., Boston, Mass.
[2]Sr. Consulting Engr., Stone & Webster Engrg., Corp., Boston, Mass.
[3]Assoc. Prof. of Civ. Engrg., Massachusetts Inst. of Tech., Cambridge, Mass.; formerly, Consultant, Stone & Webster Engrg. Corp., Boston, Mass.
[4]Geologist, Stone & Webster Engrg. Corp., Cherry Hill, N.J.

Note.—Discussion open until March 1, 1982. To extend the closing date one month, a written request must be filed with the Manager of Technical and Professional Publications, ASCE. Manuscript was submitted for review for possible publication on March 11, 1981. This paper is part of the Journal of the Geotechnical Engineering Division, Proceedings of the American Society of Civil Engineers, ©ASCE, Vol. 107, No. GT10, October, 1981. ISSN 0093-6405/81/0010-1419/$01.00.

$$\tan\theta = \frac{f}{f_c} \quad \ldots\ldots\ldots\

will be seen that with increasing frequency there is a decrease of amplitude and an increase of phase angle. Because the time lag is equal to the phase angle divided by the frequency, Δt decreases as frequency increases. The waves measured in the example given below had a predominant frequency from 100 Hz to 200 Hz. For $f = 100$ Hz, the phase angle is 80.3°, and the time lag is 2.23 msec.

Transient Signals.—The signals transmitted in wave velocity measurements are not simple sinusoids. However, since the system is linear, it is possible to find the solution to transient signals by means of the Duhamel integral.

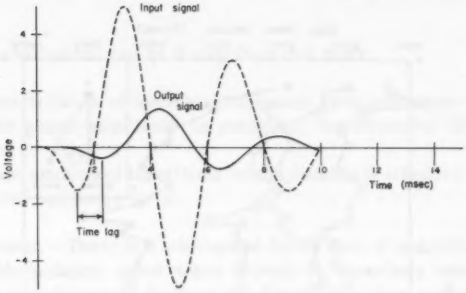

FIG. 2.—Response of Filter to Typical Transient Wave Form

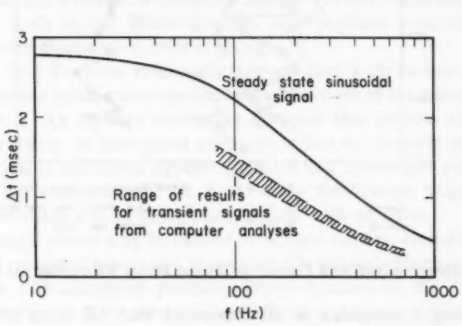

FIG. 3.—Time Lag Caused by Filter for Transient and Steady State Conditions

A typical result is shown in Fig. 2, where the time lag can be seen clearly. The shape of the wave form and its dominant frequency were varied to obtain the values of time lag for a range of transient signals as plotted in Fig. 3, which also shows the steady state time lag for comparison. The results between 100 Hz and 200 Hz indicate that time lags from 0.8–1.2 msec can be expected.

Example.—A recent field determination of shear wave velocity by cross-hole measurements in a competent rock was performed using three borings to a depth of over 300 ft. The energy was imparted to the walls of the holes by

a Bison Model 1465 hammer. The Bison 1580 seismograph was used to record all signals. The surface configuration of the holes is shown in Fig. 4, but evaluation of verticality indicated considerable horizontal drift in the positions of the holes at depth. Corrected horizontal distances were used in all calculations.

The shear wave velocity was originally computed by assuming no time lags in the seismograph and no delay in the trigger timing. The velocity appeared to increase for longer distances (Fig. 4), a result that indicated significant time delays may have been introduced by the seismograph. Therefore, at each depth a linear regression analysis was made of the travel time versus distance from all three legs of the triangle. The results showed that the mean of the zero

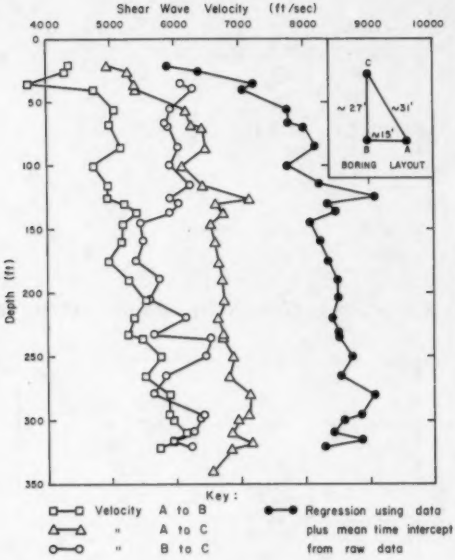

FIG. 4.—Uncorrected and Corrected Shear Wave Velocities for Rock Site

distance intercepts computed at all elevations was 1.0 msec with a standard deviation of 0.3 msec. These values are consistent with those predicted from the filter analysis for a transient wave of similar form to that recorded in the field.

With the mean of 1.0 msec as an additional data point for each elevation, a new linear regression analysis was performed to compute the shear wave velocity profile plotted on the right in Fig. 4. Due to the high velocity of these materials, the difference between the corrected and uncorrected velocities is large. For soil sites, the influence of a 1 msec timing delay would be less significant.

The time lags calculated in the regression analysis of the field data also contain other effects such as errors in picking wave arrivals, delays in transmitting

energy to the soil, and errors in the trigger; but in this case, filtration is the major effect. The agreement between the predicted and calculated time delay induced by the filters lends confidence to the corrected shear wave velocities in Fig. 4. The computed shear wave velocities are affected by errors in the surveys by deviations of the boreholes from the vertical, especially at depths greater than 200 ft (61 m). However, since the values of corrected shear wave velocity show the anticipated gradual increase at depths below 125 ft (38.1 m), the errors in deviation surveys at large depths would seem to be less important than the filtration effects.

Conclusions

Two basic conclusions can be drawn from this work:

1. The characteristics of instrumentation can have important effects on the results of field geophysical tests. In particular, the effects of filtration should not be ignored.
2. Regression analysis of travel time versus distance is effective in determining timing error and correcting for it.

Final Comment.—There is a widespread belief that, if one utilizes a hammer with reversible polarity, shear wave arrivals in cross-hole seismic tests can be identified unambiguously because the direction of first motion in the shear wave reverses when the direction of the impact is reversed. The direction of first motion in the P-wave is assumed not to reverse. Unfortunately, shear wave sources such as the Bison hammer also produce P-waves of opposite polarity when the direction of impact changes.

The reason that P-waves reverse polarity is that a downward excitation of the hammer causes initial compression below the level of the hammer and initial tension above it. An upward excitation reverses this pattern so the P-waves must reverse polarity. A theoretical argument is that in a linearly elastic material, the superposition of equal and opposite upward and downward excitations gives a case of no net excitation. If the P-waves do not reverse polarity, they will not cancel, and there will be energy propagated with no input.

Non-reversing P-waves may be caused by several factors, including late arrivals of reflected or refracted waves and secondary dilatational effects near the source. However, this misconception probably arises because in the down-hole test, shear wave energy is often created by striking a horizontal beam or plate on the surface in opposite horizontal directions. There is almost certainly some downward component to the blow, which does not reverse when the beam is struck in the opposite horizontal direction. This unreversed vertical load causes an unreversing P-wave, which can be observed in field data.

Acknowledgments

Valuable assistance and criticism were provided by T. S. Coughlin, J. H. Mullin, and M. Gaa of Stone & Webster Engineering Corporation.

Total Lateral Surcharge Pressure Due to Strip Load

By Ramon Jarquio,[1] M. ASCE

Introduction

The calculation of lateral surcharge pressure against a vertical retaining wall due to a point load, line load, and strip load is being performed using the modified forms of the Boussinesq's equations. For the strip load type of surcharge, only the equation for the unit lateral surcharge pressure is given (1). It is left to the user to evaluate the total lateral surcharge pressure by mechanical integration procedures which obviously are time-consuming.

This paper is presented to show that a direct solution for the total lateral surcharge pressure can be derived by mathematical manipulation of the variables in the given equation for the unit lateral surcharge pressure. Simplified expressions for the location of the centroid of the total lateral surcharge pressure and the point of maximum unit lateral pressure are also derived to complete the analysis.

Retaining wall structures supporting continuous wall footing, highway, and railroad loadings are practical examples in which strip load type of surcharge is applicable. The calculated total lateral surcharge pressure is then added to other lateral pressures such as earth pressure, water pressure, etc., for stability and structural analysis of the retaining wall structure.

Derivation

Elastic analysis of pressure against unyielding walls from surcharge load (3) is given by

$$\sigma_h = \frac{q}{\pi}(\beta - \sin\beta \cos 2\alpha) \quad \ldots \ldots \ldots

Fig. 1 shows the geometric representation of the variables involved in Eq. 2.

Transform Eq. 2 to a form suitable for integration. To do this, it is necessary to introduce dimensions to the soil wedge and the surcharge load in the rectangular Cartesian coordinates. Fig. 2 shows the notations introduced for this purpose, i.e., make the substitutions thus:

$$\beta = (\theta_a - \theta_b) \quad \ldots \quad (3)$$

$$\alpha = \frac{1}{2}(\theta_a + \theta_b) \quad \ldots \quad (4)$$

$$\sigma_h = x \quad \ldots \quad (5)$$

Put Eqs. 3, 4, and 5 in Eq. 2 to yield

$$x = \frac{2q}{\pi}[(\theta_a - \theta_b) - (\sin\theta_a \cos\theta_a - \sin\theta_b \cos\theta_b)] \quad \ldots \quad (6)$$

For clarity, the notations "β," "α," and "σ_h" are henceforth discarded. Introduce

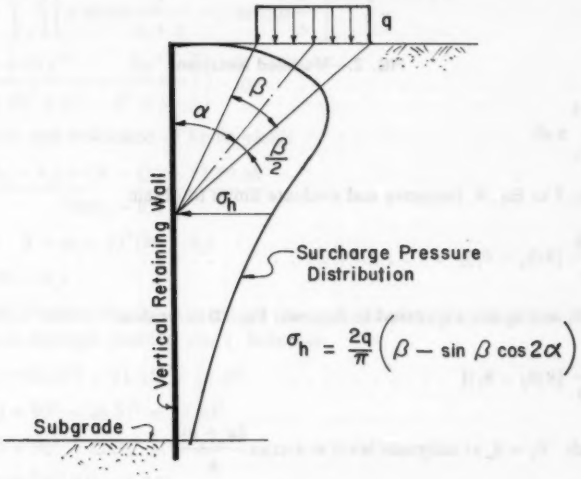

FIG. 1.—Standard Notations

trigonometric functions in terms of dimensions in Eq. 6 to obtain

$$x = \frac{2q}{\pi}\left\{\left[\operatorname{arccot}\frac{y}{a+b} - \operatorname{arccot}\frac{y}{b}\right] - \left[\frac{y}{(a+b)+\dfrac{y^2}{(a+b)}} - \frac{y}{b+\dfrac{y^2}{b}}\right]\right\} \quad (7)$$

Eq. 7 can now be integrated using standard integration formulas (2). Therefore

$$dP = x\,dy \quad \ldots \quad (8)$$

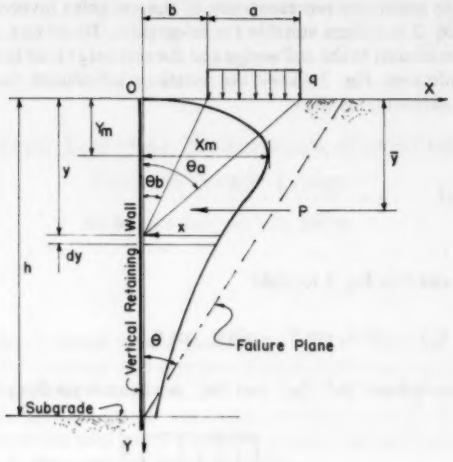

FIG. 2.—Modified Notations

$$P = \int_o^h x\,dy \quad \ldots\ldots\ldots\

$$\theta = \left(45° + \frac{\phi}{2}\right) \quad \ldots\ldots\ldots\

tiating Eq. 7 and equating the first derivative to zero and solving for Y

$$\therefore Y_m = \sqrt{\frac{\sqrt{N^2 + 4MO} - N}{2M}} \quad \ldots\ldots\ldots\ldots\ldots\ldots\ldots\ldots\ldots\ldots (18)$$

in which $M = a^2 + 3b(a + b)$ $\ldots\ldots\ldots\ldots\ldots\ldots\ldots\ldots\ldots\ldots (19)$

$N = 2b^2(a + b)^2$ $\ldots\ldots\ldots\ldots\ldots\ldots\ldots\ldots\ldots\ldots\ldots\ldots (20)$

$O = b^3(a + b)^3$ $\ldots\ldots\ldots\ldots\ldots\ldots\ldots\ldots\ldots\ldots\ldots\ldots (21)$

Example Problem No. 3.—In problem no. 1, determine the point of maximum unit lateral surcharge pressure and calculate its magnitude. Solution:

$M = (6)^2 + (3)(4)(6 + 4) = 156$

$N = (2)(4)^2(6 + 4)^2 = 3{,}200$

$O = (4)^3(6 + 4)^3 = 6{,}400$

Substitute in Eq. 18

$$Y_m = \sqrt{\frac{\sqrt{3200 - 4(156)(6400)} - 3200}{2(156)}}$$

$Y_m = 3.53$ ft (1.08 m)

Substitute this value in Eq. 7 to get the maximum unit lateral surcharge pressure

$$X_m = \frac{2(1{,}000)}{\pi}\left[\frac{\pi}{180}\left(\operatorname{arccot}\frac{3.53}{10} - \operatorname{arccot}\frac{3.53}{4}\right)\right.$$
$$\left. - \left(\frac{10 \times 3.53}{100 + (3.53)^2} - \frac{4 \times 3.53}{16 + (3.53)^2}\right)\right] X_m = 361 \text{ psf } (1{,}762 \text{ kg/sq m})$$

Conclusion

The use of the derived formulas will save the user time in computation of surcharge pressure involving the strip load type of surface load.

The reader should note that the formulas are general solutions considered applicable to yielding or unyielding retaining wall structures with the soil wedge behind it either in the active or passive mode of failure depending on the given condition of the problem. (The complete derivation may be furnished by the author upon request.)

Appendix.—References

1. Bowles, J. E., *Foundation Analysis and Design*, Second Edition, McGraw-Hill Book Company, 1977, p. 357.
2. Burington, R. S., *Handbook of Mathematical Tables and Formulas*, Fourth Edition, McGraw-Hill Book Company, 1965, pp. 77–102.
3. Design Manual DM—7, U.S. Navy Bureau of Yards and Docks, U.S. Government Printing Office, Washington, D.C., 1958, p. 7-5-4.
4. U.S.S. Steel Sheet Piling Design Manual, ADUSS 25-3848-04, Feb., 1974, p. 16.

EMBEDDED FOUNDATIONS UNDER VERTICAL VIBRATION

By A. Sridharan,[1] M. V. Nagendra[2] and C. Chinnaswamy[3]

INTRODUCTION

Foundations, especially those for machines, are usually embedded. For embedded footings, damping exists from the friction and adhesion at the side interface of the footing and the soil, in addition to that due to radiation. During translational movements, radiation damping is very large when compared with internal damping and hence it can be neglected. Exact solution for steady-state vibration of a system damped by a combination of dry and viscous friction (Fig. 1) has been given by Dem Hartog (2) for frequency independent excitation. Anandakrishnan and Krishnaswamy (1), following the same procedure, gave a solution for the case of frequency dependent excitation. The exact solution given in the previously cited sources is very complicated and lengthy.

In this note, a simplified procedure based on energy consideration, has been developed, for the solution of steady-state vibration of a system with combined viscous and Coulomb friction damping, subjected to frequency in dependent and frequency dependent excitation, which yields results essentially same as the exact solution. The proposed method uses equivalent damping (3) which assumes that if the damping in a system is small, the total damping effect can be represented by that of an equivalent damper.

Mass-Spring-Dashpot System with Coulomb Friction—Simplified Procedure.—The equation for steady-state vibration of a mass-spring-dashpot system with Coulomb friction (Fig. 1) is given by

$$M\ddot{X} + C\dot{X} + KX \pm F = Q(t) \quad \ldots\ldots\ldots\ldots\ldots\ldots\ldots\ldots\ldots\ldots (1)$$

in which M = mass; C = viscous damping coefficient; K = spring constant; F = Coulomb friction, and $Q(t) = Q_o$. Sin $(\omega t + \phi)$ = applied dynamic force, Q_o = force amplitude, ω = circular frequency, ϕ = phase difference of the dynamic force, $X = X_o \sin \omega t$ = displacement at any time t, X_o = displacement amplitude.

[1]Assoc. Prof., Dept. of Civ. Engrg., Indian Inst. of Science, Bangalore 560012, India.
[2]Research Scholar, Dept. of Civ. Engrg., Indian Inst. of Science, Bangalore 560012, India.
[3]Former Post-Grad. Student, Dept. of Civ. Engrg., Indian Inst. of Science, Bangalore 560012, India.

Note.—Discussion open until March 1, 1982. To extend the closing date one month, a written request must be filed with the Manager of Technical and Professional Publications, ASCE. Manuscript was submitted for review for possible publication on January 6, 1981. This paper is part of the Journal of the Geotechnical Engineering Division, Proceedings of the American Society of Civil Engineers, ©ASCE, Vol. 107, No. GT10, October, 1981. ISSN 0093-6405/81/0010-1429/$01.00.

Energy dissipated ΔE_1 due to viscous damping per cycle is

$$\Delta E_1 = \int_o^\tau (C\dot{X})\,\dot{X}\,dt \quad \ldots\ldots (2)$$

in which τ = the period of vibration. Integrating Eq. 2, the energy dissipated by viscous damping per cycle of vibration is given by

$$\Delta E_1 = C\omega\pi X_o^2 \quad \ldots\ldots (3)$$

Energy dissipated, ΔE_2 per cycle of vibration, due to Coulomb friction, F, is given by

$$\Delta E_2 = 4\,F\,X_o \quad \ldots\ldots (4)$$

Energy dissipated per cycle due to equivalent viscous damping C_{eq} (3) is given by

$$\Delta E = \pi\omega C_{eq} X_o^2 \quad \ldots\ldots (5)$$

from which $$C_{eq} = C + \frac{4F}{\pi\omega X_o} \quad \ldots\ldots (6)$$

Using this equivalent damping, Eq. 6, the equation of motion for a single degree

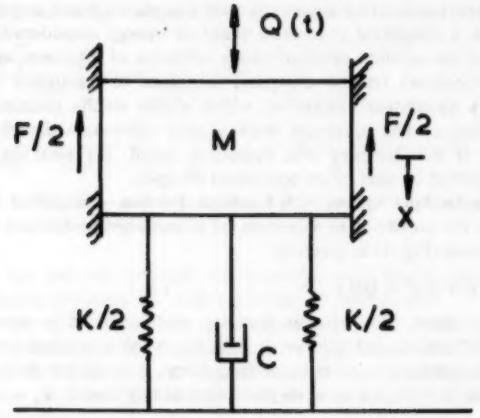

FIG. 1.—Mass-Spring Model with Combined Dry and Viscous Damping (Den Hartog)

of freedom, mass-spring-dashpot model can be written as

$$M\ddot{X} + C_{eq}\,\dot{X} + kX = Q(t) \quad \ldots\ldots (7)$$

Solving

$$X_o = \frac{Q_o}{[(K - M\omega^2)^2 + (C_{eq}\,\omega)^2]^{1/2}} \quad \ldots\ldots (8)$$

Elaborating

$$X_o = \frac{\frac{Q_o}{K}\left(-\frac{4}{\pi}\frac{C\omega}{K}\frac{F}{Q_o} \pm \left\{\left[\frac{4}{\pi}\frac{C\omega}{K}\frac{F}{Q_o}\right]^2 - \left[\left(1-\frac{M\omega^2}{K}\right)^2 + \left(\frac{C\omega}{K}\right)^2\right] \cdot \left[\left(\frac{4}{\pi}\frac{F}{Q_o}\right)^2 - 1\right]\right\}^{1/2}\right)}{\left[\left(1-\frac{M\omega^2}{K}\right)^2 + \left(\frac{C\omega}{K}\right)^2\right]} \quad \ldots\ldots\ldots\ldots\ldots (9)$$

The magnification factors $M_r = X_o M/me$, in which m = the eccentric mass; and e = the eccentricity; for frequency-dependent excitation and $M_c = X_o K/Q_o$ for frequency independent excitation are given by

$$M_r = \frac{-\frac{8D}{\pi}\frac{\omega}{\omega_n}\frac{F}{me\omega_n^2} \pm \left\{\left(\frac{8D}{\pi}\frac{\omega}{\omega_n}\frac{F}{me\omega_n^2}\right)^2 - \left[\left(1-\left(\frac{\omega}{\omega_n}\right)^2\right)^2 + \left(2D\frac{\omega}{\omega_n}\right)^2\right] \cdot \left[\left(\frac{4}{\pi}\frac{F}{me\omega_n^2}\right)^2 - \left(\frac{\omega}{\omega_n}\right)^4\right]\right\}^{1/2}}{\left\{\left[1-\left(\frac{\omega}{\omega_n}\right)^2\right]^2 + \left(2D\frac{\omega}{\omega_n}\right)^2\right\}} \quad (10)$$

and

$$M_c = \frac{-\frac{8D}{\pi}\frac{\omega}{\omega_n}\frac{F}{Q_o} \pm \left(\left(\frac{8D}{\pi}\frac{\omega}{\omega_n}\frac{F}{Q_o}\right)^2 - \left\{\left[1-\left(\frac{\omega}{\omega_n}\right)^2\right]^2 + \left(2D\frac{\omega}{\omega_n}\right)^2\right\} \cdot \left\{\left(\frac{4}{\pi}\frac{F}{Q_o}\right)^2 - 1\right\}\right)^{1/2}}{\left\{\left[1-\left(\frac{\omega}{\omega_n}\right)^2\right]^2 + \left(2D\frac{\omega}{\omega_n}\right)^2\right\}} \quad \ldots (11)$$

in which damping factor $D = C/2\,(KM)^{1/2}$. For steady-state vibration, the governing conditions are

$$\frac{F}{me\omega_n^2} < \frac{\pi}{4}\left(\frac{\omega}{\omega_n}\right)^2 \quad \ldots\ldots\ldots\ldots\ldots\ldots\ldots\ldots\ldots\ldots (12)$$

and

$$\frac{F}{Q_o} < \frac{\pi}{4} \quad \ldots\ldots\ldots\ldots\ldots\ldots\ldots\ldots\ldots\ldots\ldots\ldots (13)$$

for frequency dependent and frequency independent excitations respectively.

Conclusions

Figs. 2 and 3 present the variation of magnification factor for frequency independent and dependent excitation with frequency ratio, ω/ω_n, for D =

0.2 and for different frictional force ratios—(F/Q_o) or $F/me\omega_n^2$—obtained from the simplified method presented in this note. They are compared with the results obtained from Den Hartog (2) and Anandakrishnan and Krishnaswamy (1) respectively. It can be seen that the results obtained by the proposed method compare very well with the exact solution.

Figs. 4 and 5 present the relation between the magnification factor at resonance, and the frictional force ratio obtained from the proposed method, and from

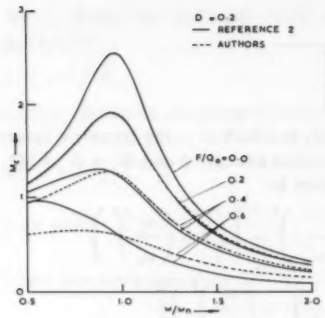

FIG. 2.—Variation of Magnification Factor M_r with ω/ω_n for Various Values of F/Q_o—Frequency Independent Excitation

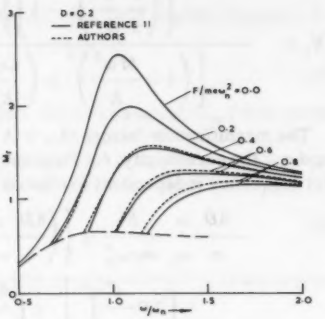

FIG. 3.—Variation of Magnification Factor M_r with ω/ω_n for Various Values of $F/me\omega_n^2$—Frequency Dependent Excitation

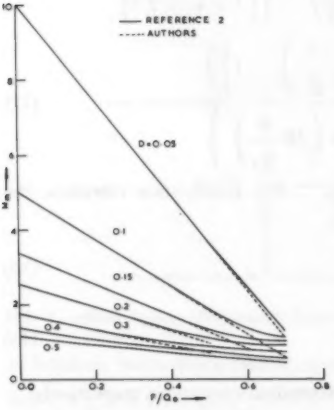

FIG. 4.—Variation of Magnification Factor at Resonance M_m with F/Q_o for Various Values of Damping Factor D—Frequency Independent Excitation

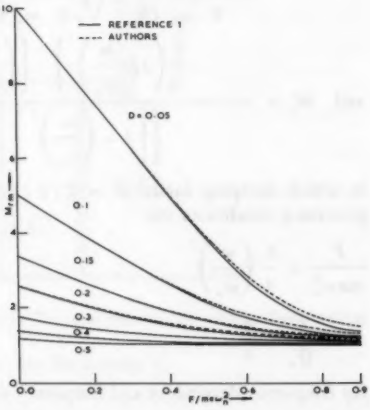

FIG. 5.—Variation of Magnification Factor at Resonance M_{rm} with $F/me\omega_n^2$ for Various Values of Damping Factor D—Frequency Dependent Excitation

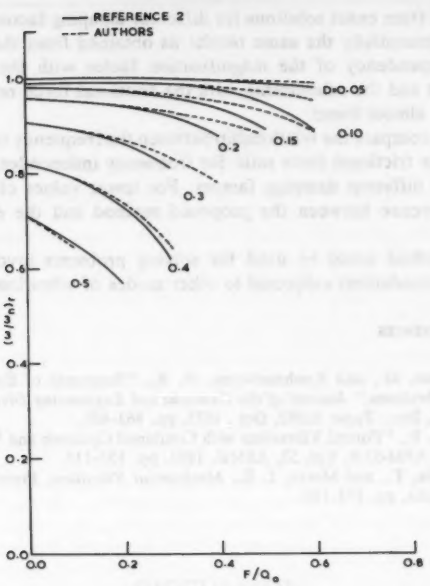

FIG. 6.—Variation of ω/ω_n at Resonance with F/Q_o for Various Values of Damping Factor D—Frequency Independent Excitation

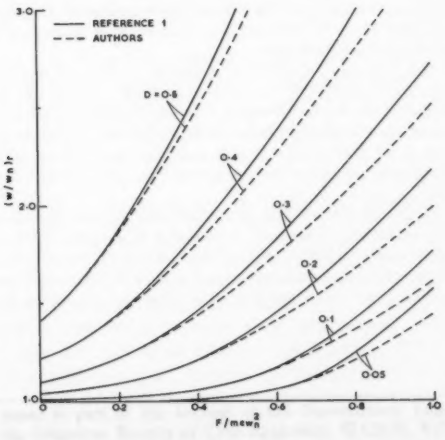

FIG. 7.—Variation of ω/ω_n at Resonance with $F/me\omega_n^2$ for Various Values of Damping Factor D—Frequency Dependent Excitation

those obtained from exact solutions for different damping factors. The proposed method gives essentially the same results as obtained from the exact solution. The strong dependency of the magnification factor with the frictional force ratio is evident and the relationship with the frictional force ratio up to a value of about 0.5 is almost linear.

Figs. 6 and 7 compare the relationship between the frequency ratio at resonance $(\omega/\omega_n)_r$ and the frictional force ratio for frequency independent and dependent excitations for different damping factors. For lower values of frictional force ratio, the difference between the proposed method and the exact solution is negligible.

The new method could be used for solving problems involving vibrations of embedded foundations subjected to other modes of vibration.

Appendix.—References

1. Anandakrishnan, M., and Krishnaswamy, N. R., "Response of Embedded Footings to Vertical Vibrations," *Journal of the Geotechnical Engineering Division*, ASCE, Vol. 99, No. SM10, Proc. Paper 10092, Oct., 1973, pp. 863–883.
2. Den Hartog, J. P., "Forced Vibrations with Combined Coulomb and Viscous Friction," *Transactions*, APM-53-9, Vol. 53, ASME, 1931, pp. 107–115.
3. Tse, R., Hinkle, T., and Morse, I. E., *Mechanical Vibration*, Prentice-Hall of India, New Delhi, India, pp. 173–180.

DISCUSSION

Note.—This paper is part of the Journal of the Geotechnical Engineering Division, Proceedings of the American Society of Civil Engineers, ©ASCE, Vol. 107, No. GT10, October, 1981. ISSN 0093-6405/81/0010-1437/$01.00.

Discussions

Discussions may be submitted on any Proceedings paper or technical note published in any *Journal* or on any paper presented at any Specialty Conference or other meeting, the *Proceedings* of which have been published by ASCE. Discussion of a paper/technical note is open to anyone who has significant comments or questions regarding the content of the paper/technical note. Discussions are accepted for a period of 4 months following the date of publication of a paper/technical note and they should be sent to the Manager of Technical and Professional Publications, ASCE, 345 East 47th Street, New York, N.Y. 10017. The discussion period may be extended by a written request from a discusser.

The original and three copies of the Discussion should be submitted on 8-1/2-in. (220-mm) by 11-in. (280-mm) white bond paper, typed double-spaced with wide margins. The length of a Discussion is restricted to two *Journal* pages (about four typewritten double-spaced pages of manuscript including figures and tables); the editors will delete matter extraneous to the subject under discussion. If a Discussion is over two pages long it will be returned for shortening. All Discussions will be reviewed by the editors and the Division's or Council's Publications Committees. In some cases, Discussions will be returned to discussers for rewriting, or they may be encouraged to submit a paper or technical note rather than a Discussion.

Standards for Discussions are the same as those for Proceedings Papers. A Discussion is subject to rejection if it contains matter readily found elsewhere, advocates special interests, is carelessly prepared, controverts established fact, is purely speculative, introduces personalities, or is foreign to the purposes of the Society. All Discussions should be written in the third person, and the discusser should use the term "the writer" when referring to himself. The author of the original paper/technical note is referred to as "the author."

Discussions have a specific format. The title of the original paper/technical note appears at the top of the first page with a superscript that corresponds to a footnote indicating the month, year, author(s), and number of the original paper/technical note. The discusser's full name should be indicated below the title (see Discussions herein as an example) together with his ASCE membership grade (if applicable).

The discusser's title, company affiliation, and business address should appear on the first page of the manuscript, along with the *Proceedings* paper number of the original paper/technical note, the date and name of the *Journal* in which it appeared, and the original author's name.

Note that the discusser's identification footnote should follow consecutively from the original paper/technical note. If the paper/technical note under discussion contained footnote numbers 1 and 2, the first Discussion would begin with footnote 3, and subsequent Discussions would continue in sequence.

Figures supplied by the discusser should be designated by letters, starting with A. This also applies separately to tables and references. In referring to a figure, table, or reference that appeared in the original paper/technical note use the same number used in the original.

It is suggested that potential discussers request a copy of the *ASCE Authors' Guide to the Publications of ASCE* for more detailed information on preparation and submission of manuscripts.

Particle Contacts in Discrete Materials[a]

Discussion by Roland Gourves[3]

The experimental technique developed by the authors seems to be extremely interesting. However it does not appear that the results obtained can only be analysed qualitatively as indicated by the authors. In fact a granular material can be considered as isotropic in so far as its uniformity coefficient is superior to 5, which is normally quite common. It is then obvious that the structural joint of the particles is stochastic, which means that the mean number of contacts per particle, N_c, is equal to six. This is due to the fact that the structure made up by the particles is isostatic if the presence of inactive particles is ignored (these being the particles which can be extracted from the mixture without any geometrical modification).

The writer thinks that there is no definite relation between N_c and n. The variable, N_c, depends on the arrangement of the particles (stochastic, cubic, hexagonal . . .); n depends on the granulometry of the material, the shape of the particles, their mineralogic nature, the size of the mould containing the material, and essentially the energy exerted, including the specific weight.

A number of contacts superior to six probably results from the fact that in some places in the material, geometrical arrangement have occured. Besides, a number of particles do exist in stochastic structures which can be very close to one another without being in contact. The experimental technique and the viscosity of paint might explain the fact that such cases are considered as real contacts.

Finally the writer wishes to congratulate the authors for their fine study on the relative displacements between particles. The experimental technique seems very promising and should lead to better approach in the knowledge of the difficult problem of the relative movement of particles in granular material.

Discussion by Robert D. Holtz,[4] M. ASCE

The author's observation that the product of the number of contacts per particle, N_c, and the porosity, n, is approximately three is most intriguing, and it prompted the writer to look at some other data. These data suggest that the relationship may not be so simple. For example, Oda (4) in his studies of coordination number (average number of contacts per particle) and shear strength reported on some experiments with glass spheres. These data are summarized in Table 1. Only in a few cases does the product, $N_c \times n$ (Col.

[a]May, 1980, by Dimitri Athanasiou-Grivas and Milton E. Harr.

[3]Asst. Dir., Dept. of Civ. Engrg., Univ. of Clermont II, Clermont-Fd, France.
[4]Assoc. Prof., School of Civ. Engrg., Purdue Univ., West Lafayette, Ind. 47907.

TABLE 1.—Data on Glass Spheres from Oda (1977)

Description (1)	Void ratio, e (2)	Porosity, n (3)	Average number of contacts, N_c (4)	$N_c \times n$ (5)
Uniform diameter	0.612	0.38	7.26	2.76
	0.605	0.38	6.90	2.60
	0.692	0.41	6.67	2.73
	0.807	0.45	5.33	2.38
	0.950	0.49	4.00	1.95
	1.080	0.52	3.70	1.92
	1.313	0.57	2.77	1.57
	2.205	0.66	1.40	0.96
Two different diameters (5.2 mm and 12.3 mm)	0.612	0.38	7.26	2.76
	0.618	0.38	7.41	2.82
	0.589	0.37	7.30	2.70
	0.536	0.35	7.28	2.55
	0.517	0.34	7.55	2.57
	0.513	0.34	8.16	2.77
	0.580	0.37	7.89	2.92
	0.560	0.36	7.56	2.72
Four different diameters (5.2 mm, 12.3 mm, 16.4 mm, and 24.7 mm)	0.469	0.32	8.24	2.64
	0.456	0.31	8.91	2.76
	0.512	0.34	8.38	2.85

TABLE 2.—Data on 10 Granular Soils from Marsal (1973)

Material (1)	Effective size D_{10}, in millimeters (2)	Coefficient of uniformity, C_u (3)	Initial void ratio, e (4)	Porosity, n (5)	Average number of contacts, N_c (6)	$N_c \times n$ (7)
Pinzardarán sand and gravel	0.27	113	0.29	0.22	5.36	1.20
Malpaso conglomerate	0.22	81.8	0.42	0.30	5.36	1.59
Mica granitic gneiss gradation X	3.80	19.2	0.31	0.24	5.32	1.26
San Francisco basalt gradation 2	1.06	18.9	0.30	0.23	6.27	1.45
El Infiernillo silicified conglomerate	7.50	11.5	0.45	0.31	5.64	1.75
San Francisco basalt gradation 1	0.96	11.5	0.34	0.25	6.71	1.70
El Granero slate gradation A	11.0	9.8	0.45	0.31	5.94	1.84
El Infiernillo diorite	12.5	7.7	0.48	0.32	6.15	1.99
El Granero slate gradation B	26.0	4.2	0.64	0.39	7.71	3.01
Mica grantic gneiss gradation Y	50.0	2.4	0.58	0.37	9.96	3.66

5), approach three most of the time, especially for looser packings, the product is significantly less than three. From a comprehensive study by Marsal (3) of ten granular materials primarily from rock-fill dams (Table 2), it appears that the average value of the product, $N_c \times n$ (Col. 7), may be two or less, rather than three.

These data are plotted on the authors' Fig. 9. Neither the linear nor the proposed hyperbolic relationship fits these data very well. Can the authors explain this apparent discrepancy? Are Oda's glass spheres and Marsal's real rock-fill materials that different from the materials previously examined by the authors and others? Since the deviation seems to be greatest for very loose and very

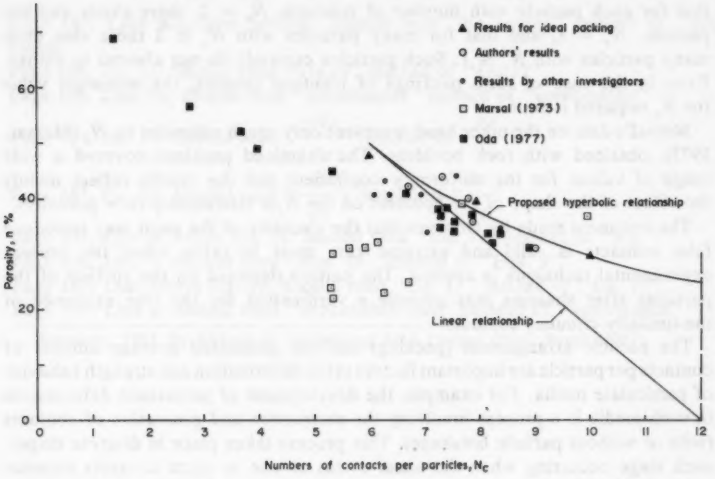

FIG. 9.—Relation between Porosity n and Number of Contacts per Particle N_c, with additional data by Marsal (1973) and Oda (1977)

dense packings, should relative density or density index somehow be considered in the proposed relationship?

APPENDIX.—REFERENCES

3. Marsal, R. J., "Mechanical Properties of Rockfill," *Embankment-Dam Engineering, Casagrande Volume*, R. C. Hirschfeld and S. J. Poulos, Eds., John Wiley & Sons, New York, N.Y., 1973, pp. 109–200.
4. Oda, M., "Co-ordination Number and Its Relation to Shear Strength of Granular Material," *Soils and Foundations*, Tokyo, Japan, Vol. 17, No. 2, June, 1977, pp. 29–42.

Closure by Dimitri A-Grivas,[5] A. M. ASCE and Milton E. Harr,[6] M. ASCE

The writers thank both Holtz and Gourves for their interesting comments on the experimental technique employed and the results obtained in this study.

Indeed, some of Oda's data mentioned by Holtz are different from those examined as they correspond to packings of glass spheres made under special conditions. The writers were aware of these results at the time of their study, they chose however not to include them in their analysis. How could there exist a real soil with an average value for the number of contacts per particle, $\bar{N}_c$, approximately equal to 1.5 (left-most point in the figure)? That would mean that for each particle with number of contacts, $\bar{N}_c = 2$, there exists another particle, $N_c = 1$, and that for many particles with $N_c \geq 2$ there also exist many particles with $N_c \leq 1$. Such particles certainly do not abound in nature. Even in the case of ideal packings of identical spheres, the minimum value for N_c required is four.

Marsal's data on the other hand represent only rough estimates on $\bar{N}_c$ (Marsal, 1973), obtained with rock boulders. The examined packings covered a wide range of values for the uniformity coefficient and the results reflect mainly the effect of the shape of the boulders on the $\bar{N}_c$-n relationship (n = porosity).

The comment made by Gourves that the viscosity of the paint may introduce false contacts is valid and extreme care must be taken when the present experimental technique is applied. The pattern depicted on the surface of the particles after shearing may provide a verification for the true existence of the (initially circular) contacts.

The particle arrangement (packing) and the associated average number of contacts per particle are important factors in the deformation and strength behavior of particulate media. For example, the development of permanent deformation in such media is a process involving the *destruction* and *generation* of contacts (with or without particle breakage). This process takes place in discrete stages, each stage occurring when the shear stress at one or more contacts exceeds a thrusthold value (i.e., the available frictional resistance). Although there exists no physical relationship between the number of contacts per particle and porosity, a relationship between their statistical representatives, $\bar{N}_c$ and n (n is also an average quantity) may be sought through a statistical analysis of measurements taken on many packings.

There are many factors on which $\bar{N}_c$ depends, the uniformity coefficient mentioned by Gourves being one of them. To uncover the effect of each of these factors on the $\bar{N}_c$-n relationship and, subsequently, on the deformation and strength behavior of particulate media requires a considerable amount of additional experimental as well as theoretical study on the subject.

[1]Assoc. Prof., Dept. of Civ. Engrg., Rensselaer Polytechnic Inst., Troy, N.Y. 12181.
[2]Prof., School of Civ. Engrg., Purdue Univ., W. Lafayette, Ind. 47907.

Response of Buried Structures to Traveling Waves[a]

Errata

The following corrections should be made to the original paper:

Page 185, Line 4th from bottom: Should read "no longer" instead of "not longer"
Page 186, Eq. 11: Should read "$x(s,t)$" instead of "$x(x,t)$"
Page 186, Line 16: Should read "coordinates" instead of "corrdinates"
Page 187, Eq. 15: Should read "$\frac{-\partial y}{\partial s}$" instead of "$\frac{\partial y}{\partial s}$"
Page 187, Eq. 15: Should read "$\frac{-\partial x}{\partial t}$" instead of "$\frac{\partial x}{\partial t}$"
Page 187, Line 4, below Eq. 18: Should read "Eq. 17" instead of "Eq. 7"
Page 188, Line 1: Should read "Eqs. 19" instead of "Eqs. 9"
Page 189, Line above Eq. 29: Should read "Eq. 17" instead of "Eq. 7"
Page 190, Line 2: Should read "approaches zero" instead of "approaches"

[a]February, 1981, by Richard N. Hwang and John Lysmer (Proc. Paper 16052).